

Liverpool John Moores University

Investigating the Spectroscopic Diversity of Luminous Peculiar Type Ia Supernovae

by

Charles J.Aouad

A thesis submitted in partial fulfillment for the
degree of Doctor of Philosophy

in the
Faculty of Science
Astrophysics Research Institute

October 2026

Declaration

The work presented in this thesis was carried out at the Astrophysics Research Institute, Liverpool John Moores University. Unless otherwise stated, it is the original work of the author.

While registered as a candidate for the degree of Doctor of Philosophy, for which submission is now made, the author has not been registered as a candidate for any other award. This thesis has not been submitted in whole, or in part, for any other degree.

CHARLES J.AOUAD
Astrophysics Research Institute
Liverpool John Moores University
Twelve Quays House
Egerton Wharf
Birkenhead
CH41 1LD
UK

October 2026

Abstract

Despite their importance as cosmological probes, the nature of Type Ia supernovae (SNe Ia) remains elusive. While many of these objects are classified as "normal" owing to their relatively homogeneous photometric and spectroscopic properties, growing observational samples have revealed a diverse population of peculiar events spanning a wide range of properties, leading to the identification of several spectroscopic subclasses. This diversity challenges the notion that they arise from a single progenitor–explosion channel. Understanding the physical origin of this diversity is particularly important for the most luminous events, due to their importance for cosmology. This thesis investigates the spectroscopic diversity of luminous peculiar SNe Ia through abundance tomography, a technique that reconstructs the chemical structure of the ejecta from modeling a time-series of spectra. Particular emphasis is placed on objects exhibiting properties that bridge multiple spectroscopic subclasses, in particular, the transitional SN 1999aa, the peculiar 91T-like event iPTF16abc, and the 03fg-like SN 2012dn. SN 1999aa and iPTF16abc reveal an ejecta structure shared with SN 1991T, characterised by the confinement of intermediate-mass elements to a narrow velocity shell. This suggests that the transition from normal to 91T-like SNe Ia cannot be explained by a simple luminosity sequence, but instead requires a distinct outer ejecta structure produced by a sharp decline in burning efficiency. While the progression from SN 1999aa to SN 1991T can largely be understood as a luminosity sequence within this common abundance structure, the lower outer iron abundance and deeply carbon pockets inferred for iPTF16abc despite its luminosity being comparable to that of SN 1991T suggest that variations in burning and ejecta structure contribute to the diversity even within the 91T-like subclass. The inferred kinetic energies and central concentrations of stable neutron-rich Fe-group elements support Chandrasekhar-mass progenitors with a common inner ejecta structure,

while variations in the outer layers, suggest an explosion scenario that modifies only the outer layers.

SN 2012dn contains a central oxygen-rich region and an ejecta mass exceeding the Chandrasekhar limit, strongly favouring a double-degenerate merger origin. The inferred ^{56}Ni mass is insufficient to account for its luminosity, suggesting an additional contribution from interaction with a carbon-rich circumstellar medium. More broadly, these results suggest that mergers may provide a common framework for the 03fg-like subclass, with their diversity reflecting variations in both ^{56}Ni production and the strength of ejecta–circumstellar-medium interaction. The exceptionally low iron abundance inferred in the outer ejecta further points to a sub-solar metallicity progenitor, supporting the picture that 03fg-like events originate in metal-poor environments.

Taken together, these results suggest that luminous peculiar SNe Ia do not form a single continuous sequence governed by a smoothly varying parameter such as luminosity, but instead arise from variations in progenitor and explosion mechanisms that produce overlapping observational properties across nominally distinct subclasses.

Publications

In the course of completing the work presented in this thesis, the contents of Chapters 4, 5 have been submitted and accepted for publication in a refereed journal and chapter 6 has been submitted and is under review :

Aouad, C. J., Mazzali, P. A., Hachinger, S., Teffs, J., Pian, E., Ashall, C., Benetti, S., Filippenko, A. V. & Tanaka, M., 2022, 'Abundance stratification in Type Ia supernovae – VI. The peculiar slow decliner SN 1999aa', *Monthly Notices of the Royal Astronomical Society*, 515, 4445.

Aouad, C. J., Mazzali, P. A., Ashall, C., Tanaka, M.& Hachinger, S., 2024, 'Abundance stratification in Type Ia supernovae – VII. The peculiar, C-rich iPTF16abc: highlighting diversity among luminous events', *Monthly Notices of the Royal Astronomical Society*, 529, 3838.

Aouad, C. J., Mazzali, P. A., Hachinger, S. & Ashall, C., 2026, 'Abundance stratification in Type Ia supernovae – VIII. The 03fg-like SN 2012dn: a double-degenerate merger interpretation', submitted to *Monthly Notices of the Royal Astronomical Society* ***(under review)***.

Acknowledgements

I extend my heartfelt gratitude to my supervisor, Paolo Mazzali, whose unwavering support made this journey possible despite numerous challenges. I am deeply thankful to him for providing me with the opportunity to pursue this PhD, for turning my dream into reality, for constantly challenging my thinking, pushing me beyond my limits, and for embodying the spirit of a true chevalier. I also express my sincere appreciation to P.A. James for his genuine support, wisdom, and encouragement, for fostering belief in my abilities, and for granting me the opportunity to publish my first work, a challenge I once doubted myself capable of, yet one that gave me the confidence to pursue my passion for astrophysics.

I am indebted to all my collaborators and co-authors for their invaluable insights and guidance.

I owe a deep gratitude to my mother, Marie, who raised us with love, and who gave me the freedom to grow with an independent mind, a gift that has shaped who I am throughout my life. Then to my father, Joseph, who ignited my passion for astronomy at a small age by purchasing my first astronomy book for 100 LL in 1984, a sum worth little more than a tenth of a US cent today, yet a gift whose value has proven immeasurable. That book remains a cherished possession to this day. To my wife, Shereen, I am profoundly grateful for her unwavering support, patience, and understanding throughout this journey, despite the inevitable stresses it brought into our lives. Without her constant encouragement, this achievement would not have been possible. To my children, Jo, Mark, and Karl, whose presence has been a constant source of joy and pride.

Lastly, I extend my appreciation to my extended family, my true friends and all those who have contributed to my journey in ways both visible and unseen.

Declaration of Authorship

I, Charles J. Aouad, declare that this thesis titled, 'Investigating the Spectroscopic Diversity of Luminous Peculiar Type Ia Supernovae' and the work presented in it are my own. I confirm that:

- This work was done wholly or mainly while in candidature for a research degree at this University.
- Where any part of this thesis has previously been submitted for a degree or any other qualification at this University or any other institution, this has been clearly stated.
- Where I have consulted the published work of others, this is always clearly attributed.
- Where I have quoted from the work of others, the source is always given. With the exception of such quotations, this thesis is entirely my own work.
- I have acknowledged all main sources of help.
- Where the thesis is based on work done by myself jointly with others, I have made clear exactly what was done by others and what I have contributed myself.

Signed:
Charles J. Aouad

Date:
28 July 2026

"He had only heard of dragons, and although he had never seen one, he was sure they existed."

Dee Marie, Sons of Avalon: Merlin's Prophecy

"I beg you, to have patience with everything unresolved in your heart and to try to love the questions themselves as if they were locked rooms or books written in a very foreign language. Don't search for the answers, which could not be given to you now, because you would not be able to live them. And the point is to live everything. Live the questions now. Perhaps then, someday far in the future, you will gradually, without even noticing it, live your way into the answer."

Rainer Maria Rilke, Letters to a Young Poet (1929)

Contents

Declaration ii

Abstract iii

Publications v

Acknowledgements vi

Declaration of Authorship vii

List of Figures xiii

List of Tables xxiv

Abbreviations xxv

Physical Constants xxvii

Symbols xxviii

1 Introduction and Scientific Context 1

1.1 Introduction . . . 1
1.2 Historical background . . . 3
1.3 SNe classification . . . 6
1.4 The importance of Type Ia supernovae . . . 9
1.4.1 Astrophysical relevance . . . 9
1.4.2 Type Ia Supernovae in Cosmology . . . 10

2 Observational and theoretical aspects 15

2.1 Light curves of type Ia supernovae . . . 16
2.1.1 Physical Drivers of Light-Curve Evolution . . . 18
2.1.1.1 Early-Time Emission and Shock Breakout . . . 19
2.1.1.2 Radioactive Energy Deposition and Diffusion . . . 20
2.1.1.3 Peak Luminosity and Light-Curve Width . . . 23
Peak Luminosity . . . 24
Light-Curve Width and the Phillips Relation . . . 26
2.2 Spectra of type Ia supernovae . . . 28

2.2.1 The photospheric phase . . . 28
2.2.2 The nebular phase . . . 29
2.3 Diversity and Empirical Classification Schemes of SNe Ia . . . 31
2.3.1 Diversity . . . 31
2.3.1.1 Normal SNe Ia . . . 31
2.3.1.2 1991T-like . . . 33
2.3.1.3 1991bg-like . . . 34
2.3.1.4 SN 2003fg-like or super-Chandrasekhar SNe Ia . . . 37
2.3.1.5 SN 2002cx-like: Type Iax Supernovae . . . 39
2.3.1.6 SNe Ia-CSM: SN 2002ic-like . . . 39
2.3.2 Empirical Classification Schemes . . . 40
2.3.2.1 Nugent et al. (1995a) Line ratio classification . . . 40
2.3.2.2 Benetti et al. (2005): Velocity gradient classification . . . 41
2.3.2.3 Branch et al. (2006): Spectral pEW Classification . . . 42
2.3.2.4 Wang et al. (2009): Velocity-based classification . . . 42
2.3.2.5 Colour-Stretch s_{BV} and i-Band Maximum Timing . . . 43
2.4 Progenitors . . . 44
2.4.1 Composition . . . 45
2.4.2 Mass . . . 46
2.4.2.1 Near Chandrasekhar mass progenitor . . . 46
2.4.2.2 Sub-Chandrasekhar mass progenitor . . . 47
2.4.2.3 Super-Chandrasekhar mass progenitor . . . 48
2.4.3 Binary scenarios . . . 49
2.4.3.1 The Single-Degenerate (SD) scenario: . . . 49
2.4.3.2 The Double-Degenerate (DD) scenario: . . . 52
2.4.3.3 The Core-Degenerate (CD) scenario: . . . 55
2.5 SNe Ia host galaxies . . . 57
2.6 Explosion mechanisms and nucleosynthesis . . . 58
2.6.1 Explosion mechanism . . . 58
2.6.1.1 Pre-Explosive Evolution: Smoldering and Dynamical Runaway . . . 58
2.6.1.2 Deflagrations . . . 59
2.6.1.3 Detonation . . . 59
2.6.1.4 Deflagration-to-Detonation Transition (DDT) . . . 60
The Zorro diagram . . . 60
2.6.1.5 Pulsation driven explosions . . . 61
2.6.1.6 Double detonation models . . . 63
2.6.2 Explosive Nucleosynthesis . . . 64

3 Spectral Modeling of Type Ia Supernovae **67**
3.1 Radiative transfer . . . 67
3.1.1 Specific and mean Intensity . . . 67
3.1.2 The radiative transfer equation . . . 68
3.2 MC code . . . 70
3.2.1 Radiative Transfer in Supernova Ejecta . . . 70
3.2.1.1 Homologous Expansion and the Velocity Law . . . 70
3.2.1.2 The Sobolev Approximation . . . 71

3.2.2 Concept of the Monte–Carlo Radiative–Transfer Code 72
3.2.3 Photospheric Boundary, Initial Conditions, and Line List Initialisation. 73
3.2.4 Ionization, Excitation, and Line Optical Depth Calculation. 76
3.2.5 Radiation Field and Temperature Update. 77
3.2.6 The Monte Carlo experiment. 77
Photon Packet Initialization 78
Propagation and Event Selection 78
3.3 Modelling techniques 79
Distance modulus 80
Extinction 81
Rise time 81
$L_{\rm bol}$ and $v_{\rm ph}$ 82

4 SN1999aa **84**
4.1 Introduction 84
4.2 Data 85
4.3 Modeling set up 86
4.3.1 Spectra photo-calibration 86
4.3.2 Distance, extinction and rise time 88
4.4 The photospheric phase 89
4.4.1 The early-time spectra 89
4.4.2 Pre-maximum-light spectra 94
4.4.3 Spectra at maximum brightness 95
4.4.4 Post-maximum-light spectra 98
4.5 Spectra in the nebular phase 99
4.6 Abundance tomography 101
4.7 Light curve 104
4.7.1 Building the bolometric light curve 104
4.7.2 Modelling the bolometric light curve 105
4.8 Conclusions 107

5 iPTF16abc **113**
5.1 Motivation 113
5.2 Data 114
5.3 The photospheric phase 115
5.3.1 The pre-maximum spectra 117
5.3.2 Post-maximum spectra 125
5.4 A modified density profile 129
5.5 The nebular phase 131
5.6 Abundance tomography 132
5.7 Bolometric light curve 135
5.7.1 Construction of the observed bolometric light Curve 135
5.7.2 Modelling the bolometric light curve 137
5.8 Conclusions 137

6 SN 2012dn **146**

6.1 Motivation . . . 146
6.2 Data . . . 147
6.2.1 Host Galaxy, Distance, and Reddening . . . 147
6.2.2 Spectra . . . 148
6.2.3 Photometric Evolution and Late-Time Dimming . . . 150
6.3 Photospheric phase models . . . 151
6.3.1 The pre-maximum spectra . . . 152
6.3.2 The spectra near maximum light . . . 158
6.3.3 The spectra post-maximum light . . . 164
6.3.4 Comparison Between W7 and DD profiles: Density structure and its effect on line formation . . . 166
6.4 The Nebular Phase . . . 167
6.5 Estimating of the Bolometric Dimming Factor . . . 169
6.6 Abundance Tomography . . . 170
6.7 Bolometric Light Curve . . . 170
6.8 Viable Progenitor-Explosion Channels . . . 172
6.9 Conclusions . . . 176

7 Conclusions and future work **179**
7.1 Conclusions . . . 179
7.2 Future work . . . 182

A Derivation of the Arnett's law **186**

Bibliography **190**

List of Figures

1.1 Supernovae classification scheme 7

1.2 Representative spectra of the main supernova types near maximum light, illustrating the key spectral features used for classification. From bottom to top: Type Ia (SN 2003du), Type Ib (SN 2008D), Type Ic (SN 1994I), and Type IIP (SN 1999em). Spectra are offset vertically for clarity. The principal line identifications are marked for each type. 8

1.3 The observed fractions of the subclasses of SNe in an ideal magnitude-limited sample. (Li et al., 2011a) 9

1.4 The observed fractions of the subclasses of SNe in a volume-limited sample. (Li et al., 2011a) 9

1.5 Hubble diagram for 329 SNe from the Dark Energy Survey Supernova Program (DES-SN) sample. Top: distance modulus μ versus redshift, z. Black bars, represent weighted-average bias-corrected distance moduli in 18 redshift bin while individual SNe are depicted in red and orange circles. The dashed gray line shows the best-fit model, while the green and blue dotted lines show models with no dark energy and matter densities of Ω_m and 1.0 respectively. Bottom: residuals to the best-fit model; 1σ error bars show 68% confidence (Abbott et al., 2019). 14

2.1 Comparative UBVRI light curves of SN 1999aa, SN 2003du, and SN 2012dn, plotted as a function of phase relative to B-band maximum and normalized to their peak magnitudes. 16

2.2 Peak absolute magnitude M_B as a function of the decline-rate parameter $\Delta m_{15}(B)$ for a sample of SNe Ia. Different symbols and colours indicate the various spectroscopic subclasses. The data are compiled from the Carnegie Supernova Project (CSP; (Ashall et al., 2020, 2021, Bose et al., 2025, Phillips et al., 2022)), and include both normal and peculiar subclasses reproduced from publicly available data. 18

2.3 Peak absolute magnitude M_B as a function of the colour-stretch parameter s_{BV} for a sample of SNe Ia. Different symbols and colours represent the various spectroscopic subclasses. A clear correlation is observed, analogous to the Phillips relation, with s_{BV} providing a more robust description of fast-declining events. The data are drawn from the Carnegie Supernova Project (CSP; (Ashall et al., 2021, Bose et al., 2025)). 19

2.4 Schematic bolometric light curves (solid lines) and instantaneous ^{56}Ni+^{56}Co radioactive energy input rates $\epsilon_{\rm rad}$ (Equation 2.12, dashed lines) for different values of synthesised ^{56}Ni mass illustrating the physical regimes discussed in the text. 23

2.5 Formation of a P Cygni profile in an expanding supernova ejecta. *Left:* Decomposition of the profile into a symmetric emission component centred at the rest wavelength λ_0, produced by the full expanding shell, and a blue-shifted absorption trough at $v \approx -v_{\max}$, caused by absorption along the line of sight; their superposition yields the characteristic P Cygni profile. *Right:* Schematic geometry illustrating how the approaching ejecta column between the photosphere and the observer produces the blue-shifted absorption, while the remainder of the shell contributes to the emission peak. 29
2.6 Spectra of the normal SN 2003du at day −11 (top) and day +1 (bottom) relative to B-band maximum light, with the major spectral features identified and their corresponding rest wavelengths indicated. 32
2.7 Comparison of the early-time spectra of different SNe Ia subtypes, including 03fg-like, 91T-like, normal, and 91bg-like events, with the major spectral features identified. 35
2.8 Same as Fig. 2.7, but showing the spectra near maximum light. 36
2.9 Same as Fig. 2.7, but showing the spectra at the nebular phase. 37
2.10 The colour-stretch parameter s_{BV} as a function of the epoch difference between the i- and B-band maxima ($t_i^{\max} - t_B^{\max}$) for a sample of SNe Ia. Different symbols and colours denote the various spectroscopic subclasses, which occupy distinct regions of the parameter space. This representation highlights the ability of s_{BV}, combined with the timing of the i-band maximum, to discriminate between normal and peculiar SNe Ia. Data from the Carnegie Supernova Project (CSP; (Ashall et al., 2020)), reproduced with permission. 44
2.11 The "Zorro" diagram showing the distribution of the main burning products in SNe Ia as a function of the decline-rate parameter $\Delta m_{15}(B)$. SNe are colour-coded according to their velocity evolution: HVG (blue), LVG (green), and faint events (red). Open circles represent stable Fe-group material, filled circles correspond to ^{56}Ni, open triangles indicate the total NSE mass, and crosses show the total burned mass (NSE + IMEs). The diagram reveals an inverse relationship between the masses of IMEs and ^{56}Ni, while the total mass processed by nuclear burning remains approximately constant. This behaviour is difficult to reconcile with a pure deflagration, in which more energetic explosions would be expected to burn a larger fraction of the white dwarf, increasing both the ^{56}Ni and IME yields and producing significant variations in the total burned mass. Instead, the observed anti-correlation suggests that luminosity variations arise primarily from a redistribution of burned material between NSE and IME products. In a delayed-detonation scenario, differences in the degree of pre-expansion determine the density at which the detonation propagates, regulating whether burning proceeds to NSE or terminates at IMEs while maintaining a nearly constant total burned mass. Figure taken from Mazzali et al. (2007), reproduced with permission. 62

3.1 Iteration scheme of the Monte Carlo radiative-transfer code. The photospheric temperature and initial radiation field are established in steps (1) and (1b). Photon packets then propagate through the ejecta via Thomson scattering, Sobolev line interactions, and photon branching (2). Ionization, excitation, and Sobolev optical depths are updated in each shell via the modified nebular approximation (3). The frequency moment yields T_R (4), from which W is derived (5). If not converged, the MC experiment restarts; once T_R, W, and shell luminosities have converged (6), the emergent spectrum is obtained from a formal solution of the radiative transfer equation. 74
3.2 This plot illustrates the effect of reddening on the synthetic spectra, where $E(B-V)$ values are varied in steps of 0.02. The example corresponds to the earliest available spectrum of SN 2012dn at day −14. 81
3.3 Effect of varying the rise time on the synthetic spectra: the longer rise-time model (red) produces a redder spectrum, while the shorter rise-time model (blue) is bluer and more highly ionised, exhibiting weak singly ionised IME features and stronger Si III. The positions of the C II and Si III lines near 6300 and 4300 Å are marked for each model in the corresponding colour; in the shorter rise-time model, these features are blueshifted to higher velocities. 83

4.1 *Left:* Early-time spectra of SN 1991T (top), SN 1999aa (middle), and the normal SN 2003du (bottom). Major absorption features are marked, and epochs are given in days relative to B-band maximum brightness. *Right:* Same comparison, but for spectra obtained near maximum light. 85
4.2 Example of the photometric calibration of the SN 1999aa spectrum at day −10. The original spectrum is shown in black, while the calibrated spectrum is shown in red. The calibration is achieved by matching the synthetic photometry of the spectrum to the observed broadband photometry through a smooth wavelength-dependent correction. 88
4.3 The three density profiles used in the modelling: W7 (Nomoto et al., 1984), DD2, and DD3 (Iwamoto et al., 1999). Vertical dashed lines mark the photospheres of the synthetic spectra. 89
4.4 Early-time spectra. Epochs are shown with reference to B maximum. Features in the −10.2 day spectrum near 6780 Å (very weak) and 7500 Å (weak) are telluric. The spectra have been shifted in flux by a constant value. The horizontal dashed lines mark the zero flux for each epoch. . . . 90
4.5 A close-up view of the day −11 spectrum showing the region where the strongest Fe III lines are seen. Adding small packets of stable Fe, the Fe mass fraction can be inferred. 91
4.6 A close-up view of the Ca II H&K region, showing the observed spectrum at day −11 compared to models computed with the W7 density profile using different abundances of Ca coupled with various amounts of H in the outermost shells. 92
4.7 Effect of adding hydrogen at the outer shells on the earliest spectrum. A hydrogen mass fraction in the range of 0.3 will give rise to an Hα feature that is not seen in the observed data. 93
4.8 A close-up view of the spectrum showing the Si II–C II region. Small amounts of carbon can create an absorption line redward of the Si II line. A prominent C line is not seen in the observed spectrum. 94

4.9 Spectra one week before B-band maximum. Epochs are shown with reference to B maximum. Features in the -6.2 day spectrum near 6780 Å (weak) and 7500 Å are telluric. The spectra have been shifted in flux by a constant value. The horizontal dashed lines mark the zero flux for each epoch. 95
4.10 Pre-maximum-brightness spectra. Epochs are shown with reference to B maximum. The spectra have been shifted in flux by a constant value. The horizontal dashed lines mark the zero flux for each epoch. 96
4.11 Near-maximum-light spectra. Epochs are shown with reference to B maximum. Features in the $+1.8$ day spectrum near 6780 Å (weak) and 7500 Å are telluric. The spectra have been shifted in flux by a constant value. The horizontal dashed lines mark the zero flux for each epoch. 97
4.12 Post-maximum-light spectra. Epochs are shown with reference to B maximum. Features in the $+7.8$ day spectrum near 6780 Å (very weak) and 7500 Å (weak) are telluric. The spectra have been shifted in flux by a constant value. The horizontal dashed lines mark the zero flux for each epoch. 98
4.13 Nebular-phase spectra obtained on 1999 Nov. 9 (left) and Dec. 5 (right), corresponding to 255 and 281 rest-frame days after B maximum brightness, respectively. The emissions near 5200 and 7200 Å are dominated by [Fe II] lines, while the emission near 4700 Å is dominated by [Fe III]. The blue, green, and red curves represent synthetic spectra from DD3, DD2, and W7 models. 99
4.14 Upper panel: abundances obtained from spectral models using the delayed detonation DD2 density profile. Lower panel: the original nucleosynthesis from DD2 (Iwamoto et al., 1999). 103
4.15 Spectral energy distributions (SEDs) of SN 1999aa at four epochs (days -11, -7, -2, and $+17$ relative to B-band maximum), constructed from $UBVRI$ photometry. The shaded regions indicate the contribution of each wavelength interval to the pseudo-bolometric flux over the range 3000–10,000 Å. 105
4.16 The $UBVRI$ bolometric light curve of SN 1999aa (black dots), compared to the synthetic light curves computed using the density and abundance profiles of the three explosion models: W7 (red), DD2 (green), and DD3 (blue). Red points represent luminosities at the epochs when NIR observations are available from Krisciunas et al. (2000) 106
4.17 The bolometric light curve of SN 1999aa (green) compared to those of SN 1991T (Sasdelli et al., 2014, blue) and SN 2003du (Stanishev et al., 2007, red). The UV contribution was removed from the light curve of SN 2003du to allow a proper comparison, as no UV information is available for the other two SNe. Error bars for SN 1999aa and SN 1991T represent statistical errors due to distance moduli uncertainties $\delta\mu$, to the host galaxies using the Tully-Fisher relation: $\delta\mu$[99aa]=0.34, $\delta\mu$[91T]= 0.30. The error bar for SN 2003du is calculated taking $\delta\mu$[03du]=0.19 (Stanishev et al., 2007) 108

4.18 Elemental distribution in SN 99aa, SN 1991T, and spectroscopically normal SNe Ia. Left: Si, S, and Ca (top to bottom). Right: stable Fe, ^{56}Ni, and O (top to bottom). SNe 1999aa and 1991T exhibit similar stratification: ^{56}Ni dominates the inner layers (2000–10,000,km s^{-1}), while a narrow IME shell peaks near 11,000,km s^{-1} and terminates above $\sim$ 12,000,km s^{-1}. The higher oxygen abundance in the outer layers reflects less complete burning in these regions. In the first panel, dashed lines indicate $v_{\rm ph}$ at day -11.2 and B maximum. Continuous lines mark $v_{\rm ph}$ at the onset of Fe II lines for SN 1999aa (green) and SN 1991T (blue). 110
4.19 The effect of changing the Si abundance in the outermost layers. 111
4.20 Early-time spectra of SNe 1999aa and 1991T compared to synthetic spectra computed for increasing luminosity but the same composition. As the luminosity increases the spectra morph from looking like SN 1999aa to looking like SN 1991T. 111

5.1 Comparison of iPTF16abc spectra with SN 1991T, SN 1999aa, the normal SN 2003du, and the 03fg-like SN 2012dn at early times (left) and one week post-maximum (right). All epochs are shown relative to B maximum light. 114
5.2 Nebular spectrum of iPTF16abc in comparison with SN 1991T, SN 1999aa, the normal SN 2003du and the 03-fg-like SN 2012dn. Epochs are shown with reference to B maximum. 115
5.3 Density profiles used in the modeling process: W7 (Nomoto et al., 1984), DD2, DD3 (Iwamoto et al., 1999), and the modified DD2. In the modified DD2, a mass of 0.05 M$_\odot$ has been removed at $v >$ 14,000 km s^{-1}and redistributed in the inner layers to conserve the total mass. The total kinetic energy is not significantly changed due to the small mass shift. Vertical dashed lines mark the photospheres of the synthetic spectra. . . . 116
5.4 Observed light curves of iPTF16abc compared with synthetic light curves derived from the models. Photometric data are taken from Miller et al. (2018). 117
5.5 Observed early spectra of iPTF16abc (black), compared to synthetic spectra (colours) corresponding to different density profiles as indicated in the legend. Epochs are shown with reference to B maximum. 118
5.6 Observed early spectra of iPTF16abc (black) compared to synthetic spectra (colours) corresponding to different density profiles as indicated in the legend. Epochs are shown with reference to B maximum. 119
5.7 Observed day -8 spectrum of iPTF16abc (black), compared to the synthetic spectra in colours, corresponding to different density profiles as indicated in the legend. Epoch is shown with reference to B maximum. . . 120
5.8 Comparison of synthetic spectra illustrating the effect of the outer iron abundance in iPTF16abc. The blue spectra correspond to a model with an outer iron abundance similar to that of SN 1999aa, while the red spectra show the preferred model for iPTF16abc. Notably, despite the outermost shells of iPTF16abc exhibiting super-solar abundances, its iron content in these layers remains lower than that of both SNe 1999aa and 1991T. Epochs Epochs are given relative to B-band maximum. 120
5.9 Comparison of synthetic spectra illustrating the effect of the outer ^{56}Ni abundance in iPTF16abc. A ^{56}Ni mass fraction of 0.014 is required at the outermost shell at $v >$ 13,450 km s^{-1}to replicate the Co III $\lambda\lambda$ 3287, 3305 line observed near 3200 Å . Epoch is shown with reference to B maximum 121

5.10 Detail of the spectral region around ∼ 3700 Å. The preferred model for iPTF16abc is compared with a model excluding high-velocity Ca II, demonstrating the limited contribution of HV Ca II to the blue component. Spectra of SNe 1999aa and 2003du are included for comparison. Epochs are given in square brackets relative to B-band maximum. 123
5.11 Probing silicon in the outer layers. The optimal replication of the Si II λ 6355 absorption line observed at on day −15 is attained with a silicon mass fraction of 0.013 at $v > 13,450$ km s^{-1}. In the corresponding figures, the observed spectrum is represented in black, while models featuring varying silicon mass fractions are depicted in different colours as specified in the legend. 124
5.12 Comparison of the observed spectrum with synthetic spectra computed using different outer carbon abundances. The figure illustrates the effect of the carbon mass fraction on the strength of the C II absorption features at day −15. The observed spectrum is shown in black, while the models are shown in the colours indicated in the legend. 125
5.13 Comparison of post-maximum observed spectra of iPTF16abc (black) with synthetic spectra in various colours, corresponding to different density profiles as specified in the legend. Features near 6780 Å (weak) and 7400 Å (strong) are telluric. Epochs are presented with reference to B maximum. 127
5.14 Comparison of day + 8 observed spectrum of iPTF16abc (black) with synthetic spectra in various colours, corresponding to different density profiles as specified in the legend. Epochs are presented with reference to B maximum. 128
5.15 Probing carbon at the inner layers: spectra taken approximately 4 to 8 days after the peak. To accurately replicate the observed feature at around 6400 Å , carbon presence is required down to velocities as low as v=9,200 km s^{-1} . Introducing carbon at even lower velocities would cause the absorption line to shift redder from its observed position, as depicted in the yellow synthetic spectrum generated at day + 8.5. Epochs are presented with reference to B maximum. 130
5.16 Nebular spectrum of iPTF16abc on day +342 with reference to B maximum light, displayed in black, compared with the synthetic spectrum in red. 133
5.17 Upper panel: abundances obtained from spectral models using the DD3 density profile. Lower panel: the original nucleosynthesis from DD3 (Iwamoto et al., 1999). 134
5.18 Total mass of Intermediate Mass Elements (IMEs), against the total mass of Iron Group Elements (IGEs) for iPTF16abc, compared to other SNe and explosion models. Notably, the 91T-like events are observed to occupy a distinct region within this space. 136

5.19 The modeled bolometric light curve of iPTF16abc (red line) is shown together with those of SNe 1991T, 1999aa, and 2003du. Phases are given relative to the adopted explosion time. Black points correspond to bolometric luminosities derived from the photometric data of Miller et al. (2018) as described in section 5.7, while crosses indicate bolometric luminosities used as inputs when modeling the synthetic spectra. The dashed curves in the inset represent the instantaneous radioactive energy input from ^{56}Ni decay for different nickel masses inferred from the modeling of SNe 1991T (blue), 2003du (red), 1999aa (green) and iPTF16abc (black) (see Aouad et al., 2022, 2024, Sasdelli et al., 2014, Tanaka et al., 2011). The plotted points in the inset include photometric uncertainties, and the error bars additionally account for distance uncertainties, assuming an error of 0.15 mag in the distance modulus (Makarov et al., 2014). 138

5.20 Comparison of the pseudo equivalent width of the Fe III trough, around 4800 Å, in the early spectra of iPTF16abc with those measured for SNe 1999aa and 1991T. The measurements were carried out following the approach described in Hachinger et al. (2006). Days are with reference to B maximum. 140

5.21 The observed spectra of SN 2003du, SN 1999aa, iPTF16abc, and SN 1991T are shown at the bottom, ordered from lower to higher luminosity (red, green, black, and blue, respectively). Overlaid is a sequence of synthetic spectra constructed from the best-fit model of iPTF16abc, in which the luminosity is progressively increased in steps of 0.5 dex (in solar units). At the same time, the iron abundance in the outer ejecta is systematically enhanced. As the sequence evolves, the models approach SN 1991T at higher luminosities and SN 1999aa at lower luminosities, demonstrating that iPTF16abc occupies an intermediate position between these objects. However, the comparison also reveals that luminosity alone cannot reproduce the full spectral diversity. Matching the observed sequence requires simultaneous changes in the iron abundance of the outer layers, indicating that the differences are not driven purely by temperature effects. This result highlights that the spectroscopic sequence among these events is governed by both ionization and composition, and underscores the intrinsic complexity within supernovae that are commonly classified within the same subclass. 141

5.22 Same as Fig. 5.21, but with the iron abundance in the outer layers kept fixed while only the luminosity is varied. In this case, increasing the luminosity alone fails to reproduce the observed spectral sequence between SN 1999aa, iPTF16abc, and SN 1991T. 142

5.23 The distribution of the most important elements in SNe iptf16abc, 1991T, 1999aa and some spectroscopically normal SNe Ia. Left-hand side, top to bottom: Si, S and Ca. Right-hand side, top to bottom: stable Fe, ^{56}Ni, O and C. iptf16abc exhibits very similar stratification properties to SNe 1999aa and 1991T which are different than the spectroscopically normal events: the IMEs shell is narrow and is suddenly depleted above $\sim$ 12,000 km s^{-1}, oxygen dominates the outer shells and is sharply depleted below $\sim$ 12,000 km s^{-1}. Carbon extends deep and increases creating a noticeable peak around 10,000 km s^{-1}. The dashed lines in the first panel represent the velocities probed by our photospheric phase models, spanning from approximately days -15.3 to $+8.5$ relative to B maximum, while the regions below are probed by the nebular phase model. 143
5.24 Left panel: Pseudo equivalent width (PEW) of the C II 6580 Å observed in iPTF16abc, compared to a set of SNe 2003fg-like taken from Ashall et al. (2021). The line initially shows notable strength at an early stage but experiences a subsequent weakening before ultimately strengthening again, approximately one week after maximum light. Right panel: Velocity of the same line 144

6.1 The early spectra of the 03fg-like, SNe 2012dn, 2009dc compared to SN 1991T, and the normal SN 2003du, highlighting their distinct IME-dominated features and weak Fe III signatures as discussed in the text. 147
6.2 Spectra one week after B maximum of the 03fg-like, SNe 2012dn, 2009dc compared to SN 1991T, and the normal SN 2003du. 148
6.3 Density profiles of the W7, DD1, DD2, and DD3 models, each scaled to an epoch of 100 s. The blue line shows the density structure adopted in this work, modified to a total ejecta mass of 1.66 $M_\odot$. Vertical lines mark the photospheric velocities of the synthetic spectra at their respective epochs with respect to B-band maximum light. 149
6.4 $UBVRI$ light curves or SN 2012dn compared to the ones of SN 2003du (Stanishev et al., 2007) normalized at peak. The evolution of SN 2012dn exhibits a notable wavelength-independent (grey) extinction that persists across all bands through the late phases. 151
6.5 Light curves from the synthetic spectra compared to the light curves from observation. 152
6.6 Early-time spectra of SN 2012dn (at -14.1 and -12.8 days relative to B-band maximum) overlaid with the synthetic spectra using the W7 and the DD2 density profiles depicted in red and blue respectively. 153
6.7 Early-time spectra of SN 2012dn (at -10.1 and -9.1 days relative to B-band maximum) overlaid with the synthetic spectra using the W7 and the DD2 density profiles depicted in red and blue respectively. 154
6.8 Early-time spectra of SN 2012dn (at -7.6 and -5.1 days relative to B-band maximum) overlaid with the synthetic spectra using the W7 and the DD2 density profiles depicted in red and blue respectively. 155

6.9 Comparison of synthetic spectra illustrating the effect of the outer-layer iron abundance. Left panel shows the day −14 spectrum with a sub-solar model ($Z = 0.1\,Z_{\odot}$) at $v > 15,000$ km s^{-1}. Right panel compares solar (blue) and super-solar (purple; matching SN 1999aa) abundances. Solar and super-solar abundances fail to replicate the observed spectral features. Furthermore, they enhance backscattering, heating the photosphere and shifting the ionization balance from Si II toward Si III. This results in the unobserved strengthening of the Si III $\lambda\lambda$4552, 4567, 4574 multiplet near 4300 Å, which is absent in the observed spectra of SN 2012dn. 156
6.10 U–B colour evolution of SN 2012dn compared with synthetic spectra and other SNe (Taubenberger et al., 2019). The 03fg-like events exhibit notably blue pre-maximum colourss, likely due to a lack of iron-group elements (IGEs) reducing UV line blanketing (Mazzali et al., 2014). This contributes to the distinct early colour evolution observed in this subclass. 157
6.11 Comparison between a synthetic model excluding carbon (blue) and a model incorporating 0.01 $M_{\odot}$ of carbon ($X(C) = 0.05$) within the velocity range 9,100 $< v <$ 10,200 km s^{-1} (red) is shown in the left panel. The right panel displays the results for the outer layers, where the observed C II feature near 6200 Å is accurately reproduced by including 0.003 $M_{\odot}$ of carbon at $v >$ 14,000 km s^{-1} (red). 159
6.12 Spectra of SN 2012dn near maximum light (at −3.6 and −1.1 days relative to B-band maximum) overlaid with the synthetic spectra using the W7 and the DD2 density profiles depicted in red and blue respectively. 160
6.13 Spectra of SN 2012dn near maximum light (at +2.9 and +4.9 days relative to B-band maximum) overlaid with the synthetic spectra using the W7 and the DD2 density profiles depicted in red and blue respectively. 161
6.14 Left: The 4300 Å region shows Fe III absorption characteristic of 91T-like SNe, whereas Mg II dominates this feature in normal and 03fg-like SNe. The Si III contribution remains consistent across all types. Right: The 5000 Å region distinguishes 03fg-like events, where the blue component is driven by Si II $\lambda\lambda$5041, 5056, unlike the Fe II/Fe III blend seen in normal and 91T-like objects. The degree of blending of the two components reflects the temperature: they are well separated in 03fg-like events but gradually merge into a single absorption feature in the hottest SN 1991T. . 162
6.15 Comparison of synthetic spectra illustrating the effect of the stable iron abundance in the intermediate shells. A stable iron abundance at the 10% level (increasing from 7% to 21% across the shells) is required to reproduce the absorption feature near 5000Å, which is dominated by a complex of Fe II and Fe III lines. 163
6.16 Spectra one week after maximum light (at +5.9 and +413.9 days relative to B-band maximum) of SN 2012dn overlaid with the synthetic spectra using the W7 and the DD2 density profiles depicted in red and blue respectively. 165
6.17 Comparison of observed and synthetic spectra at days −14 and −13 is presented. The W7 model successfully reproduces the narrow Si II feature near 6000 Å, the Mg II O I blend near 7400 Å, and the Si II feature near 5800 Å, which the DD models fail to capture. 166

6.18 Ionization conditions in the ejecta at day −13. In the W7 model, the density bump enhances recombination and lowers the overall ionization level, confining singly ionized Mg, Si, and S, as well as neutral O, within a narrow velocity region around ∼16,000 km s^{-1}. In contrast, the DD1 and DD2 profiles distribute these ions over a broader velocity range, causing line formation to occur across a more extended region of the ejecta and producing correspondingly bluer line wings (see Fig. 6.17). 167
6.19 Nebular spectrum at 290 days after B maximum light. The red line is the model. 168
6.20 Abundance distributions of SN 2012dn (upper panel) compared to the normal SN 2003du (lower panel). The two events show markedly different core compositions: while the innermost layers of SN 2003du are dominated by neutron-rich iron-group elements and are entirely depleted of oxygen, SN 2012dn exhibits a central oxygen reservoir. In this model, oxygen extends to the core, intermixed with silicon and sulphur, alongside a notably low ^{56}Ni abundance. 171
6.21 *UBVRI* pseudo-bolometric light curve of SN 2012dn compared with SNe 1991T, 2003du, 2011fe, 2009dc, 1999aa and iPTF16abc (Aouad et al., 2022, 2024, Sasdelli et al., 2014, Stanishev et al., 2007, Taubenberger et al., 2011, Zhang et al., 2016). By ∼60 days post-maximum, SN 2012dn undergoes a sharp decline, becoming significantly less luminous than the rest of the sample by day 300. SN 2009dc exhibits a similar drop ∼100 days later; notably, both events follow a nearly identical, steep decline slope. The vertical error bar reflects the peak luminosity range of SN 2012dn based on the minimum and maximum distance moduli in the literature. . 173
6.22 *UBVRI* pseudo-bolometric light curve of SN 2012dn (black dots) compared to synthetic models (red lines) for $M(^{56}\mathrm{Ni}) = 0.45$–$0.49\,\mathrm{M}_{\odot}$. The light curve of SN 2003du (Tanaka et al., 2011), normalised to the observed peak (dashed blue), reveals a late-time attenuation of ∼0.7 dex by day +300 highlighting SN 2012dn's significant late-time luminosity dimming. Despite similar morphology, the SN 2012dn model is broader than that of SN 2003du, reflecting its higher total ejecta mass. 174
6.23 Comparison of observed and modeled spectra incorporating a blackbody (BB) component at two epochs (early and near-maximum light). The observed spectra are shown in black. The initial models are represented by red solid lines, while the models with reduced radioactive luminosity are shown in green. In these final models, the input luminosity was reduced by 25% for the early spectrum and 20% for the near-maximum spectrum. The red dashed lines represent the additional BB component required to account for the total luminosity, with temperatures of 14,000 K and 11,000 K for the early and near-maximum epochs, respectively. The blue solid lines represent the total synthetic flux (the sum of the green model and the BB component). 177

7.1 Schematic representation of the spectroscopic diversity of luminous peculiar SNe Ia. Characteristic spectroscopic properties of the normal, 91T-like, and 03fg-like subclasses are shown together with the features linking SN 1999aa, iPTF16abc, and SN 2012dn to each class. The figure illustrates the overlapping nature of the traditional classifications and the absence of a simple one-parameter sequence among luminous peculiar SNe Ia. 180

7.2 Schematic summary of the spectroscopic relationships inferred from abundance tomography. The transition from normal SNe Ia to the 91T-like subclass requires the confinement of IMEs to a narrow velocity range. Within the 91T-like subclass, the spectroscopic differences between SN 1999aa and SN 1991T are largely explained by a luminosity (temperature) sequence. The transition from SN 1991T to iPTF16abc requires additional abundance differences, including lower outer iron abundances and the presence of carbon both in the outer ejecta and at intermediate velocities 181

7.3 Starting with a model of 2011 fe (Mazzali et al., 2014), luminosity is increased in steps of 0.1 dex. The evolution of the spectra does not converge to a 91T-like event. In particular, even though the Si II 6355 feature starts fading for *log* L $>$ 9.1 $L_{\odot}$, a Si III feature near 5500 Å becomes prominent, a feature absent in all members of the 91T-like class. Most importantly, the Fe III features, typical of the 91T-like class, do not appear in the spectra. The Fe III feature near 5000 Å remains weak, and the Fe III feature near 4200 Å does not strengthen with increasing temperature. Instead, it becomes split into two components, both dominated by Si III, replacing the Mg II line observed in all normal events. Finally, the most luminous model of SN 2011fe, with *log* L=9.2 $L_{\odot}$,similar to the model input in 99aa, shows no sign of convergence toward 91T-like behaviour. This suggests that luminosity evolution alone cannot account for the spectral transition from normal to 91T-like events. 183

7.4 Starting with a model of SN 1999aa, the luminosity is decreased in steps of 0.1 dex while keeping the composition unchanged. The evolution of the spectra does not converge toward a normal-like event. In particular, although the Si II 6355 feature begins to emerge as luminosity decreases, the S II complex near 5400 Å does not develop. The feature near 4300 Å, typically dominated by Mg II and Si III in normal events, fails to form, and the Ca II H&K feature near 3700 Å completely fades. An Fe II feature near 4700 Å appears in the models, a feature not typically observed in events classified as normal. Additionally, the flux in the *U* band decreases substantially. 184

List of Tables

4.1 Late-time photometry of SN 1999aa. 86
4.2 Spectra of SN 1999aa and modelling parameters. 87
4.3 Nucleosynthetic yields and kinetic energies from the modelling using different density profiles compared to the original hydrodynamic models. Results from other SNe are also shown. 101

5.1 Spectra of SN iPTF16abc and modelling parameters. 116
5.2 Nucleosynthetic yields and kinetic energies from the modelling compared to the original hydrodynamic models. Results from other SNe are also shown. $E_{\rm k}$ for models is calculated using equation 5.1 in the text. 135

6.1 Spectra of SN 2012dn and modeling parameters. 149
6.2 Band-dependent extinction values, corresponding flux transmission factors, SED fractions, and weighted transmitted flux contributions used to estimate the bolometric attenuation. 169
6.3 Nucleosynthetic yields and kinetic energies from the modelling compared to the original hydrodynamic models. Results from other SNe are also shown. 170
6.4 Bolometric luminosity of SN 2012dn in the U, B, V, R, I. 172

Abbreviations

COWD	Carbon Oxygen White Dwarf
CSM	Circumstellar Medium
DD	Double Degenerate, Delayed-Detonation or Double Detonation (depending on context)
EC	Electron Capture
EW	Equivalent Width
PEW	Pseudo Equivalent Width
FWHM	Full Width at Half Maximum
IME	Intermediate Mass Elements
Fe-group elements	Iron Group Elements
IR	Infrared
LC	Light Curve
LTE	Local Thermodynamic Equilibrium
MC	Monte-Carlo
NLTE	Non-Local Thermodynamic Equilibrium
NIR	Near Infrared
SD	Single Degenerate
SN	Supernova
SNe	Supernovae
SNe Ia	Type Ia Supernovae

SN Ia	Type Ia Supernova
TE	Thermodynamic Equilibrium
UV	Ultraviolet
WD	White Dwarf

Physical Constants

Speed of light	$c = 2.998 \times 10^{8}\,\mathrm{m\,s^{-1}}$
Planck constant	$h = 6.626 \times 10^{-34}\,\mathrm{J\,s}$
Boltzmann constant	$k_B = 1.381 \times 10^{-23}\,\mathrm{J\,K^{-1}}$
Electron mass	$m_e = 9.109 \times 10^{-31}\,\mathrm{kg}$
Electron charge	$e = 1.602 \times 10^{-19}\,\mathrm{C}$
Stefan–Boltzmann constant	$\sigma = 5.670 \times 10^{-8}\,\mathrm{W\,m^{-2}\,K^{-4}}$
Solar mass	$M_\odot = 1.989 \times 10^{30}\,\mathrm{kg}$
Solar luminosity	$L_\odot = 3.828 \times 10^{26}\,\mathrm{W}$
Parsec	$1\,\mathrm{pc} = 3.086 \times 10^{16}\,\mathrm{m}$
Hubble constant	$H_0 = 67.4\,\mathrm{km\,s^{-1}\,Mpc^{-1}}$
Electron volt	$1\,\mathrm{eV} = 1.602 \times 10^{-19}\,\mathrm{J}$

Symbols

A_{ul}	Einstein coefficient for spontaneous emission
$B_\nu(T)$	Planck function at temperature T
$B(T)$	Frequency-integrated Planck function, $\sigma T^4/\pi$
$E(B-V)$	Colour excess, measure of dust extinction
f_{lu}	Oscillator strength of transition $l \rightarrow u$
F_ν	Spectral flux density
$g_u,\ g_l$	Statistical weights of upper and lower levels
I_ν	Specific intensity
J_ν	Mean intensity
J	Frequency-integrated mean intensity
j_ν	Emission coefficient (per unit mass)
$L_{\rm bol}$	Bolometric luminosity
m_e	Electron rest mass
n_e	Electron number density
n_l	Population of lower level of a transition
$R_{\rm ph}$	Photospheric radius
S_ν	Source function
$t_{\rm exp}$	Time since explosion
T_e	Electron temperature
$T_{\rm eff}$	Effective photospheric temperature
$T_{\rm ph}$	Photospheric temperature
T_R	Radiation temperature
$v_{\rm ph}$	Photospheric velocity
W	Dilution factor
$W_g(r)$	Geometric dilution factor

$X_i(v)$	Abundance of element i as a function of velocity
χ_j	Ionization potential of ion j
κ_ν	Opacity (per unit mass)
λ_0	Rest wavelength of a spectral line
μ	Distance modulus; also directional cosine $\cos\theta$
$\langle\nu\rangle$	Mean frequency
ν_0	Rest frequency of a spectral line
ν'	Co-moving frame frequency
ρ	Mass density
σ_T	Thomson cross section
τ_ν	Optical depth
τ_S	Sobolev optical depth

To my friends . . .

Sorry for going quiet on you all this time, this thesis took over my life completely. I hope you haven't written me off yet. The first rounds are on me, and similar to the MC code, I hope convergence will be fast.

Chapter 1

Introduction and Scientific Context

1.1 Introduction

Supernovae (SNe) are among the most luminous transients in the Universe. They are primary contributors to the synthesis of heavy elements, particularly those in the iron group, and influence their host galaxies through powerful feedback processes.

Of particular interest are Type Ia supernovae (SNe Ia), which, owing to their high intrinsic luminosities and empirical standardisation through the width–luminosity relation (WLR) (Phillips, 1993), have become powerful tools in observational cosmology. Their application led to one of the most significant discoveries in modern cosmology, the accelerated expansion of the Universe (Perlmutter et al., 1998, Riess et al., 1998).

Despite their success, SNe Ia are not perfectly homogeneous. Increasingly large and precise datasets have revealed significant diversity in their observed properties, the physical origin of which remains an open question. The majority of SNe Ia are classified as normal events. Near maximum light, their spectra are dominated by intermediate-mass elements (IMEs), most notably Si II, S II, Ca II, and Mg II, while Fe-group features become increasingly prominent as the spectra evolve. Alongside this normal population, several peculiar spectroscopic subclasses have been identified.

At one extreme lie the sub-luminous 91bg-like events, characterised by low luminosities, rapid light-curve evolution, and spectra indicative of low temperatures and ionisation states (Mazzali et al., 1997a). At the opposite end are the luminous 91T-like events, whose early spectra display weak Si II and Ca II absorptions together with prominent Fe III features (Phillips et al., 2022, 2024). In addition, peculiar subclasses such as the 2003fg-like show strong IME features, persistent carbon signatures, and weak Fe-group

absorptions, combined with slow light-curve evolution and luminosities that often equal or exceed those of the 91T-like subclass (Ashall et al., 2021).

This raises fundamental questions: does the observed diversity reflect a continuous luminosity sequence, or does it point to multiple progenitor systems and explosion mechanisms? Addressing these questions is essential not only for understanding the physics of SNe Ia, but also for assessing the precision with which they can be used as cosmological distance indicators.

In addition to the established spectroscopic subclasses, observations have revealed a growing number of peculiar objects exhibiting hybrid properties that bridge multiple subclasses. By blurring the boundaries between traditional classes, these transitional events offer unique insight into the physical origin of SN Ia diversity. This thesis focuses on such objects at the bright end of the luminosity distribution.

The transitional SN 1999aa occupies an intermediate spectroscopic position between normal and 91T-like SNe Ia, with Si II and Ca II features of intermediate strength and a faster evolution toward a spectroscopically normal appearance than SN 1991T (Aouad et al., 2022). The peculiar 91T-like event iPTF16abc reaches a luminosity comparable to that of SN 1991T, yet displays unusually weak Fe III features and a distinctive carbon evolution, with C II lines re-emerging after maximum light, a rare occurrence within this subclass (Aouad et al., 2024). Finally, the 03fg-like SN 2012dn combines the narrow IME features and persistent carbon signatures typical of its subclass with a luminosity comparable to that of a bright normal SN Ia. It also exhibits unusual late-time grey bolometric dimming together with prominent nebular [O I] emission, a rare feature among thermonuclear supernovae (Taubenberger et al., 2019).

Abundance tomography is applied to reconstruct the chemical structure of the ejecta as a function of depth through the modeling of a time-series of spectra. This approach provides direct constraints on the physical mechanisms responsible for the diversity of SNe Ia and on their possible progenitor–explosion channels.

The remainder of this chapter reviews the historical background of supernovae, their classification schemes, the observational properties that distinguish their principal subclasses, and their astrophysical importance, with particular emphasis on the use of Type Ia supernovae as cosmological distance indicators. The thesis is then structured as follows. Chapter 2 reviews the observational and theoretical aspects of SNe Ia. Chapter 3 presents the spectral modelling framework and abundance tomography techniques used throughout the thesis. Chapters 4 to 5 apply this methodology to the transitional SN 1999aa, the peculiar 91T-like event iPTF16abc, and the 03fg-like SN 2012dn. Finally,

Chapter 7 summarizes the main conclusions of this work and discusses directions for future research.

1.2 Historical background

The transient nature of supernovae has long captured human curiosity, initially interpreted as omens or divine messages. Their significance later extended beyond mythology to become central to scientific inquiry, contributing to the understanding of stellar evolution and the Universe at large. In particular, the appearance of these “guest stars” challenged the Aristotelian view of an unchanging and perfect celestial sphere.

The term "supernova" was originally coined by Fritz Zwicky to describe transients that appeared as exceptionally bright novae (derived from the Latin for “new”). This nomenclature emerged following the discovery that many optical nebulae were, in fact, distant galaxies; consequently, the transients observed within them had to be intrinsically much more luminous than the common novae found in the Milky Way. As observational astronomy progressed, it became evident that supernovae are not merely bright novae, but represent cataclysmic cosmic events marking the violent terminal transition in the life of a star.

Over the past millennium, five supernovae have been recorded in our Galaxy: AD 1006, 1054, 1181, 1572, and 1604, all observed before the advent of the telescope. While nearly 300 supernova remnants (SNRs) have since been identified in the Milky Way through radio, optical, and X-ray observations, these historical events provide a unique temporal baseline for studying remnant expansion over centuries. Most records originate from East Asian chronicles, particularly in China, Japan, and Korea, with additional contributions from Arabic sources. For the most recent events, SN 1572 (Tycho) and SN 1604 (Kepler), detailed European observations offer more quantitative data. When combined with modern classifications, these records enable a reconstruction of the events summarized below:

- **SN 185:** The earliest supernova for which written records exist, documented by Chinese astronomers in the *Hou Hanshu* (Book of the Later Han) on December 7, 185 A.D. Located in the direction of Alpha Centauri between the Circinus and Centaurus constellations, the “guest star” was described as being as large as half a bamboo mat (*yan*) with scintillating, variegated colors. It remained visible for approximately seven months before disappearing in mid-186 A.D. In the 20th century, telescope observations identified its modern counterpart as the shell-like remnant **RCW 86** (initially discovered as the radio source MSH 1-63). Modern estimates

place the remnant at a distance of approximately 2.5 kpc, with an age of roughly 2,000 years, providing a strong physical link to the second-century Chinese accounts (Sollerman et al., 2003, Vink et al., 2006).

- **SN 386 & SN 393:** Recorded by Chinese astronomers, these two events present interesting challenges in remnant identification. **SN 386** was initially associated with the symmetric shell remnant **G11.2-0.3**, which has a diameter of 4 arcminutes. While its expansion rate suggests an age of approximately 1,900 years (Borkowski et al., 2016), radio measurements of the central pulsar's spin-down rate indicate a much older age of 20,000 to 23,000 years, leading to ongoing debate regarding this association (Torii et al., 1999). **SN 393** was similarly recorded as a "guest star" in the constellation Scorpius. Its remnant, **RX J1713.7-3946**, remained unknown to modern astronomy until its discovery in 1996 by the *ROSAT* All Sky Survey. It is now identified as a shell-type remnant located approximately 1.0 kpc away.

- **SN 1006:** Widely considered the brightest stellar event in recorded history, reaching an estimated apparent magnitude of $m_v \approx -7$ (Stephenson & Green, 2002). It was the first supernova to be documented by multiple independent groups of observers across China, Japan, the Arabic world, and Europe; its extreme luminosity rendered it visible during the day and it remained a fixture in the night sky for three years. By analyzing these diverse historical sky positions, researchers were able to reconstruct its probable location, which coincides with a large (≈ 30 arcminutes in diameter) limb-brightened shell of radio emission. Identified as the remnant **SNR G327.6+14.6** by Gardner & Milne (1965), it continues to be a primary subject for studying shock-wave physics and cosmic ray acceleration (Reynoso et al., 2013)

- **SN 1054 (The Crab Nebula):** Recorded on July 4, 1054, this event was documented extensively by astronomers in China and Japan, with only brief accounts from Constantinople and Arabic sources, but was poorly observed Europe and the Near East (Brecher, 1978). Its visibility was so remarkable that it was potentially recorded in North American petroglyphs at Chaco Canyon, where a star is depicted adjacent to a crescent moon in an orientation matching the sky on July 5, 1054 (Miller, 1955). The remnant of this cataclysm, known as the **Crab Nebula (Messier 1 or M1)**, was rediscovered in the 18th century and became the first entry in Charles Messier's catalog of nebulae (Messier, 1781). It was not until the 1920s that the nebula was definitively associated with the 1054 "guest star" (Hubble, 1928, Lundmark, 1921). Today, it is recognized as a pulsar wind nebula, powered by a central, rapidly rotating magnetized neutron star (Reifenstein et al., 1969).

- **SN 1181:** Recorded by observers in southern China and Japan on August 6, 1181, this event marked the third Galactic supernova within a two-century span. Due to inaccuracies in the surviving historical records, the precise location of the SN was not well constrained for centuries. It was not until 1971 that the radio-bright source **3C 58** was identified as the remnant of SN 1181 (Stephenson, 1971). The remnant is particularly notable because its center appears to be filled and illuminated by a central pulsar, making it one of the few remnants where the interior emission is driven by a neutron star's energetic wind (Camilo et al., 2002). At an estimated distance of 2.8 kpc, it remains a vital subject for studying the evolution of young, pulsar-driven nebulae.

- **SN 1572 (Tycho's Supernova):** Appearing in the constellation Cassiopeia, this event was first observed in early November 1572 by European and Korean astronomers. It is most famously associated with Tycho Brahe, who began a rigorous series of measurements on November 11, 1572. Brahe's observations were revolutionary; by proving the object lacked a measurable parallax relative to the background stars, he concluded it must reside far beyond the Moon on the eighth shell of the "fixed stars." This directly contradicted the Aristotelian view of a constant, unchanging sky. Brahe documented his findings in the treatise *Progymnasmata*, providing a location accurate to within a few arcminutes. The remnant was later identified as the bright radio source **3C 10** (Hanbury Brown & Hazard, 1952). Recently, reflections of the supernova's original light from interstellar dust clouds, known as "light echoes", were detected, allowing modern telescopes to spectroscopically classify SN 1572 as a **Type Ia supernova** (Krause et al., 2008b).

- **SN 1604 (Kepler's Supernova):** First observed in Europe on October 9, 1604, by Ilario Altobelli and Raffaello Gualterotti, this event occurred in the constellation Ophiuchus. Remarkably, the sky had been under intense observation just one day prior, on October 8, as astronomers watched a conjunction of Mars, Jupiter, and Saturn; the lack of a reported transient at that time provides a strict upper limit on the explosion date, suggesting the supernova was at least 9 magnitudes fainter than its eventual peak ($m_{max} \approx -3$) only 20 days before maximum brightness (Stephenson & Green, 2002). Johannes Kepler began his observations on October 17 and subsequently published the definitive treatise, *De Stella Nova in Pede Serpentarii* ("On the New Star in the Foot of the Serpent Bearer"). The remnant, identified as the radio source **3C 358**, was discovered by Baade (1943). While historical light curves are consistent with multiple classifications, modern analysis of the remnant's chemical composition and X-ray emission strongly indicates that SN 1604 was a **Type Ia supernova**.

Interestingly, the historical record is incomplete due to interstellar dust obscuration. Two significant events occurred in the post-Kepler era but went unrecorded by naked-eye observers:

- **Cassiopeia A (c. 1680):** Despite being the youngest known core-collapse remnant in the Galaxy and one of the brightest radio sources in the sky, there are no definitive historical records of its explosion. It is estimated to have occurred around 1680, a period when astronomers like John Flamsteed were actively mapping the sky; however, the event was likely obscured by significant interstellar dust, which absorbed the majority of its optical emission. The remnant, **SNR G111.7-02.1**, has since become a laboratory for supernova physics. In 2005, the detection of a light echo allowed for the retrospective spectroscopic classification of the event as a **Type IIb supernova**, confirming that the progenitor was a red supergiant that had lost most of its hydrogen envelope prior to core collapse (Krause et al., 2008a).

- **SNR G1.9+0.3 (c. 1890–1908):** Currently the youngest known supernova remnant in the Milky Way, G1.9+0.3 resulted from an explosion whose light reached Earth at the turn of the 20th century. Despite its recent occurrence, the event was not observed by contemporary astronomers as it was obscured by the dense gas and dust near the Galactic Center. While first identified in 1984, its extreme youth was confirmed in 2008 when Chandra X-ray data showed the remnant had expanded by nearly 15 % since its discovery. Further observations made with the VLA in 2008 verified this increase in size, implying the remnant was no more than 150 years old (Reynolds et al., 2008) . Subsequent estimates have further refined its observable age to approximately 110 years as of 2008 (Green et al., 2008) . Modern analysis suggests the event was a **Type Ia supernova**, likely triggered by the merger of two white dwarfs, making it a critical laboratory for studying the early evolution of the double-degenerate scenario (Chakraborti et al., 2016).

1.3 SNe classification

The foundation for supernova classification was established by Minkowski (1941) through spectroscopic observations. This system divided supernovae into two primary classes, distinguished by a key feature: the presence or absence of hydrogen in their spectra near maximum light. Type II supernovae displayed hydrogen signatures, while Type I supernovae did not. Over time, this classification scheme evolved, revealing nuances.

Type I supernovae were further subdivided into three categories; Types Ia, Ib, and Ic (Elias et al., 1985, Wheeler & Harkness, 1986). Although all lack hydrogen, they exhibit

distinct spectral features. Type Ia supernovae, are characterised by a prominent Si II λ 6355 Å feature, a defining hallmark of this subtype. Type Ib supernovae display strong He I λ ,λ 5876 6678 7065, whereas Type Ic supernovae lack these helium features.

Type II supernovae were initially divided into two main subclasses, Type IIP and Type IIL, based on their light curve behaviours (Barbon et al., 1979). Type IIP supernovae exhibit a characteristic plateau in their light curves that lasts 2–3 months after reaching peak brightness, before beginning to decline. In contrast, Type IIL supernovae display a more rapid, linear decrease in luminosity following their peak.

Further observations revealed additional spectroscopic peculiarities in some Type II supernovae, leading to the classification of two more subclasses: Type IIb and Type IIn. Type IIb supernovae are initially dominated by hydrogen lines in their spectra, which vary in strength and persistence across events; these lines gradually give way to prominent helium lines, similar to those seen in Type Ib supernovae. Type IIn supernovae are distinguished by their narrow Balmer emission lines, often accompanied by complex profiles, in addition, they exhibit a considerably slower evolution than other SNe II. (cf. Turatto et al., 2007). An illustrative classification scheme is shown in Fig. 1.1, and representative spectra of each subtype near maximum light are presented in Fig. 1.2, highlighting the key spectral features used to distinguish between them.

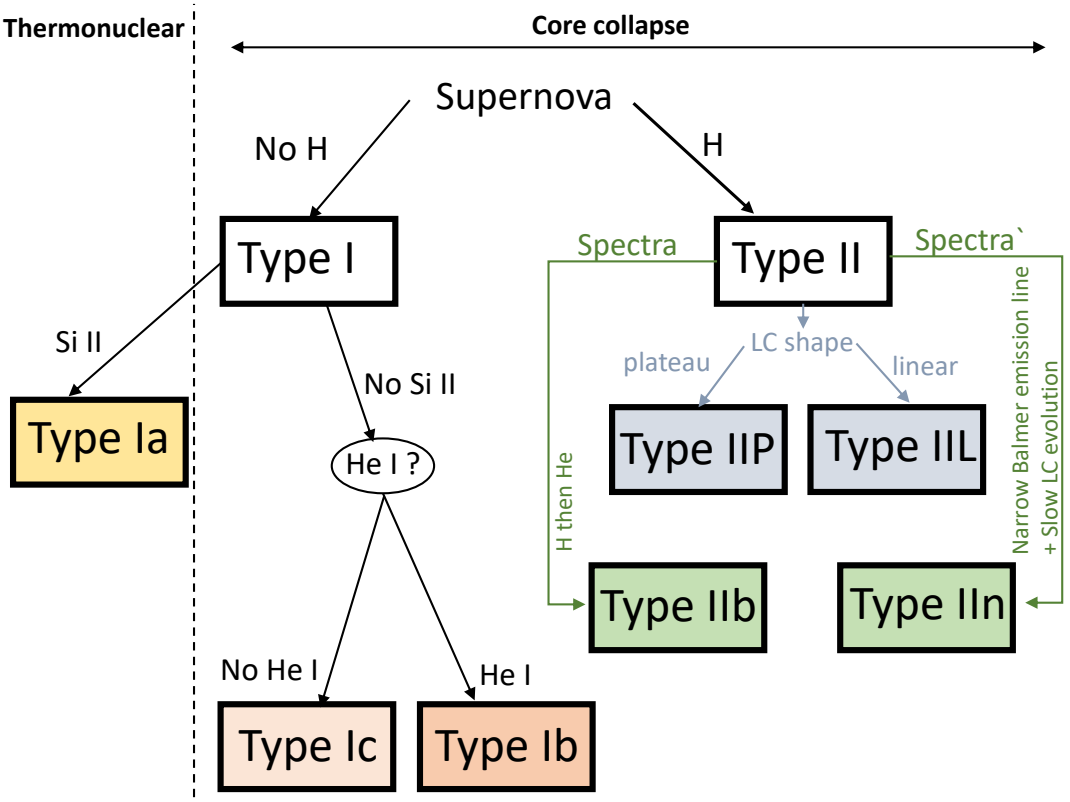


FIGURE 1.1: Supernovae classification scheme

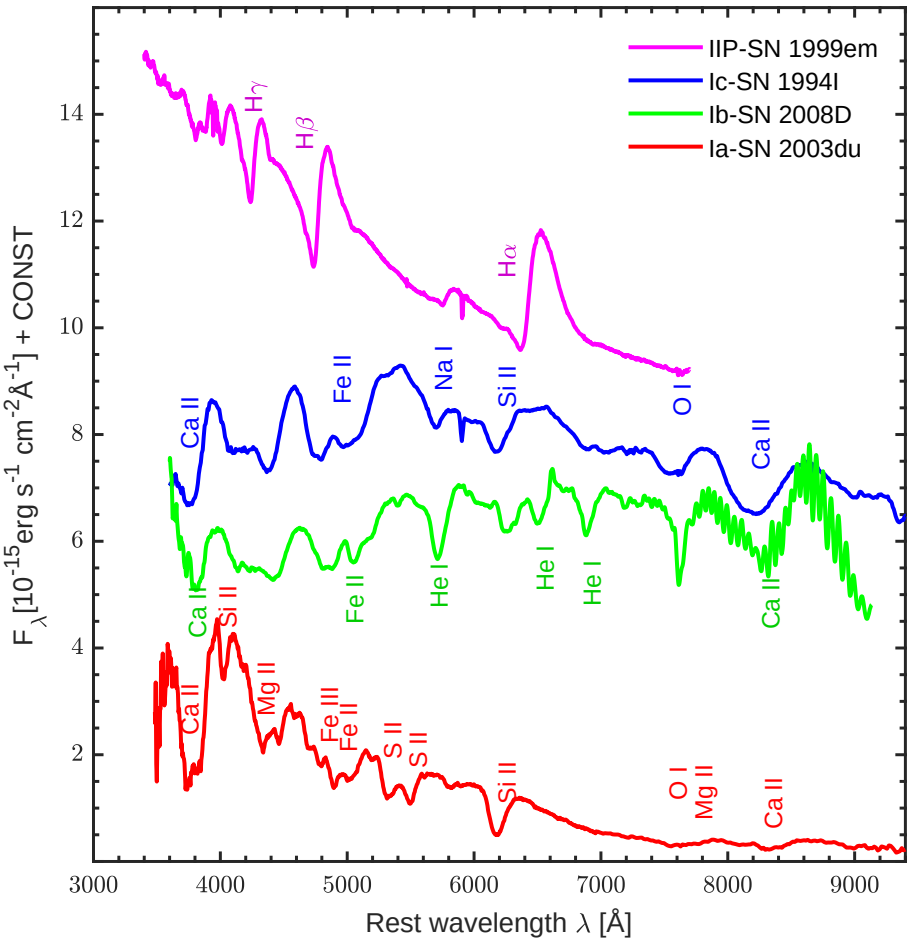


FIGURE 1.2: Representative spectra of the main supernova types near maximum light, illustrating the key spectral features used for classification. From bottom to top: Type Ia (SN 2003du), Type Ib (SN 2008D), Type Ic (SN 1994I), and Type IIP (SN 1999em). Spectra are offset vertically for clarity. The principal line identifications are marked for each type.

It is now well established that Type II, Ib, and Ic supernovae arise from the core collapse of massive stars. The absence of hydrogen in Type Ib supernovae, and of both hydrogen and helium in Type Ic supernovae, is indicative of progenitor stars that have shed their hydrogen or hydrogen–helium envelopes prior to explosion. For Type IIP supernovae, the characteristic plateau in the light curve is powered by hydrogen recombination in an extended envelope, which maintains a nearly constant luminosity over several weeks. By contrast, Type IIL supernovae exhibit a more rapid decline, likely reflecting a progenitor with a less massive hydrogen envelope. Type Ia supernovae are believed to result from the thermonuclear disruption of a carbon–oxygen white dwarf. These events exhibit complex spectroscopic and photometric behaviours, which will be explored in greater

detail in Sec. 2.3

The relative rates of different types of SNe were measured by Li et al. (2011a) using data from the Lick Observatory Supernova Search (LOSS). In a volume-limited sample, which better reflects the intrinsic cosmic rates, SNe II dominate (57%), while SNe Ia and SNe Ibc account for 24% and 19%, respectively. In contrast, magnitude-limited samples are biased toward more luminous events, with SNe Ia becoming dominant (79%), while SNe II and SNe Ibc decrease to 17% and 4%. These selection effects also extend to subclasses, with intrinsically faint events such as SN 1991bg-like and SNe II-P significantly underrepresented in magnitude-limited surveys. This distribution is illustrated in Figs. 1.3 and 1.4.

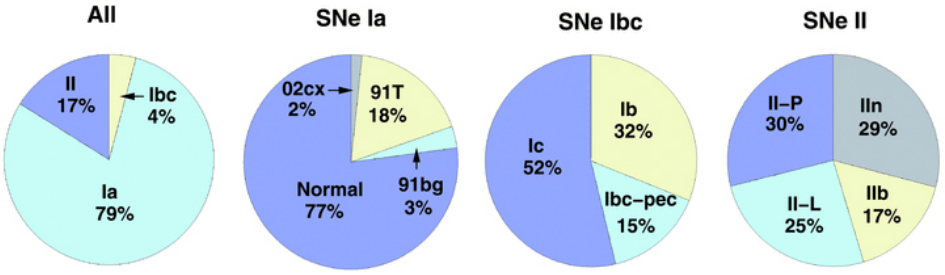


FIGURE 1.3: The observed fractions of the subclasses of SNe in an ideal magnitude-limited sample. (Li et al., 2011a)

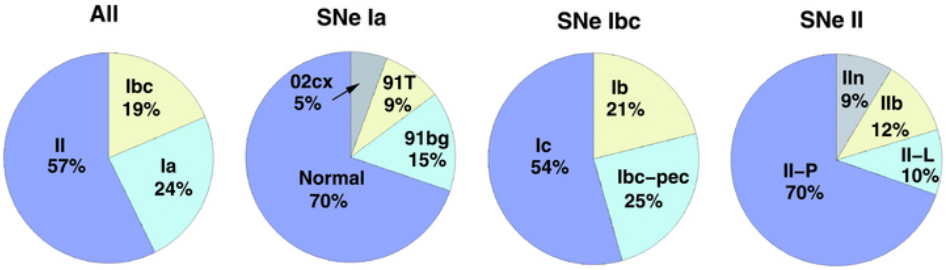


FIGURE 1.4: The observed fractions of the subclasses of SNe in a volume-limited sample. (Li et al., 2011a)

As this thesis focuses specifically on Type Ia supernovae, discussions of other supernova types will be limited to the overview provided in this introduction.

1.4 The importance of Type Ia supernovae

1.4.1 Astrophysical relevance

Type Ia supernovae play a pivotal role in the chemical enrichment of galaxies and the evolution of stellar populations (Greggio & Renzini, 1983, Matteucci & Greggio, 1986).

They efficiently produce intermediate-mass elements (with atomic numbers between 11 and 20) and are the primary contributors of iron and other iron-group elements (Nomoto et al., 2013), with approximately 70% of solar iron attributed to SNe Ia (Keegans et al., 2023). Additionally, since the thermonuclear explosion completely disrupts the white dwarf leaving no compact remnant, the entire stellar interior, including nucleosynthetic products normally hidden from view, is ejected and observable. This makes SNe Ia a rare laboratory for studying the physics of degenerate matter and explosive nucleosynthesis, offering direct insights into the final stages of stellar evolution. Beyond their astrophysical importance, SNe Ia are also of central importance to cosmology, where they serve as standardizable candles for measuring extragalactic distances. Their cosmological applications are discussed in the following section.

1.4.2 Type Ia Supernovae in Cosmology

One of the most direct ways to investigate the expansion of the Universe is by examining how redshift, z, varies with distance. The importance of Type Ia supernovae in this context is that they enable the measurement of both quantities: their standardisable light curves provide distances, while the corresponding redshifts are determined from their host galaxies.

Redshift and Hubble's Law The redshift z is defined as the fractional change in wavelength between emission and observation:

$$z = \frac{\lambda_{\text{obs}} - \lambda_{\text{emit}}}{\lambda_{\text{emit}}} = \frac{\lambda_{\text{obs}}}{\lambda_{\text{emit}}} - 1, \tag{1.1}$$

where λ_{obs} and λ_{emit} are the observed and emitted wavelengths respectively. In an expanding Universe, the scale factor $a(t)$ describes the relative size of the Universe at time t, and is typically normalised to its present-day value $a_0 = a(t_0)$. Physical distances scale proportionally with $a(t)$, and therefore the wavelength of a photon is stretched as the Universe expands. In particular, a photon emitted at time t will have its wavelength increased according to

$$\frac{\lambda_{\text{obs}}}{\lambda_{\text{emit}}} = \frac{a_0}{a(t)}.$$

It follows that the redshift can be expressed in terms of the scale factor as

$$z = \frac{a_0}{a(t)} - 1, \tag{1.2}$$

where $a_0 = a(t_0)$ is the present-day value of the scale factor. Thus,

$$a(t) = \frac{a_0}{1+z}. \tag{1.3}$$

Normalizing to the present epoch by setting $a_0 = 1$, we obtain

$$a(t) = \frac{1}{1+z}. \tag{1.4}$$

The rate of expansion of the Universe is quantified by the Hubble parameter $H(t)$, defined as

$$H(t) = \frac{\dot{a}(t)}{a(t)}, \tag{1.5}$$

where $\dot{a}(t)$ is the time derivative of the scale factor. Its present-day value, H_0, is known as the Hubble constant.

Distances in Cosmology Measuring distances in cosmology is crucial. Two key distance measures are the comoving distance $r(z)$, which represents the separation between two points measured in comoving coordinates, and remains constant as the Universe expands, and the luminosity distance $d_L(z)$, which is inferred from the observed flux f and intrinsic luminosity L of an object, accounting for the expansion of the Universe.

The study of the large-scale structure and evolution of the Universe is governed by fundamental cosmological principles. One of the cornerstones is the Cosmological Principle, which states that the Universe is homogeneous (invariant under translation) and isotropic (invariant under rotation) on large scales. Under this assumption, and using Einstein's field equations of general relativity, the geometry of the Universe is described by the Friedmann–Lemaître–Robertson–Walker:

$$ds^2 = -c^2dt^2 + a^2(t)\left(\frac{dr^2}{1-kr^2} + r^2d\theta^2 + r^2\sin^2\theta\, d\phi^2\right), \tag{1.6}$$

where $a(t)$ is the scale factor, c is the speed of light, k represents the spatial curvature ($k = -1, 0, +1$ for open, flat, and closed universes, respectively), and r, θ, ϕ are the comoving radial coordinate, polar angle, and azimuthal angle, respectively.

In the context of cosmology, we are interested in how photons propagate radially through spacetime, i.e., light-like intervals where $ds = 0$ and $d\theta = d\phi = 0$. Assuming a spatially flat Universe, $k = 0$, the FLRW metric becomes

$$0 = -c^2dt^2 + a^2(t)dr^2. \tag{1.7}$$

This leads to:

$$dr = \frac{c\,dt}{a(t)}. \tag{1.8}$$

To express dr as a function of redshift z, we differentiate $a(t)$ with respect to time:

$$\dot{a} = \frac{da}{dt} = -\frac{1}{(1+z)^2}\frac{dz}{dt}. \tag{1.9}$$

Since $a = 1/(1+z)$, we obtain

$$H(t) = \frac{\dot{a}}{a} = -\frac{1}{1+z}\frac{dz}{dt}. \tag{1.10}$$

Thus,

$$dt = \frac{-dz}{(1+z)H(z)}. \tag{1.11}$$

Substituting this into $dr = c\,dt/a(t)$, and using $a(t) = 1/(1+z)$, gives

$$dr = \frac{c}{a(t)}\frac{-dz}{(1+z)H(z)} = -\frac{c\,dz}{H(z)}. \tag{1.12}$$

The comoving distance is therefore obtained by integrating from the emission redshift to the present:

$$r(z) = \int_z^0 \left(-\frac{c\,dz}{H(z)}\right). \tag{1.13}$$

The negative sign reflects that redshift increases in the direction opposite to photon propagation. Reversing the integration limits yields the positive comoving distance

$$r(z) = c\int_0^z \frac{dz}{H(z)}. \tag{1.14}$$

This represents the comoving distance, which remains invariant under the expansion of the Universe.

The luminosity distance $d_L(z)$ is defined by the relationship between the observed flux f and intrinsic luminosity L:

$$f = \frac{L}{4\pi d_L^2}. \tag{1.15}$$

In an expanding Universe, the observed flux is further attenuated by two additional effects: first, photon energies are reduced by a factor $(1+z)$ due to redshift; second, their arrival rate is reduced by the same factor due to time dilation. Together, these effects lead to an additional $(1+z)^2$ dimming of the flux. This yields

$$f = \frac{L}{4\pi(r_z\,(1+z))^2} \tag{1.16}$$

and thus,

$$d_L(z) = (1+z)r(z), \tag{1.17}$$

which is the expression for the luminosity distance as a function of the comoving distance.

The final expression for d_L as a function of redshift can be expressed as:

$$d_L(z) = (1+z)\,c\int_0^z \frac{dz}{H(z)}, \tag{1.18}$$

where $H(z)$ is the dimensionless Hubble parameter:

$$H(z) = H_0\sqrt{\Omega_r(1+z)^4 + \Omega_m(1+z)^3 + \Omega_k(1+z)^2 + \Omega_\Lambda} \tag{1.19}$$

(Chen et al., 2017, Wei & Wu, 2017). Here, Ω_r, Ω_m, Ω_Λ, and Ω_k are the density parameters for radiation, matter, dark energy, and curvature, respectively.

The distance modulus μ is related to the luminosity distance by:

$$\mu = m - M = 5\log_{10}\left(\frac{d_L}{10\,\mathrm{pc}}\right), \tag{1.20}$$

where m is the apparent magnitude and M is the absolute magnitude.

This is the context in which SNe Ia serve as their most powerful cosmological tool. Their standardizable light curves enable precise measurements of absolute magnitudes M, using empirical calibrations (i.e., the Phillips relation (Phillips, 1993)). Knowing M and observing the apparent magnitude m, the distance modulus μ, or equivalently, the luminosity distance d_L, can be computed. Redshifts are measured using narrow emission lines from host galaxies (with uncertainties $\lesssim 0.0001$) or broader absorption lines from supernova spectra (with uncertainties up to ~ 0.01) (Steinhardt et al., 2020).

By measuring μ and z for a large sample of SNe Ia, cosmological models can be fit to the expansion history of the universe, with the variables Ω_r, Ω_m, Ω_Λ, and Ω_k and H_0.

In 1998, Two independent groups of astronomers, Perlmutter et al. (1998) and Riess et al. (1998) used this method to reveal that high-redshift SNe Ia were dimmer than expected, implying an accelerating cosmic expansion. The best fits are with $\Omega_m{\approx}0.3$, and $\Omega_\Lambda{\approx}0.7$. Where Λ denotes the cosmological constant, attributed to the enigmatic dark energy.

A persistent tension has emerged between the value of H_0 inferred from SNe Ia distance ladders ($H_0 \approx 73$ km s^{-1} Mpc^{-1}; Riess et al., 2022) and that derived from cosmic microwave background observations ($H_0 \approx 67$ km s^{-1} Mpc^{-1}; Planck Collaboration et al., 2020), now significant at the 5σ level. Whether this discrepancy reflects systematic uncertainties in the SN Ia distance ladder or new physics beyond the standard cosmological model remains an open question.

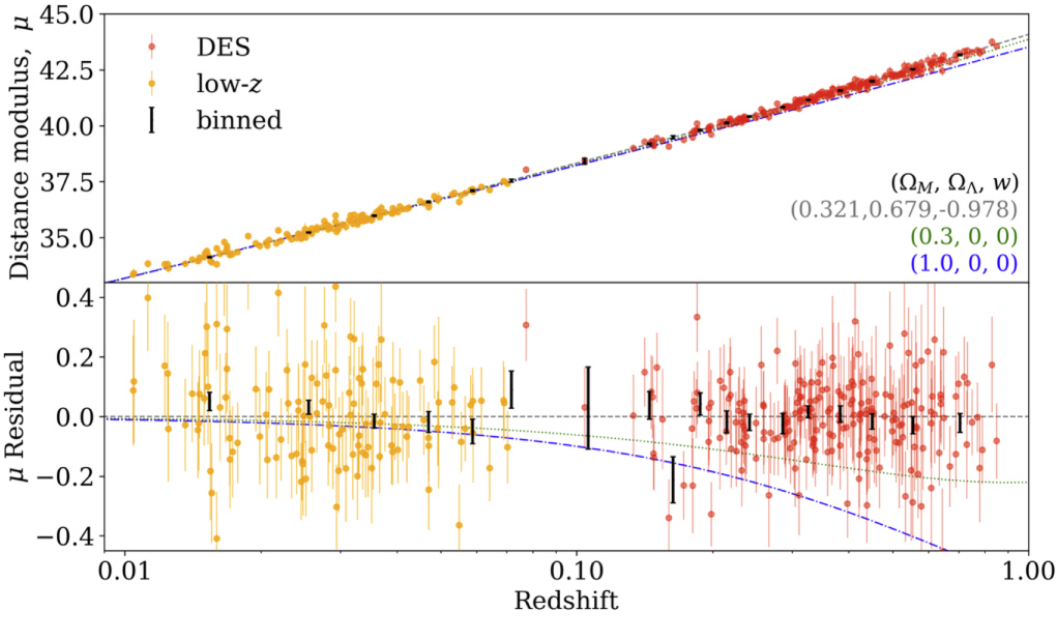


FIGURE 1.5: Hubble diagram for 329 SNe from the Dark Energy Survey Supernova Program (DES-SN) sample. Top: distance modulus μ versus redshift, z. Black bars, represent weighted-average bias-corrected distance moduli in 18 redshift bin while individual SNe are depicted in red and orange circles. The dashed gray line shows the best-fit model, while the green and blue dotted lines show models with no dark energy and matter densities of Ω_m and 1.0 respectively. Bottom: residuals to the best-fit model; 1σ error bars show 68% confidence (Abbott et al., 2019).

Chapter 2

Observational and theoretical aspects

Having established the importance of Type Ia supernovae in the previous chapter, we now turn to their observational properties and physical nature.

Type Ia supernovae are widely understood to arise from the thermonuclear disruption of carbon–oxygen white dwarfs in binary systems (Hillebrandt & Niemeyer, 2000, Mazzali et al., 2007). The explosion is triggered by a thermonuclear runaway under degenerate conditions, releasing sufficient nuclear energy to unbind the star, while the observed optical emission is powered by radioactive decay.

Despite this general framework, several key aspects remain uncertain. The nature of the progenitor system is still debated, with growing evidence that both single- and double-degenerate channels may contribute (Iben & Tutukov, 1984, Livio & Mazzali, 2018, Whelan & Iben, 1973). The origin of the observed diversity is likewise unclear, whether it arises from variations in white dwarf mass, progenitor, metallicity, explosion mechanism, or viewing angle effects. Key processes, such as carbon ignition and flame propagation, remain poorly constrained (Hillebrandt & Niemeyer, 2000, Hillebrandt et al., 2013). Observationally, SNe Ia exhibit a wide range of peak luminosities and spectroscopic properties, which remain difficult to interpret despite numerous classification schemes (Benetti et al., 2005, Branch et al., 2006, Nugent et al., 1995b, Wang et al., 2009).

This chapter presents an overview of the observational and theoretical framework of SNe Ia. It first describes their main observational characteristics, including light-curve and spectral evolution, before introducing their diversity and the key physical processes that govern these events.

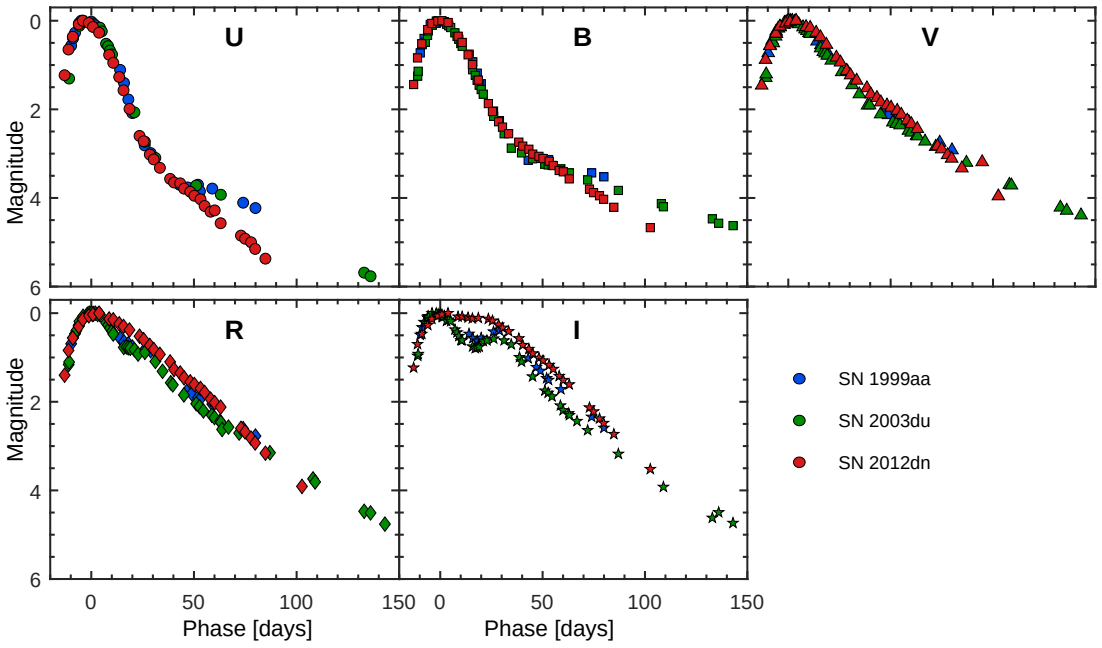


FIGURE 2.1: Comparative UBVRI light curves of SN 1999aa, SN 2003du, and SN 2012dn, plotted as a function of phase relative to B-band maximum and normalized to their peak magnitudes.

2.1 Light curves of type Ia supernovae

The luminosity evolution of SNe Ia, is a key observational probe. It reflects the energy source, ejecta structure, radiative processes, and the distribution of radioactive material and underpins their use as standardisable candles in cosmology.

Observations of SNe Ia light curves across multiple wavelength bands reveal a well-defined photometric evolution. These events were initially thought to be highly homogeneous; however, improved observational coverage has revealed nuances. They typically reach peak brightness within ∼15–21 days after explosion (Ganeshalingam et al., 2011), with absolute B-band magnitudes ranging from approximately −18 to −19.5 mag and peak bolometric luminosities of a few 10^{43} erg s^{-1}.

Following maximum light, the B and V bands decline by ∼3 magnitudes over 30–50 days, followed by a slower decay of ∼1 magnitude per 100 days. In normal SNe Ia (see Section 2.3.1.1), near-infrared (NIR) light curves peak a few days before the optical (Contardo et al., 2000). While the blue bands decline monotonically after maximum, the NIR bands (I, J, H, and K) display a prominent secondary maximum, whose timing varies significantly among events, typically occurring ∼15–100 days later (Elias et al., 1981). This feature is common among SNe Ia, but becomes weaker or absent in some peculiar events, mainly fast-declining 91bg-like and super-Chandrasekhar SNe Ia (see Sections 2.3.1.4 and 2.3.1.3) (Ashall et al., 2021). Figure 2.1 illustrates the multiband

light-curve evolution of the transitional SN 1999aa, the normal SN 2003du, and the peculiar 03fg-like SN 2012dn, all normalized at peak.

Early studies by Phillips (1993) showed that more luminous SNe Ia have broader light curves, while fainter ones decline more rapidly. This behaviour is quantified by the $\Delta m_{15}(B)$ parameter, defined as the decline in B-band magnitude 15 days after maximum light (Phillips, 1993, Phillips et al., 1999), with smaller values corresponding to brighter, more slowly evolving events.

The $\Delta m_{15}(B)$ parameter underlies the Phillips relation, which enables the standardisation of SNe Ia as cosmological distance indicators. Being distance-independent and directly measurable, it is calibrated using nearby SNe Ia with independently determined distances, including stellar parallaxes (within 10 pc), Cepheid and RR Lyrae variables (up to ∼10 Mpc), and the Tully–Fisher relation (up to ∼100 Mpc).

However, as shown in Fig. 2.2, $\Delta m_{15}(B)$ becomes unreliable for rapidly declining SNe Ia ($\Delta m_{15}(B) \gtrsim 1.7$ mag), which are typically cooler and intrinsically fainter. In these rapid decliners, the transition from the initial steep decline to the linear tail occurs before day 15, rendering $\Delta m_{15}(B)$ a poor proxy for the overall B-band evolution (Burns et al., 2014, Phillips, 2012). These objects are often classified as 1991bg-like events (see Section 2.3.1.3; Filippenko et al. 1992a, Leibundgut et al. 1993). The same limitation applies to peculiar super-Chandrasekhar (03fg-like) events (Ashall et al., 2021) and to SN 1999aa (Aouad et al., 2022).

Alternative parametrisations, including light-curve stretch factor, (s) (Perlmutter et al., 1999), the Multi-colour Light Curve Shape (MLCS), Δ (Jha et al., 2007, Riess et al., 1996), and the Spectral Adaptive Lightcurve Template (SALT) (Guy et al., 2005), have been proposed, but they also face challenges when applied to fast-declining events.

To overcome these limitations, Burns et al. (2014) introduced the colour-stretch parameter s_{BV}, defined as the time between B-band maximum and the epoch of maximum $B-V$ colour, normalised to 30 days. Since normal SNe Ia reach their reddest colour around this epoch, they typically have $s_{BV} \approx 1$, whereas fast-declining events show significantly smaller values ($s_{BV} < 0.5$).

Compared to $\Delta m_{15}(B)$, s_{BV} is less sensitive to extinction and remains well correlated with both optical and near-infrared light-curve behaviour, including the presence and timing of secondary maxima (Burns et al., 2018). Physically, the epoch of maximum $B-V$ colour reflects the recombination of Fe III to Fe II in the ejecta: as the ejecta cool, the strengthening of Fe II absorption, particularly in the V-band, modifies the spectral energy distribution and contributes to the emergence of secondary maxima in the near-infrared. Because the timing of this transition is governed by the energy input

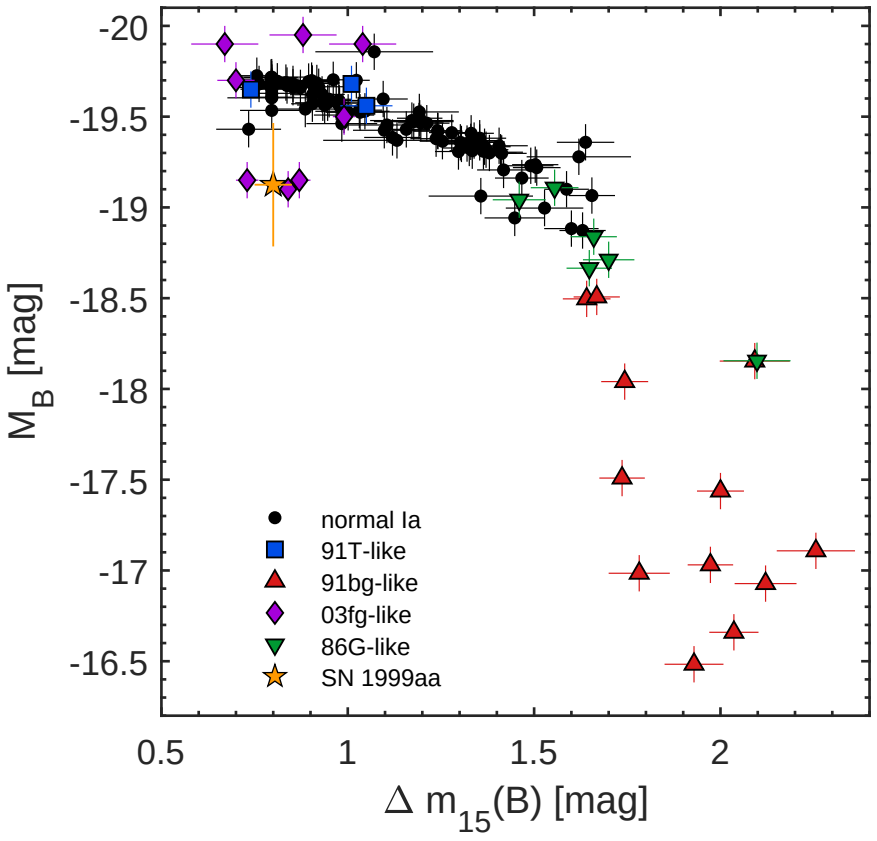


FIGURE 2.2: Peak absolute magnitude M_B as a function of the decline-rate parameter $\Delta m_{15}(B)$ for a sample of SNe Ia. Different symbols and colours indicate the various spectroscopic subclasses. The data are compiled from the Carnegie Supernova Project (CSP; (Ashall et al., 2020, 2021, Bose et al., 2025, Phillips et al., 2022)), and include both normal and peculiar subclasses reproduced from publicly available data.

from ^{56}Ni decay, s_{BV} effectively traces the explosion energetics, providing a more robust standardisation parameter and significantly reducing the scatter in the Phillips relation, particularly for fast-declining SNe Ia (see Fig.2.3; Ashall et al. 2020, 2021).

2.1.1 Physical Drivers of Light-Curve Evolution

A Type Ia supernova is initiated by explosive carbon ignition under degenerate conditions, once the white dwarf reaches a critical density of approximately $2 \times 10^9\,\mathrm{g\,cm^{-3}}$ (Iwamoto et al., 1999). This triggers a thermonuclear runaway that propagates through the star, converting carbon and oxygen into heavier elements including radioactive ^{56}Ni. The energy released exceeds the binding energy of the white dwarf, leading to its complete disruption with no compact remnant. The observed light curve is governed by a

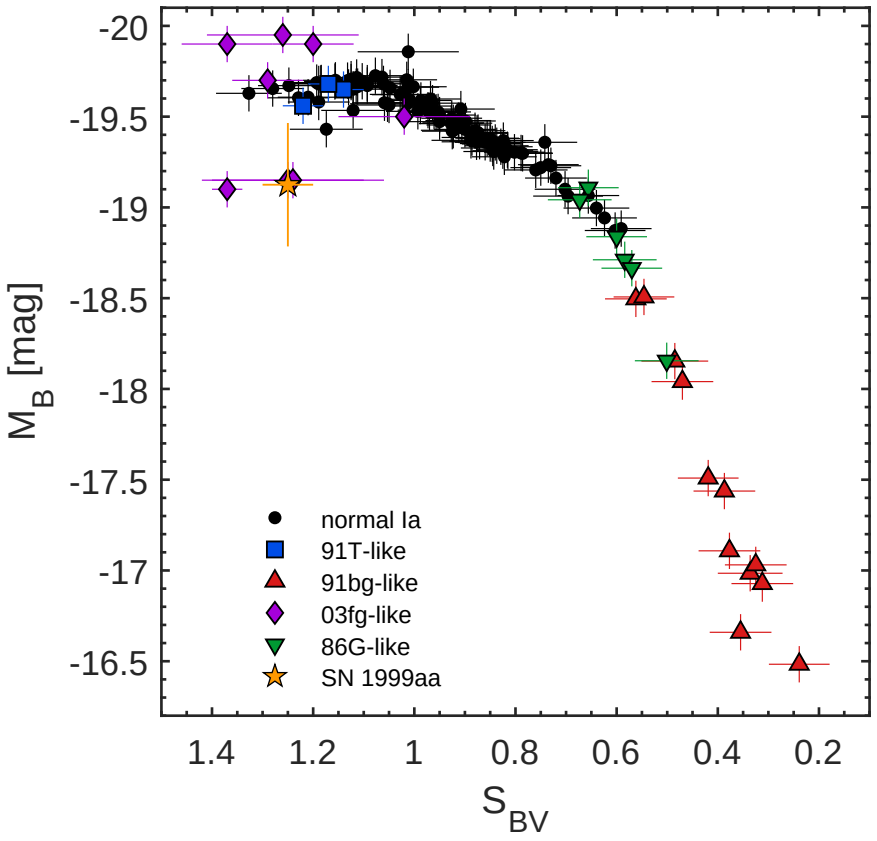


FIGURE 2.3: Peak absolute magnitude M_B as a function of the colour-stretch parameter s_{BV} for a sample of SNe Ia. Different symbols and colours represent the various spectroscopic subclasses. A clear correlation is observed, analogous to the Phillips relation, with s_{BV} providing a more robust description of fast-declining events. The data are drawn from the Carnegie Supernova Project (CSP; (Ashall et al., 2021, Bose et al., 2025)).

balance between energy input (heating) and energy loss (cooling). The primary energy source is the radioactive decay of unstable isotopes synthesized in the ejecta, primarily ^{56}Ni and its daughter products, while cooling occurs through radiative diffusion and adiabatic expansion.

2.1.1.1 Early-Time Emission and Shock Breakout

Following the thermonuclear runaway, the rapid release of energy drives the ejecta into supersonic expansion, generating a shock wave that propagates through the progenitor and eventually emerges at the surface, producing a brief flash of radiation known as shock breakout. The luminosity of this emission scales approximately as $L \propto R^2T^4$, linking it directly to the progenitor's radius and surface temperature.

For compact progenitors such as Type Ia supernovae ($R \sim 10^8$ cm), the shock breakout is intrinsically faint compared to that of extended stars, such as red supergiants ($R \sim 10^{13}$ cm). In addition, the signal is extremely short-lived (of order minutes to an hour) and has not yet been observationally confirmed in SNe Ia (Bersten & Mazzali, 2017a, Piro et al., 2010, Waxman & Katz, 2017). The subsequent evolution is instead governed entirely by radioactive heating, as described below.

2.1.1.2 Radioactive Energy Deposition and Diffusion

The decay of ^{56}Ni synthesised during the explosion, and that of its daughter nuclei, releases the γ-rays and positrons that thermalise within the expanding ejecta and are reprocessed into the optical emission powering the observed light curve. The decay chain proceeds as:

$$^{56}\mathrm{Ni} \xrightarrow{\mathrm{EC}\, t_{1/2}=6.10\,\mathrm{days}} {}^{56}\mathrm{Co} + \gamma + \nu_e \tag{2.1}$$

$$\left.\begin{aligned} {}^{56}\mathrm{Co} &\xrightarrow{\mathrm{EC}\ (81\%)\, t_{1/2}=77.27\,\mathrm{days}} {}^{56}\mathrm{Fe} + \gamma + \nu_e, \\ {}^{56}\mathrm{Co} &\xrightarrow{\beta^+(19\%)\, t_{1/2}=77.12\,\mathrm{days}} {}^{56}\mathrm{Fe} + \gamma + e^+ + \nu_e \end{aligned}\right\} \tag{2.2}$$

(Colgate & McKee, 1969, Pankey, 1962). ^{56}Ni decays via electron capture (EC) into ^{56}Co with a half-life of $t_{\mathrm{Ni},1/2} = 6.1$ days — a timescale short enough that ^{56}Ni is largely exhausted within the first few weeks, contributing primarily to the pre-maximum rise rather than the post-maximum decline. ^{56}Co subsequently decays into stable ^{56}Fe with a half-life of $t_{\mathrm{Co},1/2} = 77$ days, long enough that it remains the dominant energy source for months and sets the timescale of the post-maximum decline. It proceeds either via EC (81%) or β^+ decay (19%), producing γ-rays and positrons respectively, which couple to the ejecta with different opacities and dominate the heating at different epochs, as discussed below. Of the total decay energy, 96% is carried by γ-rays ($Q_\gamma = 5.36$ MeV) and 4% by positrons ($Q_{e^+} = 0.12$ MeV); the neutrino fraction escapes without interaction and is neglected throughout (Branch & Wheeler, 2017).

At early times, the ejecta are optically thick to γ-rays ($\kappa_\gamma \approx 0.03\,\mathrm{cm^2\,g^{-1}}$), effectively trapping them and progressively degrading their energy through Compton scattering while transferring kinetic energy to electrons, which thermalise via collisions, depositing their energy by ionising and exciting atoms. The subsequent de-excitation produces lower-energy optical photons powering the observed emission. At the relevant energies of order 1 MeV, the distinction between interactions with bound and free electrons is

negligible, so the deposition is largely independent of the ionisation state of the gas. As photon energies decrease, photoelectric absorption on Fe-group elements (Ni, Co, Fe) becomes increasingly important; their high atomic numbers enhance the photoelectric absorption cross-section, which scales as $\sigma_{\rm pe} \propto Z^5 E_\gamma^{-3}$, leading to more efficient energy deposition. As the ejecta expand and dilute, their optical depth to γ-rays declines and the escaping fraction grows, so the deposition fraction falls steadily with time (Cappellaro et al., 1997).

At late times, once γ-ray trapping becomes inefficient, positrons progressively dominate the deposited energy as the fraction of escaping γ-rays increases. Positrons carry a much higher effective opacity ($\kappa_{e^+} \approx 7\,\mathrm{cm^2\,g^{-1}}$ (Colgate et al., 1980)) than γ-rays and, confined by magnetic fields, deposit their energy locally by scattering off electrons. As they decelerate, the probability of annihilation with an ambient electron increases, producing two γ-ray photons each at $m_e c^2 = 0.511\,\mathrm{MeV}$, which may themselves deposit further energy or escape. Although positrons contribute only $\sim$4% of the total decay energy, they become the dominant source driving the light curve during these phases.

The total energy input at any given time is the combined contribution from the ^{56}Ni $\rightarrow$ ^{56}Co and ^{56}Co $\rightarrow$ ^{56}Fe decay chains. The time-dependent evolution of the nuclide populations is governed by a system of first-order differential equations:

$$\frac{dN_{\rm Ni}}{dt} = -\frac{N_{\rm Ni}}{\tau_{\rm Ni}}, \tag{2.3}$$

$$\frac{dN_{\rm Co}}{dt} = \frac{N_{\rm Ni}}{\tau_{\rm Ni}} - \frac{N_{\rm Co}}{\tau_{\rm Co}}, \tag{2.4}$$

$$\frac{dN_{\rm Fe}}{dt} = \frac{N_{\rm Co}}{\tau_{\rm Co}}, \tag{2.5}$$

with initial conditions $N_{\rm Ni}(0) = N_{\rm Ni,0}$, $N_{\rm Co}(0) = 0$, $N_{\rm Fe}(0) = 0$. Solving, we obtain:

$$N_{\rm Ni} = N_{\rm Ni,0}\, e^{-t/\tau_{\rm Ni}}, \tag{2.6}$$

$$N_{\rm Co} = N_{\rm Ni,0}\, \frac{\tau_{\rm Co}}{\tau_{\rm Co} - \tau_{\rm Ni}} \left(e^{-t/\tau_{\rm Co}} - e^{-t/\tau_{\rm Ni}} \right), \tag{2.7}$$

$$N_{\rm Fe} = N_{\rm Ni,0} \left(1 + \frac{\tau_{\rm Ni}}{\tau_{\rm Co} - \tau_{\rm Ni}}\, e^{-t/\tau_{\rm Ni}} - \frac{\tau_{\rm Co}}{\tau_{\rm Co} - \tau_{\rm Ni}}\, e^{-t/\tau_{\rm Co}} \right). \tag{2.8}$$

The total specific power at any given time is:

$$\epsilon_{\rm rad} = \epsilon_{\rm Ni} + \epsilon_{\rm Co}, \tag{2.9}$$

where

$$\epsilon_{\rm Ni} = -\langle Q_{\rm Ni}\rangle \frac{dN_{\rm Ni}}{dt}, \qquad \epsilon_{\rm Co} = -\langle Q_{\rm Co}\rangle \frac{dN_{\rm Co}}{dt}, \tag{2.10}$$

and $\langle Q_{\rm Ni}\rangle$ and $\langle Q_{\rm Co}\rangle$ are the mean energies deposited per decay of ^{56}Ni and ^{56}Co, respectively. Substituting and writing $M_{\rm Ni} = 56\, m_u\, N_{\rm Ni,0}$, where m_u is the atomic mass unit, leads to:

$$\epsilon_{\rm rad} = \left(\frac{1}{\tau_{\rm Ni} - \tau_{\rm Co}} \left[\langle Q_{\rm Ni}\rangle \left(\frac{\tau_{\rm Co}}{\tau_{\rm Ni}} - 1 \right) - \langle Q_{\rm Co}\rangle \right] e^{-t/\tau_{\rm Ni}} + \langle Q_{\rm Co}\rangle\, e^{-t/\tau_{\rm Co}} \right) \times \frac{M_{\rm Ni}}{56\, m_u}. \tag{2.11}$$

With $\tau_{\rm Ni} = t_{\rm Ni,1/2}/\ln 2 = 8.80\,$days, $\tau_{\rm Co} = t_{\rm Co,1/2}/\ln 2 = 111.3\,$days, $\langle Q_{\rm Ni}\rangle = 1.75\,$MeV, and $\langle Q_{\rm Co}\rangle = 3.73\,$MeV, the above expression reduces to:

$$\epsilon_{\rm rad} = \left(6.45 \times 10^{43}\, e^{-t/8.8} + 1.45 \times 10^{43}\, e^{-t/111.3} \right) \frac{M_{\rm Ni}}{M_\odot} \quad {\rm erg\,s^{-1}}, \tag{2.12}$$

where t is measured in days from the explosion (Branch & Wheeler, 2017, Nadyozhin, 1994, Stritzinger & Leibundgut, 2005). In general, the observed bolometric luminosity is determined by two coupled processes: the fraction of radioactive decay energy deposited in the ejecta by γ-rays and positrons, and the fraction of the resulting optical radiation that escapes through the expanding ejecta. An exact treatment therefore requires both computing the γ-ray deposition fraction as a function of time and solving the radiative transfer problem for the optical photons. This is achieved through Monte Carlo radiative transfer calculations in which the deposition of γ-rays and positrons is tracked through the ejecta, with the opacity dominated by line opacity and treated as a function of composition (Cappellaro et al., 1997, Mazzali & Podsiadlowski, 2006, Mazzali et al., 2001a, Pauldrach et al., 1996).

The different physical regimes governing the light curve evolution are illustrated schematically in Figure 2.4. During the rising phase, radioactive energy deposition exceeds the radiated luminosity over a period lasting 15–21 days, reaching maximum when the two balance — Arnett's rule (Arnett, 1982, Pinto & Eastman, 2000) — so that $L_{\rm peak} = \epsilon_{\rm rad}(t_{\rm peak})$ and $M_{\rm Ni} \propto L_{\rm peak}$ (see Section 2.1.1.3 for an analytical derivation).

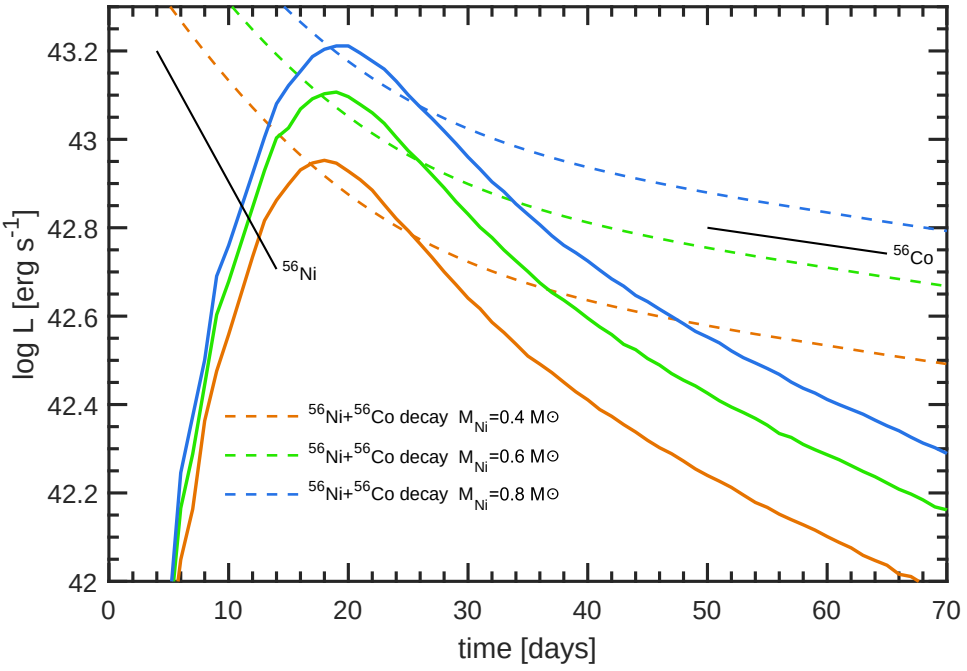


FIGURE 2.4: Schematic bolometric light curves (solid lines) and instantaneous ^{56}Ni+^{56}Co radioactive energy input rates $\epsilon_{\rm rad}$ (Equation 2.12, dashed lines) for different values of synthesised ^{56}Ni mass illustrating the physical regimes discussed in the text.

Past maximum, previously trapped photons diffuse outward and the instantaneous luminosity temporarily exceeds $\epsilon_{\rm rad}$ for a few tens of days. By this time the majority of ^{56}Ni has decayed to ^{56}Co, which becomes the dominant energy source. The light curve then settles onto an exponential decline, typically steeper than the ^{56}Co decay rate alone due to increasing γ-ray escape as the ejecta density drops substantially. Between ∼150 and 300 days past maximum, γ-ray trapping becomes increasingly inefficient and positrons progressively dominate the deposited energy, sustaining emission for few hundred days at ∼1 mag per 100 days.

2.1.1.3 Peak Luminosity and Light-Curve Width

Having established the qualitative framework of radioactive energy deposition and radiative diffusion, we now develop a quantitative description of the two principal observables of SN Ia light curves: the peak luminosity and the light-curve width. These quantities provide direct constraints on the synthesised ^{56}Ni mass, ejecta mass, opacity, and kinetic energy of the explosion.

Peak Luminosity In the Arnett model (Arnett, 1982), the evolution of the radiation field is governed by the first law of thermodynamics applied to the expanding ejecta (see Appendix A for the full algebraic steps). The change in internal energy plus the work done by expansion equals the net heat supplied to the system:

$$\Delta U + W = Q, \tag{2.13}$$

which in terms of time derivatives becomes:

$$\frac{dE}{dt} + P\frac{dV}{dt} = \epsilon_{\rm rad} - \frac{E}{\tau_d(t)}, \tag{2.14}$$

where dE/dt is the rate of change of internal energy, $P\,dV/dt$ is the work done by expansion, $\epsilon_{\rm rad}$ is the radioactive energy input per unit mass from ^{56}Ni decay, and $E/\tau_d(t)$ is the luminosity, i.e. the rate at which energy is lost by radiative diffusion, with $\tau_d(t)$ being the time-dependent diffusion timescale governing how rapidly photons escape the ejecta. The internal energy of the ejecta comprises the kinetic energy of particles, the radiation field energy, and the potential energy associated with excitation and ionisation.

In a radiation-dominated gas, where matter contributes negligibly to the pressure and thermal energy, the internal energy and pressure take the form:

$$E = aT^4V, \qquad P = \frac{1}{3}aT^4. \tag{2.15}$$

The diffusion timescale is:

$$\tau_d = \frac{3R^2}{\pi^2\lambda c}, \tag{2.16}$$

where $\lambda = 1/(\rho\kappa)$ is the mean free path. Substituting the expressions for E and P into equation (2.14) and dividing through by $4aT^3V$ yields:

$$4\left(\frac{\dot{T}}{T} + \frac{\dot{R}}{R}\right) = \frac{1}{\tau_{\rm heat}} - \frac{1}{\tau_d}, \tag{2.17}$$

where $1/\tau_{\rm heat} = \epsilon_{\rm rad}/E$ is the radioactive heating rate, and we have used $\dot{V}/3V = \dot{R}/R$, which follows from $V = \frac{4}{3}\pi R^3$ for a uniformly expanding sphere. Substituting the expressions for E and τ_d into the diffusion approximation for the luminosity, leads to:

$$L = \frac{16\pi^4 acT^4 R^4}{27\kappa M}. \tag{2.18}$$

The peak luminosity occurs when $dL/dt = 0$. Taking the total time derivative of equation (2.18), assuming M is constant, and substituting equation (2.17) (see Appendix A):

$$\frac{dL}{dt} = L\left(\left(4\frac{\dot{T}}{T} + 4\frac{\dot{R}}{R}\right) - \frac{\dot{\kappa}}{\kappa}\right). \tag{2.19}$$

Setting $dL/dt = 0$ at maximum light and substituting equation (2.17):

$$\frac{1}{\tau_{\rm heat}} - \frac{1}{\tau_d} = \frac{\dot{\kappa}}{\kappa}. \tag{2.20}$$

For constant opacity ($\dot{\kappa} = 0$), equation (2.20) reduces to $\tau_{\rm heat} = \tau_d$: the timescale on which radioactive decay supplies energy equals the timescale on which photons escape by diffusion. Since the luminosity is $L = E/\tau_d$ and the heating rate is $\epsilon_{\rm rad} = E/\tau_{\rm heat}$, the condition $\tau_{\rm heat} = \tau_d$ directly implies $L_{\rm max} = \epsilon_{\rm rad}$, which is Arnett's rule:

$$L_{\rm max} = \alpha\, \epsilon_{\rm rad}(t_{\rm max}), \tag{2.21}$$

Here α is a correction factor accounting for deviations from the idealised model (Arnett, 1982, Pinto & Eastman, 2000); in the simplest case $\alpha = 1$ and the peak luminosity is directly proportional to the ^{56}Ni mass. The approximation holds as long as the ejecta are fully opaque to γ-rays at maximum light, which is well justified for normal SNe Ia. Its limitation lies in the adoption of a simplified point source geometry that neglects the spatial distribution of ^{56}Ni within the ejecta; a more reliable approach is to model the bolometric light curve directly, accounting for the full density and composition structure (Cappellaro et al., 1997, Mazzali et al., 2001a).

The ^{56}Ni mass synthesised in SNe Ia spans $\sim$0.1–1 $M_\odot$ (Mazzali et al., 2001a, 2008), giving rise to the observed diversity in peak luminosity. The origin of this range remains debated, with proposed explanations involving differences in progenitor mass, burning regime, or both (Mazzali et al., 2001a, 2008). In some peculiar SNe Ia, and possibly entire subclasses, an additional non-radioactive contribution from ejecta–CSM interaction causes Arnett's rule to overestimate the ^{56}Ni mass, introducing a systematic discrepancy with respect to the mass inferred from abundance tomography (Hachinger et al., 2012, Taubenberger et al., 2011, 2019).

Light-Curve Width and the Phillips Relation The width of the light curve, or inversely its decline rate, is proportional to the diffusion timescale $t_{\rm diff}$, which can be derived from first principles as follows.

A photon diffusing through the ejecta does not travel in a straight line, it scatters off electrons and ions repeatedly, each step covering a mean free path l. After N such steps the photon displaces a net distance

$$R \sim \sqrt{N} \cdot l \quad \Rightarrow \quad N \sim \left(\frac{R}{l}\right)^2, \tag{2.22}$$

which is the standard random walk result, where displacement grows as the square root of the number of steps rather than linearly. Since each step is traversed at the speed of light in time l/c, the total diffusion time over N steps is

$$t_{\rm diff} = N \cdot \frac{l}{c} = \left(\frac{R}{l}\right)^2 \cdot \frac{l}{c} = \frac{R^2}{l\,c}. \tag{2.23}$$

Since R/l corresponds to the optical depth τ, this gives $t_{\rm diff} \sim \tau R/c$. Assuming uniform density and grey opacity, $\tau = \kappa\rho R$, and substituting $\rho = M_{\rm ej}/(4\pi R^3)$ yields $t_{\rm diff} \sim \kappa M_{\rm ej}/(Rc)$. Under homologous expansion at peak light, the ejecta radius scales as $R = v\,t_{\rm diff}$, where v is the characteristic ejecta expansion velocity, giving $t_{\rm diff}^2 \sim \kappa M_{\rm ej}/(vc)$. Substituting $v \sim (E_k/M_{\rm ej})^{1/2}$ gives $t_{\rm diff}^2 \sim \kappa M_{\rm ej}^{3/2} E_k^{-1/2}/c$, and taking the square root yields

$$t_{\rm diff} \sim \Phi_{\rm Ni}\, \kappa^{1/2}\, M_{\rm ej}^{3/4}\, E_k^{-1/4}, \tag{2.24}$$

where $\Phi_{\rm Ni}$ is a dimensionless scaling factor that absorbs geometric constants and accounts for the distribution of ^{56}Ni within the ejecta (Arnett, 1982).

The diffusion timescale depends primarily on the ejected mass, with weaker dependencies on opacity and kinetic energy. More massive ejecta retain radiation for longer, producing broader and more slowly declining light curves, while more energetic explosions tend to reduce the diffusion time by accelerating the expansion of the ejecta.

The kinetic energy of the supernova ejecta can be estimated following Woosley et al. (2007a) as

$$E_k = \left[1.56\, M(^{56}\mathrm{Ni}) + 1.74\, M(\mathrm{Fe}) + 1.24\, M(\mathrm{IME}) - E_{\rm bind}\right] \times 10^{51}\,\mathrm{erg}, \tag{2.25}$$

where $M(^{56}\mathrm{Ni})$, $M(\mathrm{Fe})$, and $M(\mathrm{IME})$ are the synthesised masses of ^{56}Ni, Fe-group elements, and intermediate-mass elements (primarily silicon and sulphur) in solar masses, respectively, and $E_{\mathrm{bind}} = 0.46 \times 10^{51}$ erg is the gravitational binding energy of the progenitor white dwarf.

The coefficients 1.56, 1.74, and 1.24 represent the nuclear energy released per solar mass of each burning product, derived from the difference in nuclear binding energy per nucleon between the carbon-oxygen fuel and the respective ash species.

The opacity is also strongly composition dependent. In the hydrogen-poor ejecta of SNe Ia, continuum opacity is negligible and line opacity dominates (Pauldrach et al., 1996). Fe-group elements, possess a very large number of line transitions that efficiently trap photons and impede diffusion. The effective opacity therefore scales approximately with the mass of nuclear statistical equilibrium (NSE) material and, to a lesser extent, with the IME mass,

$$\kappa \propto M(\mathrm{NSE}) + 0.1\, M(\mathrm{IME}) \tag{2.26}$$

(Mazzali & Podsiadlowski, 2006, Mazzali et al., 2007). Consequently, events synthesizing larger amounts of ^{56}Ni are not only hotter and more luminous, but also have higher opacities and longer diffusion timescales, producing broader and more slowly declining light curves. This naturally gives rise to the observed width–luminosity relation in SNe Ia (Arnett, 1982, Bersten & Mazzali, 2017b, Colgate & McKee, 1969, Mazzali et al., 2001a, Pankey, 1962).

The B-band decline rate is further modulated by the ionisation state of the ejecta. As the ejecta cool after maximum light, Fe-group elements recombine from doubly to singly ionised species, and Fe II/Co II absorption features become increasingly important in the B-band. Less luminous SNe Ia are on average cooler, so this ionisation transition occurs earlier, redistributing flux to longer wavelengths more rapidly and producing a faster B-band decline (Hoeflich et al., 1996, Kasen & Woosley, 2007).

2.2 Spectra of type Ia supernovae

2.2.1 The photospheric phase

In the early phases of a SN Ia, radiation emerges from an optically thick region known as the photosphere; a pseudo-surface defined by the layer at which the optical depth reaches $\tau \approx 2/3$, below which the ejecta are opaque and above which they become transparent. The inner ejecta at this stage contain most of the radioactive ^{56}Ni synthesised during the explosion, which serves as the primary energy source and, together with other Fe-group elements, as the dominant contributor to opacity. Within this region, matter and radiation are tightly coupled, and local thermodynamic equilibrium (LTE) is a reasonable approximation, particularly at early times, such that the radiation field closely follows a Planck distribution at the local temperature.

Photons diffusing outward from the photosphere pass through the overlying ejecta layers, which, although they generate no additional energy, interact with the radiation field through absorption and scattering. In radiative equilibrium, energy is transported purely by radiation with no net gain or loss. Some photons escape the atmosphere and are observed, while others are scattered back toward the photosphere, contributing to its heating.

Following the explosion, the ejecta rapidly enter a phase of homologous expansion in which each element of matter coasts at constant velocity, so that $v = r/t$ at all times. A key consequence is that velocity serves as a direct coordinate for depth: a measured line velocity maps to the lower boundary of the layer in which the line forms, since lines form at or above the photosphere. As the ejecta expand and become more transparent, the photosphere recedes in mass coordinates, progressively exposing deeper, lower-velocity layers; the principle underlying abundance tomography, which maps the full composition structure from a time series of spectra (Lucy, 1999, Stehle et al., 2005). For lines whose lower level is an excited state, such as Si II λ 6355, the population of the lower level drops rapidly in the outer low-density ejecta, so the absorption minimum forms near the photosphere and directly traces its velocity. For resonance lines from the ground state, such as Ca II H&K, the line remains optically thick even in the low-density outer ejecta, so the absorption minimum forms well above the photosphere and appears more blueshifted, making such lines sensitive tracers of high-velocity material (Branch & Wheeler, 2017).

A direct consequence of this expansion is the formation of characteristic P-Cygni profiles in the spectrum: atoms in the observer's line of sight moving toward the observer absorb photons, producing a blue-shifted absorption trough, while atoms moving in other directions scatter photons back into the line of sight, generating an emission component

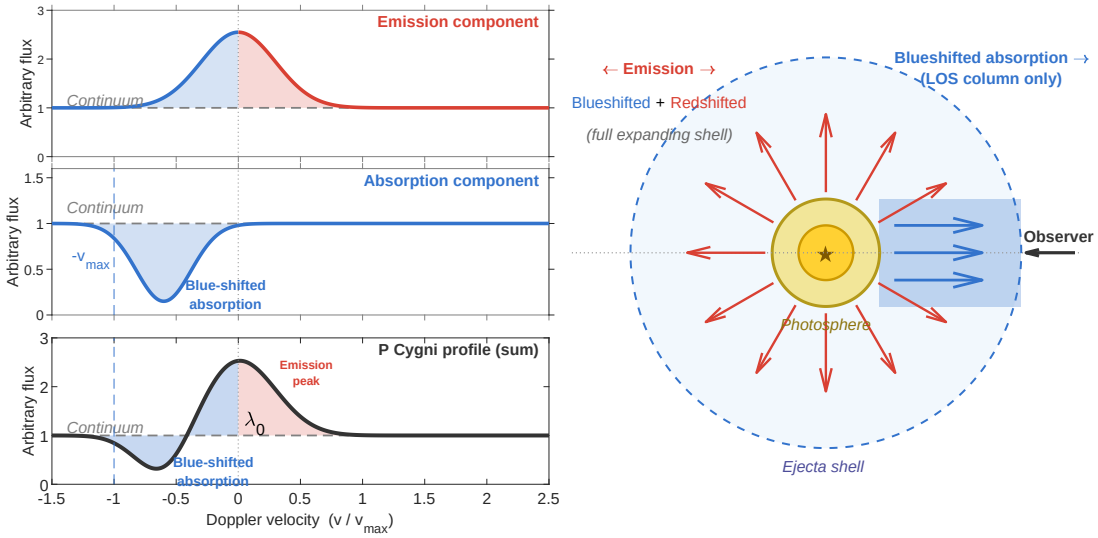


FIGURE 2.5: Formation of a P Cygni profile in an expanding supernova ejecta. *Left:* Decomposition of the profile into a symmetric emission component centred at the rest wavelength λ_0, produced by the full expanding shell, and a blue-shifted absorption trough at $v \approx -v_{\max}$, caused by absorption along the line of sight; their superposition yields the characteristic P Cygni profile. *Right:* Schematic geometry illustrating how the approaching ejecta column between the photosphere and the observer produces the blue-shifted absorption, while the remainder of the shell contributes to the emission peak.

centred approximately on the rest wavelength (Filippenko, 1997). The degree of blue-shift directly reflects the velocity of the absorbing layer. An illustrative schematic is shown in Fig.2.5.

At the typical expansion velocities of SN Ia ejecta, 10,000–15,000 km s^{-1}, the large number of spectral lines from Fe-group elements are Doppler-shifted across broad wavelength ranges, resulting in significant line overlap particularly in the UV. This gives rise to line blanketing: flux suppression as overlapping lines block photon escape. Following absorption, photons cascade through intermediate transitions to lower energy states (Mazzali, 2000), redistributing flux from the ultraviolet to the red.

2.2.2 The nebular phase

As the ejecta expand and their density decreases, the inner regions eventually become optically thin and the supernova enters the nebular phase. Unlike the photospheric phase, there is no longer a thermal continuum generated from a photosphere; the spectrum consists of discrete emission lines on a negligible continuum background.

The gas is heated by γ-rays and positrons from the decay of ^{56}Co for several hundred days past maximum. At these late epochs, the ejecta are largely transparent to γ-rays, which deposit their energy non-locally, while positrons deposit their energy locally. Energetic non-thermal electrons are generated as γ-rays undergo Compton scattering in the ejecta and positrons deposit their kinetic energy. Under the low-density conditions of the nebular phase, collisional de-excitation becomes inefficient, allowing forbidden-line emission to dominate the cooling of the ejecta as photons escape. The ionisation and excitation state of the gas must therefore be treated in NLTE, as the ejecta depart strongly from LTE conditions (Mazzali et al., 2001b).

The characteristic nebular emission-line profile peaks near the rest wavelength, since forbidden lines originate in the slow-moving inner ejecta (typically a few thousand km s^{-1}). In the optically thin limit, the line profile directly traces the spatial distribution of the emitting material and typically exhibits a parabolic shape, since the observed flux at each wavelength is proportional to the projected circular area of ejecta moving at a given line-of-sight velocity, which decreases quadratically toward higher velocities. Centrally concentrated emission produces peaked profiles, while a central deficit or blobs of material moving in different directions can produce flat-topped or double-peaked features (Mazzali et al., 2022). Nebular spectra therefore provide direct constraints on the distribution of Fe-group elements, the total ^{56}Ni mass, and the geometry of the inner ejecta, with wavelength shifts of line peaks tracing asymmetries along the line of sight (Branch & Wheeler, 2017, Mazzali et al., 1998, 2014).

The nebular spectrum of a normal SN Ia is dominated by two prominent emission features: one near 4700 Å dominated by [Fe III] and one near 5200 Å dominated by [Fe II]. The ratio of these features provides a diagnostic of the ionisation state of the inner ejecta and, by extension, of the central density of the exploding white dwarf: a high [Fe III]/[Fe II] ratio indicates a high ionisation state, generally indicative of a lower central density at the time of explosion, as observed for example in SN 2003hv (Mazzali et al., 2011). Additional prominent features include a blend of [Na I] D and [Fe II] near 6000 Å, a feature near 7200 Å dominated by [Fe II] and [Ca II], and a feature near 7400 Å attributed to [Fe II] and [Ni II] $\lambda\,\lambda$ 7380, 7410 (Mazzali et al., 2015). The latter is particularly useful as it sets an upper limit on the mass of stable nickel in the innermost ejecta. Figure 2.9 shows typical nebular-phase SNe Ia spectra with the major emission features marked.

The photospheric and nebular phases provide complementary constraints on the ejecta structure, probing the outer and inner layers respectively. Together, they enable reconstruction of the abundance stratification through abundance tomography.

2.3 Diversity and Empirical Classification Schemes of SNe Ia

2.3.1 Diversity

SNe Ia exhibit significant photometric and spectroscopic diversity, with many events deviating from the normal population (Filippenko, 1997, Jha et al., 2019, Siebert et al., 2019, Silverman et al., 2012a). While this diversity complicates their use as standard candles, it also provides important constraints on thermonuclear explosion physics and progenitor systems. The need for subclassification became evident following the discovery of SN 1991bg (Filippenko et al., 1992a, Leibundgut et al., 1993) and SN 1991T (Filippenko et al., 1992b). Since then, several additional peculiar subclasses have been identified. The main subclasses are briefly outlined below.

2.3.1.1 Normal SNe Ia

Normal SNe Ia are characterized by relatively homogeneous spectroscopic properties and a strong adherence to the Phillips relation, representing roughly 70% of volume-limited samples (Li et al., 2011a). They reach absolute B-band magnitudes of $M_B = -19.1 \pm 0.06$ mag (Ashall et al., 2016), with decline rates $\Delta m_{15}(B)$ between 1.19 ± 0.01 and 1.29 ± 0.08 mag (Ashall et al., 2016, Hakobyan et al., 2020). They are observed in both star-forming and passive galaxies, indicating progenitor populations spanning a broad range of stellar ages (Sullivan et al., 2006).

At photospheric epochs, the defining spectral feature is Si II λ 6355 — a blend of Si II $\lambda\,\lambda$ 6347, 6371 with a gf-weighted rest wavelength of 6355 Å, observed near 6100 Å. A second silicon feature, Si II λ 5972, is observed blueward and varies in strength among events. A characteristic "W"-shaped from S II $\lambda\,\lambda$ 5428, 5432, 5453 and $\lambda\,\lambda$ 5606, 5639, 5640 appears between 5200 and 5600 Å, while further to the blue, Si III $\lambda\,\lambda$ 4553, 4568, a blend of Mg II λ 4481 and Fe III, and Si II λ 4130 produce prominent absorptions near 4800, 4400, and 4000 Å, respectively. Near 3700 Å, the Ca II H&K feature consists of both photospheric-velocity (PV) and high-velocity (HV) components, the latter reaching $\sim$18,000 km s^{-1} and dominating the broad absorption profile (Childress et al., 2014). Additional features include a broad blend of O I λ 7773 and Mg II $\lambda\,\lambda$ 7877, 7896 near 7500 Å, and the Ca II NIR triplet near 8000 Å.

Toward and beyond maximum light, Si II λ 6355 strengthens while its velocity decreases as the photosphere recedes to slower inner layers. The region between 4600 and 5000 Å becomes increasingly dominated by blends of Fe II and Fe III as the ejecta cool and recombine, eventually shaping much of the spectrum a few weeks after maximum (Filippenko,

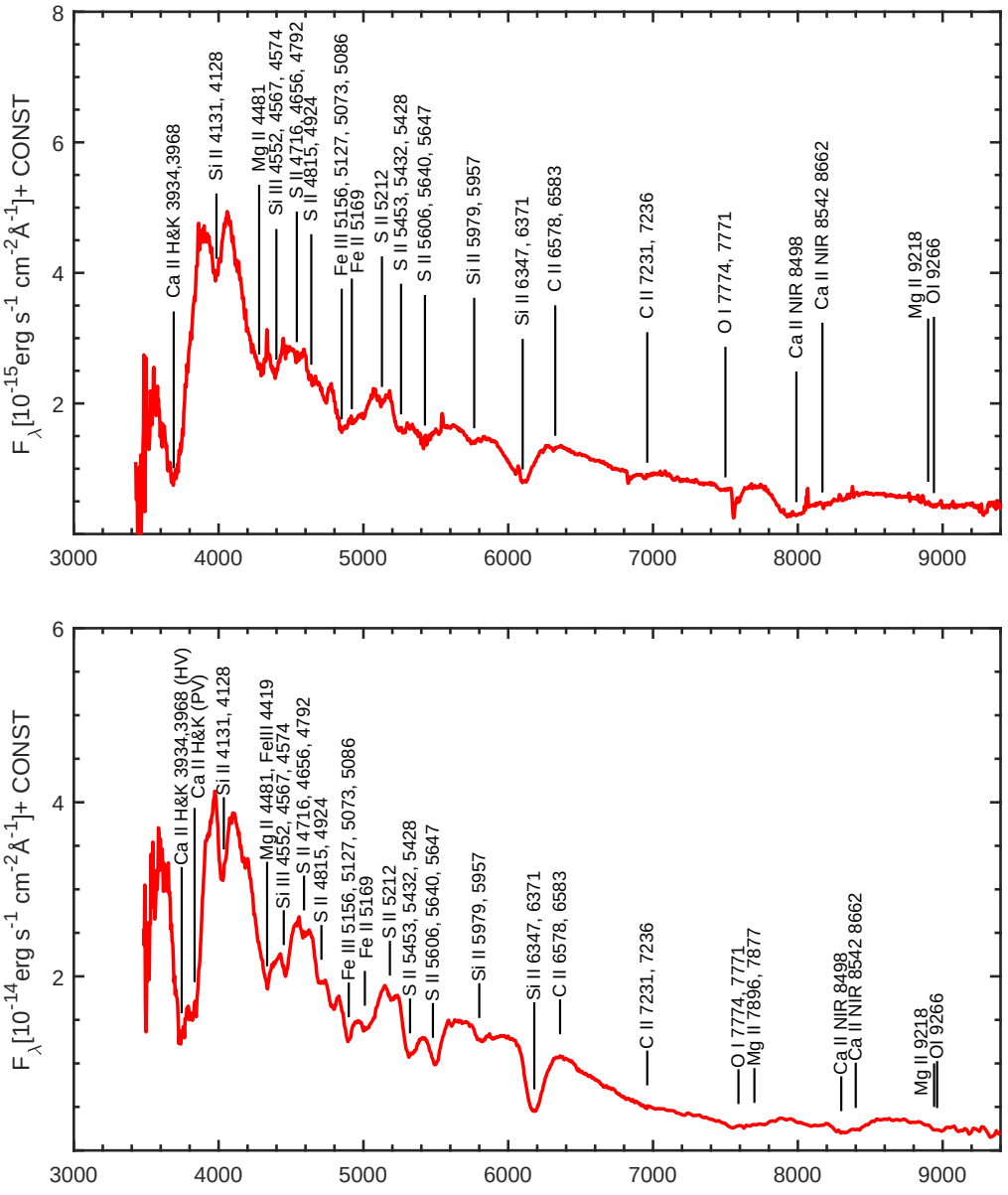


FIGURE 2.6: Spectra of the normal SN 2003du at day −11 (top) and day +1 (bottom) relative to B-band maximum light, with the major spectral features identified and their corresponding rest wavelengths indicated.

1997, Parrent et al., 2014). Figure 2.6 shows an early and a maximum-light spectrum of the normal SN 2003du, with the main absorption features identified (Tanaka et al., 2011).

In the nebular phase, the ejecta become optically thin and the spectra transition to emission-dominated, with prominent forbidden Fe-group complexes near 4700 and 5200 Å attributed to [Fe III] and a blend of [Fe II]/[Fe III], respectively (Mazzali et al., 2015).

2.3.1.2 1991T-like

This subclass is named after SN 1991T (Filippenko et al., 1992b, Phillips et al., 2024), the first SN Ia observed with these distinctive properties. 1991T-like events are slow decliners, typically exhibiting $\Delta m_{15}(B)$ values between 0.8 and 1.0, and are intrinsically brighter than normal SNe Ia, often showing negative Hubble residuals corresponding to overluminosities of $\sim$ 0.1−0.6 mag (Phillips et al., 2022). They are rare in the local Universe, with reported fractions of 4–9% of all SNe Ia (Desai et al., 2024, Li et al., 2011a). However, their association with younger stellar populations suggests they may dominate the SNe Ia population in the early Universe ($z \sim$ 4–11) (Chakraborty et al., 2024), making their characterisation critical for high-redshift cosmology (Phillips et al., 2024).

The early optical spectra of 91T-like objects are nearly featureless redward of ∼6000 Å, with a very weak or absent Si II λ 6355. Instead, their spectra are dominated by prominent Fe III absorption near 4230 and 4910 Å, attributed to Fe III λ 4404 and λ 5129, whose strengths vary significantly between objects (Aouad et al., 2024, Phillips et al., 2022). They also lack the "W"-shaped S II feature and display only a faint or nearly invisible Ca II H&K feature.

The Si III $\lambda\lambda$ 4553, 4568 feature is often stronger than in normal SNe Ia and varies little between objects, unlike the highly variable Fe III features despite their similar ionisation potentials. This suggests that abundance differences, rather than ionisation alone, may contribute to the diversity in Fe III strength.

Phillips et al. (2022) established a quantitative classification criterion based on the pEW of Si II λ 6355: $\lesssim$ 20 Å at −10 days, $\lesssim$ 40 Å at maximum, and $\lesssim$ 50 Å at +10 days. Additionally, 91T-like events exhibit a flat Si II λ 6355 velocity at ∼10,000 km s^{-1} with a blue wing extending to ∼20,000 km s^{-1}, while Si III $\lambda\lambda$ 4553, 4568 covers a much larger velocity range. Phillips et al. (2024) interpret these as evidence that higher ionisation in the outer ejecta suppresses the Si II lines rather than IMEs being confined to a narrow shell, a view challenged by abundance stratification studies and spectral modelling which consistently find IMEs depleted from the outermost layers (Aouad et al., 2022, 2024, O'Brien et al., 2023, Sasdelli et al., 2014).

As these spectra evolve, they gradually shift to resemble those of normal SNe Ia. The Si II λ 6355 line becomes visible almost a week before maximum light, gaining strength though never reaching the prominence observed in normal events. The "W"-shaped S II feature, and the O I λ 7773 feature also start to strengthen and appear a few days before maximum light, while the Fe III feature near 4230 Å remains strong, a set of Fe II features begin to dominate the feature near 4800 Å. The Ca II H&K feature emerges

with a distinct characteristic compared to normal SNe Ia, displaying a double absorption profile: a red component attributed to photospheric-velocity Ca II and a blue component likely resulting from Si III λ λ 3796, 3806 and Co III λ3782 lines. In the normal events, the blue wing is instead dominated by high-velocity Ca II absorption and the two features often blend into a single deep line. By approximately two weeks after maximum light, the optical spectra of 91T-like SNe become almost indistinguishable from those of normal events.

In the nebular phase, the spectra of 91T-like events closely resemble those of normal and slow-declining Branch CN SNe, with the two prominent emission features attributed to [Fe III] and a blend of [Fe II]/[Fe III] near 4700 and 5200 Å respectively. These emission lines appear broader in more luminous events due to the more extended velocity distribution of ^{56}Ni (Mazzali et al., 1998). A notable exception is the region between 7000 and 7600 Å, where strong [Ca II] λ λ 7291, 7324 emission contaminates the [Fe II] and [Ni II] features in the 1991T-like events (Phillips et al., 2024).

Within the 91T-like class, some events display intermediate properties between normal and 91T-like SNe Ia. The prototypical example is SN 1999aa (Aouad et al., 2022, Garavini et al., 2004). Its early spectra, similar to those of SN 1991T, are dominated by Fe III features, but display an Si II λ 6355 line and a high-velocity Ca II H&K feature with strengths intermediate between normal and 91T-like events. In addition, SN 1999aa evolves toward a spectroscopically normal SN Ia at earlier phases. These objects occupy an intermediate position between normal and 91T-like SNe Ia. Their luminosities are intermediate between those of 91T-like events and slow-declining Branch CN SNe with similar decline rates (Aouad et al., 2022, Phillips et al., 2022). Whether such objects represent members of a continuous spectroscopic sequence governed by smoothly varying physical parameters or instead arise from distinct progenitor channels and explosion mechanisms remains an open question. A comparison with other SNe Ia subtypes is shown in Figs. 2.7, 2.8, and 2.9.

2.3.1.3 1991bg-like

Named after the prototype SN 1991bg (Filippenko et al., 1992a), these events are intrinsically subluminous, typically $\sim$ 2 mag fainter than normal SNe Ia in optical bands and significantly redder in colour. They are characterized by rapidly declining light curves with $\Delta m_{15}(B) \approx 1.8{-}2.1$, and notably lack the secondary near-infrared (NIR) maximum commonly observed in normal SNe Ia. Although they constitute roughly 15–16% of volume-limited SN Ia samples (Li et al., 2011a), their low luminosities make them strongly underrepresented in flux-limited surveys. 1991bg-like SNe Ia occur preferentially

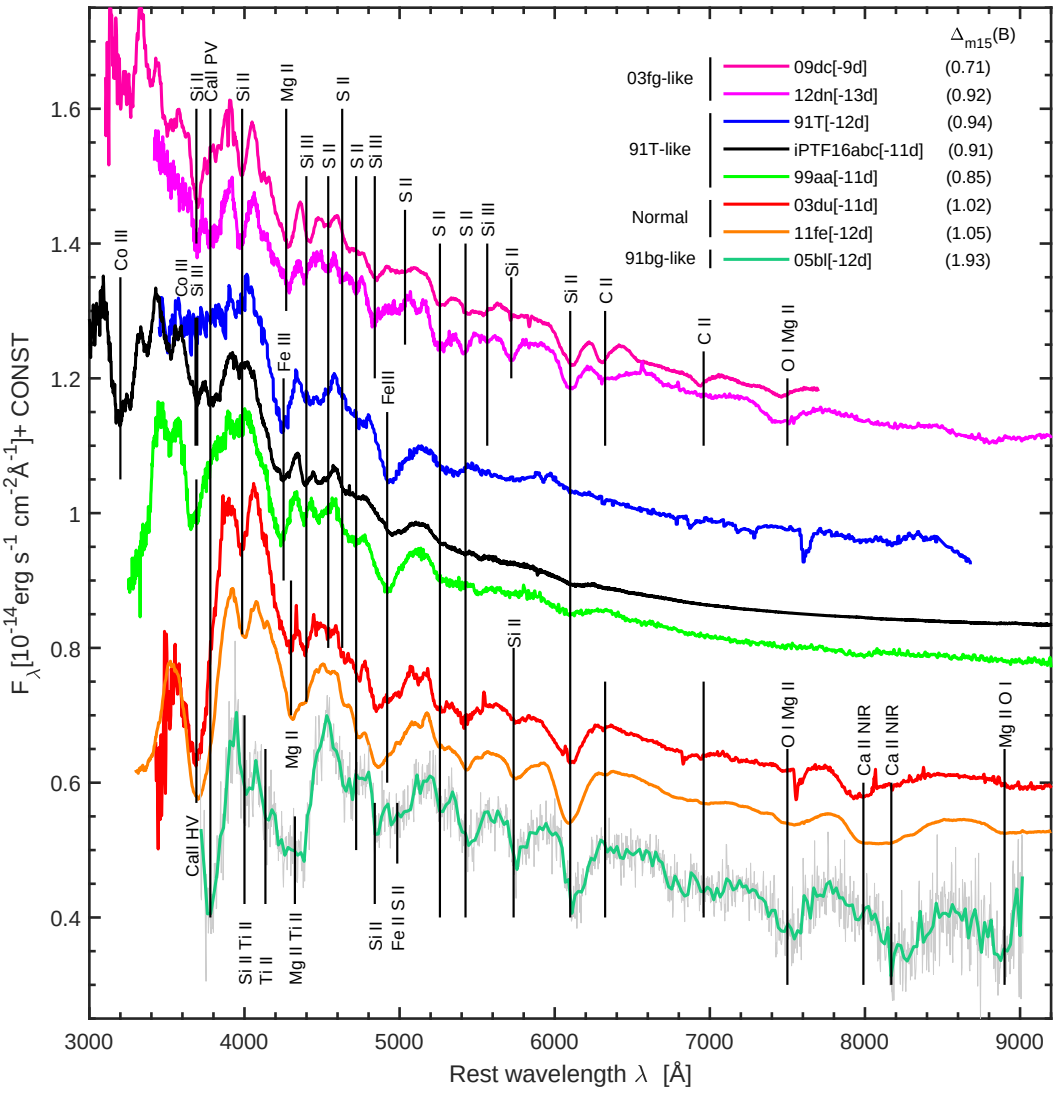


FIGURE 2.7: Comparison of the early-time spectra of different SNe Ia subtypes, including 03fg-like, 91T-like, normal, and 91bg-like events, with the major spectral features identified.

in old stellar populations and are most commonly found in elliptical and lenticular galaxies (Hamuy et al., 2000). This is consistent with the broader trend that fast-declining SNe Ia are preferentially associated with massive, passive galaxies hosting older stellar populations (Sullivan et al., 2010).

Spectroscopically, 91bg-like SNe Ia are characterized by a cool, low-ionisation state that distinguishes them from the normal population. Their most prominent hallmark is a broad absorption trough between 4000 and 4500 Å, produced by blends of Fe-group elements dominated by Ti II (Filippenko et al., 1992a, Mazzali et al., 1997b). They also exhibit strong O I λ 7774 absorption and deep Si II λ 5972 lines. Their expansion velocities near maximum light are broadly consistent with those of normal SNe Ia (Blondin

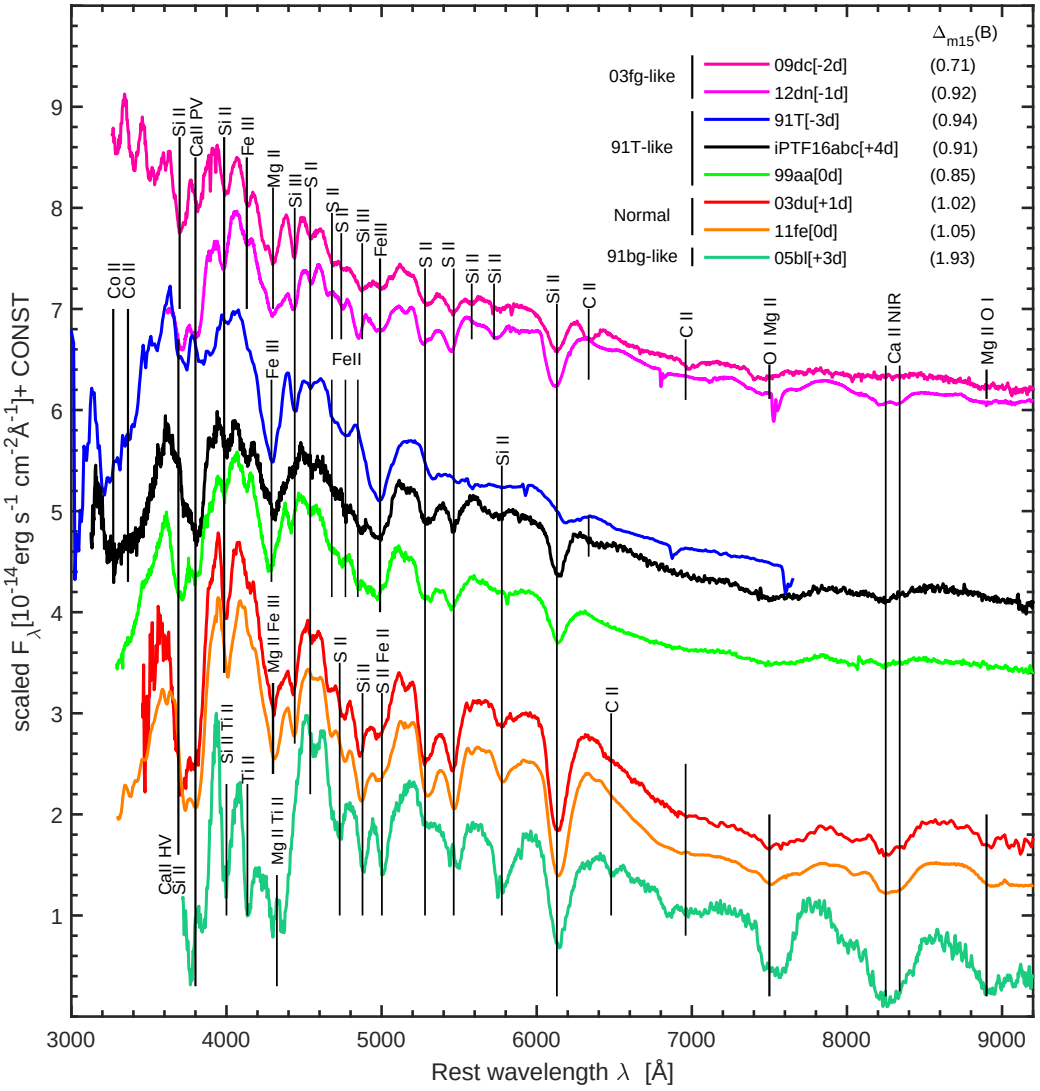


FIGURE 2.8: Same as Fig. 2.7, but showing the spectra near maximum light.

et al., 2017, Silverman et al., 2012b), their nebular spectra differ significantly, displaying strong [Fe II] emission and a prominent [Ca II] $\lambda\lambda$ 7291, 7323 doublet, a feature absent in normal-luminosity SNe Ia. These nebular Fe-group lines are also significantly narrower than in other subclasses, suggesting that ^{56}Ni is confined to a restricted velocity range with limited outward mixing.

An important question is whether 91bg-like SNe Ia constitute a physically distinct class or represent the extreme end of a continuous distribution. Transitional objects, such as the 86G-like subclass (including SN 1998bp, SN 2003gs, and iPTF 13ebh), appear to bridge this gap (Ashall et al., 2016). These intermediate events exhibit hybrid properties, including weak secondary NIR maxima and intermediate ionisation states, playing a role analogous to that of SN 1999aa between normal and 91T-like SNe Ia by linking normal

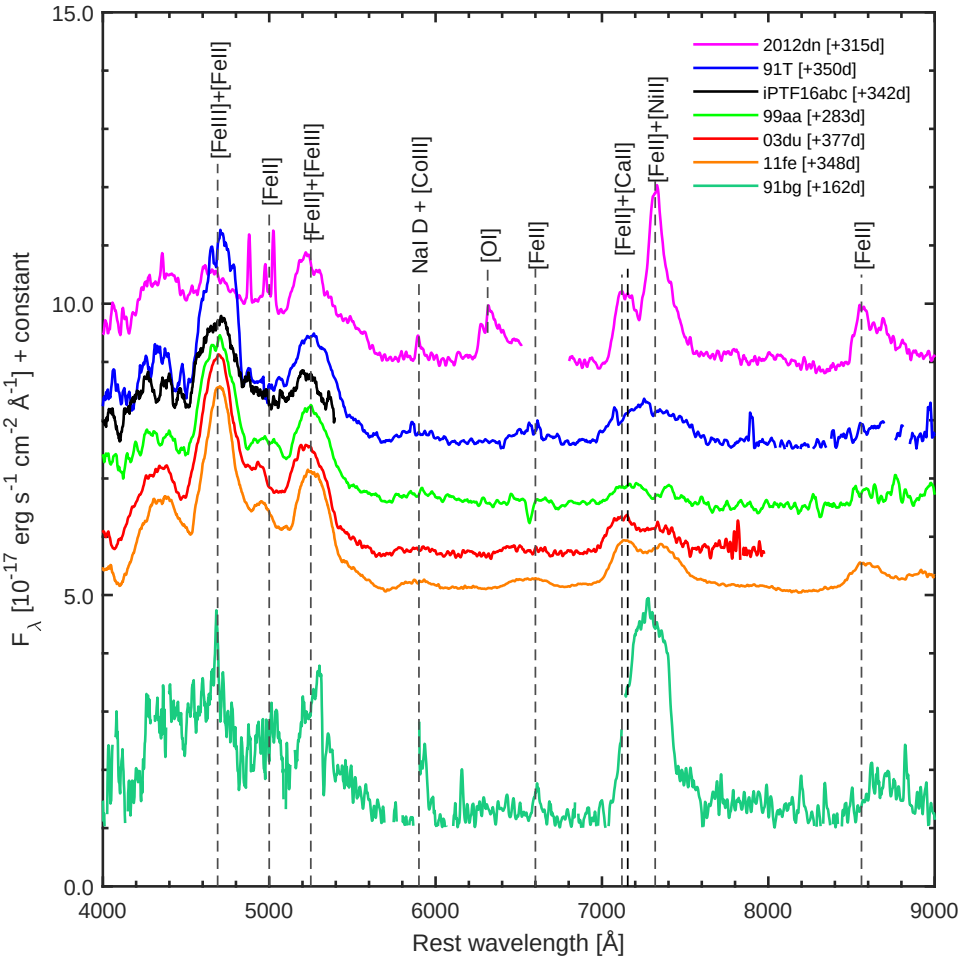


FIGURE 2.9: Same as Fig. 2.7, but showing the spectra at the nebular phase.

and subluminous events. A comparison with other SNe Ia subtypes can be seen in Figs. 2.7, 2.8 and 2.9.

2.3.1.4 SN 2003fg-like or super-Chandrasekhar SNe Ia

This subclass is named after its prototype, SN 2003fg (Howell et al., 2006). Photometrically, they exhibit several key departures from a standard Type Ia behaviour. Despite possessing broad light curves, they lack the secondary near-infrared maximum typically observed in the H band around +10 days in standard SNe Ia. Furthermore, uniquely among these subclasses, the i-band maximum occurs after the B-band peak (Ashall et al., 2021). These transients are further characterized by exceptionally blue early-time colourss and high UV luminosities (Brown et al., 2014). Additionally, some members of

this class experience "gray" bolometric dimming at late times, with onset periods ranging from 80 days post-maximum (e.g., SN 2012dn; Taubenberger et al., 2019) to 200 days post-maximum (e.g., SN 2009dc; Taubenberger et al., 2011). The majority of 03fg-like supernovae are found in low-surface-brightness galaxies characterized by high specific star formation rates (sSFRs) and they preferentially arise from metal-poor progenitors (Ashall et al., 2021, Childress et al., 2011, Hsiao et al., 2020, Khan et al., 2011, Lu et al., 2021).

Their luminosities span a remarkably broad range, from $M_B \approx -19$ to -21. At the luminous end, events such as SN 2007if ($M_B = -20.54 \pm 0.04$; Akerlof et al., 2007, Scalzo et al., 2010), SN 2003fg ($M_B = -20.18 \pm 0.05$; Howell et al., 2006), and SN 2009dc ($M_B = -20.09 \pm 0.17$; Taubenberger et al., 2011, Yamanaka et al., 2016) reach luminosities intermediate between 91T-like SNe Ia and superluminous supernovae (SLSNe) (Moriya et al., 2025). Such luminosities require exceptionally large ^{56}Ni masses, exceeding the amount of ^{56}Ni typically synthesized in standard Chandrasekhar-mass explosions, and therefore suggest super-Chandrasekhar-mass progenitors. However, some members, including ASASSN-15hy (Lu et al., 2021), SN 2006gz (Hicken et al., 2007), and SN 2012dn (Taubenberger et al., 2019), display the characteristic photometric and spectroscopic properties of the subclass while remaining comparable in peak luminosity to normal SNe Ia.

Their early-time spectra are characterized by multiple narrow absorption lines from singly ionized intermediate-mass elements (IMEs), specifically Si II, S II, and Mg II. A key diagnostic of this group is that Fe III lines are notably weak or absent compared to normal SNe Ia. Additionally, the high-velocity Ca II H&K feature is typically missing; the absorption on the blue side of this region is instead primarily attributed to Si II $\lambda\lambda$ 3854, 3856, 3863. A defining hallmark of these supernovae is the persistence of the strong C II $\lambda\lambda$ 6578, 6582 line, which remains visible for several weeks past maximum light (Taubenberger et al., 2019). These events are further distinguished by a unique double narrow absorption profile in the blue component of the 5000 Å feature (centered near 4800 Å). This feature is produced by a blend of Si II $\lambda\lambda$ 5041, 5055, a region usually dominated by broad blends of Fe II and Fe III lines in normal and 91T-like events. Throughout their evolution, 03fg-like SNe exhibit slowly evolving ejecta velocities and a consistently low ionisation state that persists well into the nebular phase (Ashall et al., 2021, Taubenberger et al., 2011).

Several progenitor scenarios have been proposed for these events, including super-Chandrasekhar-mass white dwarfs supported by rapid rotation or magnetic fields (Yoon & Langer, 2005), interaction between the SN ejecta and a dense carbon-rich envelope (Ashall et al., 2021, Hachinger et al., 2012, Noebauer et al., 2016), and violent mergers of two white dwarfs

with a combined mass exceeding $M_{\rm Ch}$ (Hachinger et al., 2012, Howell et al., 2006, Scalzo et al., 2010). A comparison with other SNe Ia subtypes can be seen in Figs. 2.7, 2.8 and 2.9.

2.3.1.5 SN 2002cx-like: Type Iax Supernovae

Commonly referred to as Type Iax SNe, this class is defined by the prototype SN 2002cx and its twin SN 2005hk (Li et al., 2003, Phillips et al., 2007, Sahu et al., 2008).

They are consistently subluminous ($M_V \approx -14$ to -19) and lack the secondary NIR maximum, though their light curves are often broader than their low luminosity would suggest. Their host-galaxy distribution is strongly skewed toward late-type systems, with no confirmed events found in elliptical galaxies, suggesting a younger progenitor population than that of normal SNe Ia (Foley et al., 2009, 2013a). They occur with a frequency between 5 and 30 per cent of the normal type Ia rates (McCully et al., 2014).

Spectroscopically, they resemble 91T-like events near maximum light, exhibiting prominent high-ionisation Fe III lines but with remarkably low expansion velocities (2,000–7,000 km s^{-1}), roughly half those of normal SNe Ia (Jha, 2017). Unlike normal SNe Ia, their late-time spectra remain dominated by narrow permitted Fe II features with only weak forbidden emission, indicating that the ejecta has not fully transitioned to the nebular phase (Foley et al., 2013b). This persistent "pseudo-photospheric" state suggests that the ejecta is extremely dense and characterized by unusually low expansion velocities, or potentially that a significant portion of the progenitor remains intact as a bound remnant. The leading theoretical model is a"failed" deflagration of a Chandrasekhar-mass CO white dwarf that only partially disrupts the star, potentially leaving behind a bound stellar remnant (Kromer et al., 2013a).

2.3.1.6 SNe Ia-CSM: SN 2002ic-like

This subclass consists of SNe Ia showing strong interaction with a dense, hydrogen-rich circumstellar medium (CSM) (Silverman et al., 2013). These transients are notably overluminous at peak ($-19 > M_R > -21.3$) and exhibit relatively slow post-maximum declines, together with early UV and strong late-time IR emission (Silverman et al., 2013). Their excess luminosity is thought to arise primarily from the ejecta–CSM interaction rather than radioactive decay (Aldering et al., 2006). SNe Ia-CSM are rare, representing roughly 1% of the total SN Ia rate (Li et al., 2011a), and are preferentially found in younger stellar populations.

The first recognized member, SN 2002ic (Hamuy et al., 2003), exhibited early spectra resembling 91T-like events with notably muted photospheric features, however, its spectra were accompanied by narrow Hα emission lines, a characteristic typically reserved for Type II core-collapse supernovae (Hamuy et al., 2003,?). These transients are further distinguished by narrow, blueshifted absorption features of He I, Na I, Ca II, Ti II, and Fe II, indicating complex interaction with multiple CSM shells as seen in PTF11k (Dilday et al., 2012). Despite the presence of dense circumstellar shells, SNe Ia-CSM exhibit little or no He I emission together with unusually large Balmer decrements, suggesting that the hydrogen emission is dominated by collisional excitation in shocked gas produced as the SN ejecta interacts with slower-moving circumstellar material (Silverman et al., 2013).

Additional evidence for ejecta–CSM interaction includes dust formation, inferred from the suppression of the red wing of the Hα profile 75–100 days after maximum light, together with late-time spectra showing low [Fe III]/[Fe II] ratios and strong [Ca II] emission indicative of dense, low-ionisation gas (Fox et al., 2015). Roughly half of the known population also exhibits strong Na I D absorption (Silverman et al., 2013). Other examples include SN 2005gj (Aldering et al., 2006), SN 2008J (Taddia et al., 2012), and SNe 2012ca and 2013dn (Fox et al., 2015). Proposed progenitor scenarios include SD systems with dense CSM produced through enhanced mass loss, recurrent novae, rotating red-giant winds (Hachisu et al., 2008, Han & Podsiadlowski, 2006, Lü et al., 2009, Wood-Vasey & Sokoloski, 2006), or the core-degenerate scenario (Livio & Riess, 2003) . Their similarity to some Type IIn SNe and possible associations with gamma-ray bursts have also led to suggestions of a core-collapse origin (Benetti et al., 2005, Inserra et al., 2014, Trundle et al., 2008).

2.3.2 Empirical Classification Schemes

To organise the observed diversity described above, several complementary empirical classification schemes have been proposed, each sensitive to different aspects of the ejecta structure and composition. These schemes, however, do not capture the full observed diversity of SNe Ia, as several subclasses fall outside their defined parameter space (e.g., SN 2002cx-like/Type Iax and SN 2002ic-like events), reflecting the limitations of frameworks developed primarily around the normal population and its immediate neighbours.

2.3.2.1 Nugent et al. (1995a) Line ratio classification

Nugent et al. (1995b) introduced a classification scheme based on the depth ratio of Si II λ 5972 (a doublet of λ λ 5958, 5979) to Si II λ 6355 (a doublet of λ λ 6347, 6371),

denoted as $\mathcal{R}$(Si II). This parameter was proposed as a temperature indicator for SNe Ia, linking spectroscopic properties to photometric behaviours. Objects with low $\mathcal{R}$(Si II), such as SN 1991T, tend to have slower-declining light curves and higher luminosities, whereas events with larger ratios, such as SN 1991bg, are generally cooler and exhibit faster light-curve declines.

The physical origin of the $\mathcal{R}$(Si II)–luminosity relation lies in the different behaviour of the Si II λ5972 and λ6355 absorption features. As shown by Hachinger et al. (2008), the strength of the λ5972 line increases markedly from luminous to dim SNe Ia, primarily due to ionisation effects. Although the λ5972 transition originates from a high-excitation level, which would normally imply stronger absorption at higher temperatures, this effect is outweighed by changes in the ionisation balance. In cooler and less luminous events, recombination from Si III to Si II substantially increases the population of Si II, more than compensating for the decrease in excited-level occupation numbers. In contrast, the Si II λ6355 line remains saturated because of its large optical depth and therefore varies little in strength. As a result, the temperature-sensitive growth of the λ5972 feature primarily drives the increase of $\mathcal{R}$(Si II) toward lower luminosities.

2.3.2.2 Benetti et al. (2005): Velocity gradient classification

By studying 26 SNe Ia, Benetti et al. (2005) introduced an empirical classification scheme based on the post-maximum velocity gradient of the Si II λ 6355 absorption minimum, $\langle \dot{v} \rangle$, measured near 6100 Å. They identified three groups forming distinct clusters in the $\langle \dot{v} \rangle$–$\Delta m_{15}(B)$ plane: the FAINT, High-Velocity Gradient (HVG), and Low-Velocity Gradient (LVG) classes.

The FAINT group corresponds primarily to 91bg-like SNe Ia, characterized by large decline rates and relatively low expansion velocities. The HVG class includes spectroscopically normal SNe Ia with high expansion velocities and rapidly evolving Si II velocities, such as SN 2002bo and SN 2004eo. In contrast, the LVG group exhibits slower Si II velocity evolution and includes both normal and 91T-like SNe Ia.

Subsequent studies showed that HVG SNe Ia exhibit stronger Si II λ 6355 absorptions that do not correlate with $\Delta m_{15}(B)$, together with a broad dispersion in maximum-light velocities, whereas LVG events display more homogeneous velocity evolution (Hachinger et al., 2006). Additional correlations were also identified between photospheric and nebular properties: LVG SNe Ia tend to exhibit blueshifted nebular Fe-group emission lines and early-time C II absorption, while HVG events more commonly show redshifted nebular features and redder $B - V$ colours near maximum light (Maeda et al., 2010b). One

interpretation is that these trends may reflect intrinsically similar asymmetric explosions viewed from different directions (Maeda et al., 2010a).

2.3.2.3 Branch et al. (2006): Spectral pEW Classification

Based on the relative strength of the pseudo-Equivalent Width (pEW) of the Si II λ 6355 and Si II λ 5980 lines, Branch et al. (2006) classified SNe Ia into four groups: Core-Normal (CN), Shallow Silicon (SS), Cool (CL), and Broad-Line (BL).

The Cool (CL) SNe Ia align with the FAINT category in Benetti et al. (2005)'s classification, consistent with expectations that less luminous SNe Ia, due to reduced ^{56}Ni synthesis, tend to have lower temperatures. The Broad-Line (BL) group matches Benetti's HVG classification, likely because Si II is spread across a wide velocity range, leading to substantial evolution of the Si II line velocity over time and a broader line profile. Both Core-Normal (CN) and Shallow Silicon (SS) SNe Ia correspond to Benetti's LVG category, which notably includes both normal and 91T-like SNe Ia. The latter subclass, whose shallow Si II line, evolves minimally over time suggesting a silicon shell distributed over a narrow velocity range, a pattern further supported by abundance stratification studies (Aouad et al., 2022, 2024, Sasdelli et al., 2014).

This pEW-based classification, similarly to Nugent's line-depth ratio $\mathcal{R}$(Si II), suggests that much of the observed spectral diversity in SNe Ia is driven by temperature variations, pointing toward a continuous distribution of properties across the different subclasses rather than the distinct SN Ia groups proposed by Benetti et al. (2005).

2.3.2.4 Wang et al. (2009): Velocity-based classification

Wang et al. (2009) classified 158 SNe Ia into "high-velocity" (HV) and "normal-velocity" (NV) groups based on the expansion velocity of Si II λ 6355 at maximum light. The NV group has an average velocity of 10,600 $\pm$ 400 km s^{-1}, while the HV group includes events with velocities exceeding 11,800 km s^{-1}. This scheme broadly corresponds to the LVG/CN and HVG/BL classifications of Benetti et al. (2005) and Branch et al. (2006), respectively. However, the velocity distribution appears continuous rather than bimodal, suggesting that the division into HV and NV groups does not necessarily reflect two physically distinct populations.

2.3.2.5 Colour-Stretch s_{BV} and i-Band Maximum Timing

Based on the fact that s_{BV} significantly reduces the scatter in the Phillips relation, particularly for fast-declining SNe Ia (Burns et al., 2014), and noticing that subtypes lacking a prominent secondary i-band maximum, such as 91bg-like events, SNe Iax, and 03fg-like events, have their i-band maximum occurring after that of the B-band, Ashall et al. (2020) combined s_{BV} with the epoch difference $t_{\max}^{i-B}$ to introduce a purely photometric subclassification approach that reveals distinct groupings among known SNe Ia subtypes, covering the full range of subclasses, including those not captured by the spectroscopic classification schemes discussed above, without requiring spectroscopic observations. This makes the framework particularly valuable for large photometric surveys where spectroscopic follow-up is not available for all events (see also Ashall et al., 2021). This classification is illustrated in Fig. 2.10.

These empirical classification schemes broadly overlap in their separation of SNe Ia subtypes, but they likely oversimplify the intrinsic complexity of SNe Ia spectral evolution. Because they rely on different observables, the resulting subclass boundaries frequently overlap, making it difficult to establish clear divisions between populations or to infer unique physical origins. Transitional objects such as SN 1986G, SN 2004eo, and SN 1999aa illustrate this ambiguity by satisfying the criteria of multiple classification schemes simultaneously. Their existence does not necessarily imply a continuous physical sequence between subclasses, but may instead only reflect the partial overlap of the observational properties on which the classifications are based.

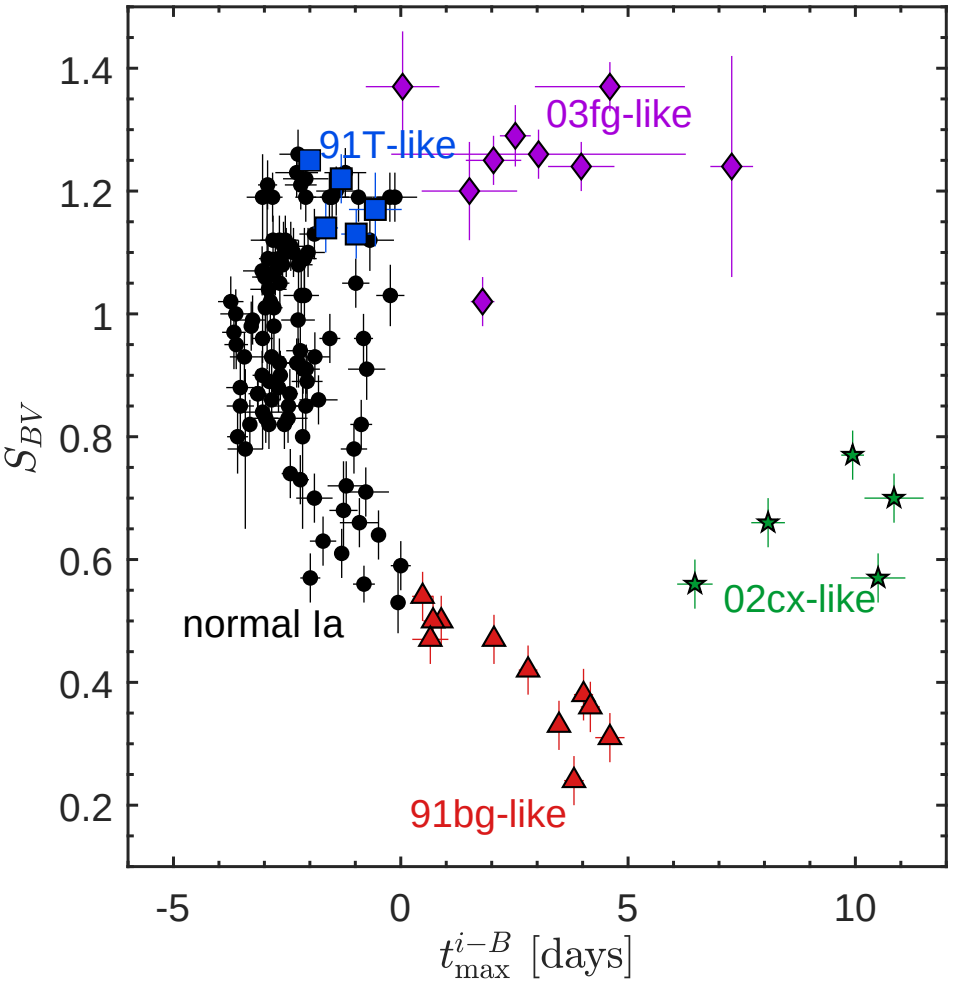


FIGURE 2.10: The colour-stretch parameter s_{BV} as a function of the epoch difference between the i- and B-band maxima ($t_i^{\max} - t_B^{\max}$) for a sample of SNe Ia. Different symbols and colours denote the various spectroscopic subclasses, which occupy distinct regions of the parameter space. This representation highlights the ability of s_{BV}, combined with the timing of the i-band maximum, to discriminate between normal and peculiar SNe Ia. Data from the Carnegie Supernova Project (CSP; (Ashall et al., 2020)), reproduced with permission.

2.4 Progenitors

Despite decades of research, the progenitors of SNe Ia remain unobserved and only partially understood. The central challenge encompasses three interconnected questions: the composition and mass of the progenitor star, the nature of the binary system, and the mechanism driving the explosion.

Current research strongly supports a carbon-oxygen white dwarf (COWD) as the progenitor, yet critical questions remain: whether the exploding white dwarf approaches

the Chandrasekhar mass or remains sub-Chandrasekhar, the configuration of the binary system, and the precise ignition and burning mechanism. Both single-degenerate and double-degenerate scenarios remain viable, as do Chandrasekhar-mass and sub-Chandrasekhar-mass explosion models, each consistent with different aspects of the observed diversity. The absence of direct progenitor detections, combined with the possibility that multiple evolutionary pathways lead to similar outcomes, makes disentangling these scenarios particularly challenging. These fundamental questions are addressed in turn below.

2.4.1 Composition

Both observational and theoretical arguments suggest that the progenitor star is a C-O white dwarf (COWD) The strongest evidence supporting this hypothesis can be attributed to the following:

- *Absence of Hydrogen and Helium Lines:* The lack of H and He lines in SNe Ia spectra rules out main-sequence progenitors. These elements are unlikely to have been present and completely burned, as the burning front quenches before reaching the low-density outer layers. The absence of He further rules out helium white dwarfs. Oxygen-neon white dwarfs (ONe WDs) are also excluded: accreting ONe WDs are expected to undergo accretion-induced collapse to a neutron star rather than thermonuclear explosion (Nomoto & Kondo, 1991), and their low occurrence rate is inconsistent with the observed SNe Ia rate (Livio & Truran, 1992). This leaves COWDs as the most plausible progenitor.
- *Presence of Oxygen and Carbon in Early Spectra:* Oxygen lines detected at high velocities in early spectra indicate substantial unburned oxygen in the outer ejecta. Unburned carbon has been sporadically detected across all subtypes, directly implicating carbon as a constituent of the progenitor (Parrent et al., 2011, Silverman & Filippenko, 2012).
- *Size of the Progenitor:* Observations of SN 2011fe constrain the progenitor radius to less than 0.1 $R_{\odot}$ (Bloom et al., 2012), consistent only with a compact degenerate object.
- *Explosive Nature of the Event:* The violent explosion points to a runaway burning process under degenerate conditions, where pressure is nearly independent of temperature, preventing the self-regulation that would otherwise quench the burning.
- Layered abundance structure: Simulations indicate that CO white dwarfs can explode upon reaching the Chandrasekhar limit, producing a layered structure in the

ejecta, with Fe-group elements near the center, intermediate-mass elements further out and oxygen and carbon in the outermost layers. This structure is consistent with abundance tomography studies and observed spectral evolution (Mazzali et al., 2007, Stehle et al., 2005).

- *The Energy of the Event:* The typical kinetic energy of the explosion, $\sim 1.5 \times 10^{51}$ ergs, is consistent with the nuclear energy released by transforming a few tenths of a solar mass of C and O into ^{56}Ni, exceeding the gravitational binding energy of a white dwarf ($\sim 5 \times 10^{50}$ ergs).

2.4.2 Mass

The variation in peak luminosity of SNe Ia, driven primarily by differences in ^{56}Ni mass, raises a fundamental question: does this diversity reflect a wide range of progenitor masses? With ^{56}Ni production spanning 0.1–1 $M_\odot$ (Mazzali et al., 2001a, 2008), the progenitor mass could potentially vary by an order of magnitude, encompassing both sub- and super-Chandrasekhar mass white dwarfs, each linked to distinct explosion mechanisms. While spectroscopic classification schemes suggest that most SNe Ia form a largely continuous sequence of properties rather than clearly separated subclasses, the observed spectral diversity beyond the normal events, from the subluminous 91bg-like subclass to the overluminous 03fg-like events, further hints at a broad range of progenitor scenarios.

Both Chandrasekhar-mass and sub-Chandrasekhar-mass models have been extensively studied theoretically. The following discussion addresses these different mass scenarios independently of the binary system configuration, which is considered separately in a subsequent section.

2.4.2.1 Near Chandrasekhar mass progenitor

The primary appeal of these masses lies in their ability to explain the similarities observed in a significant fraction of SNe Ia. This is because explosions in this model occur only when the CO WD approaches its maximum stable mass, i.e., the Chandrasekhar mass. Theoretical support for this scenario is based on the main arguments outlined below.

- Smooth ^{56}Ni distribution: The observed distribution of ^{56}Ni masses appears relatively smooth and strongly peaked around 0.5−0.7 $M_\odot$ (Mazzali et al., 2007). Since thermonuclear burning rates depend sensitively on the central density of the white dwarf, lower-mass progenitors would be expected to synthesize disproportionately smaller amounts of ^{56}Ni, potentially leading to a more discontinuous distribution

of ^{56}Ni masses than is observed. This suggests that the masses of the exploding white dwarfs in at least a significant fraction of SNe Ia are relatively similar (Livio & Mazzali, 2018).

- The central density: Neutron-rich isotopes, primarily ^{58}Ni and ^{54}Fe, dominate the innermost ejecta and play a crucial role in nebular-phase spectral models, where they are required to reproduce the observed [Fe III]/[Fe II] emission-line ratios near 4800 and 5200 Å (Aouad et al., 2022, 2024, Mazzali et al., 2014). The production of these neutron-rich species requires efficient electron-capture reactions during nuclear burning, which occur only at the high central densities reached in near-Chandrasekhar-mass white dwarfs ($\sim 2 \times 10^9\,\mathrm{g\,cm^{-3}}$). Under these conditions, the electron fraction reaches values around $Y_e \approx 0.481$, required to reproduce the solar abundances of stable Fe-group isotopes (Arnett, 1982, 1996). Such conditions arise naturally in Chandrasekhar-mass explosion models (Iwamoto et al., 1999), but are difficult to achieve in sub-Chandrasekhar-mass scenarios.

- The total burned mass: All SNe Ia exhibit a stratified ejecta structure, with stable Fe-group elements concentrated in the innermost regions ($\sim 0.1{-}0.2\,\mathrm{M_\odot}$), followed by a ^{56}Ni-rich layer and then an intermediate-mass element (IME) zone. The outermost $\sim 0.2{-}0.4\,\mathrm{M_\odot}$ consists primarily of oxygen-rich material, sometimes mixed with carbon, representing incompletely burned or unprocessed layers of the original white dwarf. Mazzali et al. (2007) showed that variations in IME masses largely compensate for differences in ^{56}Ni production, resulting in a nearly constant mass of $\sim 1{-}1.2\,\mathrm{M_\odot}$ processed into elements heavier than oxygen in normal SNe Ia. This suggests that the ejecta masses of at least normal SNe Ia are relatively uniform and close to the Chandrasekhar mass.

2.4.2.2 Sub-Chandrasekhar mass progenitor

The idea that a CO WD below the Chandrasekhar mass can lead to a SN Ia event was first presented by Nomoto (1982) and later by Woosley & Weaver (1986). One widely accepted scenario is the double-detonation mechanism, where a thin helium layer on the white dwarf's surface ignites, generating an inward shock wave that triggers a central detonation. Additional pathways include the merger of two white dwarfs (Mazzali & Hachinger, 2012, Pakmor et al., 2011).

Sub-Chandrasekhar explosion models have been particularly successful in explaining 91bg-like SNe Ia. The narrow [Fe III]-dominated nebular spectrum of SN 1991bg could not be reproduced by Chandrasekhar-mass models, which predicted broader [Fe II]+[Fe III] blends. Together with the low expansion velocities measured near

maximum light, this led Mazzali et al. (1997a) to propose that SN 1991bg originated from a significantly sub-Chandrasekhar-mass progenitor (see also Mazzali & Hachinger, 2012). However, transitional objects such as SN 1986G can still be reproduced with Chandrasekhar-mass models (Ashall et al., 2016), suggesting that SN Ia diversity may not simply represent a continuous sequence of progenitor masses.

The main challenge with the sub-Chandrasekhar mass models is their inabilty to synthesize neutron-rich Fe-group elements due to low central densities. Timmes et al. (2003) suggested that enhanced progenitor metallicity could partially compensate for this deficit by increasing the neutron excess. Several studies have also argued that nebular spectra may require only small amounts of stable Fe-group elements. For example, Liu et al. (1997) reproduced the nebular spectrum of SN 1994D with a sub-Chandrasekhar double-detonation model containing only $0.02\,M_\odot$ of stable Fe-group elements. Botyánszki & Kasen (2017) suggested that a large ($\gtrsim 0.1\,M_\odot$) central stable iron-group core, often regarded as evidence for Chandrasekhar-mass explosions, is not required to reproduce the optical nebular spectra and may instead lead to an unusual flat-topped [Co III] emission profile, a result later challenged by Mazzali et al. (2014). Similarly, Flörs et al. (2020) argued that most normal SNe Ia are consistent with sub-$M_{\rm Ch}$ models based on the Fe II 7155/Ni II 7378 ratio, although this interpretation may be affected by contamination of the 7200 Å feature by Ca II λ 7291.

2.4.2.3 Super-Chandrasekhar mass progenitor

The super-Chandrasekhar-mass scenario was introduced to explain overluminous SNe Ia such as SN 2003fg (Howell et al., 2006), whose extreme luminosity implied a ^{56}Ni mass of $\sim 1.3\,M_\odot$, with an ejecta mass of $\sim 2.1\,M_\odot$ well above the Chandrasekhar limit. Similar properties were later inferred for events such as SN 2009dc (Hachinger et al., 2012, Taubenberger et al., 2011). Proposed mechanisms include rapidly rotating or highly magnetized white dwarfs (Maeda & Iwamoto, 2009, Parthasarathy et al., 2007), as well as mergers of two white dwarfs with a combined mass exceeding $M_{\rm Ch}$.

Despite these theoretical possibilities, significant challenges remain. In super-Chandrasekhar models, the increased mass of the white dwarf is expected to yield higher amounts of ^{56}Ni and lower kinetic energies, leading to longer diffusion timescales. However, Ashall et al. (2021) found no correlation between the velocity of the Si II λ 6355 line (a proxy for kinetic energy) and the B-band magnitude (linked to ^{56}Ni mass), challenging this prediction.

An alternative and promising explanation involves the interaction between the expanding ejecta and a carbon-rich envelope, which may account for the high luminosities and observed spectral features (Ashall et al., 2021, Hachinger et al., 2012, Hoeflich et al., 1996).

2.4.3 Binary scenarios

The explosion mechanism and binary system configuration are closely tied to the white dwarf's mass at the time of explosion. The two primary progenitor scenarios are the single-degenerate and double-degenerate channels. Sub-Chandrasekhar mass models involve a different explosion mechanism. Below, we discuss these key progenitor and explosion channels in detail.

2.4.3.1 The Single-Degenerate (SD) scenario:

In the single-degenerate scenario, a carbon–oxygen white dwarf accretes matter from a non-degenerate companion star until it approaches the Chandrasekhar mass, at which point carbon ignites under degenerate conditions, triggering a thermonuclear runaway that disrupts the star (Nomoto et al., 1984, Whelan & Iben, 1973). The donor may be a main-sequence, subgiant, red giant, AGB, or helium star, with mass transfer occurring through Roche lobe overflow or stellar winds.

A key requirement of this scenario is a finely tuned accretion rate. At low rates ($\lesssim 10^{-8}\,\mathrm{M_\odot\,yr^{-1}}$), nova outbursts tend to eject more mass than is accreted (Livio & Truran, 1992, Yaron et al., 2005), while at high rates ($\gtrsim 10^{-6}\,\mathrm{M_\odot\,yr^{-1}}$) the white dwarf expands into a red-giant-like configuration, leading to a common-envelope phase that prevents further mass growth toward the Chandrasekhar limit (Nomoto et al., 1979, Wolf et al., 2013).

Therefore, only within a narrow range of accretion rates can the white dwarf grow efficiently through stable nuclear burning, where hydrogen is converted into helium at a rate comparable to the accretion rate (Fujimoto & Sugimoto, 1982, Livio, 1989, Paczynski & Zytkow, 1978). During this phase, the system is expected to appear as a supersoft X-ray source with effective temperatures of $30-100$ eV. To bypass the limitation imposed by this narrow accretion window, Hachisu et al. (1996) proposed that optically thick winds may enlarge the parameter space for SNe Ia by stripping away excess material, thereby preventing the formation of a common envelope and allowing mass growth even at accretion rates above the stable-burning limit. However, this mechanism is strongly metallicity dependent and may become ineffective at low Fe-group abundances (Kobayashi & Nomoto,

2009). After prolonged stable accretion, compressional heating ignites carbon near the center of the WD as it approaches the Chandrasekhar mass, triggering a thermonuclear runaway (Han & Podsiadlowski, 2004, Nomoto, 1982, Whelan & Iben, 1973).

Challenges and Caveats for the SD Scenario The main challenge of this scenario remains the lack of observational signatures expected from the presence of a companion star.

- Models predict that interaction between the SN ejecta and either a companion star or surrounding circumstellar material should produce observable signatures, including an early optical/UV excess during the first few days after explosion, as well as detectable radio and X-ray emission from particle acceleration and magnetic-field amplification (Boehner et al., 2017, Chevalier, 1998, Kasen, 2010). However, extensive observational campaigns, including high-cadence *Kepler* observations, have failed to detect any of these signatures (Chomiuk et al., 2016, Olling et al., 2015, Russell & Immler, 2012).

- The SD scenario predicts that hydrogen stripped from the companion star should appear in the supernova spectra at velocities of approximately 1000 km s^{-1} once the outer layers become optically thin (Liu et al., 2012, Meng et al., 2007). However, systematic searches in normal SNe Ia have consistently failed to detect hydrogen, yielding strict upper mass limits of 0.01–0.03 $M_{\odot}$ (Leonard, 2007, Lundqvist et al., 2013).

- Evidence for a surviving companion remains absent in both pre-explosion imaging and SN remnants. Observations of SN 2011fe and SN 2014J ruled out red-giant donors and found no evidence of prior nova activity or expanding shells (Li et al., 2011b, Margutti et al., 2014). Similarly, searches in remnants such as SNR 0509–67.5, SN 1006, have failed to identify any convincing companion star (González Hernández et al., 2012, Schaefer & Pagnotta, 2012). Even in debated cases such as Tycho's SN 1572, no surviving companion has been conclusively identified (Kerzendorf et al., 2013, Ruiz-Lapuente et al., 2004). To reconcile these null detections with the SD scenario, spin-down models propose that the explosion is delayed long enough for the donor star to evolve into a faint helium white dwarf before the SN occurs (Di Stefano & Kilic, 2012, Meng & Podsiadlowski, 2013).

- Based on the known rate of one SN Ia every few hundred years per galaxy, theory predicts a population of roughly 10^2 to 10^3 such accreting systems at any given time. However, integrated X-ray luminosities from nearby elliptical galaxies are actually 30–50 times lower than these models require, suggesting the SD channel

may account for no more than 5% of SNe Ia in these environments (Gilfanov & Bogdán, 2010). The problem is compounded by the fact that searches for indirect signatures, such as UV-bright objects or ionized helium lines resulting from reprocessed X-ray emission (Hachisu et al., 2010), have also come up empty (Lepo & van Kerkwijk, 2013, Woods & Gilfanov, 2013).

- Even with modifications such as optically thick winds and donor-star mass stripping, the single-degenerate (SD) scenario struggles to replicate the observed Type Ia supernova rate at long delay times. This is mainly because binary evolution models rarely produce WD–red giant systems with long orbital periods, as most evolve through a common-envelope phase that results in much shorter periods (Yungelson & Livio, 2000a). As a result, the SD model fails to naturally produce the t^{-1} power-law behaviour observed in the delay-time distribution (DTD) across all epochs (Bours et al., 2013).

Observational and Theoretical Support for the SD Scenario

- Despite the previously mentioned challenges, a few individual events have shown possible signatures consistent with the SD scenario. For example, SN 2012cg showed an early blue excess consistent with interaction with a non-degenerate companion (Marion et al., 2016), while narrow blueshifted Na I D absorption features detected in some SNe Ia have been interpreted as circumstellar material originating from the companion star (Maguire et al., 2013). In addition, the presence of high-velocity carbon-rich ejecta in SN 2011fe (Mazzali et al., 2014) may be consistent with hydrogen-rich accretion, where surface burning converts accreted hydrogen into carbon during the accretion phase.

- It provides a natural pathway for a white dwarf to reach the Chandrasekhar mass through steady accretion. Candidate progenitor systems include recurrent novae (Alexander et al., 2011, Munari et al., 2016, Thoroughgood et al., 2001), supersoft X-ray sources (Podsiadlowski, 2010, Southwell et al., 1996), and AM CVn binaries. Although these systems exhibit the high accretion rates required for stable nuclear burning, it remains uncertain whether white dwarfs can retain sufficient accreted material over long timescales rather than ejecting it during recurrent flashes (Godon et al., 2014, Thoroughgood et al., 2001).

- The detection of high-velocity features (HVFs) in some SN Ia spectra, in particular as Ca II H&K and NIR, may be explained by the presence of small amounts of hydrogen, which increase the local electron density and favor the recombination of Ca III into Ca II (Aouad et al., 2022, Mazzali et al., 2005a, Tanaka et al., 2008).

This ionized species is highly sensitive to the electron environment; adding even 10^{-2} $M_{\odot}$ of hydrogen provides enough free electrons to enhance these singly-ionized features without producing a detectable Hα absorption line (Aouad et al., 2022, 2024). Such trace amounts of hydrogen could originate from residual accreted material or circumstellar medium (CSM) swept up by the ejecta, lending potential observational support to the single-degenerate (SD) model.

2.4.3.2 The Double-Degenerate (DD) scenario:

The main motivation behind the DD scenario is that it naturally avoids two major difficulties faced by the SD channel: the absence of a surviving companion star and the lack of hydrogen features in SNe Ia spectra. In this scenario, two CO white dwarfs lose angular momentum through gravitational-wave radiation, causing the binary to shrink until the stars merge, potentially leading to a SN Ia (Iben & Tutukov, 1984, Webbink, 1984). This channel includes several pathways spanning a wide range of timescales.

In the tidal-merger scenario, two CO white dwarfs are brought together through gravitational-wave radiation until the less massive component fills its Roche lobe and is tidally disrupted, forming a massive accretion disk around the primary WD (Iben & Tutukov, 1984, Pakmor et al., 2012, Rasio & Shapiro, 1994, Webbink, 1984). The subsequent evolution depends primarily on the accretion rate from the disk onto the primary. If the accretion rate remains below $\sim 10^{-5}\,\mathrm{M}_{\odot}\,\mathrm{yr}^{-1}$, the remnant may avoid off-center carbon ignition and eventually achieve delayed central ignition after a secular evolution phase of $\sim 10^{5}$ yr (Sato et al., 2015, Yoon et al., 2007). Since the accreted material is carbon–oxygen rich, the system naturally avoids nova eruptions and helium-shell flashes that characterize hydrogen- or helium-accreting systems.

The violent merger pathway involves a dynamical explosion during the merger itself. After a brief phase of stable mass transfer, the secondary WD becomes dynamically unstable and is rapidly disrupted, while the violent accretion of its material onto the primary compresses and heats the surface layers, forming hot spots where carbon ignition and a detonation may occur (Kromer et al., 2013b). This scenario generally requires a super-Chandrasekhar combined mass to ensure the dynamical impact reaches the ignition threshold. The outcome depends largely on the mass ratio of the two WDs, (q): in equal-mass systems ($q \approx 1$), strong tidal interactions prior to the explosion disturb the density profiles of both components, significantly reducing the central density. This lower density leads to a smaller production of ^{56}Ni and Fe-group elements, resulting in subluminous, 1991bg-like events that nonetheless possess large ejecta masses (Pakmor et al., 2010). In contrast, in unequal-mass configurations (e.g., $0.9 + 1.1$ $M_{\odot}$), the more massive primary

WD is less affected by tidal distortions, allowing it to maintain a high central density and produce significant amounts of Fe-group elements consistent with observations while successfully reproducing the light curves, line velocities, and secondary NIR peaks of normal SNe Ia (Kromer et al., 2013b, Pakmor et al., 2012).

A third pathway involves head-on collisions, which can occur in unusually dense stellar environments such as the cores of globular clusters (Lorén-Aguilar et al., 2010, Raskin et al., 2010, Rosswog et al., 2009). However, the predicted rates in these settings are too low to account for the majority of the SN Ia population. A more frequent mechanism occurs in hierarchical triple systems, where a distant third body induces Kozai-Lidov oscillations (Kozai, 1962, Lidov, 1962) in the inner white dwarf binary (Thompson, 2011). These oscillations drive the inner binary to extreme eccentricities, significantly reducing the gravitational wave (GW) merger timescale, facilitating a direct collision. Research indicates that WD-WD binaries with semi-major axes of approximately 1–300 AU have a significant probability, estimated at a few percent, of experiencing a head-on collision within 5 Gyr when perturbed by a third body (Katz & Dong, 2012). Kushnir et al. (2013) proposed that such head-on collisions could serve as a primary channel for SNe Ia formation. Collisions involving typical carbon-oxygen white dwarfs with masses between 0.5 and 1.0 $M_\odot$ result in explosions that synthesize ^{56}Ni masses ranging from $\sim$ 0.1 to 1.0 $M_\odot$ spanning the observed ^{56}Ni mass distribution.

Challenges and Caveats for the DD Scenario

- A significant challenge for the double-degenerate (DD) scenario is that the tidal merger pathway often results in accretion-induced collapse (AIC) rather than a thermonuclear explosion. In this specific configuration, the lower-mass white dwarf is disrupted into a massive accretion disk, which triggers carbon ignition at the disk-dwarf interface. If this burning front propagates inward, it can transform the carbon-oxygen core into an oxygen-neon-magnesium (ONeMg) white dwarf (Nomoto & Iben, 1985, Saio & Nomoto, 1998). As this remnant's mass approaches the Chandrasekhar limit, electron capture on ^{24}Mg and ^{20}Ne typically induces gravitational collapse into a neutron star. Consequently, Sato et al. (2015) suggest that the DD channel's contribution to the total SN Ia rate may be limited to $\lesssim 9\%$.
- Another challenge lies in the triple system variant, which relies on the presence of a third star to induce collisions. The frequency of such systems with appropriate orbital configurations is relatively low, as most may merge prematurely while still on the main sequence (Hamers et al., 2013, Leigh & Geller, 2013). Klein & Katz (2017) showed that $\sim$10% of wide-orbit double-degenerate systems would need to

collide to match the observed SNe Ia rate, contradicting Katz & Dong (2012), who found that only a few percent of triple systems with the appropriate hierarchy result in collisions.

- In violent WD mergers, the exploding white dwarf is typically sub-Chandrasekhar in mass, posing a challenge for the synthesis of the neutron-rich iron-group isotopes characteristic of normal SNe Ia. Although third-body-induced collisions may temporarily increase the density through shock compression, it remains unclear whether this is sufficient to compensate for the lower central densities relative to Chandrasekhar-mass WDs. Nevertheless, some models suggest that stable iron-group production may still occur at lower densities in the presence of small amounts of ^{22}Ne providing an additional neutron excess that partially compensates for the reduced electron-capture efficiency at lower densities (Arnett, 1996).

- The high degree of spherical symmetry observed in most normal SNe Ia and their remnants, further supported by the generally low polarization levels (Leonard et al., 2005, Wang et al., 2016), contrasts with the asymmetric structures expected from violent mergers (Wang & Wheeler, 2008). In addition, the DD scenario struggles to explain the remarkable homogeneity of normal SNe Ia, since the total merger mass is not fixed but spans a broad range of roughly 1.4−2.0 $M_\odot$ (Wang & Han, 2010).

Observational and Theoretical Support for the DD Scenario

- The DD scenario naturally produces a delay time distribution (DTD) that matches observational data, as gravitational radiation from the merger process leads to a delay time following a t^{-1} trend (Yungelson & Livio, 2000b).

- Numerical simulations have shown that merging WDs can synthesize sufficient ^{56}Ni, reproducing the light curves and spectra of normal SNe Ia (Kushnir et al., 2013, Pakmor et al., 2012).

- Double-peaked features in nebular spectra, such as the Co/Fe emission observed in certain events, suggest a bimodal ^{56}Ni velocity distribution consistent with detonations triggered by direct WD–WD collisions (Dong et al., 2015). A similar morphology was seen in the subluminous SN 2010lp, where oxygen emission was confined to two distinct, opposing blobs (Mazzali et al., 2022, Taubenberger et al., 2013b). Hydrodynamic simulations by Kromer et al. (2013b) indicate that these structures are well-reproduced by the violent merger of two white dwarfs.

- Rare nebular [O I] emission lines have recently been observed in some SNe Ia, including the 03fg-like events SN 2012dn (Taubenberger et al., 2019), SN 2021zny (Dimitriadis et al., 2023), SN 2022pul (Siebert et al., 2023b), as well as SN 2010lp (Taubenberger et al., 2013b), ASASSN-20jq (Bose et al., 2025). Such features can be naturally explained in DD mergers, where the ashes of the primary WD expand around the secondary before burning is complete, allowing unburned oxygen-rich material from the secondary to remain in the inner ejecta.

2.4.3.3 The Core-Degenerate (CD) scenario:

In the core-degenerate (CD) scenario, a CO white dwarf merges with the hot core of an AGB star during or shortly after the common-envelope phase (Ilkov & Soker, 2012, Kashi & Soker, 2011, Livio & Riess, 2003, Sparks & Stecher, 1974). The merger remnant may exceed the Chandrasekhar mass and remain temporarily supported by rapid rotation, with the explosion delayed until angular momentum is lost. Depending on the spin-down timescale, hydrogen-rich material expelled during the common-envelope phase may either remain near the system and interact with the SN ejecta or disperse before explosion.

Challenges and Caveats for the CD Scenario

- A major limitation of the CD scenario is that it may not account for the bulk of the normal SN Ia population (Livio & Mazzali, 2018).
- While the spin-up/spin-down mechanism may explain the presence or absence of hydrogen features (Di Stefano & Kilic, 2012, Di Stefano et al., 2011, Hachisu et al., 2012b, Yoon & Langer, 2005), it remains unclear whether WDs can stably grow beyond the Chandrasekhar mass and whether the merger remnant rotates rigidly or differentially (Livio & Mazzali, 2018, Livio & Pringle, 1998).
- Another limitation of the CD scenario is the lack of detailed end-to-end modeling. Only a few preliminary simulations currently exist (see Aznar-Siguán et al., 2015), and it remains uncertain whether mergers between a WD and an AGB core can robustly produce normal SNe Ia with the observed ^{56}Ni yields and spectral properties.

Observational and Theoretical Support for the CD Scenario

- The CD scenario can explain both the presence and absence of hydrogen features in SNe Ia. Hydrogen-rich material expelled during the common-envelope phase may

remain near the system if the explosion occurs shortly after the merger, producing strong ejecta–CSM interaction as observed in events such as SN 2002ic (Hamuy et al., 2003, Livio & Riess, 2003) and PTF 11kx, and possibly explosions inside planetary nebulae (Tsebrenko & Soker, 2015). Conversely, long spin-down timescales allow the hydrogen-rich material to disperse before explosion, accounting for the lack of hydrogen features, the absence of a surviving companion, and the near spherical morphology of many SN Ia remnants.

- It can explain the observed properties of 03fg-like (super-Chandrasekhar) events (Ashall et al., 2021). In this picture, a carbon-rich envelope enhances the luminosity through ejecta–CSM interaction while also explaining the slow photospheric velocity evolution and persistent carbon absorption features. The dense, cool environment may additionally favor CO molecule formation and rapid dust production, leading to rapid optical light-curve declines in events such as SN 2009dc, SN 2012dn, LSQ 14fmg, and CSS 140126 (Hsiao et al., 2020, Taubenberger et al., 2019), while efficiently reprocessing optical flux into the NIR, consistent with the strong NIR emission observed in these events (Yamanaka et al., 2016). The model further predicts late-time UV re-brightening caused by interaction between the SN ejecta and material lost during earlier AGB superwind episodes (Graham et al., 2019).

- The long delay times predicted by the core-degenerate scenario allow the white dwarf to crystallize, driving oxygen toward the core while leaving a carbon-rich outer layer (Soker, 2013). This naturally explains the carbon-rich, fast-moving ejecta observed in events such as SN 2011fe (Mazzali et al., 2014). Although some models suggest this crystallization could trigger an accretion-induced collapse into a neutron star rather than an SN Ia (Nomoto & Kondo, 1991), the mechanism remains a compelling explanation for observed carbon abundances.

- Since the duration of this spin-down delay is mass-dependent, with more massive remnants spinning down faster, the CD scenario can potentially explain why younger stellar populations produce more luminous SNe Ia (Soker, 2013).

- The unusual continuum polarization observed in some highly reddened SNe Ia resembles that of proto-planetary nebulae, possibly indicating explosions occurring during the post-AGB phase and therefore supporting the CD scenario (Cikota et al., 2017).

- Because the AGB core is still thermally expanded, the accreted material experiences a shallower gravitational potential, reducing peak temperatures during accretion and helping the remnant avoid off-center carbon ignition (Soker, 2013) that would otherwise lead to collapse into a neutron star (Ilkov & Soker, 2012).

2.5 SNe Ia host galaxies

Type Ia supernovae (SNe Ia) are observed in a broad range of host galaxies, from actively star-forming spirals to passive ellipticals, indicating that they originate from progenitor systems associated with both young and old stellar populations (Branch & van den Bergh, 1993, Sullivan et al., 2006). This diversity implies a wide range of delay times between star formation and explosion, from less than 1 Gyr to several Gyr. Observationally, the delay-time distribution (DTD) follows an approximate t^{-1} power law, consistent with theoretical predictions for the double-degenerate scenario (Greggio, 2005, Mannucci et al., 2005). The SN Ia rate is significantly higher in late-type, blue galaxies than in early-type, red ones, suggesting that a substantial fraction of SNe Ia originates from relatively young stellar populations and supporting the existence of two SN Ia components: one associated with young, star-forming environments and another linked to older stellar populations (Mannucci et al., 2005, Sullivan et al., 2006).

The photometric and spectroscopic properties of SNe Ia also correlate strongly with their host-galaxy environments. More luminous and slowly declining events preferentially occur in younger, star-forming galaxies, whereas subluminous SNe Ia are more common in older, massive, and passive systems (Branch et al., 1996, Hamuy et al., 1996, Howell, 2001, Sullivan et al., 2006). Metallicity appears to play an important role as well, with overluminous SNe Ia preferentially found in low-mass, metal-poor galaxies, while subluminous events tend to occur in more massive and metal-rich hosts (Neill et al., 2009).

Several spectroscopic observables further depend on host-galaxy properties. In particular, the velocity of Si II increases with galaxy mass, whereas the strength of high-velocity Ca II features decreases (Pan et al., 2015). In addition, correlations between host-galaxy properties and Hubble residuals suggest that SN Ia luminosities may depend on parameters beyond light-curve width and colour alone (Johansson et al., 2013, Kelly et al., 2010). If confirmed, such relations could improve SN Ia distance determinations by incorporating host-galaxy properties into luminosity standardization methods.

Overall, the diversity of host environments and SN Ia properties supports the existence of multiple progenitor channels, with the SD scenario potentially favored in younger, star-forming environments and the DD scenario more naturally associated with older, passive stellar populations (Claeys et al., 2014, Greggio, 2005, Yungelson & Livio, 1998).

2.6 Explosion mechanisms and nucleosynthesis

2.6.1 Explosion mechanism

Evaluating the success of SN Ia explosion models depends on their ability to satisfy fundamental energetic requirements, namely kinetic energy and ^{56}Ni yields, while accurately reproducing the observed spectroscopic features and light curve evolution. Initially, the remarkable uniformity of SNe Ia suggested a single, universal explosion mechanism might suffice. However, as the emergence of diverse spectroscopic sub-classes has revealed a more complex landscape, a singular explanation has become increasingly difficult to maintain. These explosion mechanisms are intrinsically linked to their respective progenitor frameworks.

2.6.1.1 Pre-Explosive Evolution: Smoldering and Dynamical Runaway

In the single degenerate scenario, (Sect. 2.4.3.1), Carbon burning in hydrostatic equilibrium is initiated deep within the degenerate white dwarf when densities reach $\rho_c \approx 2-3\times10^9$ g cm^{-3} and temperature $T \approx 3\times10^8$ K (Arnett, 1969, Barkat, 1975). Carbon fusion primarily proceeds via:

$$^{12}\mathrm{C} + ^{12}\mathrm{C} \rightarrow \begin{cases} ^{20}\mathrm{Ne} + \alpha + 4.62\,\mathrm{MeV} \\ ^{23}\mathrm{Na} + p + 2.24\,\mathrm{MeV} \\ ^{23}\mathrm{Mg} + n - 2.62\,\mathrm{MeV} \quad \text{(less common)} \end{cases}$$

Weak reactions during this phase can marginally reduce Y_e, though the effect is negligible compared to electron capture during the subsequent explosion (Chamulak et al., 2008). As the nuclear energy release increases, the temperature gradient becomes superadiabatic, driving a vigorous convective regime known as the "smoldering" or simmering period. This stage persists for approximately 100–1,000 years, during which energy is transported via large-scale fluid motions rather than a discrete flame front, allowing the star to adjust quasi-statically to the increasing thermal pressure. This prolonged phase facilitates the processing of carbon into heavier elements, creating a chemical distribution that is crucial in determining the final explosion outcome (Branch & Wheeler, 2017). The smoldering phase is characterized by a balance between convective heating and neutrino cooling, particularly through the convective Urca process. In this process, repeated cycles of electron capture and beta decay emit neutrinos that escape the white dwarf, removing energy from the stellar interior and acting as a thermal regulator (Arnett, 1969, Barkat, 1975).

As the white dwarf continues to accrete mass, the rising central density and temperature eventually cause the nuclear burning rate to overcome cooling and convective transport. This marks the end of smoldering phase leading to a thermonuclear runaway and the formation of a flame front. The subsequent propagation of this front through the high-density interior, and its specific velocity and stability, determines whether the explosion proceeds via deflagration, detonation, or a delayed detonation transition (DDT)

2.6.1.2 Deflagrations

A deflagration is a subsonic burning front sustained by thermal conduction. In the context of a white dwarf nearing $M_{\rm Ch}$, the flame begins as a slow laminar front whose surface area grows as burning progresses, accelerating the burning rate. Since deflagrations are inherently three-dimensional turbulent processes, involving complex turbulent mixing, they are difficult to capture in one dimension. The landmark W7 model (Nomoto et al., 1984) captures this in one dimension via time-dependent mixing-length theory, parameterising the ratio of mixing length to pressure scale height as $\alpha = l/H_p = 0.7$, which gives the model its name and mimics the 3D acceleration of the burning front, producing intermediate-mass elements at expansion velocities broadly consistent with observations. W7 has therefore served as a vital first-order benchmark for the density and composition structure of SN Ia ejecta. However, the deflagration speed required to match observations without a subsequent detonation transition is not physically self-consistent, the model fails to produce IMEs above 15,000 $\mathrm{km\,s^{-1}}$, and excessive electron captures at high densities yield a $^{54}\mathrm{Fe}/^{56}\mathrm{Fe}$ ratio inconsistent with solar system abundances, limitations that ultimately motivated the development of multidimensional and delayed detonation models.

2.6.1.3 Detonation

In contrast, a detonation is a supersonic, shock-driven burning front, where burning is triggered by compressional heating rather than by heat transfer. In this regime, a high-pressure shock wave traverses the stellar material, raising the temperature of the unburned fuel above its ignition threshold almost instantaneously. Because the shock propagates faster than the local sound speed, the star does not have time to expand or "respond" to the burning until the front has already passed. This leads to extremely efficient nucleosynthesis at high densities, often converting the majority of the progenitor material into Fe-group elements, leaving virtually no IMEs. Consequently, a successful model must delay the detonation until the white dwarf has undergone some expansion, reducing the densities in the outer layers and allowing burning to terminate at

intermediate-mass elements rather than proceeding all the way to iron-group elements. This led to the development of the deflagration-to-detonation transition (DDT) model.

2.6.1.4 Deflagration-to-Detonation Transition (DDT)

In this framework, the flame generally begins as a slow, laminar deflagration driven by thermal conduction. Initially stable, this flame soon encounters hydrodynamic instabilities such as Rayleigh–Taylor (Taylor, 1950) and Kelvin–Helmholtz (Helmholtz, 1868), which disrupt its structure and stretch it into a turbulent configuration (Khokhlov, 1991a). This increases the flame surface area and accelerates burning. Under certain conditions, the turbulence may become strong enough to trigger a DDT, transforming the flame from a subsonic deflagration sustained by thermal conduction into a supersonic detonation driven by shock compression.

This scenario is currently the most favoured M_{Ch} model. The explosion begins as a deflagration, which pre-expands the white dwarf and lowers the density of the outer layers before the detonation is triggered. The subsequent supersonic shock propagates fast enough to overtake the expanding ejecta before the material dilutes below the densities required for nuclear burning, sweeping through the pre-expanded lower-density material, the ideal regime for incomplete silicon burning and the synthesis of IMEs consistent with SN Ia spectra.

The Zorro diagram The seminal work of Mazzali et al. (2007) established the DDT as a unified framework for the majority of SNe Ia, providing robust observational and theoretical evidence that a Chandrasekhar-mass (M_{Ch}) progenitor explains the diversity of these events. Through a systematic "abundance tomography", they demonstrated that all SNe Ia produce a roughly constant mass of stable Fe-group elements (IGE), such as ^{54}Fe and ^{58}Ni ($0.20 \pm 0.05\,M_{\odot}$), in the high-density central regions irrespective of their brightness. Beyond this core, the mass of radioactive ^{56}Ni varies and correlates directly with the decline-rate parameter Δm_{15}. The centerpiece of this study is the "Zorro" diagram. By plotting the enclosed mass of burning products against Δm_{15}, the diagram reveals an inverse relationship between the masses of ^{56}Ni and IMEs. This anti-correlation places a strong constraint on the explosion mechanism. In a pure deflagration, more energetic explosions would be expected to burn a larger fraction of the white dwarf, increasing both the ^{56}Ni and IME yields and leading to significant variations in the total burned mass. Instead, the Zorro diagram shows that the total mass processed by nuclear burning remains approximately constant, while the partition between ^{56}Ni and IMEs varies systematically. This behaviour is naturally explained in a delayed-detonation scenario, where differences in the degree of pre-expansion alter the density at which

the detonation propagates, regulating whether burned material is processed to nuclear statistical equilibrium (NSE) or terminates at IMEs.

Mazzali et al. (2007) further reinforced this picture through three-dimensional explosion simulations, demonstrating that the observed trends are naturally reproduced by the DDT mechanism. By varying the strength of the initial deflagration across three models (D5, D20, D800), they showed that the inverse relationship between ^{56}Ni and IME mass, and the roughly constant total burned mass, both emerge self-consistently. In models where the deflagration is strong, the central C/O fuel is largely exhausted before the detonation is triggered, pre-expanding the white dwarf such that the subsequent detonation sweeps through low-density outer material and produces predominantly IMEs at the expense of ^{56}Ni. Conversely, where the deflagration is weak, little material is consumed before the DDT, leaving abundant unburned fuel at high densities for the detonation to convert efficiently into ^{56}Ni and other NSE isotopes.

2.6.1.5 Pulsation driven explosions

Alternative scenarios to the standard DDT model often rely on the star's dynamical response to trigger a detonation. In the Pulsating Delayed Detonation (PDD) model (Dessart et al., 2014, Khokhlov, 1991a), a weak initial deflagration provides insufficient energy to unbind the white dwarf, causing the star to expand and then violently contract. This pulsation leaves a characteristic region of low density and weak burning in the outer layers. The final explosion is only triggered after the re-collapse phase. An interesting outcome of pulsation-driven detonations is that they confine intermediate-mass elements (IMEs) to a relatively narrow velocity range. This abruptly depletes silicon and sulphur from the outer shells, leaving the ejecta clearly divided into two consecutive zones of efficient and weak burning regimes. This particular structure is consistent with the abundance stratification studies of SNe 1999aa, 1991T and iPTF16abc (Aouad et al., 2022, 2024, Sasdelli et al., 2014). These models can explain the specific early "blue" light curves observed in some events but they often suffer from excessive iron features in synthetic spectra (Baron et al., 2008a).

The Pulsating Reverse Detonation (PRD) model (Bravo & García-Senz, 2009, Bravo et al., 2009), is a multidimensional evolution of the PDD concept that accounts for the buoyancy of hot ash plumes. These plumes penetrate the outer stellar layers to create an inverted composition, characterized by an unburned C/O core surrounded by hot deflagration ashes. This energy deposition ensures a large-amplitude expansion, followed by a contraction phase where an accretion shock ignites an inward-propagating "reverse" detonation. While PRD models can reach the peak luminosities of typical SNe Ia, they

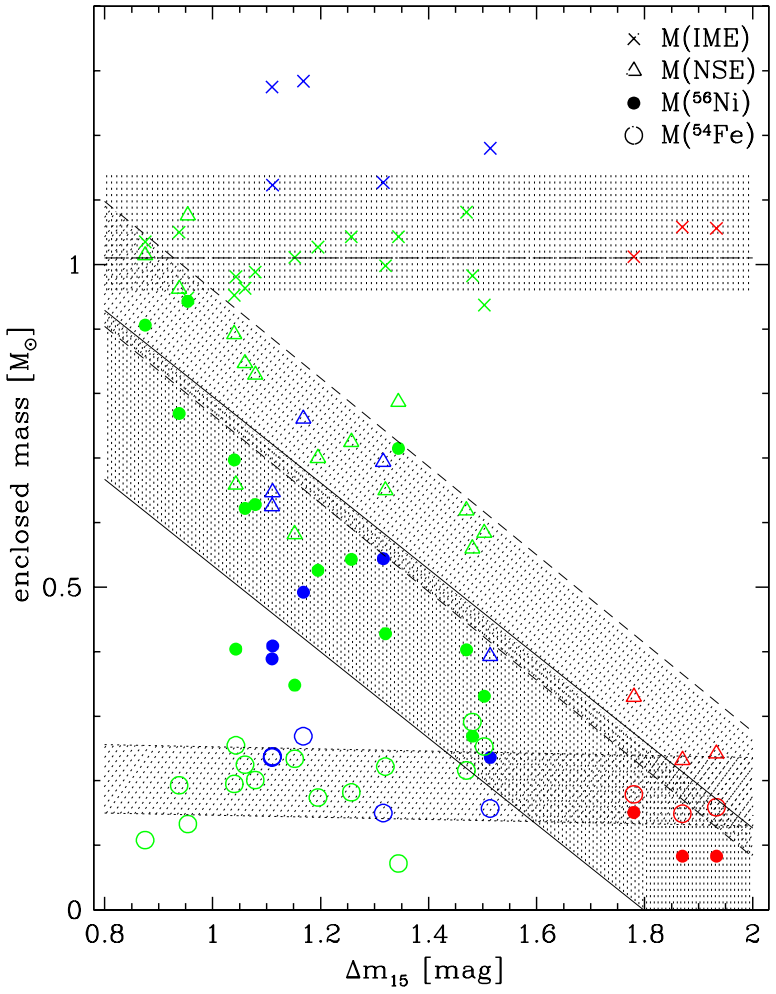


FIGURE 2.11: The "Zorro" diagram showing the distribution of the main burning products in SNe Ia as a function of the decline-rate parameter $\Delta m_{15}(B)$. SNe are colour-coded according to their velocity evolution: HVG (blue), LVG (green), and faint events (red). Open circles represent stable Fe-group material, filled circles correspond to ^{56}Ni, open triangles indicate the total NSE mass, and crosses show the total burned mass (NSE + IMEs). The diagram reveals an inverse relationship between the masses of IMEs and ^{56}Ni, while the total mass processed by nuclear burning remains approximately constant. This behaviour is difficult to reconcile with a pure deflagration, in which more energetic explosions would be expected to burn a larger fraction of the white dwarf, increasing both the ^{56}Ni and IME yields and producing significant variations in the total burned mass. Instead, the observed anti-correlation suggests that luminosity variations arise primarily from a redistribution of burned material between NSE and IME products. In a delayed-detonation scenario, differences in the degree of pre-expansion determine the density at which the detonation propagates, regulating whether burning proceeds to NSE or terminates at IMEs while maintaining a nearly constant total burned mass. Figure taken from Mazzali et al. (2007), reproduced with permission.

face significant observational hurdles, including excessively strong iron features in angle-averaged spectra and a lack of the clear chemical stratification found in typical events. Furthermore, the model tends to overproduce ^{56}Ni which makes them unable to include SNe Ia that are less luminous than average. Interestingly, they leave unburned carbon in a velocity range (6,000–12,000 km s^{-1}) that has been observed in the 91T-like carbon rich iPTF16abc (Aouad et al., 2024).

2.6.1.6 Double detonation models

Because a sub-$M_{\rm Ch}$ white dwarf cannot ignite via central carbon burning, the explosion must be externally triggered. This mechanism can be operational in both the SD and the DD channels.

In SD systems, a C/O white dwarf accretes a helium-rich layer until it reaches a critical density ($\approx 10^6\,{\rm g\,cm^{-3}}$) and detonates, driving inward-propagating shocks that trigger a secondary carbon detonation and unbind the star (Fink et al., 2007, Woosley & Weaver, 1994). This mechanism is commonly referred to as the double-detonation scenario. Early thick-shell models ($\approx 0.2\,M_\odot$) overproduced ^{56}Ni and yielded over-ionized spectra (Hoeflich et al., 1996), but recent thin-shell models (0.01–0.1 $M_\odot$) have shown that a much lower He mass, in the order of 0.0035–0.05 M$_\odot$ is enough to trigger a double-detonation and a Ia event with spectral features consistent with observations.(Bildsten et al., 2007, Fink et al., 2010). Sim et al. (2010) demonstrated that pure detonations of 0.97–1.15 $M_\odot$ C/O white dwarfs produce 0.3–0.8 $M_\odot$ of ^{56}Ni, spanning nearly the full observed range of SN Ia brightness, with spectra in good agreement with Si II line ratios. However, these models currently predict a decline-rate distribution that is too narrow to account for the full photometric diversity of the SN Ia population.

In DD systems, the double-detonation mechanism is triggered during the merger of two white dwarfs, where the helium flash arises from viscous heating within the merger disk or by instabilities and "dense knots" in the accretion stream striking the primary's surface (Dan et al., 2014, Guillochon et al., 2010). The ensuing ingoing shock waves compress the C/O primary, initiating a double-detonation supernova. While this mirrors the SD process, the extreme proximity of the helium donor in the DD case introduces significant physical hurdles; the interaction between the ejecta and the unburned donor can lead to excessive asymmetry or even a "triple-detonation" if the donor itself is disrupted (Papish et al., 2015). Furthermore, the presence of intermediate-mass elements (IMEs) in the helium-burned layer in these models may provide a physical origin for the high-velocity features (HVFs) frequently observed in SN Ia spectra (Shen & Moore, 2014).

2.6.2 Explosive Nucleosynthesis

During the explosion, temperatures spike to extremely high values, completely breaking down the carbon and oxygen fuel into a plasma of nucleons and α-particles. The composition that emerges depends on the peak temperature and density experienced by each mass element, the electron fraction Y_e, and how rapidly the plasma subsequently cools. In the ρ–T plane, three main burning regimes can be distinguished (Woosley et al., 1973): incomplete silicon burning, and complete silicon burning, the latter itself subdivided into normal (particle-poor) freeze-out and α-rich freeze-out. Because density decreases monotonically outward from the center, these regimes are encountered at successive depths, imprinting a layered chemical stratification on the ejecta. We describe each regime in order of decreasing density, from the innermost burning conditions outward.

Complete Silicon Burning and Nuclear Statistical Equilibrium (NSE)

In the innermost regions, where $T \gtrsim 5 \times 10^9$ K, nuclear reactions proceed rapidly enough to establish *nuclear statistical equilibrium* (NSE) — a state in which every reaction is balanced by its reverse photodissociation rate (Clifford & Tayler, 1965). Silicon is converted to iron-peak elements through successive α-captures:

$$^{28}\mathrm{Si}(\alpha,\gamma)^{32}\mathrm{S}(\alpha,\gamma)^{36}\mathrm{Ar}(\alpha,\gamma)^{40}\mathrm{Ca}(\alpha,\gamma)^{44}\mathrm{Ti}(\alpha,\gamma)^{48}\mathrm{Cr}(\alpha,\gamma)^{52}\mathrm{Fe}(\alpha,\gamma)^{56}\mathrm{Ni} \tag{2.27}$$

The NSE composition is uniquely determined by temperature, density, and the electron fraction Y_e (related to the neutron excess $\eta = 1 - 2Y_e$). The most abundant nuclei after freeze-out are those with the highest binding energy and an electron fraction close to that of the initial fuel. For symmetric matter ($Y_e \approx 0.5$), the dominant product is ^{56}Ni, the most tightly bound nucleus with $N = Z$ and the ultimate progenitor of the ^{56}Fe observed in supernova remnants and old stellar populations. The value of Y_e is set by three successive effects: the metallicity of the progenitor star, which determines the neutron excess inherited by the white dwarf through ^{56}Fe and ^{22}Ne; convective carbon simmering prior to the explosion in M_{Ch} models, which further reduces Y_e via electron capture; and the explosion itself, which produces by far the most dramatic reduction. When Y_e is reduced well below 0.5, the NSE composition shifts away from ^{56}Ni toward neutron-rich isotopes, principally ^{54}Fe, ^{58}Ni, and ^{55}Mn (the latter decaying from ^{55}Co), making super-solar [Mn/Fe] (Seitenzahl et al., 2013) and elevated [Ni/Fe] nucleosynthetic fingerprints of the M_{Ch} channel. As temperatures and densities subsequently decrease, reactions cease to be balanced, a condition known as *freeze-out*. The freeze-out regime is determined primarily by the peak density, giving rise to two distinct sub-regimes described below.

Normal (Particle-Poor) Freeze-out

At densities larger than a few $\times 10^8\,\mathrm{g\,cm^{-3}}$ (with temperatures $T \gtrsim$ a few $\times 10^9\,\mathrm{K}$), neutrons, protons, α-particles, crucial to build heavier nuclei, are depleted before temperatures fall too low to replenish them by photodissociation. When reactions fall out of equilibrium during expansion, few free particles remain to drive the composition away from its NSE values, and the final yields therefore closely mirror the neutron-rich NSE state established prior to freeze-out, with ^{54}Fe, ^{58}Ni, and ^{55}Mn as the principal products.

Alpha-Rich Freeze-out

At the same temperatures but at lower densities (below a few $\times 10^8\,\mathrm{g\,cm^{-3}}$), and still within the complete silicon burning regime, the three-body reaction rates required to incorporate α-particles into heavier nuclei drop sharply with density, so that a substantial mass fraction of free α-particles survives in the NSE composition. As the temperature drops during expansion, these α-particles continue to participate in capture reactions – reacting with the prevailing Fe-group nuclei- most importantly α-capture chains bringing the abundance out of NSE composition, before the network fully freezes. The resulting abundance pattern is shifted relative to normal freeze-out: ^{56}Ni remains significant, but there is a pronounced enhancement of nuclei built by sequential α-addition, notably ^{44}Ti, ^{48}Cr, ^{52}Fe, and crucially ^{60}Zn and ^{64}Ge, the progenitors of zinc and germanium. Copper (^{63,65}Cu) is also produced through charged-particle reactions in this regime. Since these yields require the high α-particle abundances characteristic of low-density NSE, they are naturally associated with sub-M_{Ch} explosions and helium shell detonations, where conditions directly favour α-rich freeze-out.

Incomplete Silicon Burning

At intermediate peak temperatures, the material does not reach full NSE. Instead, two separate quasi-statistical equilibrium (QSE) clusters form: one centred on ^{28}Si and one on ^{56}Ni, separated by a bottleneck near mass number $A \approx 45$ (nuclei such as Ti and Sc), which are comparatively weakly bound and thus present only in low abundance. Because the inter-cluster flow through this bottleneck is severely restricted, intermediate-mass elements (IMEs) such as, Si, S, Ar, and Ca, survive the burning episode. This regime is therefore the primary source of IMEs in Type Ia ejecta.

Explosive Oxygen Burning

In the outer layers, where peak temperatures fall in the range $3.5\times10^9 \lesssim T \lesssim 4.5\times10^9\,\mathrm{K}$, NSE is not attained and *explosive oxygen burning* dominates:

$$^{16}\mathrm{O} + ^{16}\mathrm{O} \rightarrow \begin{cases} ^{28}\mathrm{Si} + \alpha + 9.59\,\mathrm{MeV} \\ ^{31}\mathrm{P} + p + 7.68\,\mathrm{MeV} \\ ^{31}\mathrm{S} + n + 1.46\,\mathrm{MeV} \end{cases} \tag{2.28}$$

The liberated protons and α-particles drive secondary capture reactions, and the net yields are dominated by IMEs; Si, S, Ar, and Ca.

Explosive Carbon Burning and Unburned Material

At the lowest temperatures reached by the burning front ($T \lesssim 3.5 \times 10^9\,\mathrm{K}$), *explosive carbon burning* produces Ne, Na, and Mg in the outermost ejecta alongside unburned C/O material.

The full nucleosynthetic sequence, from NSE iron-peak elements at the center to unburned C/O in the outermost layers, is a direct imprint of the temperature and density structure of the exploding white dwarf. This chemical stratification is ultimately responsible for the spectroscopic evolution observed in SNe Ia.

Chapter 3

Spectral Modeling of Type Ia Supernovae

This chapter reviews the theoretical foundations of radiative transfer in supernova ejecta and describes the Monte Carlo code used to model their spectra throughout this work.

3.1 Radiative transfer

This section introduces the basic quantities and equations of radiative transfer theory that are related to the spectral modelling presented in this work.

3.1.1 Specific and mean Intensity

The specific intensity I_ν is defined as the energy transported through a unit area dA at an angle θ to the normal, per unit frequency interval $d\nu$, per unit solid angle $d\Omega$, and per unit time dt:

$$I_\nu = \frac{dE_\nu}{\cos\theta \, dA \, d\nu \, d\Omega \, dt}. \tag{3.1}$$

The mean intensity, J_ν, is given by

$$J_\nu = \frac{1}{4\,\pi} \oint I_\nu \, d\Omega, \tag{3.2}$$

defined as the directional average of the specific intensity, where integration is done over the whole sphere of 4π steradians.

3.1.2 The radiative transfer equation

As photons propagate through a material medium, they may be absorbed or scattered out of the beam. These processes reduce the specific intensity I_ν along a path element ds. The decrease in intensity depends on three factors. First, it is proportional to the local specific intensity itself, so that a more intense beam experiences stronger attenuation. Second, it is proportional to the opacity κ_ν, a material-dependent quantity that characterizes the effectiveness of the medium in absorbing or scattering radiation. The opacity has units of $\mathrm{m}^2\,\mathrm{kg}^{-1}$ and depends on the composition, temperature, and frequency of the radiation. Third, the attenuation is proportional to the mass density ρ of the medium and to the distance traveled by the photons.

The differential loss of specific intensity due to absorption and scattering can therefore be written as

$$dI_\nu = -\kappa_\nu \rho I_\nu \, ds. \tag{3.3}$$

It is convenient to introduce the optical depth τ_ν, defined by

$$d\tau_\nu = \kappa_\nu \rho \, ds, \tag{3.4}$$

so that

$$\tau_\nu(s) = \int_0^s \kappa_\nu \rho \, ds. \tag{3.5}$$

In the absence of emission, the transfer equation reduces to

$$\frac{dI_\nu}{d\tau_\nu} = -I_\nu, \tag{3.6}$$

with the solution

$$I_\nu = I_{\nu,0}\, e^{-\tau_\nu}, \tag{3.7}$$

where $I_{\nu,0}$ is the incident specific intensity. The optical depth thus quantifies the attenuation of radiation through the relation

$$\tau_\nu = \ln\!\left(\frac{I_{\nu,0}}{I_\nu}\right). \tag{3.8}$$

In addition to absorption and scattering, emission processes contribute radiation to the beam. These are described by the emission coefficient j_ν, which represents the energy emitted per unit mass, per unit solid angle, per unit frequency, and per unit time. Including emission, the total change in intensity along a path element becomes

$$dI_\nu = -\kappa_\nu \rho I_\nu \, ds + j_\nu \rho \, ds. \tag{3.9}$$

Dividing by $d\tau_\nu$, the radiative transfer equation can be written in optical-depth form as

$$\frac{dI_\nu}{d\tau_\nu} = -I_\nu + S_\nu, \tag{3.10}$$

where

$$S_\nu = \frac{j_\nu}{\kappa_\nu} \tag{3.11}$$

is the *source function*, which represents the ratio of emission to absorption.

To solve this equation, we multiply both sides by the integrating factor e^{τ_ν}, obtaining

$$\frac{d}{d\tau_\nu}(I_\nu e^{\tau_\nu}) = S_\nu e^{\tau_\nu}. \tag{3.12}$$

Integrating between two optical depths τ_1 and τ_2, the formal solution is

$$I_\nu(\tau_2) = I_\nu(\tau_1)e^{-(\tau_2-\tau_1)} + \int_{\tau_1}^{\tau_2} S_\nu(\tau)\, e^{-(\tau_2-\tau)}\, d\tau. \tag{3.13}$$

This expression describes the variation of the specific intensity along a ray through the medium as a function of optical depth, without explicitly involving the directional cosine μ.

The behaviour of the source function depends on the dominant physical processes within the medium. Two limiting cases are commonly considered: a pure absorption atmosphere and a pure scattering atmosphere.

In a pure absorption atmosphere, all absorbed photons are destroyed and all emitted photons are newly created by the medium. Under these conditions, microscopic processes are balanced by their inverse reactions, and the system is in thermodynamic equilibrium (TE). The source function is then given by Planck's law,

$$S_\nu = B_\nu(T) = \frac{2h\nu^3}{c^2}\frac{1}{e^{h\nu/kT}-1}. \tag{3.14}$$

Integrating over all frequencies yields the Stefan–Boltzmann relation:

$$B(T) = \int_0^\infty B_\nu(T)\, d\nu = \frac{\sigma}{\pi}\, T^4, \tag{3.15}$$

from which the total luminosity of a spherical blackbody of radius R follows as:

$$L = 4\pi R^2\, \sigma\, T^4. \tag{3.16}$$

In this case, the radiation field is fully determined by the local temperature of the gas.

In contrast, a pure scattering atmosphere is one in which photons are not destroyed but only redistributed in direction. No local thermal emission occurs, and the source function is determined entirely by the radiation field itself. In this limit, the source function is given by the mean intensity,

$$S_\nu = J_\nu, \tag{3.17}$$

so that it depends on the angular-averaged specific intensity rather than on the local thermodynamic properties of the medium.

3.2 MC code

The synthetic spectra presented throughout this thesis were computed using the one-dimensional Monte Carlo radiative-transfer code originally developed by Mazzali & Lucy (1993) and subsequently extended by Lucy (1999), Mazzali (2000), Stehle et al. (2005) and Hachinger (2011). The code has been widely applied to model the spectra of Type Ia supernovae and forms the basis of the abundance tomography technique employed in this work.

3.2.1 Radiative Transfer in Supernova Ejecta

3.2.1.1 Homologous Expansion and the Velocity Law

When the supernova explosion occurs, a large amount of energy is released instantaneously deep inside the star, driving the ejecta into rapid expansion. During the first seconds, physical distances are small and the forces acting on the matter, gravity pulling inward and pressure gradients pushing outward, are substantial. This is known as the hydrodynamic phase. However, this phase is short-lived, as the rapid expansion stretches the ejecta over increasingly large distances, causing these forces to become negligible. The ejecta then enter a phase of homologous expansion, where outer layers move faster than inner ones, preserving a self-similar structure that scales linearly with time. In this regime, velocity is directly proportional to radius, leading to the velocity law:

$$v = \frac{r}{t}. \tag{3.18}$$

This law has several important consequences for the radiative transfer problem. Since velocity and radius are directly proportional, velocity serves as a natural co-moving coordinate. The density at a co-moving point scales as t^{-3}, a consequence of mass conservation in a uniformly expanding sphere whose volume grows as $r^3 \propto t^3$, while

the shape of the density profile is preserved over time, meaning that a density structure determined at one epoch can be rescaled to any other. As the ejecta expand and dilute, their optical depth decreases with time. The effective photosphere, defined approximately by the layer where the continuum optical depth is unity, therefore recedes inward in mass coordinates, progressively revealing deeper and slower-moving regions of the ejecta. Furthermore, since the velocity gradient is constant and isotropic, a consequence of equation 3.18 is that a photon of observer-frame frequency ν is seen by a matter element moving at velocity v at the co-moving frequency:

$$\nu' = \nu \left(1 - \frac{v}{c}\right). \tag{3.19}$$

Finally, to an external observer, surfaces of constant line-of-sight velocity appear as planes perpendicular to the observer's line of sight (see Fig.2.1 of Hachinger (2011)) of , a geometry that has direct consequences for the formation of spectral features in SN ejecta.

3.2.1.2 The Sobolev Approximation

In a static stellar atmosphere, the frequency of a photon relative to the local medium remains nearly constant as it propagates because the velocity of the medium is negligible. As a result, a photon may remain in resonance with a given atomic transition over an extended region, and the optical depth must be accumulated continuously along its path. Solving the radiative transfer equation therefore requires integrating over the entire photon trajectory and all directions of propagation, making radiative transfer in static atmospheres computationally demanding.

In an expanding atmosphere, such in supernovae ejecta, the situation is fundamentally different. As the photon propagates outward through the ejecta, v increases with r, so the co-moving frequency defined in equation 3.19 decreases continuously; the photon redshifts in the co-moving frame of the matter. Consequently, a photon comes into resonance with a given spectral line only at a single spatially localised region, the resonance layer, where its co-moving frequency matches the rest frequency ν_0 of the transition. The interaction with the line is therefore confined to a thin localised layer rather than being distributed over an extended region. As the photon continues outward it redshifts monotonically, bringing it into resonance with a series of lines of progressively lower rest frequency, independent of the direction of propagation, since $v \propto r$ everywhere in homologous expansion. Because the expansion velocity greatly exceeds the thermal velocity of the atoms, the resonance layer is extremely thin compared to the ejecta. The physical conditions can therefore be assumed constant across it. This is the central assumption of

the Sobolev approximation (Sobolev, 1960), which reduces the calculation of line optical depths to a local problem at the resonance point.

Derivation of the Sobolev optical depth. The line absorption coefficient per unit volume at co-moving frequency ν' near line centre is:

$$\kappa_\nu \rho = \frac{\pi e^2}{m_e c} n_l f_{lu} \, \phi(\nu'), \tag{3.20}$$

where e is the electron charge, m_e the electron rest mass, n_l the number density of absorbers in the lower level, f_{lu} the oscillator strength, and $\phi(\nu')$ the normalised line profile satisfying $\int \phi(\nu')\, d\nu' = 1$. The optical depth through the resonance layer is:

$$\tau_S = \int \kappa_\nu \rho \, ds = \frac{\pi e^2}{m_e c} n_l f_{lu} \int \phi(\nu') \, ds. \tag{3.21}$$

The integral is evaluated by changing the integration variable from ds to $d\nu'$. Differentiating equation (3.19) with respect to s and using $\nu \approx \nu_0$ at resonance gives:

$$ds = \frac{c}{\nu_0 \, (dv/ds)} \, d\nu', \tag{3.22}$$

Substituting equation (3.22) into equation (3.21), using the normalisation $\int \phi(\nu')\, d\nu' = 1$, and applying the homologous condition $dv/ds = v/r$:

$$\tau_S = \frac{\pi e^2}{m_e c} n_l f_{lu} \, \frac{c}{\nu_0} \, \frac{r}{v}. \tag{3.23}$$

Substituting $\lambda_0 = c/\nu_0$ into equation (3.23) gives the Sobolev optical depth:

$$\tau_S = \frac{\pi e^2}{m_e c} n_l f_{lu} \, \lambda_0 \, \frac{r}{v}, \tag{3.24}$$

where λ_0 is the rest wavelength of the transition. Since $r/v = t$ in homologous expansion, the Sobolev optical depth depends only on the local level population n_l, the atomic data f_{lu} and λ_0, and the time since explosion.

3.2.2 Concept of the Monte–Carlo Radiative–Transfer Code

The code computes the radiative transfer from an assumed photosphere through the expanding supernova ejecta and generates synthetic spectra that can be directly compared with observations. The ejecta are represented as a spherically symmetric atmosphere above a sharply defined photosphere, which acts as the inner boundary of the calculation. The photospheric boundary emits a blackbody flux characterized by an effective temperature $T_{\rm eff}$. Assuming the radiation field to be a geometrically diluted blackbody,

this temperature is used to construct an initial estimate of the radiation field throughout the ejecta. An initial radiation temperature $T_{\rm R}(r)$ is thereby assigned to each shell through the dilution factor $W(r)$.

This initial temperature structure is used to determine the ionization and excitation state of the gas and to compute the corresponding line opacities. The resulting opacity structure is then employed in the Monte Carlo simulation, in which photon packets, are propagated through the expanding atmosphere and interact with the ejecta through electron scattering and line absorption processes.

Radiative equilibrium is enforced through the indivisible packet scheme of Lucy (1999), in which energy is conserved during packet interactions. Packets that re-enter the photosphere due to backscattering are assumed to be reabsorbed and contribute to the thermal reservoir at the inner boundary. Following the first Monte Carlo iteration, the radiation field is no longer determined by the initial geometrical approximation. Instead, the packet statistics are used to estimate the mean intensity J and frequency moment $\langle\nu\rangle$ in each shell, from which updated values of the radiation temperature $T_{\rm R}(r)$ and dilution factor $W(r)$ are derived (Mazzali & Lucy, 1993). The updated radiation field is then used to recalculate the ionization state, excitation state, and line opacities of the gas, and the procedure is repeated iteratively until $T_{\rm R}(r)$, $W(r)$, and the level populations converge throughout the ejecta. During this process, the photospheric temperature is automatically adjusted to reproduce the prescribed bolometric luminosity, compensating for energy lost through packet backscattering. Once a self-consistent solution has been obtained, the emergent spectrum is calculated through a formal solution of the radiative-transfer equation using a source function derived from the converged Monte Carlo simulation. The following sections describe the principal components of the calculation in more detail and the steps of the code are illustrated in Fig 3.1.

3.2.3 Photospheric Boundary, Initial Conditions, and Line List Initialisation.

This subsection describes steps (0), (1), and (1b) of the iteration scheme illustrated in Figure 3.1. The calculation is initiated by specifying the bolometric luminosity L, the time since explosion $t_{\rm exp}$, and the photospheric velocity $v_{\rm ph}$. Under the assumption of homologous expansion (see Section 3.2.1.1), the photospheric radius is given by equation 3.18.

The ejecta density is rescaled from a reference explosion model (e.g. W7) according to:

$$\rho(v, t_{\rm exp}) = \rho_0(v) \left(\frac{t_0}{t_{\rm exp}} \right)^3 , \tag{3.25}$$

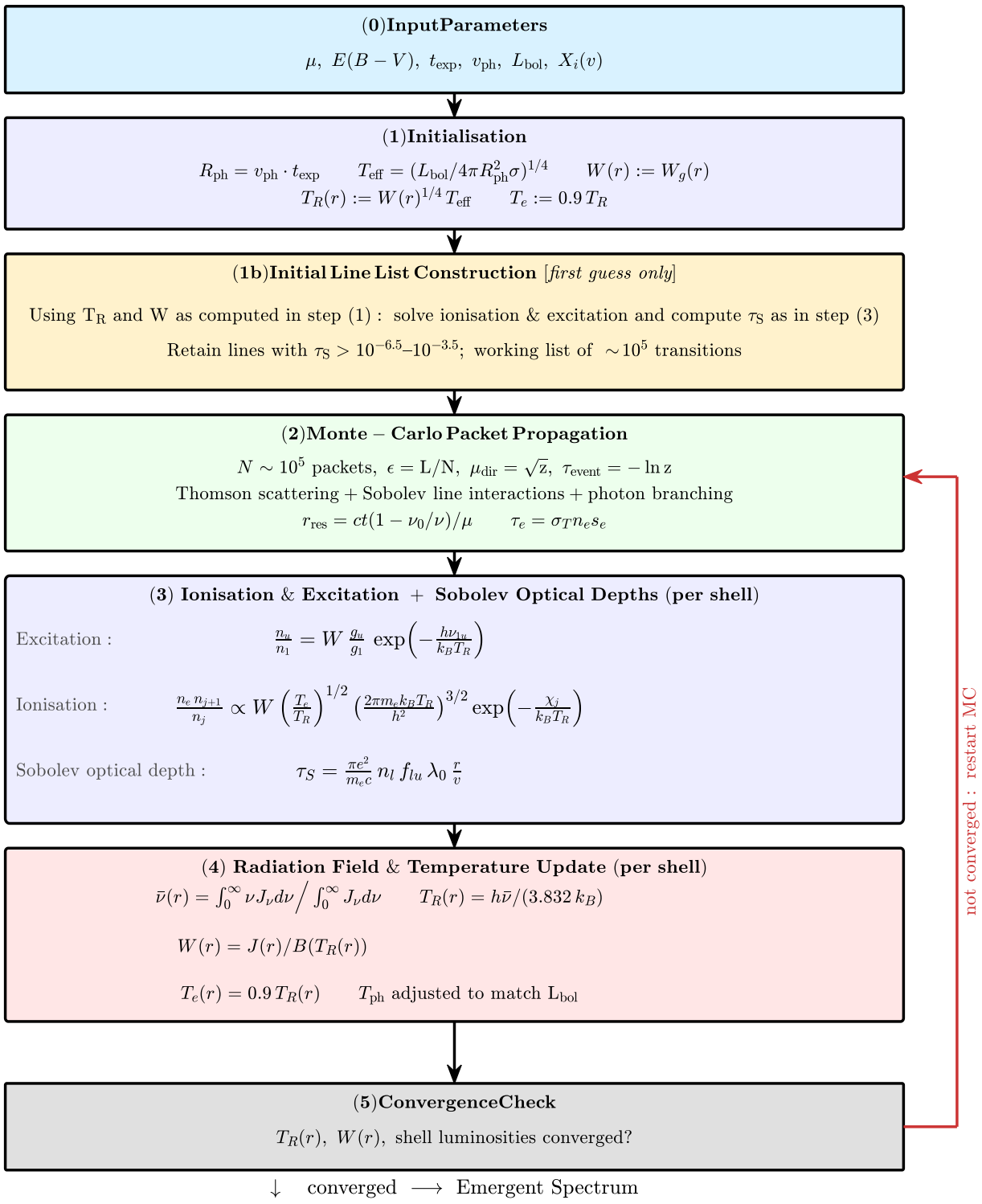


FIGURE 3.1: Iteration scheme of the Monte Carlo radiative-transfer code. The photospheric temperature and initial radiation field are established in steps (1) and (1b). Photon packets then propagate through the ejecta via Thomson scattering, Sobolev line interactions, and photon branching (2). Ionization, excitation, and Sobolev optical depths are updated in each shell via the modified nebular approximation (3). The frequency moment yields T_R (4), from which W is derived (5). If not converged, the MC experiment restarts; once T_R, W, and shell luminosities have converged (6), the emergent spectrum is obtained from a formal solution of the radiative transfer equation.

where $\rho_0(v)$ is the density profile of the reference model. The photosphere is assumed to emit a blackbody continuum, such that the effective temperature $T_{\rm eff}$ is determined from the Stefan–Boltzmann law,

$$L = 4\pi R_{\rm ph}^2 \sigma T_{\rm eff}^4. \tag{3.26}$$

The ionization and excitation calculations require knowledge of the local radiation temperature $T_{\rm R}(r)$ throughout the ejecta. Since the radiation field is not yet known at the beginning of the first iteration, an initial estimate must be constructed. This is achieved by assuming that the radiation field at each radius can be approximated by a geometrically diluted blackbody originating from the photosphere.

The dilution is described by the geometric dilution factor $W(r)$, which for a finite spherical photosphere is given by

$$W(r) = \frac{1}{2}\left[1 - \sqrt{1 - \left(\frac{R_{\rm ph}}{r}\right)^2}\right] \approx \left(\frac{R_{\rm ph}}{2r}\right)^2, \qquad (r \gg R_{\rm ph}). \tag{3.27}$$

Physically, $W(r)$ quantifies the dilution of the radiation field due to the finite angular size of the photosphere as seen from radius r. As the distance from the photosphere increases, a progressively smaller fraction of the sky is occupied by the emitting surface, resulting in a weaker radiation field. In subsequent iterations, $W(r)$ is no longer determined geometrically but is derived directly from the Monte Carlo packet statistics.

Assuming a diluted blackbody radiation field,

$$J_\nu(r) \approx W(r)\, B_\nu(T_{\rm eff}), \tag{3.28}$$

where $J_\nu(r)$ is the frequency-dependent mean intensity of the radiation field at radius r, $B_\nu(T_{\rm eff})$ is the Planck function evaluated at the photospheric temperature $T_{\rm eff}$, and $W(r)$ is the geometric dilution factor.

The corresponding radiation temperature in each shell is computed by

$$T_R(r) = W(r)^{1/4} T_{\rm eff}. \tag{3.29}$$

This relation follows directly from the assumption that the local radiation field retains the spectral shape of the photospheric blackbody, but with an intensity reduced by

the dilution factor $W(r)$. The resulting decrease in the mean intensity can therefore be represented by an equivalent blackbody of lower temperature, yielding the initial estimate of the radiation temperature $T_{\mathrm{R}}(r)$ in each shell. The dependence $T_R \propto W^{1/4}$ follows from the Stefan–Boltzmann relation 3.15, according to which the integrated intensity of a blackbody scales as T^4.

At this stage, the ejecta are divided into 15–20 radial shells of increasing thickness. The code makes use of a pre-compiled atomic database of $\sim 5 \times 10^5$ transitions. Before the Monte Carlo experiment begins, the ionization and excitation equations are solved in each shell using the initial values of T_R and W, yielding the lower level populations n_l for every transition. The Sobolev optical depth (equation 3.24) is then computed for each line, and only those transitions whose optical depth exceeds a prescribed threshold, typically in the range $10^{-6.5}$–$10^{-3.5}$, are retained. This reduces the active line list to $\sim 10^5$ transitions. Hydrogen and helium lines are always retained regardless of their optical depth, as their strengths under NLTE conditions are not reliably predicted from the initial estimate of the radiation field.

3.2.4 Ionization, Excitation, and Line Optical Depth Calculation.

This subsection describes step (3) of the iteration scheme illustrated in Figure 3.1. Computing the optical depths of spectral lines requires knowing the ionization and excitation state of the gas in each shell. A full NLTE solution coupling statistical equilibrium to the radiation field is computationally too expensive for the number of transitions involved, so the code instead uses the modified nebular approximation (Mazzali, 2000, Mazzali & Lucy, 1993). The key idea is to represent the angle-averaged local radiation field J_ν as a diluted blackbody with two parameters, $T_{\mathrm{R}}(r)$ and $W(r)$, and to treat each atom as either a two-level system (for normal excited states) or a three-level system (for metastable states), neglecting stimulated emission and collisions. For a normal excited state u, the population relative to the ground state is:

$$\frac{n_u}{n_1} = W \, \frac{g_u}{g_1} \exp\left(-\frac{h\nu_{1u}}{k_B T_R}\right), \tag{3.30}$$

where g_u, g_m, g_1 are the relevant statistical weights and ν_{1u}, ν_{1m} are the transition frequencies. For metastable levels, a similar expression is obtained. The ionization balance follows a modified Saha equation adapted to a diluted radiation field with negligible collisional contribution:

$$\frac{n_e \, n_{j+1}}{n_j} \propto W \left(\frac{T_e}{T_R}\right)^{1/2} \left(\frac{2\pi m_e k_B T_R}{h^2}\right)^{3/2} \exp\left(-\frac{\chi_j}{k_B T_R}\right), \tag{3.31}$$

where χ_j is the ionization potential of ion j and $T_e \approx 0.9\,T_R$ is the electron temperature. Correction factors accounting for recombination to excited states and UV deviations from a pure blackbody are included in the full implementation (Mazzali & Lucy, 1993).

From the resulting level populations, the Sobolev optical depth of each transition is computed using equation 3.24.

3.2.5 Radiation Field and Temperature Update.

This subsection describes step (4) of the iteration scheme illustrated in Figure 3.1. After the first Monte Carlo run (see section 3.2.6), $T_{\rm R}(r)$ and $W(r)$ are no longer estimated geometrically from equations (3.29 and 3.27), but are instead computed in each shell from the radiation field.

The mean energy of a photon in a blackbody radiation field is given by:

$$\frac{h\langle\nu\rangle}{k_B T_R} = 3.832, \tag{3.32}$$

where the frequency moment $\langle\nu\rangle$ is obtained from:

$$\langle\nu\rangle = \frac{\int_0^\infty \nu\, J_\nu\, d\nu}{\int_0^\infty J_\nu\, d\nu}. \tag{3.33}$$

The electron temperature is set to $T_e(r) = 0.9\,T_R(r)$, and the dilution factor updated via

$$W(r) = \frac{J(r)}{B(T_R(r))}. \tag{3.34}$$

Using the new computed $T_R(r)$, $W(r)$, and the electron temperature $T_e \simeq 0.9\,T_R$, the code updates ionisation and excitation via the modified nebular approximation (as described in section 3.2.4), yielding new Sobolev optical depths and scattering opacities. Packet propagation and level populations are iterated in turn until $T_R(r)$, $W(r)$, and the shell luminosities converge and radiative equilibrium is established throughout the envelope.

3.2.6 The Monte Carlo experiment.

With all quantities established in the preceding sections, the core of the iteration scheme, step (2) of Figure 3.1, can now be described. With the density, composition, and opacity now established throughout the ejecta, the radiative-transfer problem can be addressed explicitly. This is achieved by simulating the propagation of photon packets through

the expanding atmosphere using a Monte Carlo approach, as described in the following steps.

Photon Packet Initialization The total luminosity is discretized into N photon packets, each carrying equal energy $\epsilon = L/N$. Using packets of equal energy ensures both good statistical sampling near the peak of the Planck function and automatic energy conservation during branching, since only the number of photons per packet changes when a frequency jump occurs, not the packet energy. Each packet is injected at the photosphere with a frequency sampled from the Planck function at T_{eff} and a direction assigned randomly as $\mu = \sqrt{z}$, where z is a random number uniformly distributed in $(0, 1)$.

Propagation and Event Selection Once injected at the photosphere, each photon packet propagates through the ejecta in a random walk, during which it may undergo electron scattering or a line interaction, or cross a shell boundary into a region of different physical conditions. The packet has two possible fates: it either escapes the outer boundary of the ejecta, contributing to the emergent spectrum, or re-enters the photosphere, where it is reabsorbed. To determine which event occurs next, the following procedure is adopted. The propagation of photons through an opaque medium follows an exponential distribution in optical depth, such that the optical depth at which an interaction occurs is distributed as $e^{-\tau}$. This distribution is sampled by drawing a random event optical depth threshold:

$$\tau_{\text{event}} = -\ln z, \tag{3.35}$$

where z is a random number uniformly distributed in $(0, 1)$. This threshold defines the total optical depth the packet must reach before undergoing its next interaction. As the packet propagates through a shell, two processes accumulate optical depth. Electron scattering contributes continuously along the path, with optical depth

$$\tau_e = \sigma_T \, n_e \, s_e, \tag{3.36}$$

where σ_T is the Thomson cross section and n_e is the electron density, assumed constant within each shell. The path length s_e at which τ_e equals τ_{event} is directly obtained from this relation. Line interactions, on the other hand, occur at discrete resonance points rather than continuously. A line resonance occurs when the co-moving frequency of the packet matches the rest frequency ν_0 of a transition, i.e. when $\nu' = \nu_0$. Applying the Doppler condition of equation (3.19), generalised to account for the arbitrary propagation direction μ of the packet, and using the homologous relation $v = r/t$, the resonance radius

is:

$$r_{\rm res} = \frac{ct}{\mu}\left(1 - \frac{\nu_0}{\nu}\right). \tag{3.37}$$

which defines a unique spatial location for each line given the packet's observer-frame frequency ν and direction μ. Since the ejecta expand homologously, a packet emitted from the photosphere can only encounter lines at progressively longer wavelengths as it propagates outward. Line interaction zones are assumed to be infinitely thin in the Sobolev approximation and do not overlap, so each packet encounters lines sequentially from the bluest to the reddest. Three distances are then compared: s_e (Eq.3.36), the distance to the next line resonance, s_l, obtained from $r_{\rm res}$ (Eq.3.37), and the distance to the shell boundary $s_{\rm sh}$. The smallest of these determines the next event. If $s_{\rm sh}$ is smallest, the packet crosses into the adjacent shell with updated physical conditions and a new optical depth calculation begins. If it is reabsorbed by the photosphere, its energy is redistributed at the inner boundary, raising the temperature at the photosphere, $T_{\rm ph}$ above $T_{\rm eff}$ in a process known as back-warming, and $T_{\rm ph}$ is iteratively adjusted until the net emergent luminosity matches $L_{\rm bol}$. If s_e is smallest, the packet undergoes Thomson scattering, being redirected into a new random direction while retaining its co-moving frequency, and the random walk restarts with a new $\tau_{\rm event}$. If s_l is smallest, a line interaction occurs and the packet is absorbed and re-emitted through a downward branching scheme (Mazzali, 2000). In that case, the packet emerges with a new co-moving frequency, a new random direction, and a reset optical path length, while its total energy is conserved. This frequency redistribution is the mechanism behind fluorescence, through which flux is reprocessed from the ultraviolet to the optical. Finally, if a packet crosses the outer boundary it escapes and contributes to the emergent spectrum.

Once the Monte Carlo simulation has converged, the physical state of the ejecta is fully specified throughout the envelope. The emergent spectrum is not obtained directly from the escaping packets. Instead, a formal solution of the radiative transfer equation is performed using the converged source function, yielding a smooth high-resolution synthetic spectrum.

Finally, the synthetic spectrum is scaled by $1/(4\pi d^2)$ and reddened for comparison to observed data.

3.3 Modelling techniques

To initiate the modelling, the following quantities are required as input:

- the distance modulus, μ,

- the extinction towards the supernova, $E(B-V)$,
- the time since explosion $t_{\rm exp}$, determined from the epoch of observation relative to the time of B-band maximum and an assumed rise time,
- the photospheric velocity $v_{\rm ph}$, which defines the photospheric radius through $R_{\rm ph} = v_{\rm ph}\, t_{\rm exp}$,
- the bolometric luminosity $L_{\rm bol}$,
- the chemical abundance structure as a function of velocity in each shell above the photosphere.

The parameters μ, $t_{\rm exp}$, and $E(B-V)$ are explored within the ranges allowed by observational uncertainties, and different combinations are tested until a satisfactory agreement with the observed spectra is achieved. Once fixed, these parameters are kept constant throughout the modelling sequence. Modelling begins with the earliest available spectrum, adopting an initial photospheric velocity and rise time, with a small number of shells defined above the photosphere to prevent individual elements from projecting too far in velocity space. The abundances are adjusted to reproduce the observed features, and the procedure is extended to later epochs by adopting lower $v_{\rm ph}$ values and updated $L_{\rm bol}$ to match the luminosity, reflecting the deeper layers of the ejecta progressively revealed as the photosphere recedes in velocity space. As the photosphere recedes to deeper layers, it is sometimes necessary to revisit the outer shells and revise their abundances, since the composition of the outer ejecta can affect the synthetic spectra at later epochs, and the stratified abundance structure of the ejecta is built up iteratively shell by shell. In general, abundances carry an uncertainty of $\sim 25\%$ (Ashall & Mazzali, 2020), while the uncertainty on ^{56}Ni is of order 10%, as this element is independently constrained from the nebular phase and can be cross-checked against the peak luminosity.

Distance modulus Determining the distance to a supernova is essential for correctly scaling the observed flux and deriving reliable physical parameters. Since the distance is often uncertain, it is explored within the range allowed by values reported in the literature by modelling multiple spectra. Larger distances imply higher luminosities, leading to overestimated temperatures and ionisation, while smaller distances produce the opposite effect. The preferred value is selected as the one that provides the best agreement between the synthetic and observed spectra, while remaining consistent with independent constraints and other input parameters.

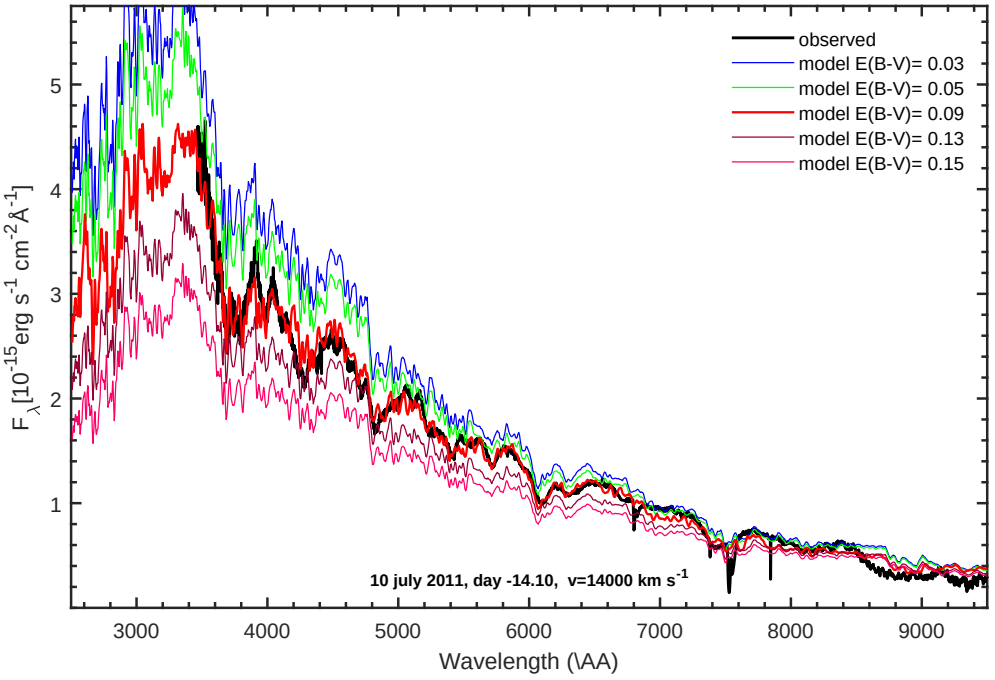


FIGURE 3.2: This plot illustrates the effect of reddening on the synthetic spectra, where $E(B-V)$ values are varied in steps of 0.02. The example corresponds to the earliest available spectrum of SN 2012dn at day -14.

.

Extinction The extinction toward a supernova is typically constrained using Galactic dust maps together with estimates of host-galaxy reddening reported in the literature. The adopted reddening value strongly affects the spectral modelling because it alters the relative flux distribution across the spectrum. If the reddening is overestimated, the blue flux is overly suppressed, requiring a higher intrinsic luminosity to reproduce the observed spectrum. This increases the temperature and modifies the ionisation conditions in the synthetic spectra; as a result, models may reproduce the blue region but overpredict the flux at redder wavelengths. Conversely, if the reddening is underestimated, the synthetic spectra tend to appear too red and require lower input luminosities. An example illustrating the effect of varying reddening values on the synthetic spectra is shown in Fig. 3.2.

As a consistency check, synthetic multi-band magnitudes derived from the models are compared with the observed photometry. Agreement across the available bands supports the adopted combination of reddening and bolometric luminosity.

Rise time The rise time is an additional variable that cannot be robustly constrained and is therefore treated as a free parameter in the modelling. A shorter rise time corresponds to a smaller photospheric radius at a given epoch, since $R \simeq v_{\rm ph}\, t$. For a fixed

luminosity, the Stefan–Boltzmann relation becomes

$$L \propto (v_{\rm ph}\, t)^2\, T^4,$$

which implies

$$T \propto \left(\frac{L}{(v_{\rm ph}\, t)^2}\right)^{1/4}.$$

Thus, for fixed $L_{\rm bol}$ and $v_{\rm ph}$, a shorter rise time leads to a higher temperature, producing spectra that are bluer and more highly ionised, while a longer rise time results in spectra that are too red.

This effect is illustrated in Fig. 3.3. For the same epoch, the model computed with a shorter rise time is bluer. In addition, when comparing to the model with larger rise time (depicted in red) a clear ionisation shift is observed: singly ionised IME features, such as Si II λ 6355, the "W"-shaped S II complex, Mg II near 4200 Å, and the Mg II/O I feature near 7500 Å, are suppressed, while Si III near 4300 Å becomes more prominent.

For a fixed $v_{\rm ph}$, shorter rise times produce more compact ejecta, since $r = v \times t$. For a fixed bolometric luminosity, this leads to a higher radiation energy density at a given velocity, resulting in increased ionisation in the inner regions. Consequently, the line-forming region for singly and doubly ionised species – the dominant contributors to the observed spectra – shifts to higher velocities, leading to larger line blueshifts. This effect is evident in the C II feature near 6300 Å, and the Si III feature near 4300 Å which appear more blueshifted in models with shorter rise times than in those with longer rise times. Furthermore, unrealistically short rise times require higher $v_{\rm ph}$ to avoid excessively hot spectra; this increase in velocity leads to larger line blueshifts.

$L_{\rm bol}$ and $v_{\rm ph}$ The bolometric luminosity, $L_{\rm bol}$, sets the overall flux level of the synthetic spectrum and is adjusted at each epoch to match the observed optical flux. The photospheric velocity, $v_{\rm ph}$, defines the inner boundary of line formation and influences the radiation field through the effective temperature, $T_{\rm eff} \propto \left(\frac{L_{\rm bol}}{(v_{\rm ph}\, t)^2}\right)^{1/4}$. Lower values of $v_{\rm ph}$ therefore lead to higher temperatures and increased ionisation, while higher $L_{\rm bol}$ produces a similar effect. In addition, $v_{\rm ph}$ is constrained by the observed positions of the spectral lines, as unrealistically high values would result in excessively blueshifted features compared to the data. Furthermore, the successive values of $v_{\rm ph}$ define the physical radii of the ejecta shells and thus the velocity intervals over which the elemental abundances inputs are distributed. If the velocity steps are too small, the resulting shells become too thin to produce a measurable effect on the synthetic spectra, In general, both

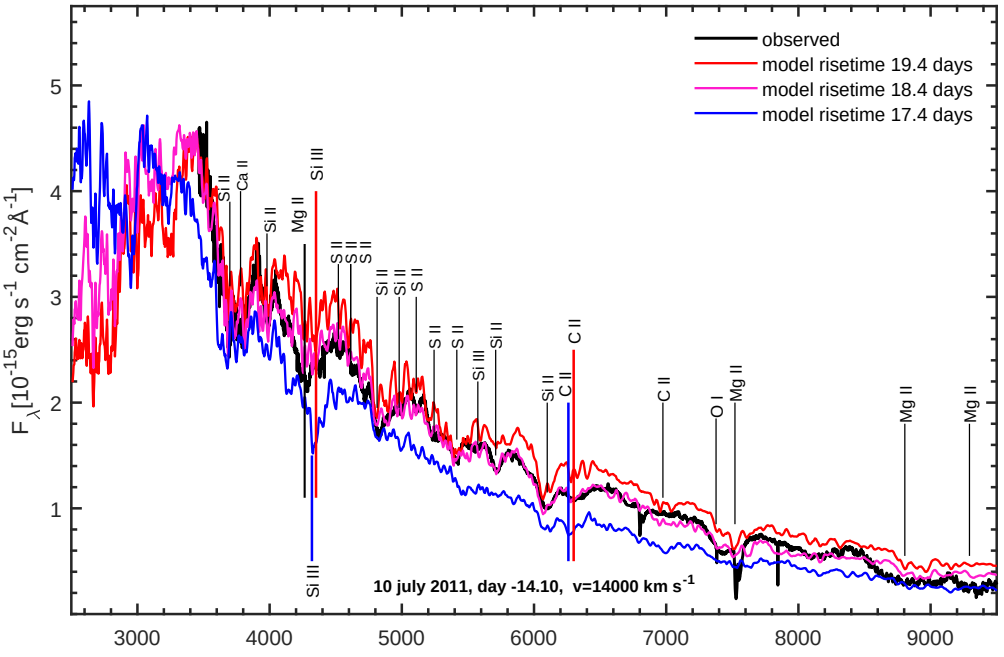


FIGURE 3.3: Effect of varying the rise time on the synthetic spectra: the longer rise-time model (red) produces a redder spectrum, while the shorter rise-time model (blue) is bluer and more highly ionised, exhibiting weak singly ionised IME features and stronger Si III. The positions of the C II and Si III lines near 6300 and 4300 Å are marked for each model in the corresponding colour; in the shorter rise-time model, these features are blueshifted to higher velocities.

parameters, $L_{\rm bol}$ and $v_{\rm ph}$ are adjusted simultaneously within reasonable limits to achieve the best agreement with the observed spectra.

Chapter 4

SN1999aa

4.1 Introduction

The importance of SN 1999aa lies in its spectroscopic properties, which place it between normal SNe Ia and the luminous 91T-like events (e.g., Filippenko et al., 1992b). Similar to SN 1991T, it is a slow decliner with $\Delta m_{15}(B)$ in the range 0.75–0.85 mag (Jha et al., 2006, Krisciunas et al., 2000). Most notably, it displays strong early Fe III features, a hallmark of the 91T-like subclass, significantly stronger than those observed in normal events. As in SN 1991T, IME lines are weak, though not as shallow as in SN 1991T; Si II λ6355 in particular shows an intermediate strength between SN 1991T and normal SNe Ia. Unlike SN 1991T, however, SN 1999aa displays a prominent HV Ca II H&K feature of intermediate strength compared to normal events, and evolves more rapidly than SN 1991T toward a normal spectroscopic appearance, with clear Si II and S II signatures already present about one week before B-band maximum. SN 1999aa is not an isolated case; similar objects have been identified, including SNe 1998es (Ayani & Yamaoka, 1998), 2012cg (Silverman et al., 2012d), 1999dq, 2001eh, 2002hu, 2006cz, and 2008Z (Silverman et al., 2012c), forming a distinct subclass with a rate comparable to that of 91T-like events (Silverman et al., 2012c). Together, 99aa-like and 91T-like events are estimated to account for ∼20 per cent of all SNe Ia (Yang et al., 2022). These intermediate properties make SN 1999aa a particularly valuable object for probing the ejecta structure, as a clear separation from both normal and 91T-like events would imply distinct physical origins, whereas a continuity of properties would suggest a sequence driven by smoothly varying parameters such as temperature or ionization. The central question is whether SN 1999aa represents an extension of a luminosity-driven sequence or whether its spectroscopic properties reflect intrinsic differences in the abundance structure, pointing to

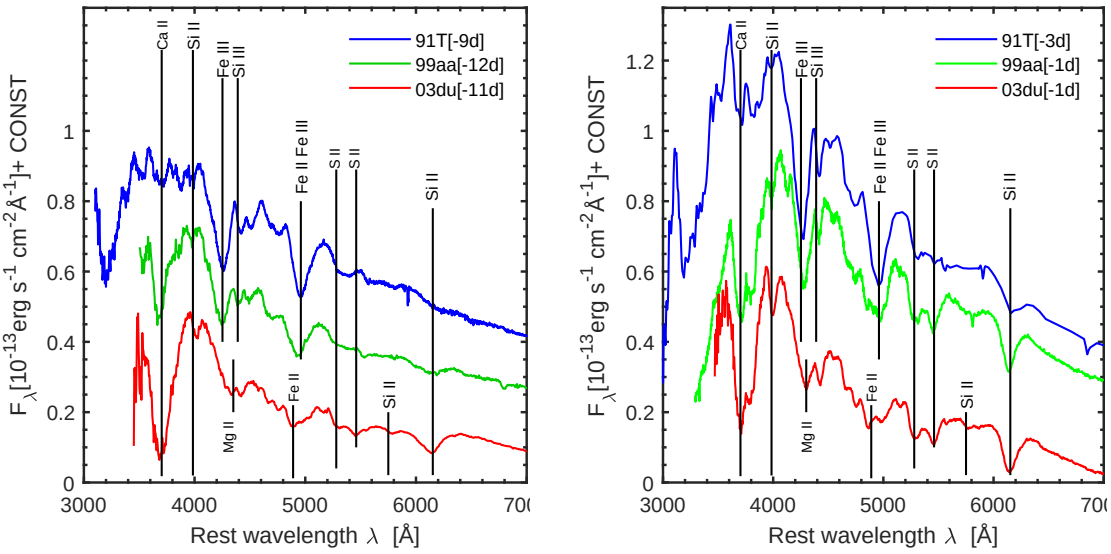


FIGURE 4.1: *Left:* Early-time spectra of SN 1991T (top), SN 1999aa (middle), and the normal SN 2003du (bottom). Major absorption features are marked, and epochs are given in days relative to B-band maximum brightness. *Right:* Same comparison, but for spectra obtained near maximum light.

distinct explosion mechanisms or progenitor systems. To address this, abundance stratification is applied and the resulting distributions are compared to those of normal SNe Ia and SN 1991T derived using the same method, providing direct insight into the physical origin of the intermediate properties observed in SN 1999aa.

The work presented here was published in Aouad et al. (2022). The modelling of the photospheric-phase spectra was carried out by the author, while the nebular-phase spectral modeling and light-curve modeling were performed by Paolo Mazzali and the observed bolometric light curve was constructed by Elena Pian

4.2 Data

The discovery of SN 1999aa was reported by Nakano et al. (1999), Armstrong & Schwartz (1999), and Qiao et al. (1999), who identified it in the barred spiral galaxy NGC2595, located at a redshift of $z = 0.0144$ (Epinat et al., 2008, Vanvan van Driel et al., 2016). This galaxy has distance estimates based on the Tully-Fisher relation, ranging from $\mu = 32.30 \pm 0.53$,mag(Bottinelli et al., 1985) to $\mu = 34.44 \pm 0.47$,mag (Theureau et al., 2007). Measurements from the light curve of SN 1999aa yield distance moduli in the range $\mu = 33.43 \pm 0.16$ mag (Amanullah et al., 2010) to $\mu = 34.58 \pm 0.24$ mag (Riess et al., 2004), assuming that the Phillips relation holds for this object.

TABLE 4.1: Late-time photometry of SN 1999aa.

UT Date	JD[a]	Epoch[b] (days)	U (1σ) (mag)	B (1σ) (mag)	V (1σ) (mag)	R (1σ) (mag)	I (1σ) (mag)
03/11/1999[c]	485.170	+248.9	22.202 (0.086)	20.987 (0.075)	20.811 (0.045)	22.019 (0.127)	...
11/12/1999[c]	523.170	+286.4	...	21.381 (0.044)	21.192 (0.029)	22.705 (0.079)	...
14/12/1999[c]	526.098	+289.2	23.067 (0.067)	21.486 (0.025)	21.189 (0.026)	22.769 (0.099)	21.494 (0.071)
05/01/2000[c]	548.086	+310.9	23.414 (0.079)	21.844 (0.028)	21.522 (0.027)	23.059 (0.050)	22.112 (0.094)

[a] JD−2 451 000.
[b] Rest-frame time since B-band maximum.
[c] Instrument: TNG + OIG.

Photometric data were obtained from Jha et al. (2006), Krisciunas et al. (2000), Qiao et al. (1999), Armstrong & Schwartz (1999), Yoshida et al. (1999), and Altavilla et al. (2004). Late-time observations, previously unpublished, were taken with the Optical Imager Galileo (OIG) at the Telescopio Nazionale Galileo (TNG) on La Palma. These $UBVRI$ images were processed using standard reduction techniques and analyzed with the ECSNOOPY package (Cappellaro, 2014), employing point spread function (PSF) fitting for the SN magnitudes. Calibration was performed using field star magnitudes from Krisciunas et al. (2000) for the $BVRI$ bands, and the U-band magnitudes were converted from SDSS catalog values according to the method in Chonis & Gaskell (2008). The final magnitudes, with their corresponding errors from artificial-star tests, are listed in Table 4.1.

The spectra used in this analysis are archived in the Weizmann Interactive Supernova Data Repository (WISeREP) (Yaron & Gal-Yam, 2012), as detailed in Table 4.3.1.

4.3 Modeling set up

Prior to the modelling, the spectra are first photometrically calibrated, and the input parameters are constrained within the ranges defined by observational uncertainties reported in the literature. The procedures adopted are described below.

4.3.1 Spectra photo-calibration

Accurate spectral calibration is essential to ensure reliable modelling results. If a spectrum is not properly calibrated across a given photometric band, it may lead to incorrect input parameters, such as the luminosity, photospheric velocity, or the estimated explosion epoch t_0. These inaccuracies propagate into the radiative transfer calculations, affecting the ionization balance and the formation of spectral lines, and ultimately leading to erroneous physical interpretations.

TABLE 4.2: Spectra of SN 1999aa and modelling parameters.

UT Date 1999	JD[a]	Epoch[b] (days)	Telescope/Instr.	$\log L$ [$L_\odot$]	v (km s^{-1})	T(rad) (K)
12/02[c]	221.5	−11.0	Lick 3 m / Kast	9.220	12600	12310
13/02[d]	222.5	−10.0	NOT 2.6 m / ALFOSC	9.315	12300	12735
14/02[e]	223.83	−8.8	FLW 1.5 m / FAST	9.440	12000	12946
15/02[e]	224.78	−7.8	FLW 1.5 m / FAST	9.470	11500	13335
16/02[e]	225.74	−6.9	FLW 1.5 m / FAST	9.510	11200	13440
17/02[d]	226.5	−6.1	APO 3.5 m / DIS	9.530	10950	13378
18/02[e]	227.75	−4.9	FLW 1.5 m / FAST	9.590	10550	13695
19/02[e]	228.78	−3.8	FLW 1.5 m / FAST	9.610	10300	13490
20/02[e]	229.79	−2.9	FLW 1.5 m / FAST	9.610	10000	13239
21/02[e]	230.79	−1.9	FLW 1.5 m / FAST	9.595	9600	13029
23/02[c]	232.5	−0.2	Lick 3 m / Kast	9.590	9300	12296
25/02[d]	234.5	+1.8	Lick 3 m / Kast	9.560	8900	11380
03/03[d]	240.5	+7.7	MDM 2.4 m / Mk III	9.310	7150	12778
09/03[c]	246.5	+13.6	Keck-1 / LRIS	9.170	5500	11663
12/03[c]	249.5	+16.6	Lick 3 m / Kast	9.130	4250	11162

[a] JD−2,451,000
[b] Rest-frame time, since B maximum
[c] Silverman et al. (2012a)
[d] Garavini et al. (2004)
[e] Matheson et al. (2008)

All spectra are calibrated for the photometric bands where data are available for the same epoch. In cases where photometric data for a specific band is missing, linear interpolation is applied between two available epochs. In the case of SN 1999aa the spectra were calibrated in the U, B, V, and R bands.

The spectral calibration is performed by matching the flux computed from the spectrum to the observed photometric measurements. The spectrum is first divided into wavelength regions corresponding to the different photometric passbands. For each band, the spectral flux is multiplied by the transmission function of the corresponding filter, and the resulting flux is computed by integrating the product over wavelength across the passband. This integrated flux is then normalized by the effective width of the filter, yielding a mean flux representative of that photometric band, which can be directly compared to the observed photometric flux.

In parallel, the observed photometric magnitudes are converted into physical flux units using the appropriate zero-points. For each filter, the ratio between the observed flux and the synthetic flux derived from the spectrum provides a scaling factor corresponding to the central wavelength of that passband.

These scaling factors, sampled at the effective wavelengths of the filters, are then fitted with a smooth function, typically a low-order polynomial or spline. This smooth correction function is subsequently applied to the original spectrum, yielding the final calibrated spectrum that is consistent with the observed photometry across all bands. The method is explained in Fig. 4.2.

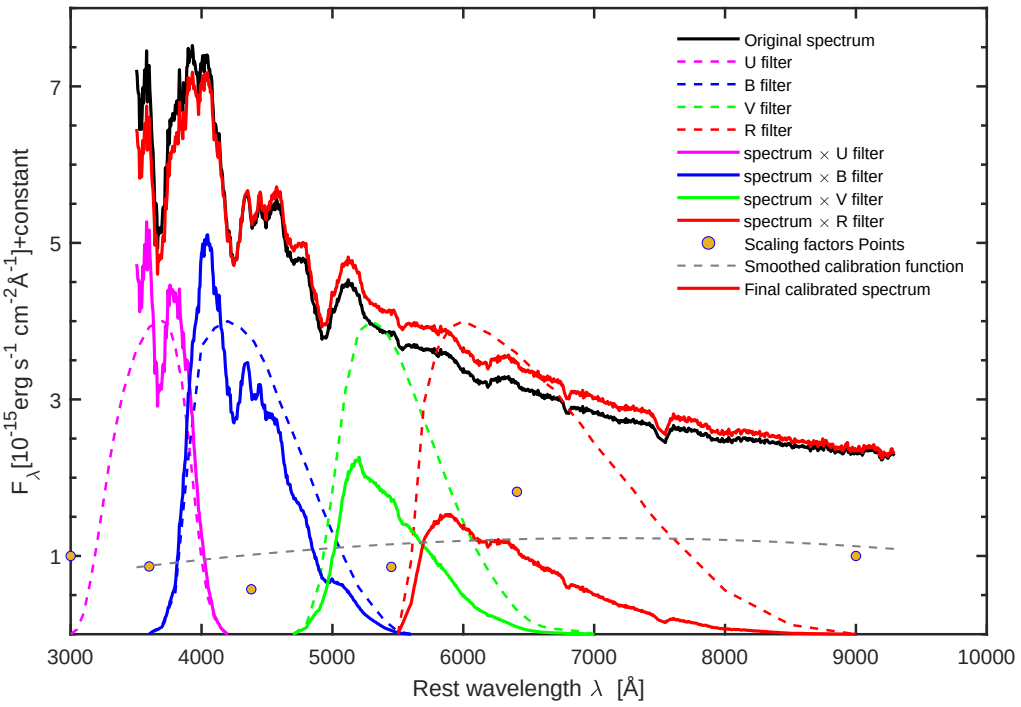


FIGURE 4.2: Example of the photometric calibration of the SN 1999aa spectrum at day −10. The original spectrum is shown in black, while the calibrated spectrum is shown in red. The calibration is achieved by matching the synthetic photometry of the spectrum to the observed broadband photometry through a smooth wavelength-dependent correction.

4.3.2 Distance, extinction and rise time

Distance: The exact distance to NGC 2595 is uncertain, therefore, it was treated as a variable within the range suggested by the literature. Several distance moduli (μ) were tested across three spectra. Larger distances resulted in higher luminosities, producing excessive temperatures and unrealistic ionization levels, while smaller distances led to the opposite. The optimal fit was achieved with $\mu = 34.00$ mag, closely aligning with the average value derived from published estimates, $\bar{\mu} = 33.975 \pm 0.34$ mag.

*Extinction:*The extinction toward SN 1999aa is well constrained. Based on the dust maps of Schlegel et al. (1998), the Galactic contribution is $E(B-V) = 0.04$ mag, while no significant reddening from the host galaxy is inferred, with $E(B-V) = 0.00$ mag (Krisciunas et al., 2000). Therefore the adopted total reddening value is $E(B-V) = 0.04$.

*Rise time:*A range of rise times between 19 and 21 days is explored, as discussed in Sect.3.3 with the best agreement achieved for a value of 20 days.

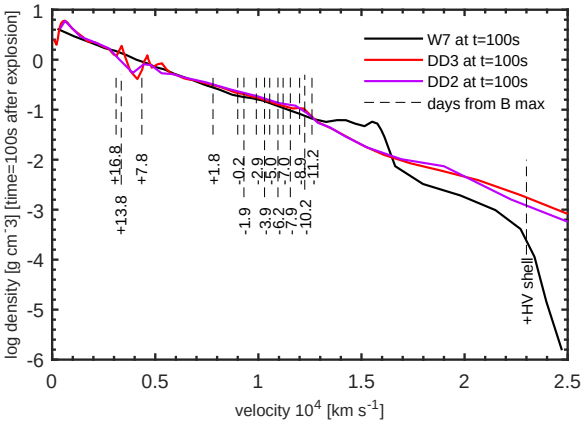


FIGURE 4.3: The three density profiles used in the modelling: W7 (Nomoto et al., 1984), DD2, and DD3 (Iwamoto et al., 1999). Vertical dashed lines mark the photospheres of the synthetic spectra.

4.4 The photospheric phase

A total of 15 spectra were analyzed, spanning from day −11 to day +14 relative to *B*-band maximum light. The input parameters adopted for the models are listed in Table 4.3.1. Figures 4.4, 4.9, 4.10 and Fig.4.12 present the synthetic spectra obtained with the three explosion models, shown in comparison with the observed spectra.

Three distinct density–velocity profiles were employed: the classical fast deflagration model W7 (Nomoto et al., 1984), and the higher-energy delayed-detonation models DD2 and DD3 from Iwamoto et al. (1999). These profiles, shown in Fig. 4.3, have been extensively used in previous abundance stratification studies, demonstrating their ability to reproduce the spectroscopic and photometric behaviour observed across a wide range of SNe Ia subclasses.

The adoption of these consistent density profiles also enables direct comparisons between different SNe Ia, which constitutes a key objective of this work.

4.4.1 The early-time spectra

In Fig. 4.4, models for the earliest spectra, spanning from −11 to −9 days relative to *B*-band maximum, are presented. The synthetic spectra reproduce the observed features well. In particular, strong absorption features of Fe III and Si III, and the overall flux level is matched, except in the redder wavelength regions. The photospheric velocity decreases from 12,600 km s^{-1} to 12,000 km s^{-1} over this phase.

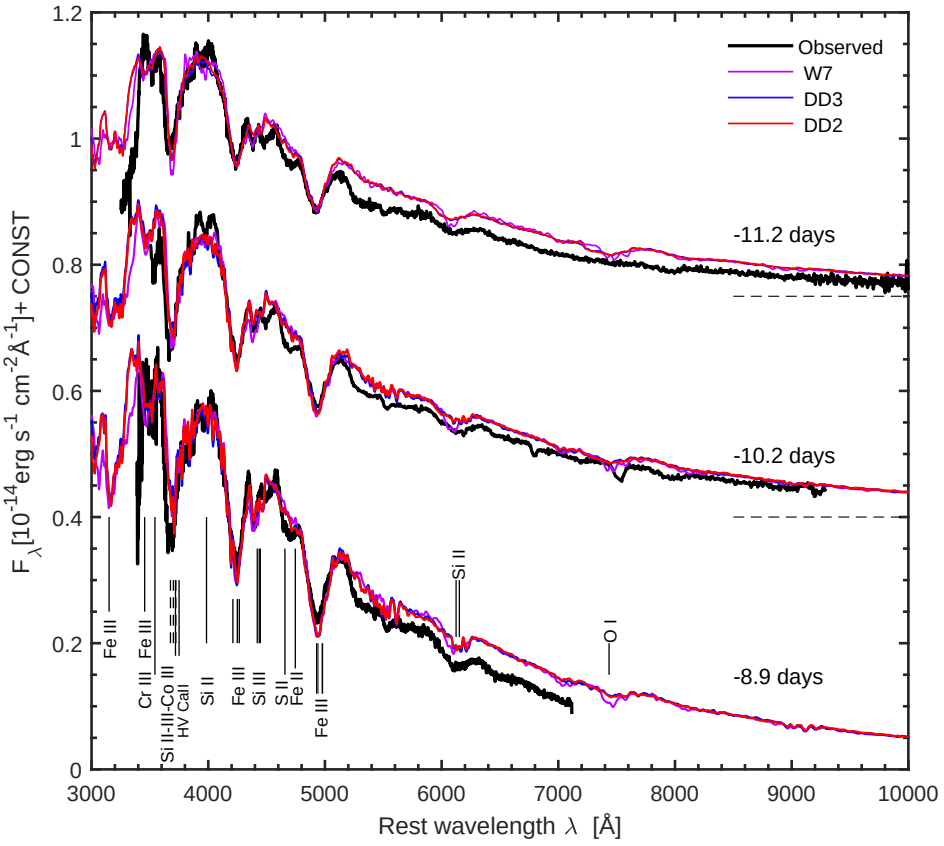


FIGURE 4.4: Early-time spectra. Epochs are shown with reference to B maximum. Features in the −10.2 day spectrum near 6780 Å (very weak) and 7500 Å (weak) are telluric. The spectra have been shifted in flux by a constant value. The horizontal dashed lines mark the zero flux for each epoch.

Fe-group elements: A small amount of stable iron (i.e., ^{54}Fe) is required in the outer shells to reproduce the prominent features near 4250 and 5000 Å. At these early epochs ^{56}Ni has not yet had sufficient time to decay into ^{56}Fe, so the iron present must be stable. The inferred Fe mass fraction is ∼0.015–0.018 at $v > 12600$ km s^{-1}, significantly super-solar ($X(\mathrm{Fe}_\odot) = 0.001$ Asplund et al., 2009), in contrast to the solar value reported for SN 1991T (Sasdelli et al., 2014) and the 0.003–0.005 range derived for SN 2003du (Tanaka et al., 2011). The iron abundance in these outer layers is constrained by testing models with progressively increasing Fe fractions until the observed features are matched, as illustrated in Fig. 4.5.

Small amounts of Ti and Cr are required at these epochs to provide line blanketing in the ultraviolet (UV) and redistribute the flux toward longer wavelengths. The abundance of ^{56}Ni is not constrained at these phases, as no optical spectral features can be reproduced by ^{56}Ni alone. The available spectra of SN 1999aa do not extend blueward of ∼ 3400 Å,

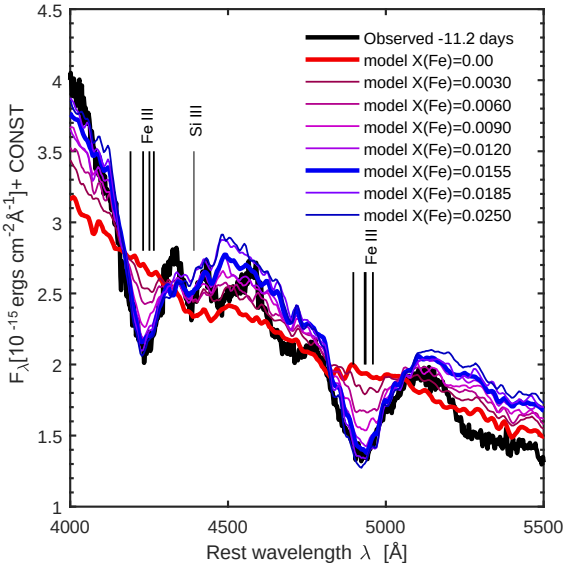


FIGURE 4.5: A close-up view of the day −11 spectrum showing the region where the strongest Fe III lines are seen. Adding small packets of stable Fe, the Fe mass fraction can be inferred.

preventing the detection of the expected Co III-dominated feature near ∼ 3200 Å (Mazzali et al., 1995, Sasdelli et al., 2014, Stehle et al., 2005).

Calcium: The early-time spectra of SN 1999aa are characterised by a prominent absorption feature near 3700 Å, with a strength intermediate between that observed in normal SNe Ia and SN 1991T (Garavini et al., 2004). This feature has been attributed to high-velocity (HV) Ca II H&K absorption (Garavini et al., 2004, Mazzali et al., 2005b).

This feature is reproduced with $X(\mathrm{Ca}) \approx 0.0035$ at $v > 21000\,\mathrm{km\ s^{-1}}$ when the W7 density profile is adopted, while the DD2 and DD3 models, which contain more mass at high velocities, require a lower abundance of $X(\mathrm{Ca}) \approx 0.00025$. A similar dependence on the density profile was reported by Tanaka et al. (2011) for SN 2003du, where the higher outer-layer mass of DD models likewise leads to a reduced Ca abundance. Both values are significantly lower than those inferred for some spectroscopically normal SNe Ia (Tanaka et al., 2008), which exhibit much stronger Ca II H&K absorption and an earlier emergence of the Ca II NIR feature compared to both SN 1999aa and SN 1991T.

The calcium abundance derived for SN 1999aa is consistent with that of SN 1991T, for which $X(\mathrm{Ca}) < 0.0003$ at $v > 17000\,\mathrm{km\ s^{-1}}$ was estimated using the DD3 profile (Sasdelli et al., 2014). In both cases the Ca abundance at high velocities is super-solar ($X(\mathrm{Ca}_\odot) = 0.00006$ Asplund et al., 2009).

The strength of the Ca II H&K feature is sensitive not only to the Ca abundance but also to the ionisation balance, in particular the electron density, whose increase favours

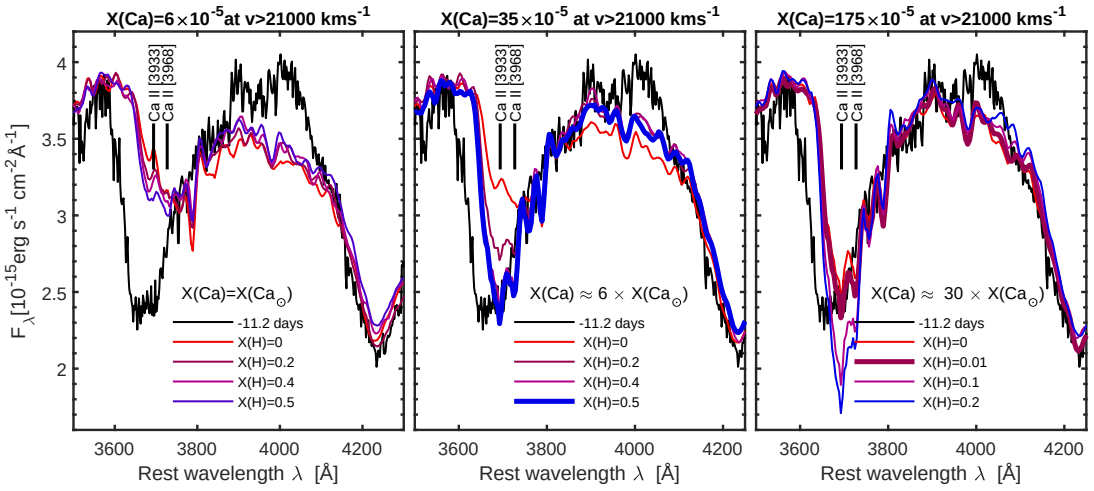


FIGURE 4.6: A close-up view of the Ca II H&K region, showing the observed spectrum at day −11 compared to models computed with the W7 density profile using different abundances of Ca coupled with various amounts of H in the outermost shells.

singly-ionised species (Mazzali et al., 2005a,b) and can be enhanced by the presence of hydrogen in the outer layers. Furthermore, the Ca II H&K transition originates from the ground state of Ca II, meaning it remains optically thick even in the outermost, most dilute layers of the ejecta, making it particularly sensitive to conditions at high velocities. Fig. 4.6 shows the Ca II H&K feature reproduced for different combinations of Ca abundance and hydrogen content at $v > 21000\,\mathrm{km\ s^{-1}}$, following the approach of Tanaka et al. (2011). Due to the degeneracy between these two parameters, the Ca mass fraction cannot be accurately constrained.

Hydrogen could be present either through ejecta–CSM interaction (Mazzali et al., 2005b) or as a remnant of accretion onto the white dwarf surface (Livio & Mazzali, 2018). Small amounts are sufficient to reduce the ionisation in the dilute outer layers and produce high-velocity features commonly observed in SNe Ia (Mazzali et al., 2005b), however larger abundances ($X(\mathrm{H}) \gtrsim 0.3$) would produce an H$\alpha$ feature, which is not observed in the spectra as can be seen in Fig. 4.7.

The absence of hydrogen signatures argues against the single degenerate scenario (Marietta et al., 2000, Panagia et al., 2006), but it is not conclusive enough to rule it out entirely (Hachisu et al., 2012a, Justham, 2011) (for a review, see Livio & Mazzali, 2018).

Silicon, Sulphur, Magnesium: The Si II λ6355 line is significantly weaker in the early spectra of SN 1999aa compared to normal SNe Ia, but strengthens as the spectra evolve, while Si II λ5972 is not visible at early epochs, reflecting the high ejecta temperature. The depth ratio of these two lines, $\mathcal{R}$(Si II), a key temperature diagnostic (Hachinger et al., 2008, Nugent et al., 1995a), is well reproduced in the synthetic spectra, confirming

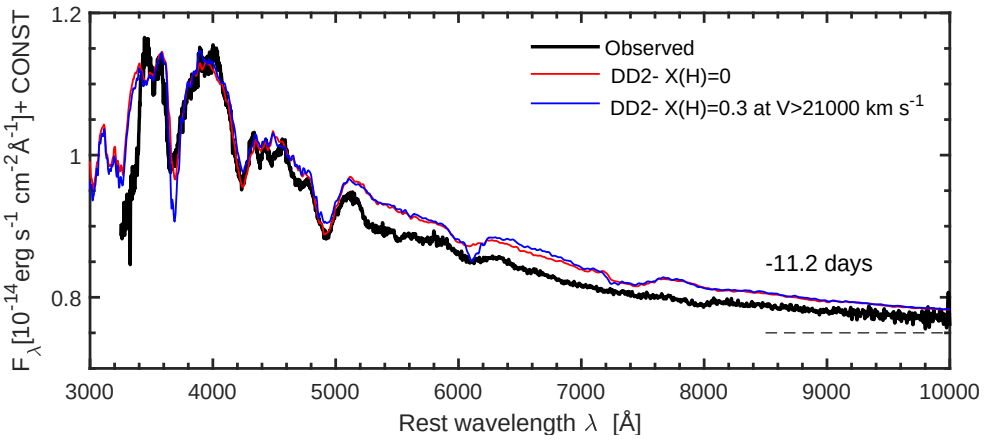


FIGURE 4.7: Effect of adding hydrogen at the outer shells on the earliest spectrum. A hydrogen mass fraction in the range of 0.3 will give rise to an Hα feature that is not seen in the observed data.

an accurate temperature structure and ionisation balance. The high ionisation state is further supported by the Si III $\lambda\lambda$4553, 4568, 4575 feature near 4400 Å, prominent in the earliest spectrum. The silicon mass fraction is 0.025 at $v > 12600\,\mathrm{km\ s^{-1}}$, rising steeply to 0.73 at $v > 12300\,\mathrm{km\ s^{-1}}$.

The two S II features at 5468 and 5654,Å are absent at early epochs, only appearing around day ~ -6. The Mg II λ 4481,Å line is not observed in the spectra of SN 1999aa, as this region is dominated by Fe III lines, a behaviour observed in all 91T-like events (Aouad et al., 2024, Sasdelli et al., 2014)

Carbon, Oxygen: A C II $\lambda\ \lambda$ 6578, 6583 line has been detected in some SNe Ia (Mazzali, 2001, Parrent et al., 2011). It can be observed on top of the Si II λ 6355 P-Cygni emission, but it is not a common feature. This line is not visible in SN 1999aa. An upper limit to the carbon abundance of ~ 0.0005 at $v > 12,600\,\mathrm{km\ s^{-1}}$ can be determined (Fig.4.8. The absence of C in the outermost layers favours delayed-detonations models (Khokhlov, 1991b, Marion et al., 2006). The absence of this feature cannot be attributed to carbon being doubly ionised, as the excitation of the lower levels of optical C III lines is not favored at the temperatures of even luminous SNe Ia. Carbon may instead be present at higher velocities, though this would require earlier observations, which are unfortunately not available for SN 1999aa.

The synthetic spectra based on the W7 model exhibit a shallow O I λ 7744 line (Fig.4.4, a feature absent in the spectra of SN 1999aa. In contrast, the DD2 and DD3 profiles, have less mass between 13,000 and 16,000 km $\mathrm{s^{-1}}$ where this line forms (Fig.4.3), and therefore produce a much weaker feature that aligns better with the observed spectra (days -11 and -10). The oxygen abundance can be inferred by analyzing the abundances

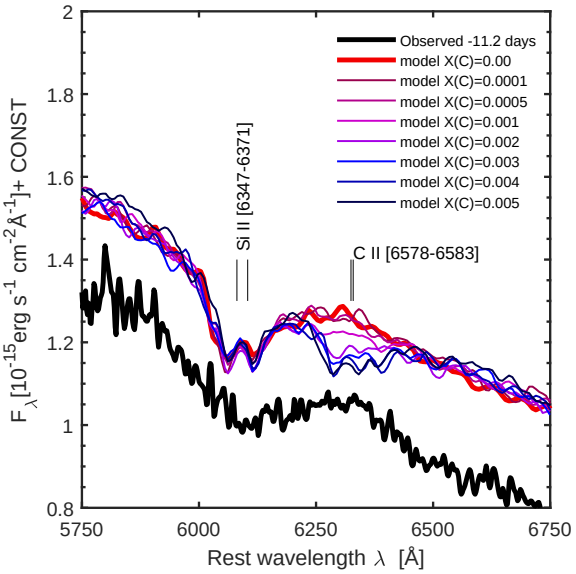


FIGURE 4.8: A close-up view of the spectrum showing the Si II–C II region. Small amounts of carbon can create an absorption line redward of the Si II line. A prominent C line is not seen in the observed spectrum.

of other high-velocity elements, such as Si, S, Ca, Fe, and ^{56}Ni. Oxygen is dominant at $v > 12,600$,km s^{-1} but disappears already by $v \approx 12,300$,km s^{-1}. This behaviour closely resembles that of SN 1991T (Sasdelli et al., 2014). In contrast, Tanaka et al. (2011) report the presence of oxygen down to a velocity of 9400 km s^{-1}for the normal SN Ia 2003du.

4.4.2 Pre-maximum-light spectra

Figures 4.9 and 4.10 show spectra ranging from -8 to -3 days from B maximum. The photospheric velocity evolves from 11,500 to 10,000 km s^{-1}.

Fe-group elements: The Fe III lines near 4300 and 5000 Å grow stronger over time, and their evolution is well reproduced in the synthetic spectra. During these epochs, the contribution of Fe from ^{56}Ni decay becomes increasingly significant, accounting for 20 percent of the total Fe mass fraction by day -7 and rising to 30 percent by day -3. Accurate fits are achieved with $X(\mathrm{Fe_{stable}}) \approx 0.1$ in the probed shells. The ^{56}Ni abundance increases from 0.05 at $v = 11,500$,km s^{-1} to 0.53 at $v = 10,950$,km s^{-1}.

Calcium: The Ca II H&K feature is accurately reproduced by the synthetic spectra. At day -6, the Ca II near-infrared (NIR) triplet is not detected in the observed spectra, a behaviour correctly captured by the synthetic spectra. The near-photospheric Ca abundance at these epochs is approximately 0.0015 across all models.

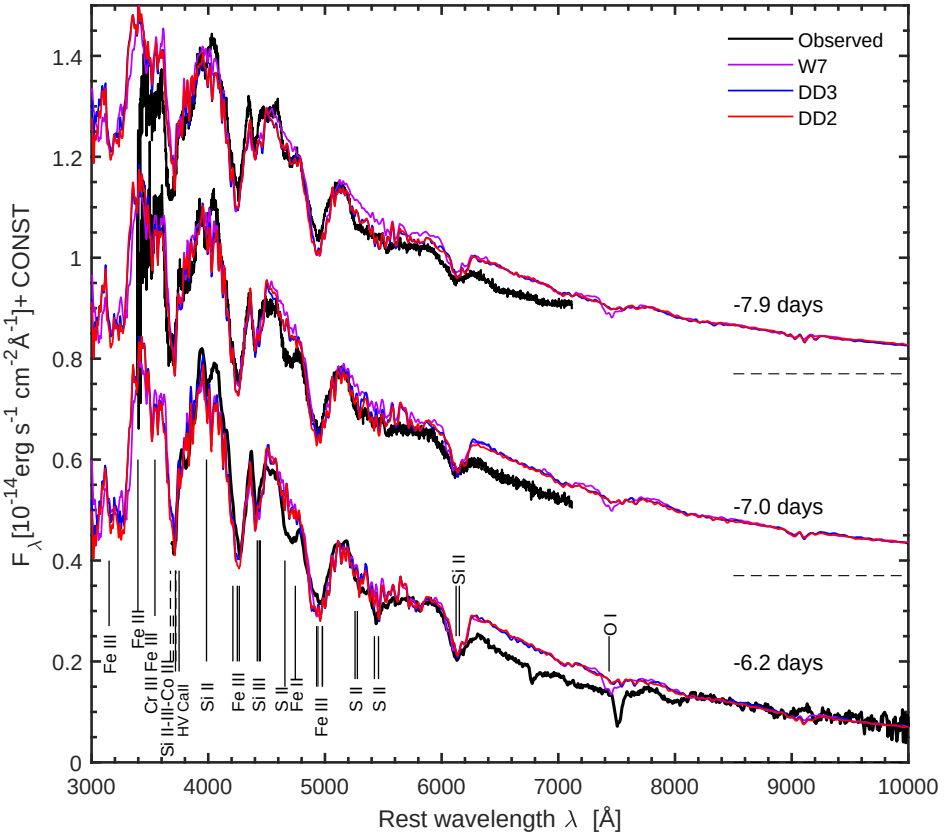


FIGURE 4.9: Spectra one week before B-band maximum. Epochs are shown with reference to B maximum. Features in the -6.2 day spectrum near 6780 Å (weak) and 7500 Å are telluric. The spectra have been shifted in flux by a constant value. The horizontal dashed lines mark the zero flux for each epoch.

Silicon, Sulphur: The Si II λ 6355 line deepens over time, a trend well reproduced in the synthetic spectra, along with the Si III feature near 4400 Å and the Si II λ 4130 line. The silicon abundance is 0.72 at $v \approx 11,500$km s^{-1}, decreasing to 0.26 at $v \approx 10,000$km s^{-1}.

Carbon, Oxygen: Carbon and oxygen are not required at these epochs. Any presence of carbon would generate a spectral line absent in the observed spectra. Similarly, oxygen is not required, as the Fe-group elements and intermediate-mass elements (IMEs) are sufficient to complete the composition at these velocities.

4.4.3 Spectra at maximum brightness

Fig. 4.11 shows spectra ranging from -2 to $+2$ days from B-band maximum, with the photospheric velocity evolving from 9600 to 8900 km s^{-1}. At these epochs the photosphere has receded into the ^{56}Ni-dominated shell, where the assumption of blackbody

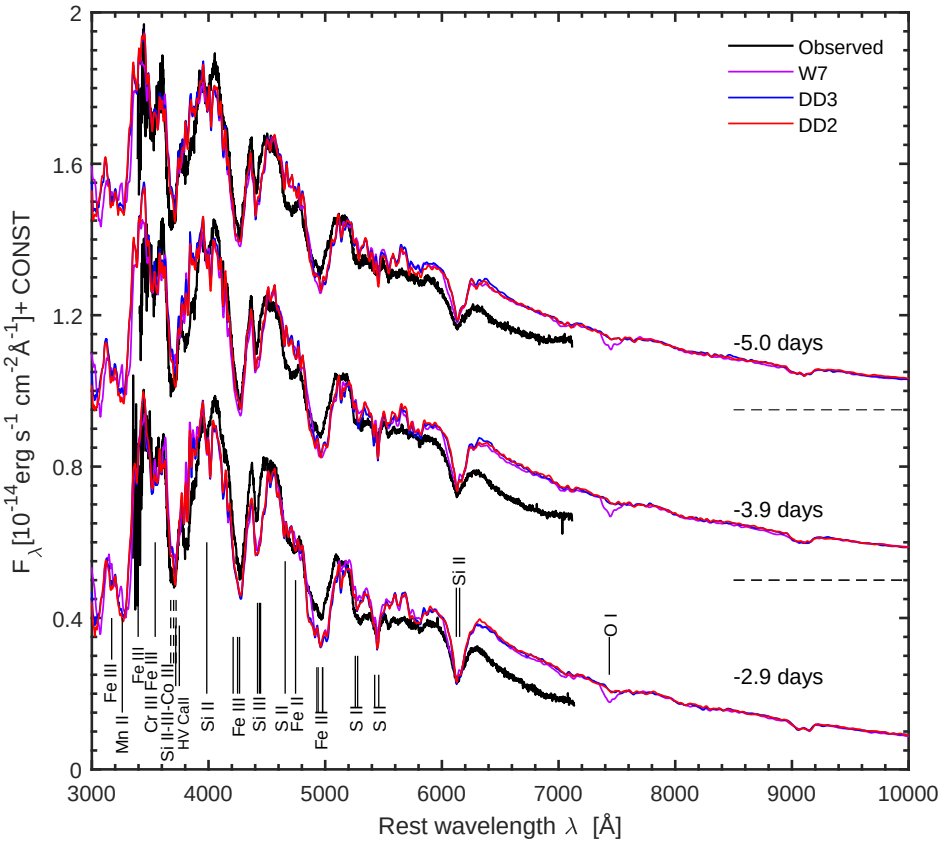


FIGURE 4.10: Pre-maximum-brightness spectra. Epochs are shown with reference to B maximum. The spectra have been shifted in flux by a constant value. The horizontal dashed lines mark the zero flux for each epoch.

emission at the photosphere becomes less accurate. In the models, all luminosity is injected at the photospheric boundary, causing photons to undergo more fluorescence in the Fe-group rich layers, being absorbed in the UV and re-emitted at redder wavelengths. In reality, radioactive energy is deposited over an extended region above the photosphere where the lower density makes this UV-to-red redistribution less efficient, resulting in a flux excess in the synthetic spectra redward of ∼6000 Å compared to the observations. Line formation and the ionisation balance are unaffected, as they depend on the velocity and abundance structure above the photosphere.

Fe-group elements: At these epochs, Fe lines are quite deep. The iron abundance is high, because Fe from ^{56}Ni decay is now a significant contribution (∼ 30%) to the total Fe abundance. The feature near 4300 Å remains primarily dominated by Fe III, while the Fe III feature near 5000 Å broadens due to contributions from Fe II lines. This evolution is captured effectively in the synthetic spectra.

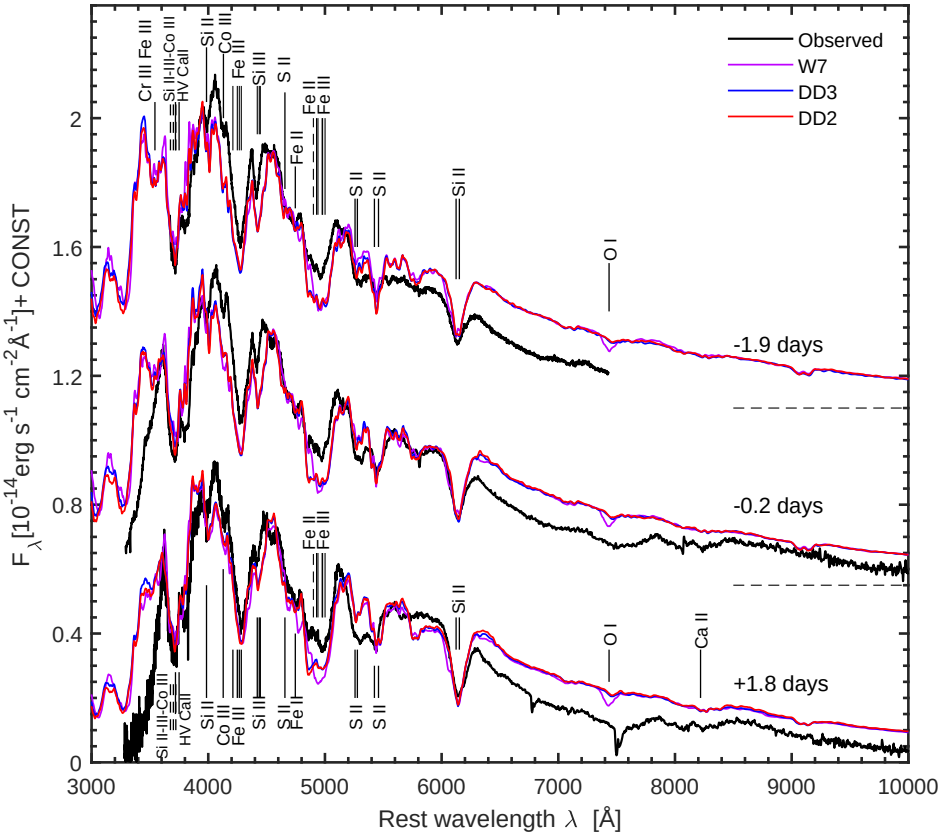


FIGURE 4.11: Near-maximum-light spectra. Epochs are shown with reference to B maximum. Features in the +1.8 day spectrum near 6780 Å (weak) and 7500 Å are telluric. The spectra have been shifted in flux by a constant value. The horizontal dashed lines mark the zero flux for each epoch.

Calcium: The Ca II H&K feature is well reproduced in the synthetic spectra, with both its depth and profile accurately matched. At these epochs, the feature is increasingly affected by line blending, with contributions from Si II and Co III on the blue side, and from Si II and Fe III on the red side (see Silverman et al., 2015). The Ca II NIR triplet begins to emerge approximately two days after B-band maximum, and this behaviour is also reproduced by the models. In spectroscopically normal SNe Ia, this feature develops significantly earlier and with greater strength, being clearly visible even ~ 12 days before maximum light (Mazzali et al., 2008, Stehle et al., 2005, Tanaka et al., 2011). In contrast, in SN 1991T and SN 1999aa, the onset of the Ca II NIR feature is delayed until a few days after maximum light. The calcium distribution extends down to $v \approx 9600\,\mathrm{km\ s^{-1}}$.

Silicon, Sulphur: The synthetic spectra effectively replicate the shape and depth of the prominent Si II λ 6355 line. The silicon abundance is 0.25 at $v \approx 9600$,km s^{-1}, decreasing to 0.1 at $v \approx 8900$,km s^{-1}. The distinctive W-shaped S II feature near 5400 Å, arising from S II λ λ4553, 5432, 5428, and S II λ λ 5660, 5639, 5640, is now prominent and

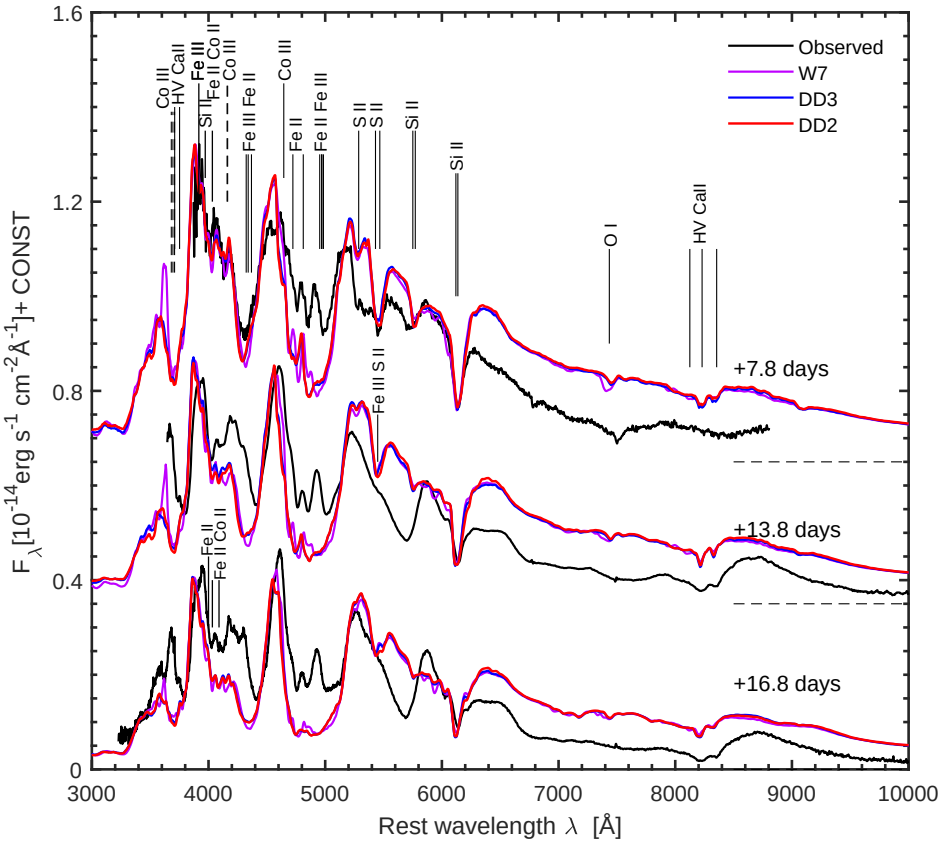


FIGURE 4.12: Post-maximum-light spectra. Epochs are shown with reference to B maximum. Features in the +7.8 day spectrum near 6780 Å (very weak) and 7500 Å (weak) are telluric. The spectra have been shifted in flux by a constant value. The horizontal dashed lines mark the zero flux for each epoch.

intensifies over time. The synthetic spectra reasonably reproduce the evolution of these lines and the ratio of their depths. The sulphur abundance is 0.12 by mass at $v \approx 9600$ km s^{-1}, decreasing to 0.05 at $v \approx 8900$ km s^{-1}.

4.4.4 Post-maximum-light spectra

Figue 4.12 shows spectra ranging from 8 to 17 days after B maximum. The photospheric velocity evolves from 7150 to 4250 km s^{-1}. At these epochs, the quality of the fits starts degrading, as the photosphere resides deep in the ^{56}Ni-dominated region. Therefore, these epochs are not used to infer abundances. Nevertheless, the synthetic spectra reproduce the major absorption lines with moderate agreement.

Fe-group elements: Around 30–40 days post-explosion, over 70 percent of the total Fe originates from the decay of ^{56}Ni. The Fe II feature near 5000 Å splits into three distinct components, a behaviour captured well in the synthetic spectra. This results from reduced line blending at lower velocities.

Calcium: The strong Ca II H&K line is still well-reproduced. The Ca II NIR triplet is now clearly visible, displaying two distinct features, which are accurately matched in shape.

Silicon, Sulphur: The synthetic spectra still replicate well the Si II λ 6355 line. Si II λ 4130 is now contaminated by Fe II $\lambda\,\lambda$ 4173, 4233, 4351 and Co II $\lambda\,\lambda$ 4160, 4145. The S II λ 5468, 5654 lines are also contaminated by a contribution from Fe III. The feature near 5700 Å may be due to Na I D absorption (Mazzali et al., 1993), or to Co III emission and could not reproduced at days +14 and +17.

4.5 Spectra in the nebular phase

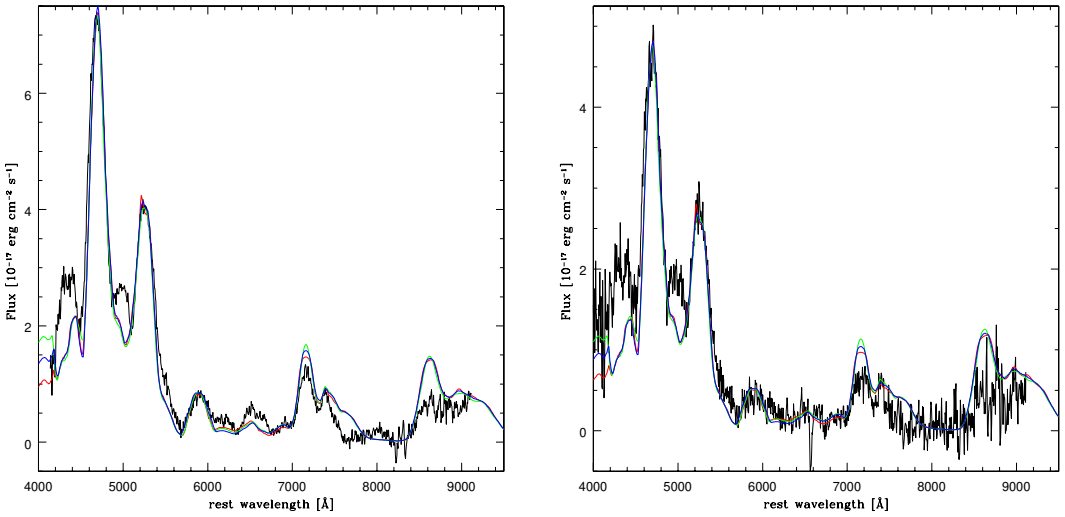


FIGURE 4.13: Nebular-phase spectra obtained on 1999 Nov. 9 (left) and Dec. 5 (right), corresponding to 255 and 281 rest-frame days after B maximum brightness, respectively. The emissions near 5200 and 7200 Å are dominated by [Fe II] lines, while the emission near 4700 Å is dominated by [Fe III]. The blue, green, and red curves represent synthetic spectra from DD3, DD2, and W7 models.

The two nebular spectra were acquired using the Low-Resolution Imaging Spectrometer (Oke et al., 1995) mounted on the Keck-I 10,m telescope. Observations were carried out on 1999 Nov. 9 and Dec. 5, with exposure times of 600 s and 300 s, respectively, both at an airmass of 1.01. These epochs correspond to 275 and 301 rest-frame days after the

explosion. Further details on the observational setup and data reduction, are provided by Silverman et al. (2012a).

The nebular spectra are modelled using the abundance distribution derived from the photospheric phase, assuming a one-dimensional stratified density and composition (Mazzali et al., 2007). Modelling the nebular spectra enables the exploration of the inner ejecta, thereby extending the abundance stratification to lower velocities and completing the tomography analysis.

A non-local thermodynamic equilibrium (NLTE) approach is adopted, following the framework introduced by Axelrod (1980). The energy input from the radioactive decay of ^{56}Ni is computed by following the propagation and deposition of γ-rays and positrons within the ejecta using a Monte Carlo scheme, as described by Cappellaro et al. (1997). The deposition is calculated assuming opacities of $\kappa_\gamma = 0.027$ cm^2 g^{-1} for γ-rays and $\kappa_{e^+} = 7$ cm^2 g^{-1} for positrons.

The deposited energy is partitioned between ionisation and heating processes: a fraction contributes to impact ionisation, while the remainder is converted into thermal energy through collisional excitation. The populations of excited levels are computed under NLTE conditions, and thermal equilibrium is established by balancing heating with radiative cooling. Cooling proceeds predominantly via forbidden line emission, especially from Fe, Co, and Ni in the inner ejecta, with additional contributions from permitted transitions, notably of Ca II. At these epochs, the ejecta are assumed to be optically thin to optical radiation, and radiative transfer effects are therefore neglected.

Using the density structure and the composition of the outer layers derived from the photospheric-phase modelling, the nebular modelling is performed in the inner ejecta at velocities $v < 8000$ km s^{-1}.

Emphasis is placed on the two dominant emission complexes, namely the Fe III feature near 4800 Å and the Fe II feature near 5200 Å, as Fe-group elements dominate the composition of the inner ejecta during the nebular phase. The intensities of these features are primarily governed by the amount of ^{56}Ni as well as of the emitting element, while their ratio is sensitive to the ionisation balance, which is further influenced by the presence of stable iron-group isotopes. Their width traces the radial distribution of the emitting elements as well as indirectly that of ^{56}Ni, since heating from radioactive decay must reach the emitting region. The models are presented in Fig.4.13.

A total ^{56}Ni mass of ~ 0.65 M$_\odot$ is inferred for all three models. Among them, the DD2 profile yields the largest amount of stable Fe, although this value remains consistent with previously reported ranges (Mazzali et al., 2001a). This excess Fe is primarily distributed between 9000 and 12,000 km s^{-1}. Its inclusion is essential to lower the ionisation level and

TABLE 4.3: Nucleosynthetic yields and kinetic energies from the modelling using different density profiles compared to the original hydrodynamic models. Results from other SNe are also shown.

	^{56}Ni	Fe [a]	Ni_{stable}	IME [b]	O	Total burned	E_k
	$M_\odot$	$M_\odot$	$M_\odot$	$M_\odot$	$M_\odot$	$M_\odot$	10^{51} ergs
1999aa (W7)	0.67	0.21	0.006	0.18	0.30	1.08	1.2
1999aa (DD2)	0.65	0.29	0.006	0.20	0.22	1.16	1.32
1999aa (DD3)	0.66	0.23	0.003	0.20	0.26	1.12	1.22
original W7	0.59	0.16	0.122	0.24	0.143	1.24	1.30
original DD2	0.69	0.10	0.054	0.33	0.066	1.31	1.40
original DD3	0.77	0.10	0.0664	0.25	0.056	1.32	1.43
1991T (DD3)	0.78	0.15	0.0006	0.18	0.29	1.09	1.24
2003du (W7)	0.62	0.18	0.024	0.26	0.23	1.15	1.25
2002bo (W7)	0.49	0.27	0.0001	0.28	0.11	1.27	1.24
2004eo (W7)	0.32	0.29	0.0005	0.43	0.3	1.1	1.1

[a] All stable isotopes except for ^{56}Fe, decay product of ^{56}Ni.
[b] ^{28}Si + ^{32}S.

to reproduce an appropriate balance between the [Fe III]- and [Fe II]-dominated emission features.

Only a small mass of stable Ni is required, as indicated by the weakness of the [Ni II] 7380 Å line. This behaviour is consistent with other SNe Ia analysed with similar methods, and suggests that the production of stable Ni remains limited even in the densest central regions.

A moderate degree of clumping is introduced in the ^{56}Ni-rich zones, corresponding to a filling factor $\gtrsim 0.5$. Stronger clumping would lead to a progressive decrease in ionisation at later epochs, as observed in objects such as SN 2011fe (Graham et al., 2015) and SN 2014J (Mazzali et al., 2020). However, the available nebular spectra of SN 1999aa are obtained at relatively early phases and cover only a narrow range in epoch, so they probe only a limited range of ejecta depths and cannot reveal such an evolution.

The combination of the early- and late-time analyses completes the abundance stratification. The resulting ejecta composition is summarised in Table 4.3, where the corresponding E_K is also listed and compared to that of the original explosion models.

4.6 Abundance tomography

The final results of the abundance experiment are shown in table 4.3 and in Fig. 4.14 compared to the original abundance distributions in the hydrodynamical models (Iwamoto et al., 1999, Nomoto et al., 1984).

The innermost region, extending to $v \approx 2500$,km s^{-1}, is dominated by stable Fe, with only a minor contribution from ^{56}Ni. These neutron-rich Fe-group elements are produced under conditions of high density and temperature ($\rho \gtrsim 10^8$ g cm^{-3}, $T \gtrsim 5\times10^9$ K), where nuclear statistical equilibrium (NSE) is established (Arnett, 1982, Iwamoto et al., 1999, Woosley et al., 2007b). In such conditions, electron captures reduce the electron fraction ($Y_e < 0.5$), favouring the synthesis of stable isotopes at the expense of radioactive ^{56}Ni. The resulting composition in this region is broadly consistent with expectations from explosion models.

The middle shells, out to $v \approx 11,000$ km s^{-1}, are dominated by ^{56}Ni. In these shells stable Ni is not found, in contrast to all explosion models. However, a significant amount of stable iron is present, at the expense of ^{58}Ni compared to the original models. A relatively narrow shell dominated by intermediate-mass elements (IMEs) is confined to velocities around 11,000–12,000 km s^{-1}, above which their abundance drops rapidly. In contrast, hydrodynamical explosion models generally predict a more extended IME distribution reaching higher velocities. A similar confinement was previously inferred by Garavini et al. (2004) from the evolution of the Si II λ 6355 line.

The presence of IMEs reflects incomplete burning at densities of order 10^7 g cm^{-3}, and their abrupt decline indicates a sharp transition in the burning conditions. This behaviour may provide important constraints on the explosion physics and the structure of the progenitor. The weakness of IME features in the early-time spectra of SN 1999aa and other SN 1991T-like SNe Ia is therefore primarily driven by abundance effects (see Filippenko et al., 1992b, Jeffery et al., 1992), rather than temperature alone. In this region, a significant amount of ^{56}Ni is still present. Above the IME-dominated region, the ejecta transition into an oxygen-rich outer layer. The carbon abundance cannot be robustly constrained, as no strong carbon features are detected. A small amount of Ca is required to account for the observed high-velocity Ca II features.

A non-negligible fraction of stable Fe, at the level of a few percent, is required to reproduce the Fe features at early epochs, implying a clearly supersolar abundance in the outer layers. At such early phases, this Fe cannot be attributed to the decay of ^{56}Ni. Its origin therefore remains uncertain, and may reflect either progenitor metallicity or the outcome of explosive nucleosynthesis. The metallicity at the location of SN 1999aa is measured to be $12+\log(\mathrm{O/H}) = 8.45$ (Galbany et al., 2016), corresponding to approximately half the solar value. This disfavors a progenitor origin and instead suggests that the Fe observed in these layers is likely synthesised during the explosion (see also Hachinger et al., 2013). In delayed-detonation models, stable Fe is predicted to be present in the outer ejecta up to velocities of $\sim$ 17,000–18,000km s^{-1}, but not beyond. In the present models, the Fe mass fraction remains above solar for $v \gtrsim 12,000$ km s^{-1}. However, the lack of very

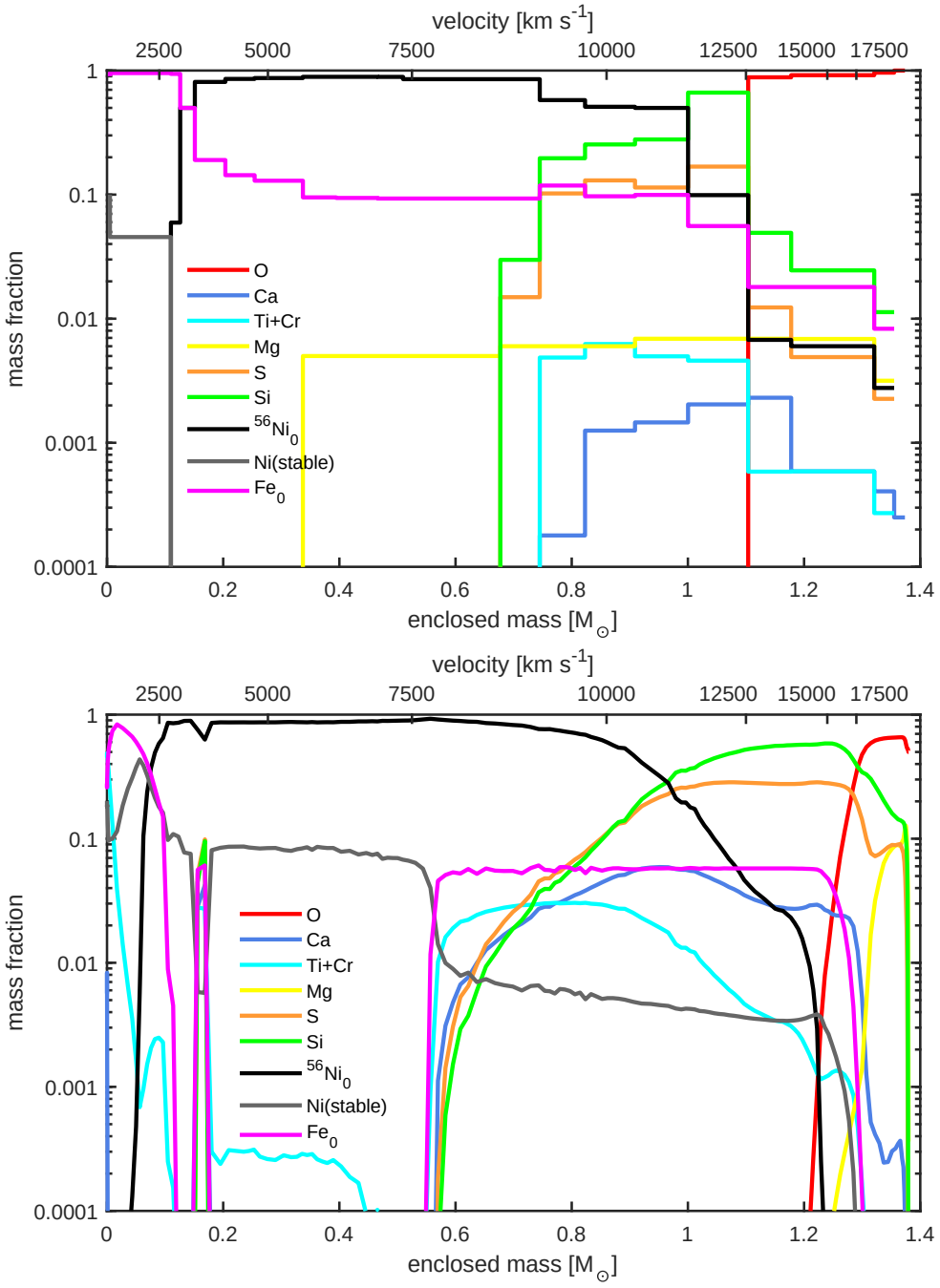


FIGURE 4.14: Upper panel: abundances obtained from spectral models using the delayed detonation DD2 density profile. Lower panel: the original nucleosynthesis from DD2 (Iwamoto et al., 1999).

early-time spectra prevents a robust determination of the maximum velocity extent of this Fe-rich material. Only a small amount of ^{56}Ni is present in the O-rich outer layers, in agreement with other SNe Ia (Stehle et al., 2005, Tanaka et al., 2011). Overall, the distribution of ^{56}Ni is broadly consistent with the predictions of explosion models.

4.7 Light curve

4.7.1 Building the bolometric light curve

The pseudo-bolometric light curve of SN 1999aa is constructed over the wavelength range 3000–10,000 Å using the available optical photometry. The $UBVRI$ light curves are first interpolated to a temporal resolution of 1 day and corrected for reddening using the extinction law of Cardelli et al. (1989), adopting $E(B-V) = 0.04$ mag (Schlegel et al., 1998). The epochs are then transformed to the rest frame using the redshift of the host galaxy, according to $t_{\rm rest} = \frac{t_{\rm obs}}{1+z}$.

For each epoch, the photometric measurements are converted into fluxes using the zero-points of Fukugita et al. (1995). A spectral energy distribution (SED) is then constructed and integrated across the U to I bands using a trapezoidal integration. The flux beyond the observed wavelength range is extrapolated assuming a flat power law toward 3,000 Å in the blue and 10,000 Å in the red as shown in Fig. 4.15, yielding the bolometric flux at each epoch. The resulting light curve is shown in Fig. 4.16.

The first four observations (prior to 1999 Feb. 13.5), which were obtained without filters, are treated as V-band measurements. A bolometric correction is applied based on the difference between the early bolometric magnitude and the simultaneous V-band magnitude. The bolometric luminosities are then computed assuming a distance of 63.1 Mpc to NGC 2595, and are shown in Fig. 4.16 as black circles.

The contribution of the near-infrared (NIR) emission is also assessed. Photometric data in the J and K bands are available at four epochs after maximum light (Krisciunas et al., 2000). The NIR luminosity in the range 10,000–24,000 Å is computed following a procedure analogous to that used for the optical bands. The flux outside the observed J and K ranges is extrapolated using flat power laws. The combined optical and NIR luminosities (3000–24,000 Å) at these epochs are shown in Fig. 4.16 as red circles. No ultraviolet (UV) observations are available for SN 1999aa, and therefore the flux contribution at wavelengths shorter than the Bessell U band ($\lambda < 3000$ Å) is not included. This omission is expected to have a significant impact only at the earliest epochs, when the UV contribution is more substantial (see below).

No UV observations are available for SN 1999aa, so we cannot account for flux at wavelengths shorter than the Bessell U filter ($\lambda < 3000$ Å). The UV should make a significant contribution only at the earliest epochs (see below).

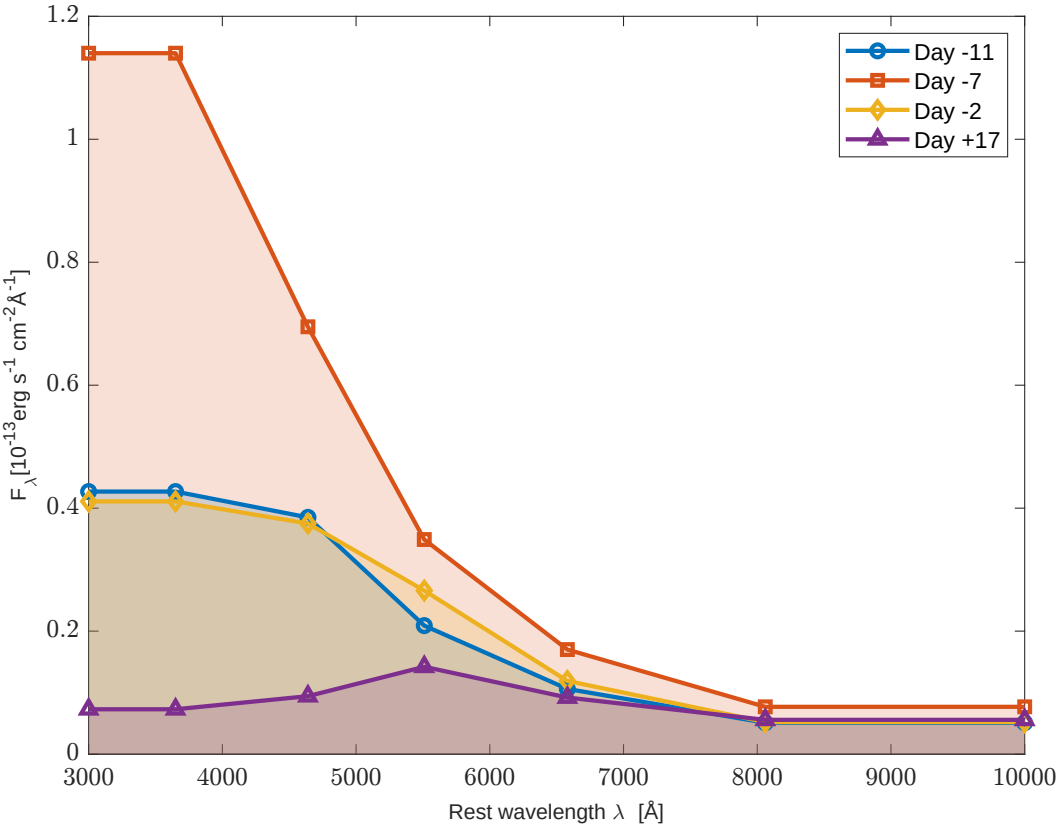


FIGURE 4.15: Spectral energy distributions (SEDs) of SN 1999aa at four epochs (days −11, −7, −2, and +17 relative to B-band maximum), constructed from $UBVRI$ photometry. The shaded regions indicate the contribution of each wavelength interval to the pseudo-bolometric flux over the range 3000–10,000 Å.

4.7.2 Modelling the bolometric light curve

An independent test of the derived abundance distribution is provided by the bolometric light curve. Synthetic light curves are computed using the density and abundance distributions of the three models tested, with a Monte Carlo code that follows the emission and deposition of gamma-rays and positrons, as in the nebular spectrum calculations. The deposited energy is assumed to be converted into optical photons, which are then transported through the ejecta using a time-dependent Monte Carlo scheme (Mazzali et al., 2001a). Photon propagation is governed by opacity, which in SNe Ia is dominated by line transitions (Pauldrach et al., 1996), parameterised based on the number of active lines per species and their relative abundances in the ejecta (Mazzali et al., 2001a). Photon diffusion is further sensitive to the ejecta mass and its expansion velocity, and thus to the kinetic energy $E_{\rm k}$.

Synthetic bolometric light curves are computed for the three explosion models and compared to the observed bolometric light curve of SN 1999aa in Fig. 4.16. All three models

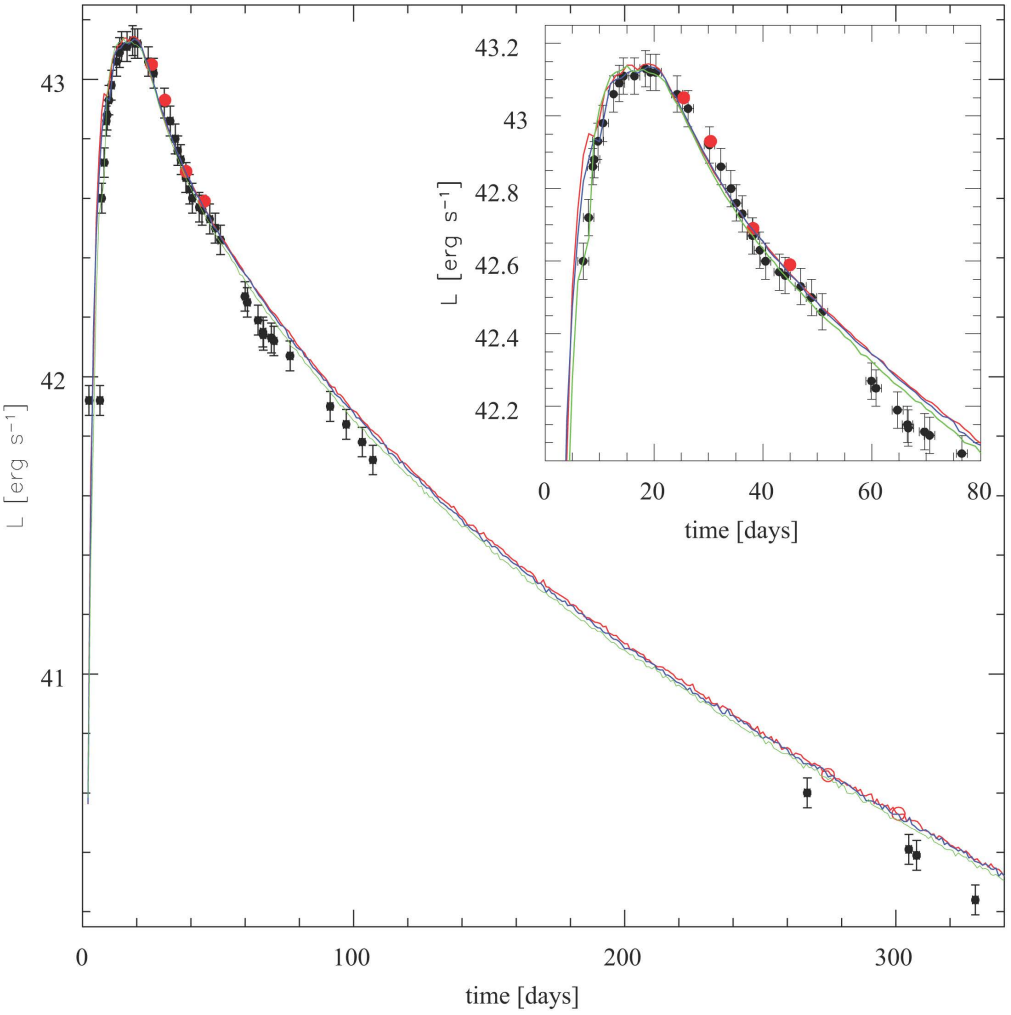


FIGURE 4.16: The $UBVRI$ bolometric light curve of SN 1999aa (black dots), compared to the synthetic light curves computed using the density and abundance profiles of the three explosion models: W7 (red), DD2 (green), and DD3 (blue). Red points represent luminosities at the epochs when NIR observations are available from Krisciunas et al. (2000)

.

provide a reasonable match to the observations, suggesting that the adopted density structures and derived abundances are physically credible. However, a unique best-fitting model cannot be identified. Although DD2 yields the closest ^{56}Ni mass to the value derived for SN 1999aa, the correspondence between the derived elemental masses and those of the original hydrodynamic models is not always consistent. The absence of early UV data further limits the constraints on the outer-layer densities. It is concluded that DD2 represents a reasonable approximation, though some modification would be required. A dedicated model tailored to SN 1999aa may ultimately be needed, likely similar to DD2 but differing in certain regions, as was found for SN 2011fe (Mazzali et al., 2014, 2015).

4.8 Conclusions

- **Model Consistency and Kinetic Energy**. Reasonably good fits to the observed spectra are obtained for all three investigated density profiles, with only minor variations between them. For instance, the Si II 6355 Å feature, the O I 7744 Å line, and the Fe II complex near 5,000 Å are more accurately reproduced by the DD2 and DD3 profiles than by the standard W7 model. However, these improvements are marginal, making it difficult to select a definitive best-fit model based on spectral morphology alone. From the elemental yields summarized in Table 3, the expected kinetic energy yield (E_k) for each model was calculated using the following relation:

$$E_K = \left[1.56\, M(^{56}\mathrm{Ni}) + 1.47\, M(\mathrm{Fe}) + 1.24\, M(\mathrm{IME}) - E_{\mathrm{bind}}\right] \times 10^{51}\ \mathrm{erg} \qquad (4.1)$$

  where $E_{\mathrm{bind}} = 0.46 \times 10^{51}$ erg, represents the binding energy of the white dwarf (Woosley et al., 2007b). The resulting values are slightly lower than those predicted by the original theoretical models. This discrepancy is attributed to suppressed burning in the outermost shells, a behaviour previously identified in SN 1991T (Sasdelli et al., 2014).

- **Non-reliability of the WLR for SN 1999aa** Although SN 1999aa is less luminous than SN 1991T, consistent with a synthesized ^{56}Ni mass of $\sim 0.65\, M_{\odot}$ compared to $\sim 0.78\, M_{\odot}$, it exhibits a slower decline rate. Specifically, $\Delta m_{15}(B)$ values for SN 1999aa range from 0.75 to 0.85 mag, whereas SN 1991T declines at 0.94 mag. A standard application of the luminosity-width relation (WLR) would therefore incorrectly imply that SN 1999aa is the more luminous event. A Comparison of the bolometric light curves is presented in Fig. 4.17: while SN 1991T remains brighter throughout, its peak occurs significantly earlier. This is caused by the higher abundance of ^{56}Ni in the outer layers of SN 1991T, which drives a

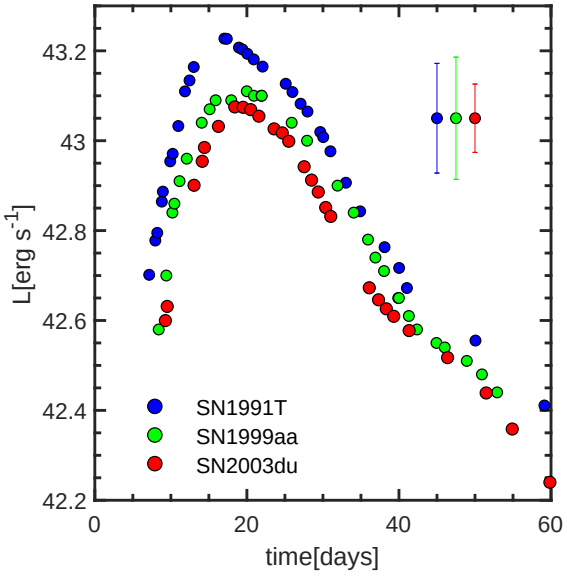


FIGURE 4.17: The bolometric light curve of SN 1999aa (green) compared to those of SN 1991T (Sasdelli et al., 2014, blue) and SN 2003du (Stanishev et al., 2007, red). The UV contribution was removed from the light curve of SN 2003du to allow a proper comparison, as no UV information is available for the other two SNe. Error bars for SN 1999aa and SN 1991T represent statistical errors due to distance moduli uncertainties $\delta\mu$, to the host galaxies using the Tully-Fisher relation: $\delta\mu$[99aa]=0.34, $\delta\mu$[91T]= 0.30. The error bar for SN 2003du is calculated taking $\delta\mu$[03du]=0.19 (Stanishev et al., 2007)
.

faster rise to a more luminous maximum. Consequently, relying solely on $\Delta m_{15}(B)$ as a luminosity indicator is shown to be misleading for the SN 1991T-like class, a discrepancy previously noted in literature for both the bright and faint ends of the SN Ia population (Ashall et al., 2018, Pinto & Eastman, 2000, Scalzo et al., 2012, Woosley et al., 2007b). This unreliability is further highlighted by SN 2003du ($\Delta m_{15}(B) = 1.13$ mag), which reaches a nearly identical peak luminosity to SN 1999aa despite the difference in decline rates.

- **Depletion of silicon in the outer layers** The abundance distributions of SN 1999aa and SN 1991T are compared with those of spectroscopically normal SNe Ia (SN 2002bo, SN 2003du, SN 2004eo) in Fig. 4.18. This comparison is particularly meaningful as the abundance stratification of all these objects was derived using the same method and the same density profiles, making the results directly comparable. In SN 1999aa, IMEs are confined to a narrow velocity range, peaking near 11,000,km s^{-1} before declining abruptly, leaving the layers above $v \approx$ 12,000,km s^{-1} depleted of silicon and dominated by oxygen. This abundance structure closely resembles that of SN 1991T but differs markedly from normal

SNe Ia, in which silicon- and sulphur-rich layers extend to significantly higher velocities. The weakness of the Si II and S II features in the earliest spectra of 91T-like events therefore reflects a genuine deficiency of IMEs in the outer ejecta rather than a temperature or ionization effect. Consequently, the spectroscopic transition from normal to 91T-like events cannot be explained solely by a temperature sequence, but instead requires fundamental differences in the abundance structure and, by implication, the explosion mechanism (Mazzali et al., 1995). This result is further tested by computing synthetic models for SN 1999aa with progressively increasing Si fractions at $v \approx 12600\,\mathrm{km\ s^{-1}}$ while keeping L_{Bol} and v_{ph} fixed. The observed Si II λ6355 line is reproduced with $X(\mathrm{Si}) \approx 0.025$, whereas the Si abundance has to be increased by a factor of four to produce an absorption feature comparable to that observed in the normal SN 2003du (Fig. 4.19).

- **The Path from SN 1999aa to SN 1991T: A Temperature Sequence.** While the transition from normal to 91T-like supernovae requires a fundamental change in the outer-shell IME abundance distribution, as discussed in the previous paragraph, reflecting a different explosion mechanism, the spectroscopic difference between SN 1999aa and SN 1991T is accounted for solely by differences in temperature. Synthetic spectra computed at day −11 show that increasing the luminosity of the SN 1999aa model, without altering its composition, produces a spectrum that closely resembles that (Fig. 4.20). The higher ionisation weakens Si II λ6355 and Ca II H&K while driving the emergence of Fe III features near 3200, 3500, 4200, and 4900 Å. Variations within the 91T-like class therefore appear to be a direct consequence of luminosity-driven ionisation rather than differences in the explosion structure, and this result provides an independent argument that SN 1999aa is intrinsically less luminous than SN 1991T.

- **Theoretical Constraints on Progenitor Models:** Because SNe Ia converge toward nearly identical properties post-maximum, a viable progenitor scenario that can explain the complete spectroscopic sequence must be one that allows for variations only in the outer layers. The abrupt depletion of IMEs in the outer shells of SN 1999aa remains difficult to reconcile with conventional delayed-detonation models (Iwamoto et al., 1999, Khokhlov, 1991b), pointing instead toward an explosion that proceeds efficiently before suddenly stopping, leaving a weakly burned outer layer. The Pulsation-Driven Detonation (PDD) scenario (Baron et al., 2008a, Hoeflich et al., 1995, Hoflich et al., 1995, Ivanova et al., 1974) remains a candidate of interest, as the pre-expansion of a white dwarf creates the steep density gradients required to confine IMEs to a narrow velocity range. Nevertheless, inconsistencies remain; PDD models predict unburned carbon and early-time IME lines that are not observed in SN 1999aa or SN 1991T (Baron et al., 2008b), and 3D simulations

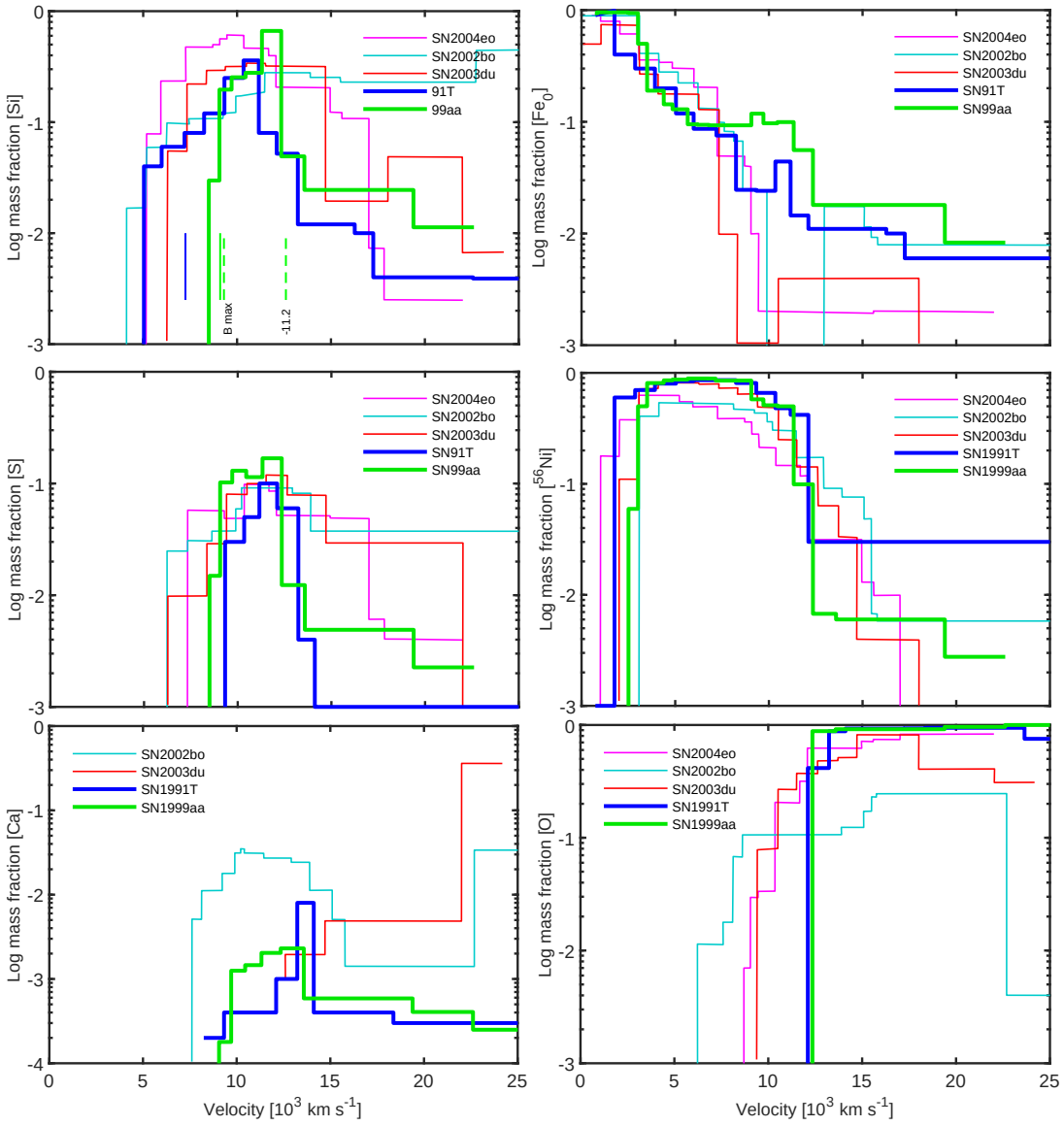


FIGURE 4.18: Elemental distribution in SN 99aa, SN 1991T, and spectroscopically normal SNe Ia. Left: Si, S, and Ca (top to bottom). Right: stable Fe, ^{56}Ni, and O (top to bottom). SNe 1999aa and 1991T exhibit similar stratification: ^{56}Ni dominates the inner layers (2000–10,000,km s^{-1}), while a narrow IME shell peaks near 11,000,km s^{-1} and terminates above $\sim 12,000$,km s^{-1}. The higher oxygen abundance in the outer layers reflects less complete burning in these regions. In the first panel, dashed lines indicate $v_{\rm ph}$ at day -11.2 and B maximum. Continuous lines mark $v_{\rm ph}$ at the onset of Fe II lines for SN 1999aa (green) and SN 1991T (blue).

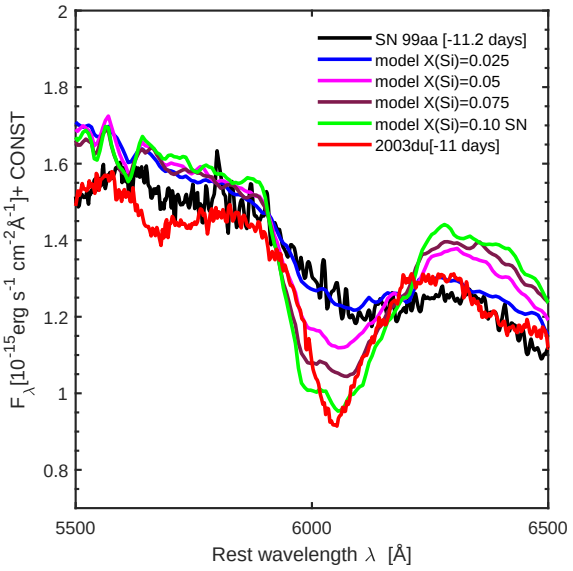


FIGURE 4.19: The effect of changing the Si abundance in the outermost layers.

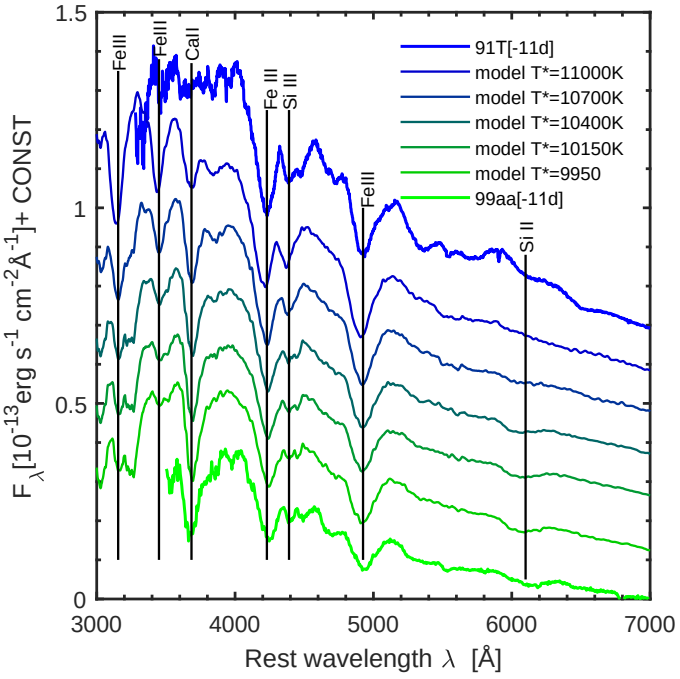


FIGURE 4.20: Early-time spectra of SNe 1999aa and 1991T compared to synthetic spectra computed for increasing luminosity but the same composition. As the luminosity increases the spectra morph from looking like SN 1999aa to looking like SN 1991T.

show IME lines at very early times and suggest mixing levels that are not consistent with observed stratification seen in SN 1999aa (Bravo & García-Senz, 2009, Bravo et al., 2009, Dessart et al., 2014, Kasen & Plewa, 2005, Plewa et al., 2004).

While no current model perfectly captures the full range of SN Ia spectroscopic diversity, the pulsation-driven framework remains a compelling candidate for the 91T-class. Its primary advantage is that it specifically modifies the structure of the outer ejecta, matching the observed peculiarities of these events. The available evidence suggests this scenario may be triggered only in cases of high ^{56}Ni production.

Chapter 5

iPTF16abc

5.1 Motivation

iPTF16abc (SN 2016bln) occupies a particularly interesting position within the spectroscopic diversity of Type Ia supernovae. Although it is generally classified as a 91T-like event, based on its weak Si II λ6355 absorption, smooth continuum redward of 6000Å, slow decline rate, and high peak luminosity, it exhibits several properties that are atypical of this subclass and suggest a more complex ejecta structure.

Like SN 1991T, iPTF16abc is a luminous, slowly declining SN Ia with a comparable value of $\Delta m_{15}(B)$. However, the characteristic Fe III absorptions near 4250 and 5000 Å, which are usually prominent in 91T-like events and are commonly associated with high temperatures and extensive iron-group material in the outer ejecta, remain surprisingly weak. This points to significant differences either in the ionisation state or the abundance structure of the outer layers, or both.

An even more remarkable feature is the presence of strong C II $\lambda\lambda$6578,6583 absorption at early times. Carbon signatures trace unburned material and are only occasionally detected in SNe Ia (Parrent et al., 2011, Silverman & Filippenko, 2012). Their presence is particularly unexpected in 91T-like objects, having been reported within this subclass only in SN 2023wrk (Liu et al., 2024). The temporal evolution of the feature is also unusual: the carbon absorption weakens before maximum light and subsequently reappears.

Further evidence of the peculiar nature of iPTF16abc is provided by its Ca II H&K high-velocity feature, which splits into two narrow absorptions, similar to SN 1991T, but deeper; yet they fall short of the strength seen in normal SNe Ia, where the two components typically blend into a single deep feature.

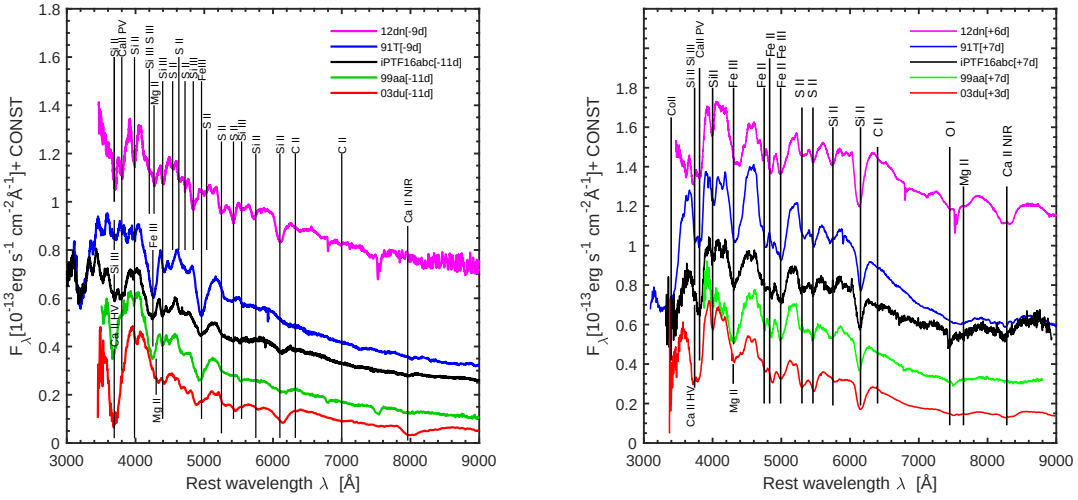


FIGURE 5.1: Comparison of iPTF16abc spectra with SN 1991T, SN 1999aa, the normal SN 2003du, and the 03fg-like SN 2012dn at early times (left) and one week post-maximum (right). All epochs are shown relative to B maximum light.

Several of these properties, most notably the weak Fe III lines and the persistence of carbon signatures, more closely resemble those of 03fg-like events than of the 91T-like subclass (Ashall et al., 2021), placing iPTF16abc at the intersection of these two spectroscopic classes. Despite these peculiarities, however, its spectra evolve rapidly and become nearly indistinguishable from those of normal SNe Ia within about one week of maximum light. This behaviour highlights the dominant role played by the outermost ejecta in shaping spectroscopic diversity and makes iPTF16abc a valuable object for investigating the physical origin of that diversity. This is highlighted by the spectral comparison at early and maximum epochs shown in Fig. 5.1.

The work presented here was published in Aouad et al. (2024). The photospheric-phase spectral modelling, abundance tomography, and construction of the observed bolometric light curve were carried out by the Charles J.Aouad, while the nebular spectral modelling and bolometric light-curve model were performed by Paolo Mazzali.

5.2 Data

iPTF16abc (SN 2016bln) was discovered by the intermediate Palomar Transient Factory on April 4, 2016 (JD 2457482.89; Gal-Yam 2016). The supernova occurred in the tidal tail of the barred spiral galaxy NGC 5221 (type SABb), at a redshift of $z = 0.023279$ (Courtois & Tully, 2015). Distance estimates to the host galaxy based on the Tully–Fisher relation span a range of distance moduli between $\mu \approx 34.69$ and 35.09 mag (Karachentsev et al., 2006, Makarov et al., 2014, Willick et al., 1997). In this work,

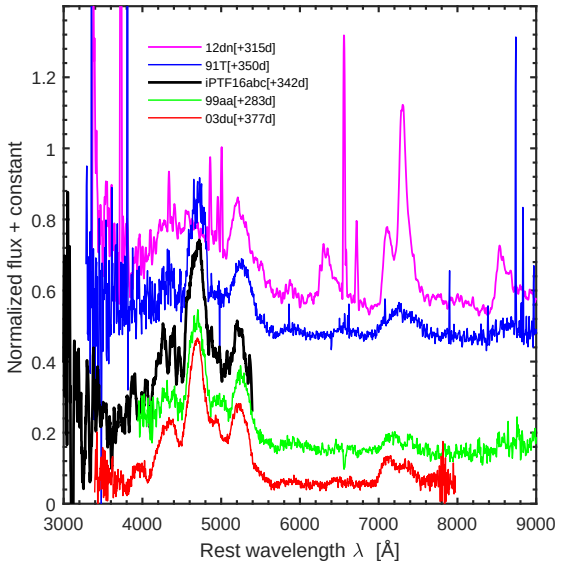


FIGURE 5.2: Nebular spectrum of iPTF16abc in comparison with SN 1991T, SN 1999aa, the normal SN 2003du and the 03-fg-like SN 2012dn. Epochs are shown with reference to B maximum.

a Galactic reddening of $E(B-V) = 0.05$ is adopted (Ferretti et al., 2017), together with a host-galaxy contribution of $E(B-V) = 0.03$ (Miller et al., 2018, Schlafly & Finkbeiner, 2011). Early-time photometric observations in the U, B, V, r, and i bands are taken from Miller et al. (2018), while late-time g-band data, along with a measured $\Delta m_{15}(B) = 0.91$ mag, are adopted from Dhawan et al. (2018). The epoch of B-band maximum is assumed to be MJD 57499.54, consistent with previous studies. A sequence of optical spectra covering the photospheric phase was obtained using multiple telescopes and instruments (see Table 5.1). In addition, a nebular-phase spectrum at +342 days relative to B-band maximum was presented by Dhawan et al. (2018). The spectra were flux-calibrated using the same methodology described in section 4.3.1. A summary of the spectroscopic data used in this work is provided in Table 5.1.

5.3 The photospheric phase

Eight spectra, collected from 15 days before to 8 days after B-band maximum, were modeled. Three density profiles were employed: the fast-deflagration model, W7 and two delayed detonation models (DD2 and DD3; Iwamoto et al. 1999, Nomoto et al. 1984). In addition a modified density profile based on the DD2 was developed (see Section 5.4). These profiles are illustrated in Fig. 5.3. W7, DD2, and DD3 have been successfully used and were able to reproduce major spectroscopic features and light curves across both photospheric and nebular phases. Using a common density profile across

TABLE 5.1: Spectra of SN iPTF16abc and modelling parameters.

UT Date 2016	JD[a]	Epoch[b] (days)	Telescope/Instr.	$\log L$ [$L_\odot$]	v (km s^{-1})	$T_{\rm ph}$ (K)
05/04[c]	483.3	−15.3	Gemini-N / GMOS	8.860	13,450	15900
10/04[c]	488.4	−11.0	Keck-I / LRIS	9.370	12,200	14670
11/04[c]	489.5	−9.8	LCO-2m / FLOYDS	9.470	12,000	14935
12/04[c]	490.4	−8.9	LCO-2m / FLOYDS	9.550	11,800	14832
13/04[c]	491.5	−7.8	LCO-2m / FLOYDS	9.580	11,200	15330
25/04[c]	503.3	+3.7	LCO-2m / FLOYDS	9.620	10,000	10187
28/04[c]	506.0	+6.3	NOT / ALFOSC	9.610	9,200	10040
30/04[c]	508.3	+8.5	LCO-2m / FLOYDS	9.520	7,500	9682
29/03/2017[c]	841.7	+342.4	Keck-I / LRIS			

[a] JD−2,457,000
[b] Rest-frame time since B maximum
[c] See Dhawan et al. (2018)

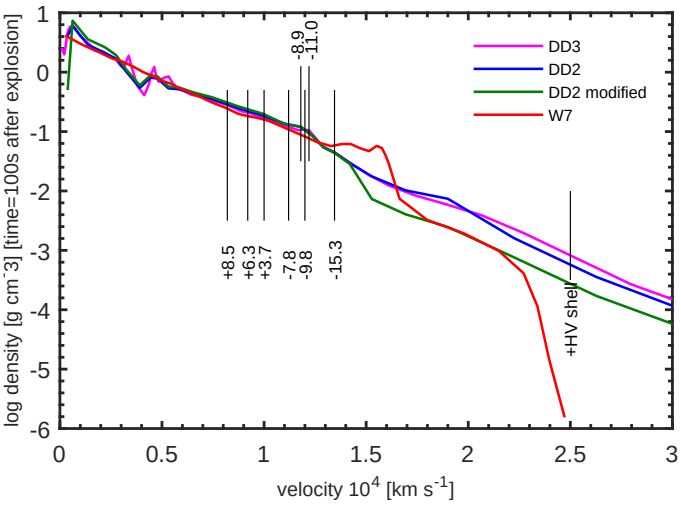


FIGURE 5.3: Density profiles used in the modeling process: W7 (Nomoto et al., 1984), DD2, DD3 (Iwamoto et al., 1999), and the modified DD2. In the modified DD2, a mass of 0.05 $M_\odot$ has been removed at $v > 14{,}000$ km s^{-1}and redistributed in the inner layers to conserve the total mass. The total kinetic energy is not significantly changed due to the small mass shift. Vertical dashed lines mark the photospheres of the synthetic spectra.

multiple supernovae ensures a consistent comparative framework, enabling a more reliable interpretation of spectroscopic diversity. This approach forms a central methodological pillar of abundance tomography studies (Aouad et al., 2022, Ashall et al., 2016, 2018, Mazzali et al., 2008, Stehle et al., 2005, Tanaka et al., 2011), including the analyses presented in this thesis.

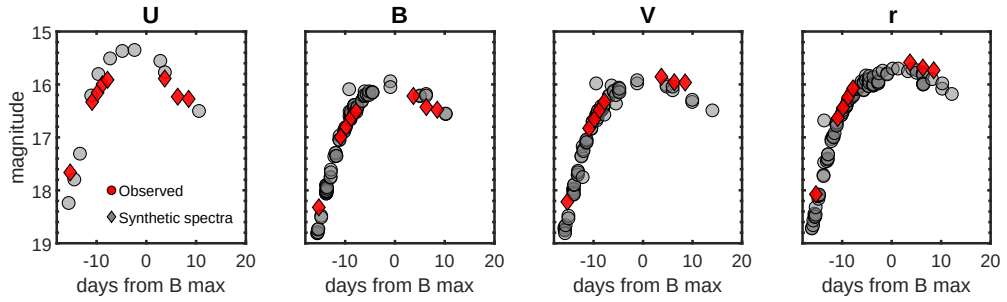


FIGURE 5.4: Observed light curves of iPTF16abc compared with synthetic light curves derived from the models. Photometric data are taken from Miller et al. (2018).

5.3.1 The pre-maximum spectra

Synthetic spectra from day −15 to day −8 are displayed in Figs. 5.5, 5.6 and 5.7, overlaid on the observational data. A high degree of fidelity is maintained across the entire wavelength range, with the synthetic models accurately replicating the observed flux. This agreement is further confirmed by the excellent match between the synthetic and observed photometric light curves shown in Fig. 5.4.

Between day −15 and day −11, the luminosity increases rapidly and is accompanied by only a modest decrease in photospheric velocity. Through the Stefan–Boltzmann relation (Sect. 3.3), the resulting small photospheric radius yields the high temperatures required to reproduce the observed ionization state of the ejecta.

Fe-group elements: In the earliest spectrum of iPTF16abc obtained at day −15, Fe III features are identified near 4250 and 5000 Å. The feature near 4250 is dominated by a blend of Fe III $\lambda\lambda$ 4420, 4431, 4396 and Co III λ 4433. The feature near 5000Å is dominated by a blend of Fe III $\lambda\lambda$5156, 5217, 5073, 5086, 5193, 5063. These lines are replicated in the models using $X(\mathrm{Fe}) = 0.0035$ at $v > 13,450$ km s^{-1}. This exceeds the solar value ($X(\mathrm{Fe}_\odot) = 0.001$; Asplund et al. 2009). By day −11, these features gain in strength, necessitating an increase in the iron mass fraction to 0.025 at $v > 12,200$ km s^{-1} (see Fig. 5.8). The Fe III absorptions are significantly weaker than those observed in SN 1991T and SN 1999aa. Correspondingly, a lower iron abundance is inferred in the outer ejecta of iPTF16abc, suggesting that the weaker Fe III features are primarily driven by a reduced iron content rather than by differences in temperature alone. At this early phase, the iron is stable (specifically ^{54}Fe), as it could not have been produced by the decay of ^{56}Ni so soon after the explosion. Notably, iron is present at $v > 25{,}000$ km s^{-1}, a feature not predicted by current explosion models.

The strength of these iron lines continues to increase through day −10 and the following epochs. The iron mass fraction rises gradually, reaching 0.038 at $v > 11,200$ km/s. At

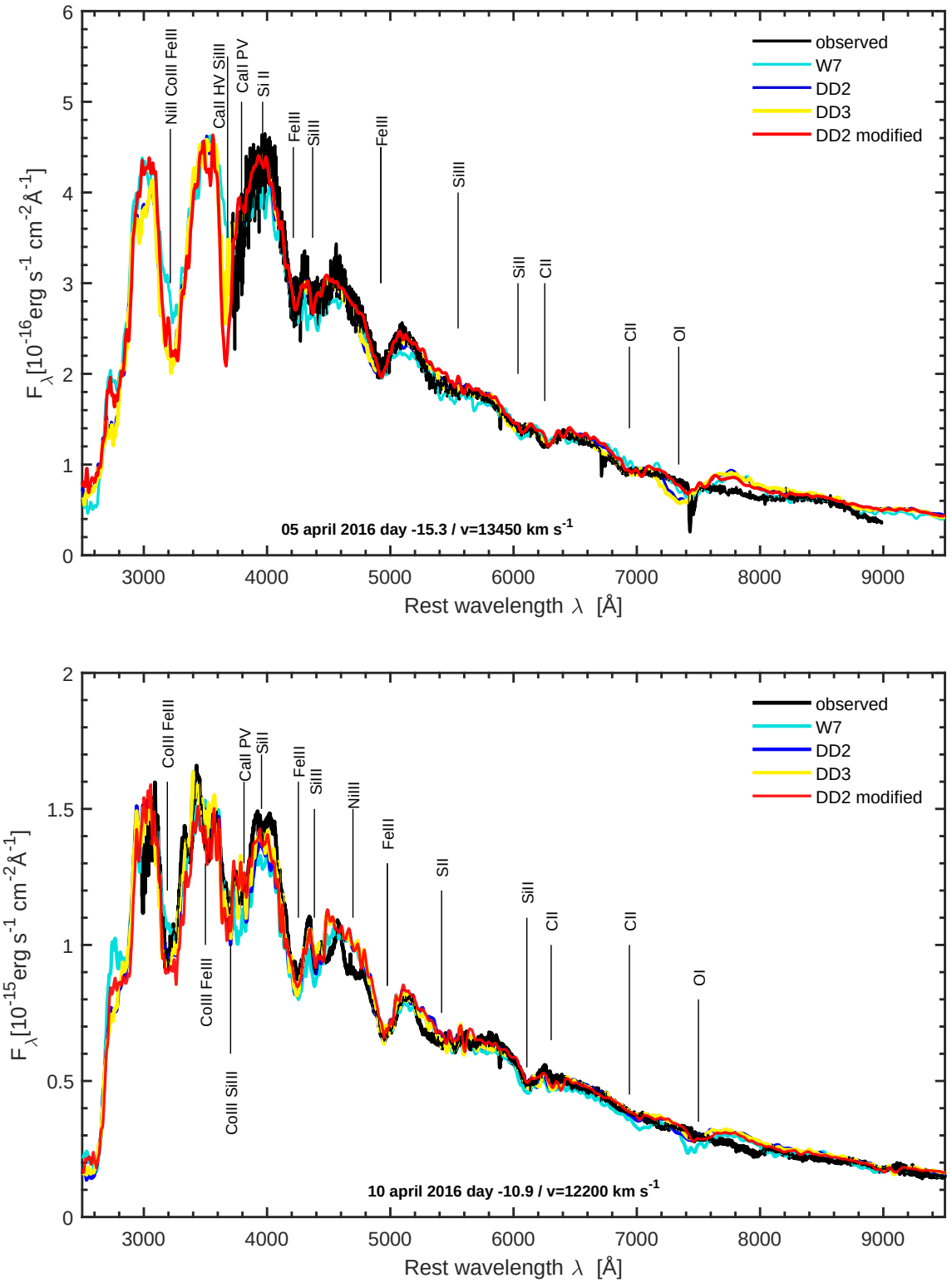


FIGURE 5.5: Observed early spectra of iPTF16abc (black), compared to synthetic spectra (colours) corresponding to different density profiles as indicated in the legend. Epochs are shown with reference to B maximum.

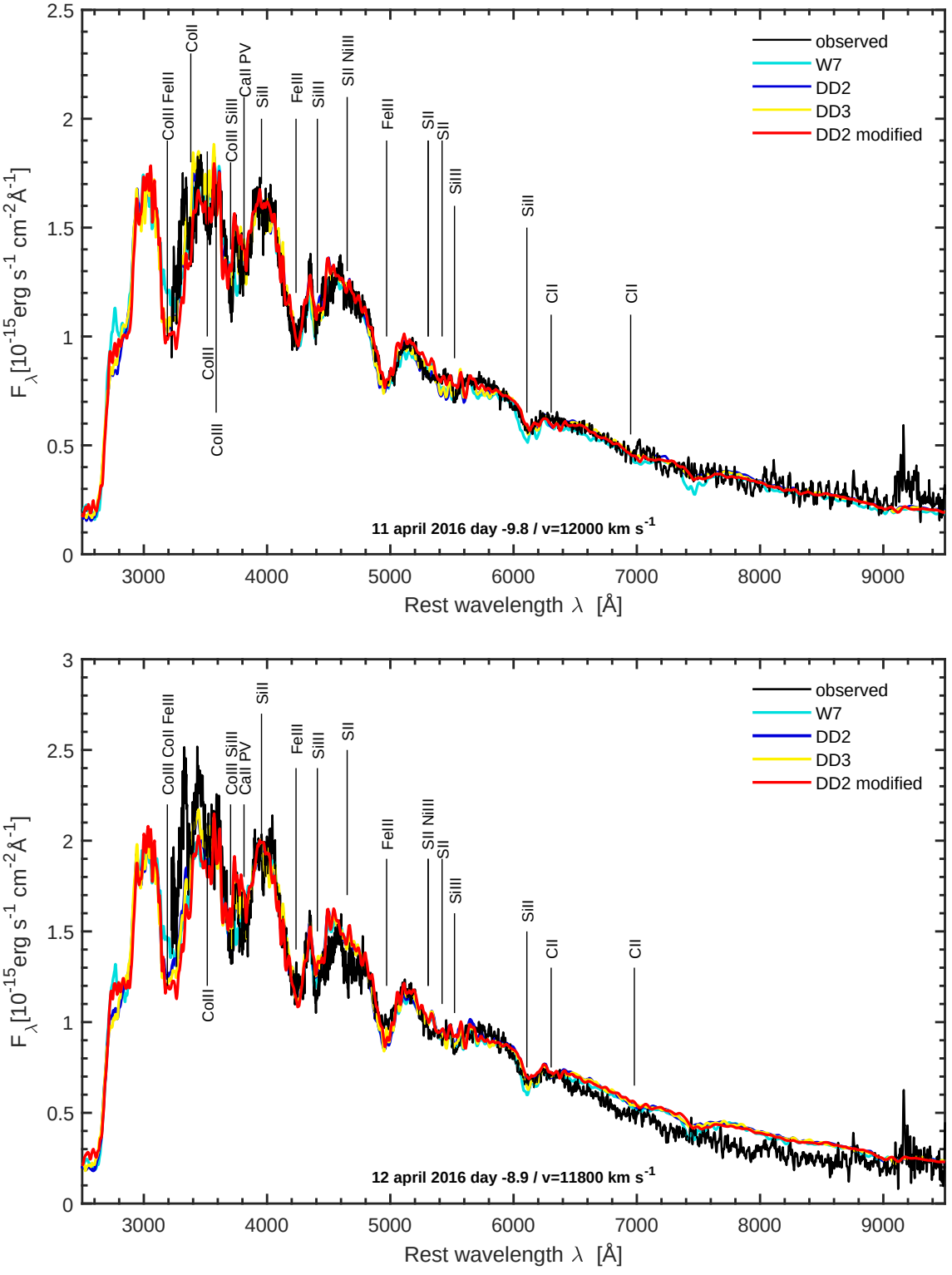


FIGURE 5.6: Observed early spectra of iPTF16abc (black) compared to synthetic spectra (colours) corresponding to different density profiles as indicated in the legend. Epochs are shown with reference to B maximum.

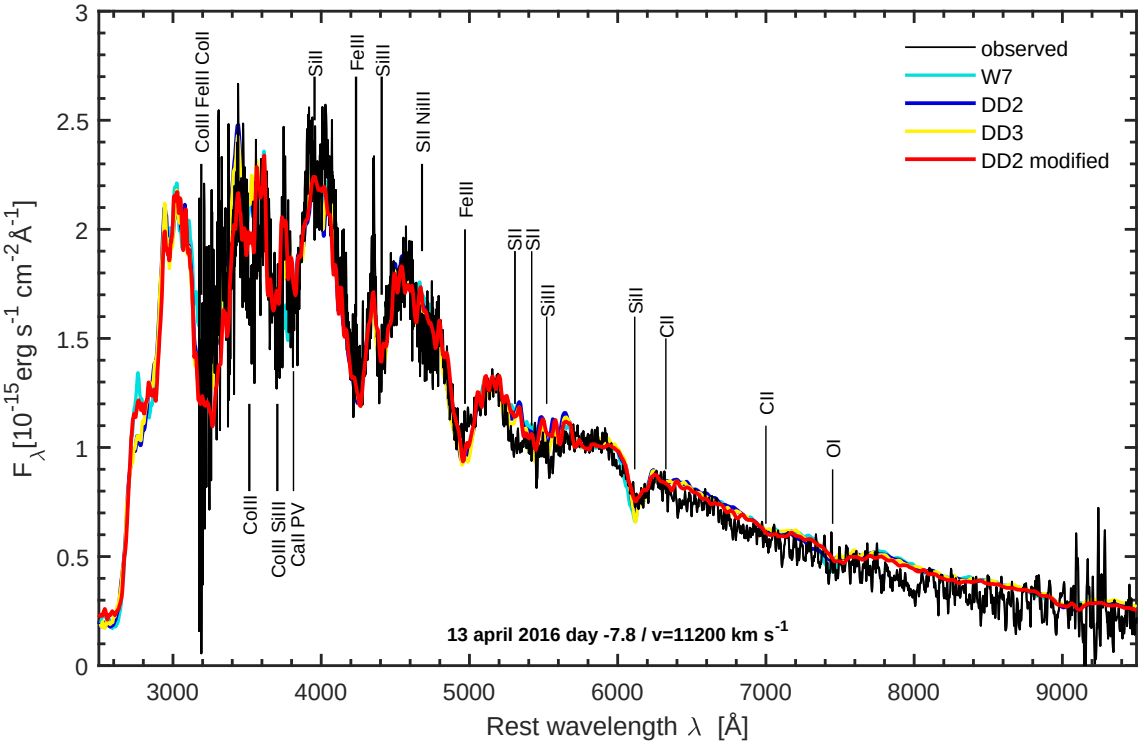


FIGURE 5.7: Observed day −8 spectrum of iPTF16abc (black), compared to the synthetic spectra in colours, corresponding to different density profiles as indicated in the legend. Epoch is shown with reference to B maximum.

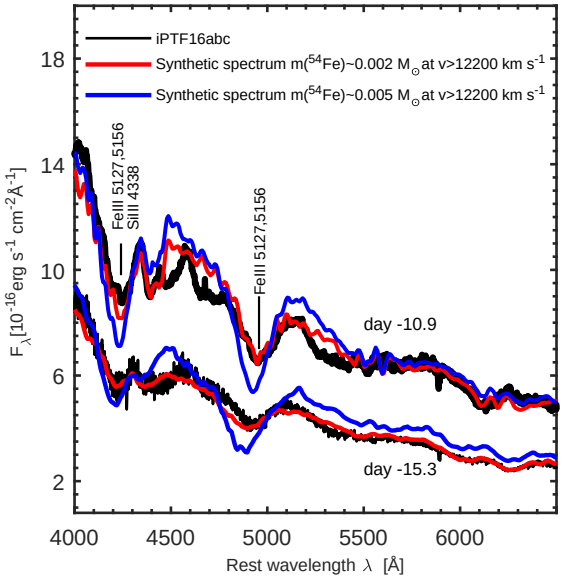


FIGURE 5.8: Comparison of synthetic spectra illustrating the effect of the outer iron abundance in iPTF16abc. The blue spectra correspond to a model with an outer iron abundance similar to that of SN 1999aa, while the red spectra show the preferred model for iPTF16abc. Notably, despite the outermost shells of iPTF16abc exhibiting super-solar abundances, its iron content in these layers remains lower than that of both SNe 1999aa and 1991T. Epochs Epochs are given relative to B-band maximum.

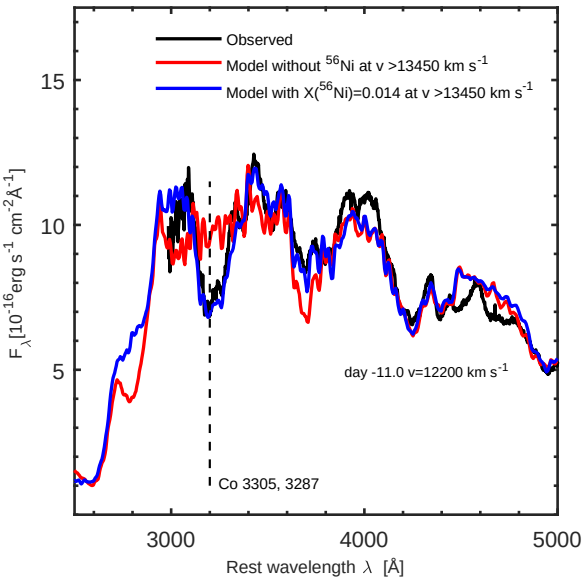


FIGURE 5.9: Comparison of synthetic spectra illustrating the effect of the outer ^{56}Ni abundance in iPTF16abc. A ^{56}Ni mass fraction of 0.014 is required at the outermost shell at $v > 13{,}450$ km s^{-1}to replicate the Co III $\lambda\lambda$ 3287, 3305 line observed near 3200 Å . Epoch is shown with reference to B maximum
.

this stage, stable iron constitutes roughly 50 percent of the total iron required for the fit, with the remaining half provided by the decay of ^{56}Ni. Fortunately, the day -10 spectrum of iPTF16abc extends down to 3000 Å, covering the wavelength region around 3200 Å where the prominent Co III $\lambda\lambda$3287,3305 feature is expected.. This provides a direct probe of the ^{56}Ni abundance in the outer ejecta. Consequently, a ^{56}Ni mass fraction of 0.013 is inferred for $v > 13,450$ km s^{-1} (Fig. 5.9). At lower velocities, the ^{56}Ni mass fraction increases, reaching 0.69 at $v > 11,200$ km s^{-1}, slightly exceeding the values inferred for SNe 1999aa and 1991T at comparable epochs. A feature around 4700 Å, dominated by blends of Ni III and S II lines, is likewise reproduced in the synthetic spectra. Unfortunately, a comparison with SNe 1999aa and 1991T at day -15 is not possible due to the lack of observations at such early phases.

Calcium: In most SNe Ia, the absorption feature near 3800 Å is commonly interpreted as a combination of photospheric-velocity (PV) and high-velocity (HV) Ca II H&K ($\lambda\lambda$3934,3968), with the HV component often dominating in spectroscopically normal events. In iPTF16abc, however, the origin of this feature is fundamentally different. Although a similar absorption is present, it is split into two distinct components, the bluer of which is not primarily produced by Ca II but instead by a blend of Si III $\lambda\lambda$3796, 3806 and Co III λ3782. The high temperatures in the outer ejecta both suppress the contribution of Ca II and favour the presence of doubly ionized species such as Si III and Co III, preventing the blue component from being shaped by Ca II as it is in normal SNe Ia.

As shown in Fig. 5.10, removing calcium from the high-velocity layers ($X(\mathrm{Ca}) = 0$ for $v > 13{,}450$,km s^{-1}) produces virtually no change in the blue component of the feature, demonstrating that high-velocity calcium contributes little to its formation. This highlights the dominant role of ionization effects in shaping the feature and cautions against attributing it to Ca II without detailed modelling.

The derived calcium abundance is 5.5×10^{-4} at $v > 25{,}000$ km s^{-1}, exceeding the Solar value ($X(\mathrm{Ca})_\odot = 6 \times 10^{-5}$; Asplund et al., 2009). This fraction decreases to 2×10^{-4} at $v > 13{,}450$ km s^{-1}, before increasing to 10^{-2} at $v > 12{,}200$ km s^{-1} and remaining approximately constant down to $v > 11{,}800$ km s^{-1}. The enhanced calcium abundance at lower velocities is required to reproduce the PV component, which is accurately matched by the synthetic spectra. The blue component, however, remains primarily shaped by Co III and Si III.

At $v = 11{,}800$ km s^{-1}, a calcium mass fraction of 5×10^{-3} is sufficient to reproduce the spectra. These values are consistent with those inferred for SNe 1999aa and SNe 1991T, but remain significantly lower than those derived for spectroscopically normal events (Tanaka et al., 2008, 2011).

The near-infrared Ca II feature, commonly present in normal SNe Ia, is absent in the early spectra of iPTF16abc and emerges only a few days after maximum light. This delayed appearance is consistent with the behaviour observed in SNe 1999aa and SNe 1991T and is well reproduced by the synthetic spectra.

Silicon, Sulphur, Magnesium: The Si II λ 6355 feature is very weak at -15 days, a characteristic hallmark of the 91T-like subclass to which iPTF16abc belongs. It strengthens slightly by -11 to -10 days, resembling the behaviour of SN 1999aa at similar epochs. In contrast, the Si III λ 4560 feature is strong and increases in intensity as the spectra evolve, reflecting the high temperatures of the ejecta.

The silicon abundance is constrained through an iterative modelling procedure in which different compositions are tested until the synthetic spectra best reproduce the observed Si II and Si III features, as illustrated in Fig. 5.11.

This procedure yields a silicon mass fraction of 0.013 at $v > 13{,}450$ km s^{-1} at -15 days, significantly lower than that required for normal events such as SN 2003du, which demands nearly 30 times more silicon at similar epochs (Tanaka et al., 2011). The silicon abundance increases sharply to 0.47 at $v > 12{,}200$ km s^{-1}, before gradually decreasing toward lower velocities. The accurate reproduction of the relative strengths of Si II and Si III lines in the synthetic spectra indicates that the ionization balance—and thus the temperature structure—is well captured by the models.

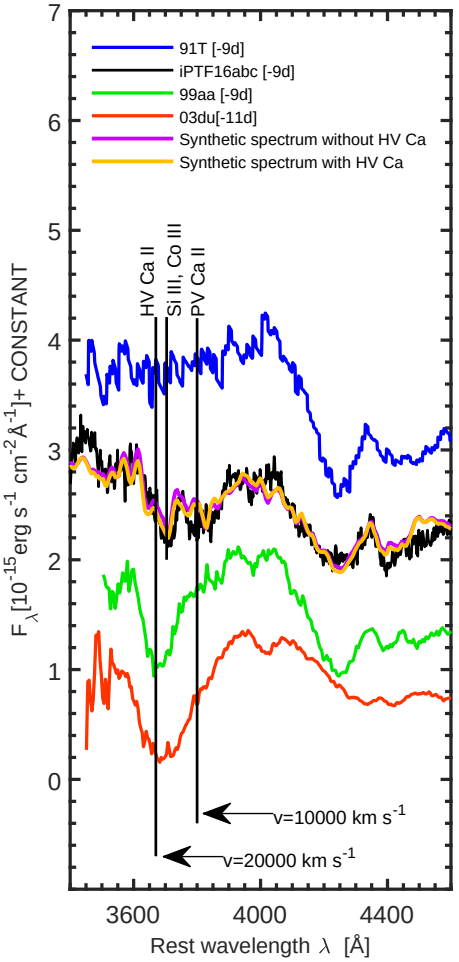


FIGURE 5.10: Detail of the spectral region around ~ 3700 Å. The preferred model for iPTF16abc is compared with a model excluding high-velocity Ca II, demonstrating the limited contribution of HV Ca II to the blue component. Spectra of SNe 1999aa and 2003du are included for comparison. Epochs are given in square brackets relative to B-band maximum.

The S II $\lambda\lambda$5468,5654 doublet, responsible for the characteristic "W" feature, first appears around day -10 and is initially weak, becoming progressively more prominent after maximum light. This contrasts with normal SNe Ia, such as SN 2011fe and SN 2003du, where these features are already well developed at early times, requiring higher sulphur abundances at similar velocities. The depletion of intermediate-mass elements in the velocity range of $\sim$12,000–13,000 km s^{-1} is consistent with that observed in SN 1999aa and SN 1991T, and differs from the behaviour of spectroscopically normal SNe Ia (Aouad et al., 2022).

The Mg II λ4481 feature is weak in iPTF16abc, as expected for a 91T-like event, with the region instead dominated by Fe III owing to the high temperatures. A magnesium mass fraction of 0.01 is required at $v > 13{,}450$ km s^{-1}.

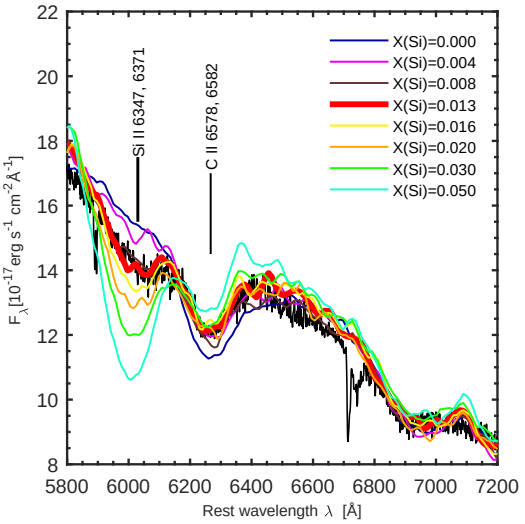


FIGURE 5.11: Probing silicon in the outer layers. The optimal replication of the Si II λ 6355 absorption line observed at on day -15 is attained with a silicon mass fraction of 0.013 at $v > 13,450$ km s^{-1}. In the corresponding figures, the observed spectrum is represented in black, while models featuring varying silicon mass fractions are depicted in different colours as specified in the legend.

Carbon, Oxygen: What makes iPTF16abc even more unusual is the presence of carbon in its early spectra, detected through the C II λ6580 and C II λ7234 features. Even more remarkably, these absorptions do not simply fade with time as expected. Since unburned carbon is generally confined to the outermost ejecta layers, its signatures are normally expected to weaken and disappear as the photosphere recedes inward. Instead, after weakening toward maximum light, the carbon features re-emerge at day +3.7 and become more pronounced by day +8.

Carbon signatures are only rarely detected in SNe Ia (Folatelli et al., 2012, Parrent et al., 2011), and remain particularly uncommon among 91T-like events. While previous abundance tomography studies of SN 1991T and SN 1999aa yielded only upper limits of 5×10^{-4} and 5×10^{-3}, respectively, in the velocity range 12,500–17,000 km s^{-1} (Aouad et al., 2022, Sasdelli et al., 2014), iPTF16abc exhibits prominent carbon features requiring significantly higher abundances. For comparison, a carbon mass fraction of 0.002 was inferred for the normal SN 2003du at $10{,}500 < v < 15{,}000$ km s^{-1} (Tanaka et al., 2011). A carbon mass fraction of $X(\mathrm{C}) = 0.007$ is inferred for $v > 13{,}450$ km s^{-1} (Fig. 5.12), decreasing to 0.005 above $v > 11{,}200$ km s^{-1} by day +8.

The absorption feature near 6300,Å, identified here as C II, has previously been attributed to Hα (Lentz et al., 2002). However, a hydrogen origin is not supported by the spectral modelling. No satisfactory reproduction of the feature is obtained when hydrogen is included at any velocity. Furthermore, the replacement of carbon by hydrogen eliminates

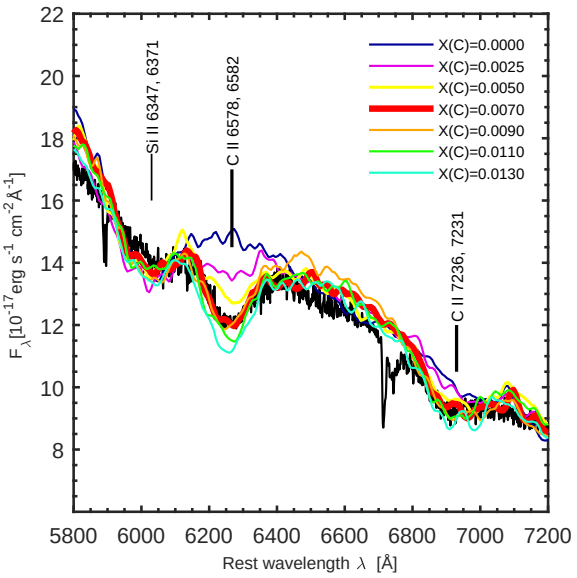


FIGURE 5.12: Comparison of the observed spectrum with synthetic spectra computed using different outer carbon abundances. The figure illustrates the effect of the carbon mass fraction on the strength of the C II absorption features at day −15. The observed spectrum is shown in black, while the models are shown in the colours indicated in the legend.

the C II λ7234 feature, which is clearly detected and accurately reproduced in the day −15 spectrum. Strong evidence is therefore provided that the 6300,Å feature originates from carbon rather than hydrogen.

One limitation of the models is the presence of an O I λ7774 feature, which appears near 7400 Å in the synthetic spectrum at day −15 but is absent from the observations. A direct comparison with SN 1999aa and SN 1991T is not possible, as spectra of these objects do not extend to such early epochs.

In the synthetic spectra, the O I line forms because its Sobolev optical depth exceeds unity under the prevailing conditions. At this epoch, the density remains relatively high ($\log \rho \approx -12.2\,\mathrm{g\,cm^{-3}}$) and the radiation temperature is of order 10^4 K, both of which favour the formation of the transition. A plausible explanation is therefore that the density in the outermost ejecta is overestimated. Reducing it would lower the Sobolev optical depth and weaken the line. This possibility is explored further in Section 5.4.

5.3.2 Post-maximum spectra

Figures 5.13 and 5.14 show spectra from 3.7 to 8.5 days after B maximum. As the ejecta expand, the photosphere recedes into the inner ^{56}Ni-rich layers. At this stage, the assumption of a sharply defined, centrally illuminated photosphere becomes increasingly

inadequate, as a significant fraction of the radioactive decay energy is deposited above the adopted photospheric boundary. Escaping photons then traverse Fe-group-rich layers where a dense forest of UV and blue transitions redistributes radiation to longer wavelengths through fluorescence, producing excess flux redward of 6000 Å. This is a known consequence of adopting a blackbody lower boundary once energy deposition is no longer confined below the photosphere. Importantly, the mismatch primarily affects the continuum shape and does not significantly alter the strength or velocity of the absorption features, indicating that the derived abundance stratification remains robust.

Fe-group elements: The feature near 5000 Å remains dominated by a blend of Fe III $\lambda\lambda$ 5156, 5127, 5073, 5086, 5193, 5114. However, as the ejecta evolve, Fe II lines progressively emerge and begin to influence the 4500–4800 Å region. The synthetic spectra successfully reproduce both the evolution of these lines and their relative strengths, indicating that the ionization balance is well captured by the models.

The feature near 4300 Å, previously split into two components with the red side dominated by Si III $\lambda\lambda$ 4552, 4567, 4574, evolves into a single, deep absorption feature dominated by a blend of Fe III lines. The behaviour of this region is common to all type Ia modelled previously (cf. Aouad et al., 2022, Sasdelli et al., 2014, Tanaka et al., 2011).

In the layers between 10,000 and 9,000 km s^{-1}, the mass fraction of stable iron remains at 0.05, accounting for approximately 30 percent of the total iron content, while the remainder is provided by the decay of ^{56}Ni. As the photosphere recedes to deeper layers ($\sim$ 7,500 km s^{-1}), the stable iron fraction increases to 0.3, a change required to reproduce the emerging emission features characteristic of the early nebular phase (see Section 5.5).

The ^{56}Ni mass fraction remains roughly constant at 0.69 within the shells probed at these epochs. The feature near 4000 Å, initially shaped by Si II λ 4130, transitions to being dominated by Co II λ 4160 as the ejecta cool. A nearby feature around 4150 Å is reproduced by a blend of Co III ($\lambda\lambda$ 4317, 4249) and Fe III (λ 4352). At shorter wavelengths, the strong absorption near 3200 Å, previously dominated by Co III becomes increasingly governed by Co II lines, reflecting the shift in ionization toward singly ionized species as the temperature declines.

Calcium: The Ca II near-infrared triplet becomes visible around +3.7 days. In comparison, this feature appears much earlier in spectroscopically normal SNe Ia, while its delayed emergence is characteristic of 91T-like events (Aouad et al., 2022, Sasdelli et al., 2014). As the spectra evolve, the feature begins to separate into two components by +6.3 days, with a clear distinction established by +8.5 days; this transition is well reproduced by the models.

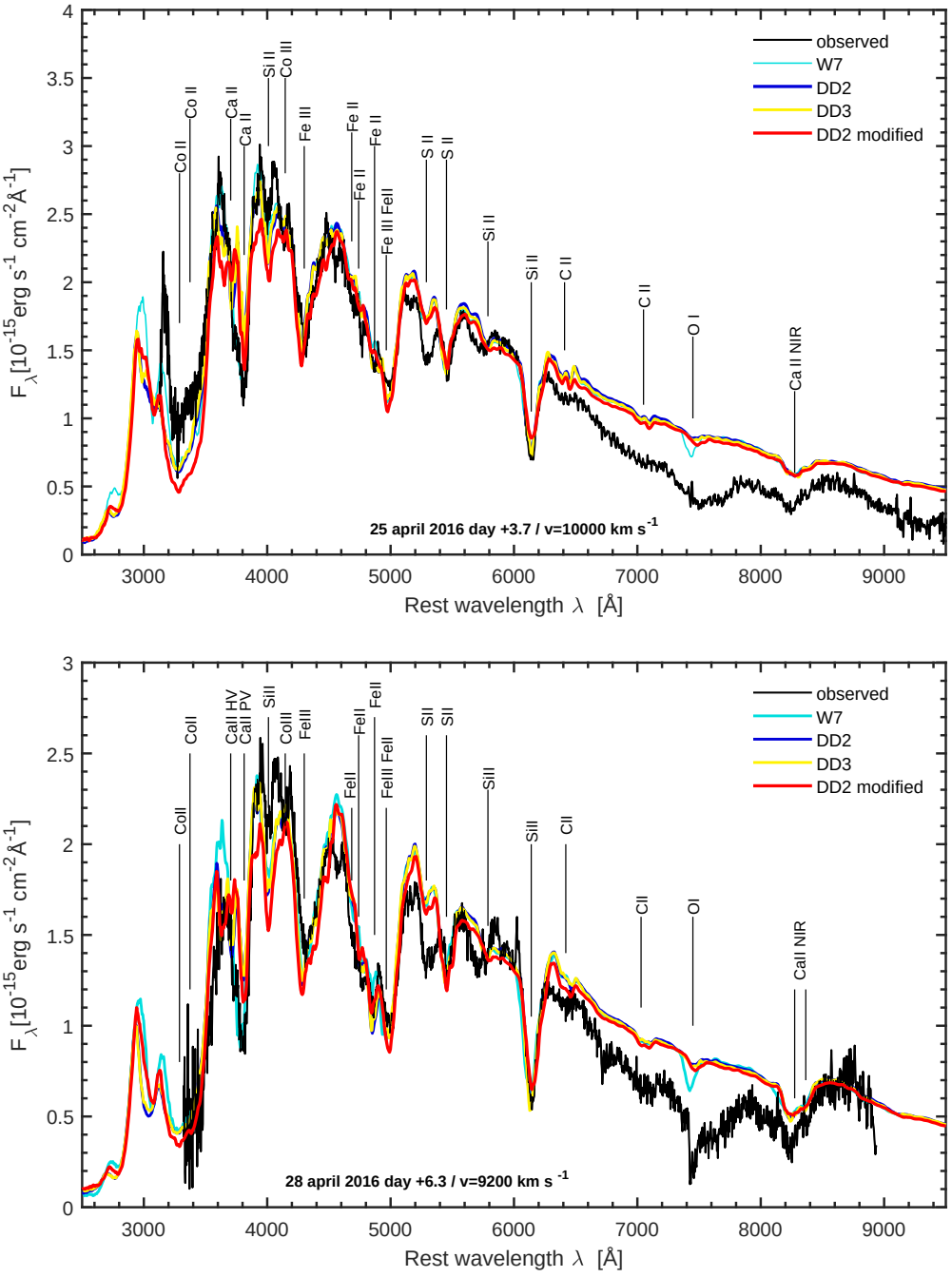


FIGURE 5.13: Comparison of post-maximum observed spectra of iPTF16abc (black) with synthetic spectra in various colours, corresponding to different density profiles as specified in the legend. Features near 6780 Å (weak) and 7400 Å (strong) are telluric. Epochs are presented with reference to B maximum.

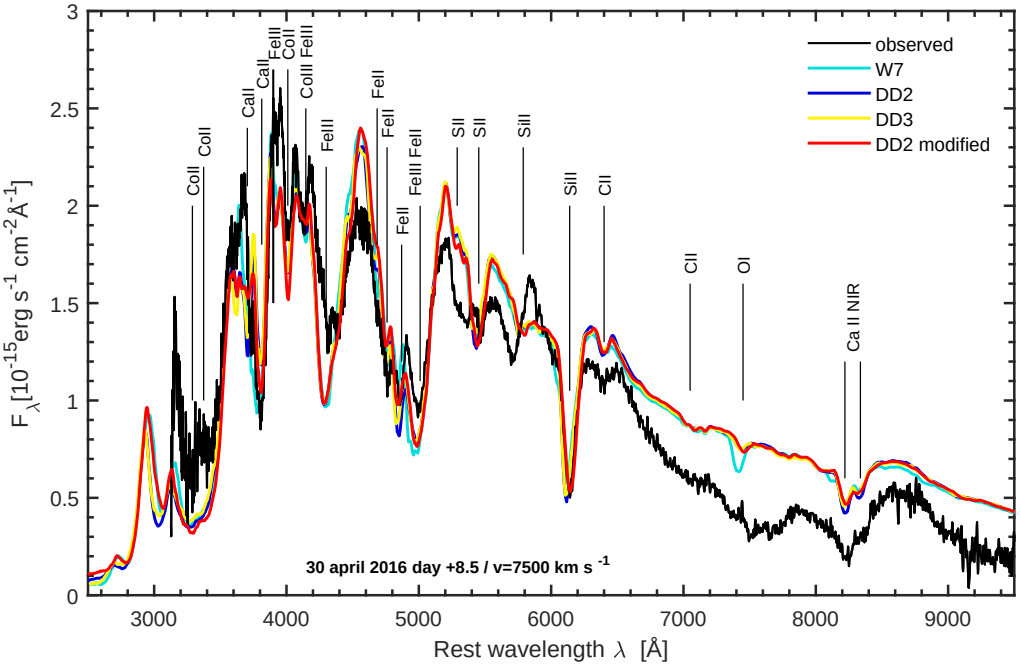


FIGURE 5.14: Comparison of day + 8 observed spectrum of iPTF16abc (black) with synthetic spectra in various colours, corresponding to different density profiles as specified in the legend. Epochs are presented with reference to B maximum.

At the same time, the feature near 3800 Å, previously dominated by Si III and Co III before maximum light, becomes increasingly influenced by Ca II H&K. Notably, the photospheric-velocity (PV) component dominates, while the high-velocity (HV) component remains comparatively weak. This behaviour contrasts with that observed in normal SNe Ia, where the HV component typically dominates even at post-maximum phases. It also differs from SN 1999aa, in which the HV Ca II component remains prominent at similar epochs.

The PV feature near 3800Å is better reproduced using the W7 density profile, (see Fig. 5.13). The delayed detonation models fail to replicate accurately its depth. This is likely due to the density enhancement in the W7 model between 13,000 and 16,000 km s^{-1} where the PV component of the line forms. The required calcium fraction decreases from 0.005 at v =10,000 km s^{-1} to 0.001 v =7500 km s^{-1}.

Silicon and sulphur:

At these epochs, the spectra become increasingly dominated by Fe-group transitions. The Si III feature that previously dominated the redward absorption near 4400,Å fades, leaving only the Si II lines visible. The Si II λ6355 feature deepens with time, while Si II λ5972 emerges around day +3.7 and continues to strengthen. Although the overall

evolution is well reproduced, the observed velocity of the latter line remains higher than predicted by the synthetic spectra.

By +6.3 days, the silicon mass fraction is ∼0.17, decreasing at lower velocities ($v <$ 7,500 km s^{-1}), where the composition becomes dominated by ^{56}Ni and stable iron.

The characteristic "W"-shaped S II feature also appears around +3.7 days. Its red component is reasonably well reproduced by the models, while the blue side remains slightly offset from the observations, likely due to contamination from the P Cygni emission associated with the Fe III complex near 5000 Å.

Carbon, oxygen: The C II λ 6580 feature weakens by +3.7 days, but subsequently re-emerges and strengthens by +8.5 days. To reproduce this evolution, the carbon mass fraction must increase from 0.005 at $v >$ 11,200 km s^{-1} to 0.025 at $v >$ 9,200 km s^{-1}. This increase is essential to match the observed behaviour of the line (see Fig. 5.15). No carbon is required below 9,200 km s^{-1}, as its presence at lower velocities would shift the line toward longer wavelengths, in disagreement with the observations. This provides a robust constraint on the minimum velocity to which carbon extends in the ejecta.

Oxygen, on the other hand, cannot be reliably constrained from the available spectral features. A similar abundance to that of carbon is therefore assumed, as it is difficult to justify the presence of carbon without a corresponding amount of oxygen.

5.4 A modified density profile

The appearance of an O I λ7771 feature in the synthetic spectra at early epochs, which is absent from the observations, suggests a mismatch between the adopted density structure and the physical conditions in the outer ejecta. In particular, the standard DD2 density profile may overestimate the density at high velocities, leading to an artificially large Sobolev optical depth for this transition.

The suppression of this feature is not straightforward. A reduction in the oxygen abundance of the outer layers would require its replacement by another species, likely introducing spectral signatures that are not observed. Likewise, shifting the ionization balance toward higher ionization states of oxygen would require an increase in temperature through modifications of global model parameters, such as a higher luminosity or lower ejecta velocities, thereby compromising the otherwise successful reproduction of the observed ionization structure.

Modifications to the density structure were therefore explored. A revised profile was constructed by redistributing a small amount of mass from the outermost ejecta to deeper

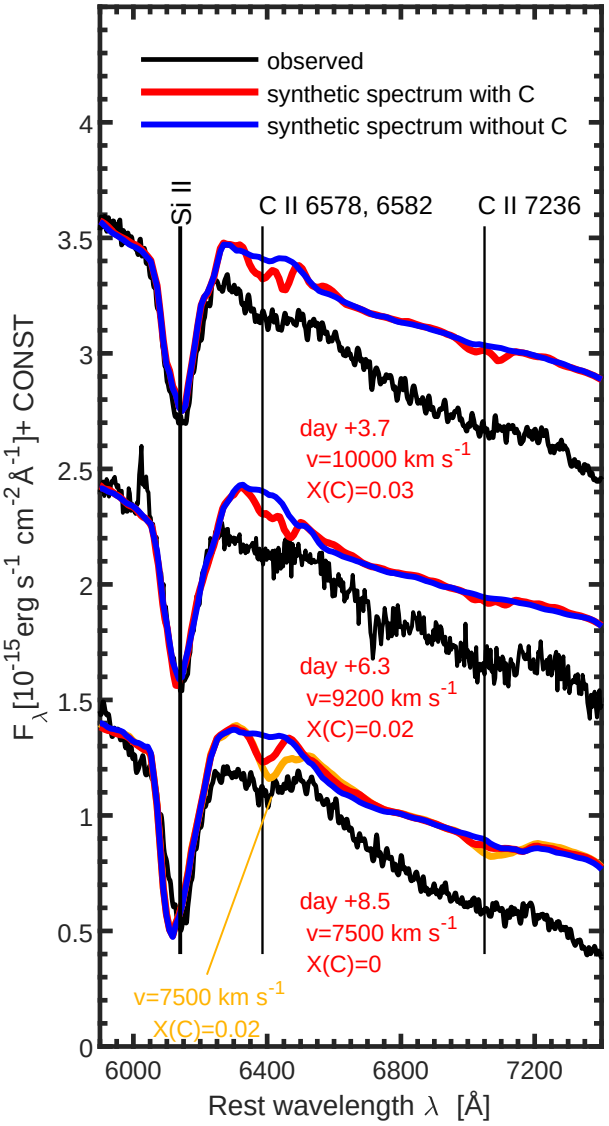


FIGURE 5.15: Probing carbon at the inner layers: spectra taken approximately 4 to 8 days after the peak. To accurately replicate the observed feature at around 6400 Å , carbon presence is required down to velocities as low as v=9,200 km s^{-1} . Introducing carbon at even lower velocities would cause the absorption line to shift redder from its observed position, as depicted in the yellow synthetic spectrum generated at day + 8.5. Epochs are presented with reference to B maximum.

layers. Specifically, 0.05 $M_\odot$ was removed from material above 13,450,km s^{-1} and redistributed at lower velocities. The total ejecta mass was thus preserved, while the kinetic energy remained essentially unchanged owing to the limited extent of the modification (Fig. 5.3). Similar adjustments have been adopted in previous studies.

Care was taken to avoid introducing sharp density gradients, which could artificially confine line formation to narrow velocity intervals and produce features inconsistent with the observed line widths. The modified profile has only a minor impact on most spectral features and leaves the inferred abundance structure largely unchanged. The strength of the O I feature, however, is significantly reduced, resulting in a substantially improved agreement with the observations. The corresponding synthetic spectra are shown in red in Figs. 5.5, 5.6, 5.7, 5.13, and 5.14.

All tested density profiles provide comparably good reproductions of the observed spectra, making it difficult to unambiguously favour a single model. This is consistent with the results obtained for SNe 1999aa. Nevertheless, the delayed-detonation (DD) models generally perform better than W7 before maximum light, particularly in the region around 3800 Å, while W7 shows a modest improvement at later epochs. The W7 model also consistently produces a strong, narrow O I λ7771 feature that is not observed. Although the modified DD2 profile successfully suppresses this feature at early times, it provides a poorer reproduction of the Si II λ6355 line and the flux around 4000,Å after maximum light. Overall, the DD models provide the most consistent results, although some refinement of the outer density structure may still be required. This preference is further supported by the inferred abundance stratification and ^{56}Ni content (Section 5.6).

5.5 The nebular phase

To extend the abundance stratification into the inner ejecta, the nebular-phase spectrum is modeled. At these late epochs, the ejecta become optically thin and the spectra are dominated by forbidden emission lines, primarily from [Fe II] and [Fe III], with additional contributions from elements such as Mg and Ca. These lines provide a direct probe of the innermost regions, which are otherwise inaccessible at earlier phases. By this epoch, the ongoing decay of ^{56}Co continues to supply energy to the ejecta. The thermal balance is then established between radioactive heating and cooling via line emission. Modeling this balance allows constraining the mass of synthesized ^{56}Ni, as well as the total mass and composition of the emitting region, thereby completing the abundance distribution in the inner layers.

The nebular spectrum of iPTF16abc at +342.4 days is of limited quality, with a low signal-to-noise ratio and wavelength coverage extending only to 5400 Å. The absence of photometric observations at this epoch further complicates the flux calibration. To mitigate this, the spectrum was calibrated using an extrapolated g-band magnitude. Since no U-band photometry was available for iPTF16abc, the U-band flux was estimated by adopting the U−g colour of SN 1999aa at a similar epoch. While this procedure is approximate and introduces systematic uncertainties, it is expected to recover the flux to within ∼20 percent.

The calibrated nebular spectrum is modeled using the SN nebular code of Mazzali et al. (2001b), as described in Sect. 4.5 adopting the DD2 density profile together with the abundance structure inferred from the photospheric phase. The resulting model, shown in Fig. 5.16, provides a good overall match to the observed spectrum. In particular, the relative strengths of the Fe II and Fe III lines are well reproduced, indicating that the ionization state is adequately captured. This balance is not determined solely by radioactive heating, but is also influenced by the presence of stable iron synthesized at high densities, which enhances cooling and promotes recombination. The nebular spectrum therefore offers a direct constraint on the mass of stable iron-group elements, a key diagnostic of the progenitor mass. Significant production of stable Fe is typically associated with explosions occurring near the Chandrasekhar mass, while lower-mass progenitors are expected to yield smaller amounts. At the same time, the inferred ^{56}Ni abundance is reasonably well constrained, as the overall flux level of the spectrum is satisfactorily reproduced. Although this estimate is affected by uncertainties in the flux calibration as described previosuly, the resulting ^{56}Ni mass estimate is independently constrained through comparison with the bolometric light curve, as discussed in Sec.5.7.2

5.6 Abundance tomography

The abundance structure is derived by combining the results from both the photospheric and nebular phases, allowing the ejecta to be mapped continuously from the innermost regions to the highest velocities (Fig.5.17). This distribution is compared with the original DD2 hydrodynamical model (Iwamoto et al., 1999).

The inner ejecta are dominated by neutron-rich, stable Fe-group elements. Stable iron extends out to approximately 3,500 km s^{-1}, while stable nickel (^{58}Ni) is confined to the very central regions below ∼ 1,000 km s^{-1}. This strong central concentration of ^{58}Ni contrasts with hydrodynamical predictions, which place it at significantly higher velocities. This is consistently recovered across all abundance studies (see Aouad et al.

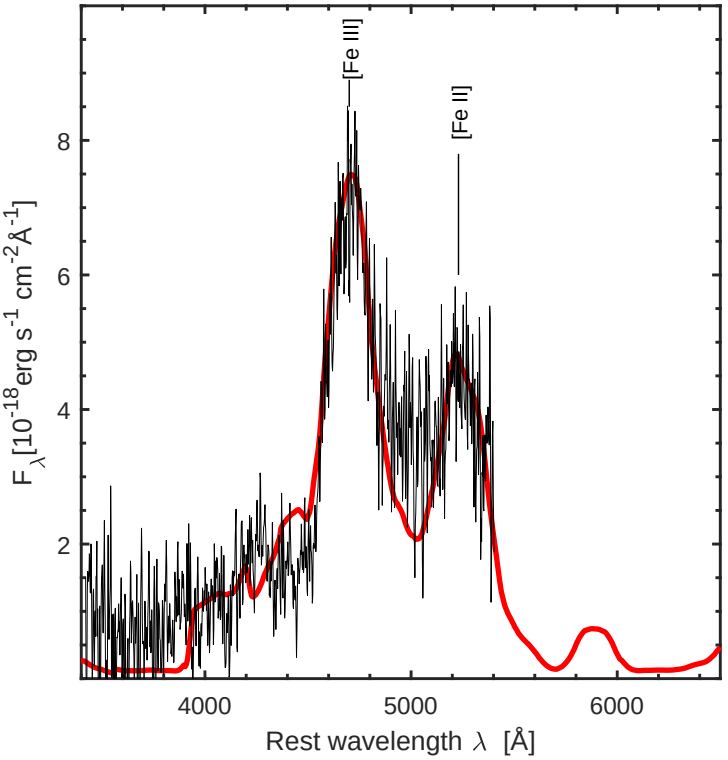


FIGURE 5.16: Nebular spectrum of iPTF16abc on day +342 with reference to B maximum light, displayed in black, compared with the synthetic spectrum in red.

2022, Sasdelli et al. 2014, Tanaka et al. 2011), suggesting a systematic discrepancy with the explosion models.

At intermediate velocities (∼5,000–12,500 km s^{-1}), ^{56}Ni dominates the composition, with a total mass of ∼0.76 M$_\odot$, mixed with a smaller fraction of stable iron. Moving outward, the decrease in density leads to incomplete silicon burning, and intermediate-mass elements (IMEs), primarily Si and S, become the dominant species, accompanied by traces of Ca.

A notable deviation from the original model is the behaviour of silicon. Rather than extending smoothly to high velocities, its abundance drops abruptly beyond ∼13,400 km s^{-1}, confining the Si-rich region to a narrower shell than predicted. This behaviour closely resembles that observed in SN 1999aa and SN 1991T, supporting a similar explosion scenario (Aouad et al., 2022, Sasdelli et al., 2014) which reduced efficient burning at this velocity. At higher velocities ($v \gtrsim$ 15,000 km s^{-1}), oxygen becomes the dominant element.

Carbon is also detected within the IME-rich layers and extends inward to ∼9,000 km s^{-1}. This is unexpected, as standard symmetric explosion models predict unburned carbon

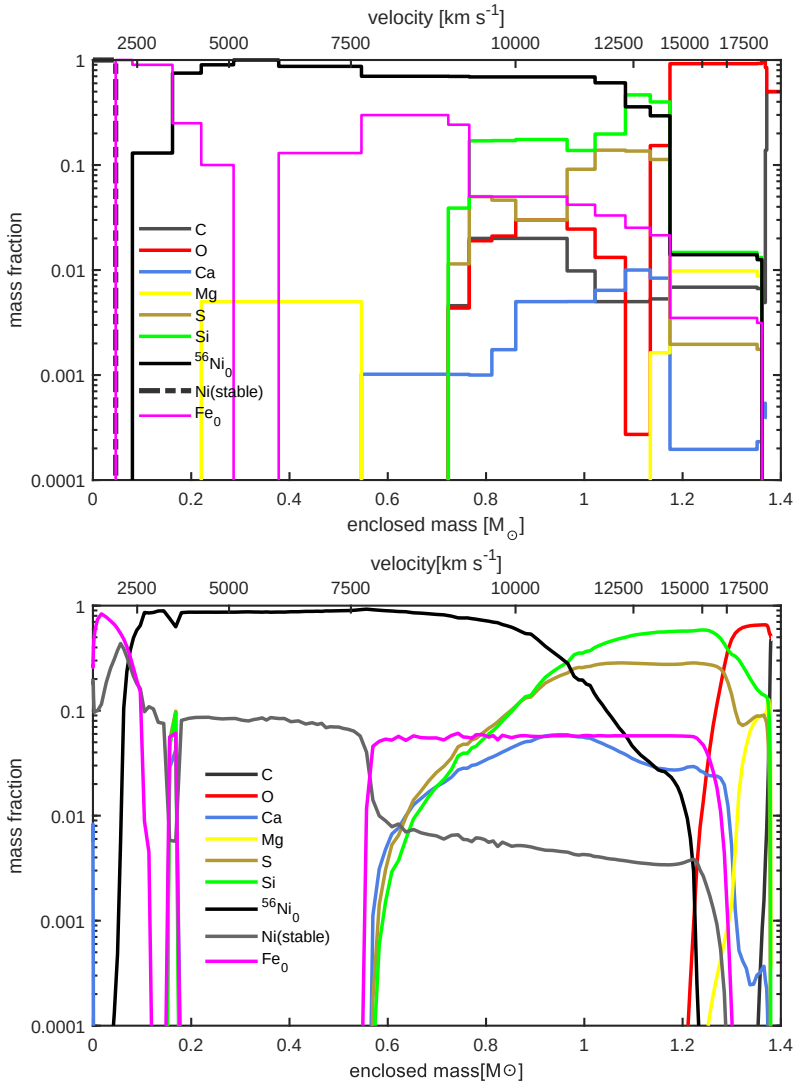


FIGURE 5.17: Upper panel: abundances obtained from spectral models using the DD3 density profile. Lower panel: the original nucleosynthesis from DD3 (Iwamoto et al., 1999).

only at much higher velocities (Iwamoto et al., 1999, Nomoto et al., 1984). The presence of carbon at these depths indicates incomplete burning in regions where it would not typically be expected.

Finally, small amounts of ^{56}Ni and stable iron are found to persist even in the outermost layers (up to $v \sim 25{,}000$ km s^{-1}). Although present only at low mass fractions, their existence further highlights deviations from classical explosion models.

Using the integrated yields from the abundance results (presented in Tab. 5.2), the total kinetic energy is computed using the formulation of Woosley et al. (2007a):

$$E_k = [1.56M(^{56}\mathrm{Ni}) + 1.74M(\mathrm{NSE}) + 1.24M(\mathrm{IME}) - 0.46] \times 10^{51}\,\mathrm{erg} \qquad (5.1)$$

TABLE 5.2: Nucleosynthetic yields and kinetic energies from the modelling compared to the original hydrodynamic models. Results from other SNe are also shown. E_k for models is calculated using equation 5.1 in the text.

Model/SN	^{56}Ni ($M_\odot$)	Fe[a] ($M_\odot$)	Ni_{stable} ($M_\odot$)	IME[b] ($M_\odot$)	O ($M_\odot$)	IME/IGE	E_k (10^{51} erg)
iPTF16abc (DD2)	0.76	0.20	0.006	0.19	0.21	0.197	1.32
original W7	0.59	0.16	0.122	0.24	0.143	0.275	1.30
original DD2	0.69	0.10	0.054	0.33	0.066	0.39	1.40
original DD3	0.77	0.10	0.0664	0.25	0.056	0.27	1.43
1991T (DD3)	0.78	0.15	0.0006	0.18	0.29	0.19	1.24
1999aa (DD2)	0.65	0.29	0.006	0.20	0.22	0.21	1.32
2003du (W7)	0.62	0.18	0.024	0.26	0.23	0.32	1.25
2002bo (W7)	0.49	0.27	0.0001	0.28	0.11	0.37	1.24
2004eo (W7)	0.32	0.29	0.0005	0.43	0.3	0.70	1.1

[a] All stable isotopes except for ^{56}Fe, decay product of ^{56}Ni.
[b] ^{28}Si + ^{32}S.

where $M(^{56}\text{Ni})$, $M(\text{NSE})$, and $M(\text{IME})$ correspond to the ejected mass of ^{56}Ni, nuclear statistical equilibrium elements, and IMEs respectively, yielding 1.32×10^{51} erg.

The ^{56}Ni mass aligns with the original DD3 model, though the kinetic energy remains slightly lower than both DD2 and DD3 (Table 5.2). This outcome is expected due to the insufficient production of IMEs, which is not compensated for by an increase in ^{56}Ni production, a trait common to all modeled 91T-like objects (Aouad et al., 2022, Sasdelli et al., 2014). These objects share a consistent IMEs/IGEs mass ratio (Table 5.2, Fig. 5.18) that is notably lower than normal events or hydrodynamic models. The Fe-group mass of $\sim 0.2\ M_\odot$ falls within the expected SN Ia range (Mazzali et al., 2007). Above 9,200 km s^{-1}, the estimated carbon mass is $\sim 0.01\ M_\odot$, consistent with the 0.001–0.01 $M_\odot$ range reported by Folatelli et al. (2012). The abundance distribution is broadly consistent with delayed-detonation models, particularly with regard to the stratification and mass of ^{56}Ni.

5.7 Bolometric light curve

5.7.1 Construction of the observed bolometric light Curve

A bolometric light curve spanning 3000–10,000 Å is generated (cf. Fig. 5.19) using the $UBVri$ photometry reported in Miller et al. (2018). This is subsequently compared to a light curve computed from the model. In cases where multiple photometric measurements are available for a given epoch, the average magnitude is calculated; an error of

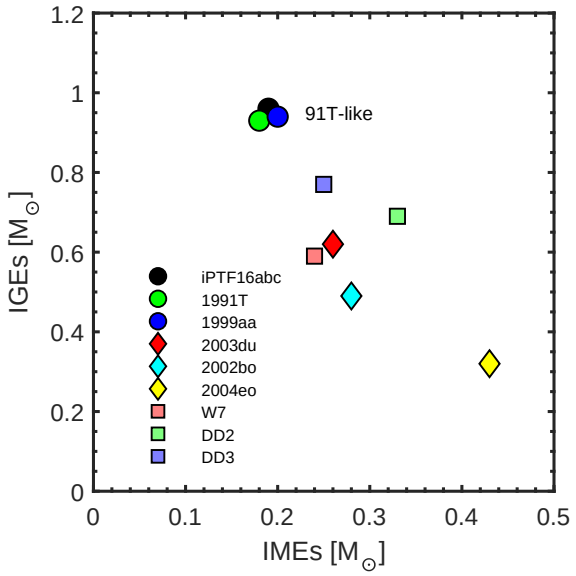


FIGURE 5.18: Total mass of Intermediate Mass Elements (IMEs), against the total mass of Iron Group Elements (IGEs) for iPTF16abc, compared to other SNe and explosion models. Notably, the 91T-like events are observed to occupy a distinct region within this space.

~ 0.1 mag is introduced by this process. U-band photometry is unavailable beyond day +22 from B maximum light. Therefore, for these epochs, U-band measurements are assumed by applying a constant $U - B$ value as computed from the last epoch where both measurements were available (i.e., day +21). Next, the data are interpolated at a daily resolution, and magnitudes are converted to fluxes by applying the flux zero-points of Fukugita et al. (1995), dereddened with the extinction curve of Cardelli et al. (1989) using $E(B-V)$=0.08 mag (Miller et al., 2018). For each epoch, the flux is computed via trapezoidal integration between the specific flux values obtained at the central wavelength of each passband. The spectrum is extrapolated with a linearly decreasing function to 3000 Å and 10,000 Å to extend the flux calculation beyond the U- and i-band central wavelengths. Adopting a flat extrapolation, similar to that used for SN 1999aa (Section 4.7.1), instead produces a nearly identical integrated flux. Finally, bolometric luminosities are computed using the adopted distance modulus of 35.01, considering an error of 0.15 mag (Makarov et al., 2014).

With a rise time of 18.74 days in the rest frame, iPTF16abc reaches a bolometric peak of $L_{\rm peak} = 1.60 \pm 0.1 \times 10^{43}$ erg s^{-1}. This peak occurs approximately one day prior to $B_{\rm max}$, consistent with previous studies examining bolometric rise time (Contardo et al., 2000, Scalzo et al., 2012). While Miller et al. (2018) reported a peak of $1.2 \pm 0.1 \times 10^{43}$ using a distance modulus of 34.89 ± 0.10 mag, a modulus of 35.01 mag is adopted here for

modeling consistency. A shorter distance requires a lower luminosity, which fails to reproduce the modeled ionization balance. Even when using the distance modulus adopted by Miller et al. (2018), a peak of $1.48 \pm 0.1 \times 10^{43}$ is obtained, remaining more luminous than SN 1999aa and closer to SN 1991T. Additionally, the bolometric luminosities derived from the synthetic spectra are in good agreement with both the modeled and reconstructed light curves, providing an independent validation of the adopted methodology and the resulting abundance stratification (see crosses in Fig. 5.19).

Based on the 0.76 $M_\odot$ of ^{56}Ni inferred from the synthetic spectra, the peak luminosity is estimated using Arnett's rule (Eq. 2.12; Stritzinger & Leibundgut 2005) and a rise time of 18.74 days. A value of $L_{\rm peak} = (1.51 \pm 0.10) \times 10^{43}$ erg s^{-1} is obtained, in good agreement with that derived from the synthetic spectra within the uncertainties associated with the distance, photometry, and flux integration. This approximation does not account for the distribution of ^{56}Ni throughout the ejecta. A more accurate assessment is therefore obtained from the detailed light-curve modeling presented in the following subsection.

5.7.2 Modelling the bolometric light curve

A consistency check of the abundance tomography is obtained by computing a synthetic light curve based on the derived density and abundance structure. Since the light curve is primarily governed by the total mass and spatial distribution of ^{56}Ni, as well as the opacity of the ejecta, a successful reproduction of the observed light curve provides an independent validation of the spectral modeling results. The bolometric light curve is computed using the code described in Section 4.7.2, and the resulting model is shown in Fig. 5.19. The agreement with the observed light curve is good from the rise to maximum light, indicating that the distribution of ^{56}Ni in the outer layers is well captured. In addition, the width of the light curve around peak is accurately reproduced, supporting the inferred values of $\mathrm{M_{ej}}$ and $E_{\rm k}$, and thus the adopted explosion model. Discrepancies at later times are probably due to the increasing contribution of infrared flux, which is not constrained by the available observations.

5.8 Conclusions

- **Modified density structure** The delayed-detonation density profiles provide the best overall reproduction of the spectroscopic evolution of iPTF16abc. In particular, the DD2 model successfully reproduces most of the observed features, although a modest reduction of the density in the outermost layers is required to suppress the spurious O I λ7774 absorption.

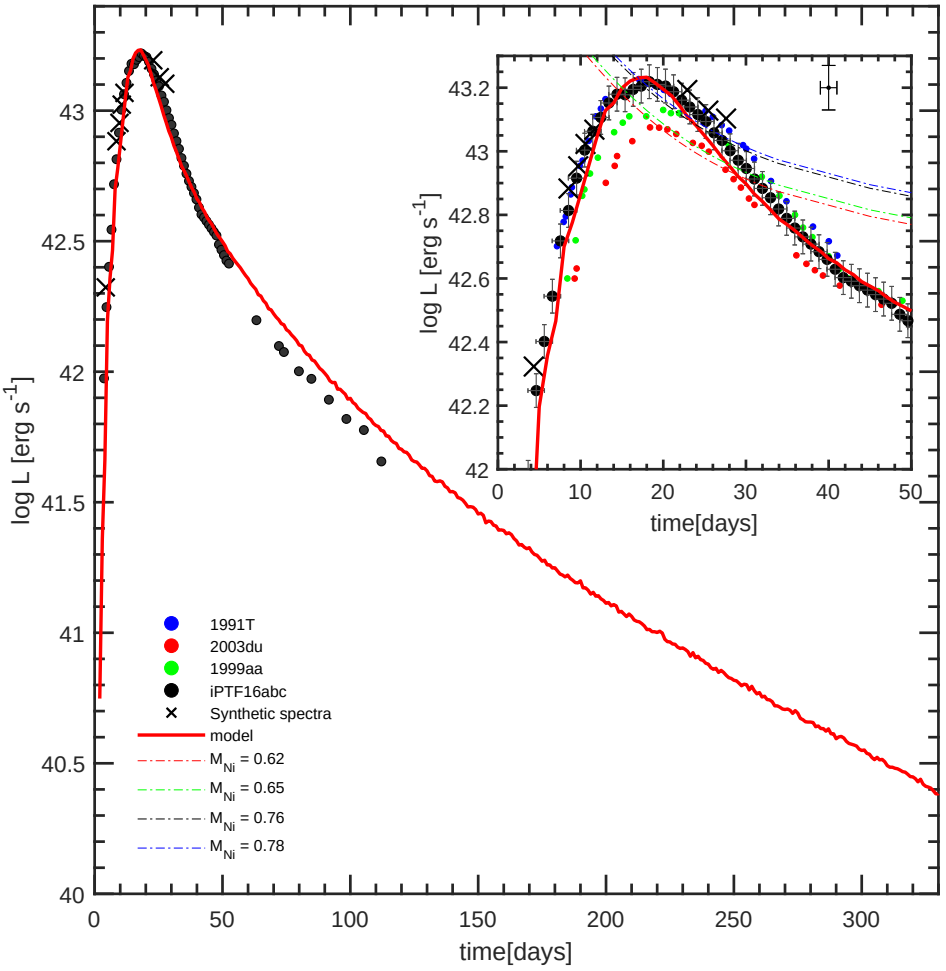


FIGURE 5.19: The modeled bolometric light curve of iPTF16abc (red line) is shown together with those of SNe 1991T, 1999aa, and 2003du. Phases are given relative to the adopted explosion time. Black points correspond to bolometric luminosities derived from the photometric data of Miller et al. (2018) as described in section 5.7, while crosses indicate bolometric luminosities used as inputs when modeling the synthetic spectra. The dashed curves in the inset represent the instantaneous radioactive energy input from ^{56}Ni decay for different nickel masses inferred from the modeling of SNe 1991T (blue), 2003du (red), 1999aa (green) and iPTF16abc (black) (see Aouad et al., 2022, 2024, Sasdelli et al., 2014, Tanaka et al., 2011). The plotted points in the inset include photometric uncertainties, and the error bars additionally account for distance uncertainties, assuming an error of 0.15 mag in the distance modulus (Makarov et al., 2014).

The inferred abundance structure is characterized by a central region dominated by stable IGEs ($0.20\,M_\odot$), as observed in all SNe Ia, surrounded by a ^{56}Ni-dominated shell containing $0.76\,M_\odot$ of radioactive material and powering a bolometric peak luminosity of $1.5 \times 10^{43}\,\mathrm{erg\,s^{-1}}$. Outside this region lies a relatively thin IME shell with a total mass of $0.18\,M_\odot$.

- **Iron Abundance and the Origin of Weak Fe III Lines.**

  iPTF16abc exhibits weaker early Fe III lines in its early spectra compared to both SNe 1999aa and 1991T. This difference is evident in the pseudo equivalent width (PEW) of the Fe III trough around 4800 Å (see Fig. 5.20), measured following the method of Hachinger et al. (2006). This trend is confirmed by abundance levels (5.17): iPTF16abc exhibits approximately 7–10 times less iron than SNe 1999aa and 1991T at $v > 15{,}000$ km s^{-1}. However, this disparity diminishes in deeper layers where abundances align with other events, as supported by nebular phase PEW measurements (Miller et al., 2018). Consequently, the relative weakness of Fe III lines during the photospheric phase is likely due to abundance variations in the outermost shells rather than ionization-related luminosity effects. To test this, a sequence of synthetic spectra was constructed in which the luminosity and outer-layer iron abundance were varied independently (see Figs. 5.21 and 5.22), while keeping the underlying model unchanged.

  These results demonstrate that objects exhibiting weak Fe III lines can reach luminosities comparable to—or even exceeding—those of events with strong Fe III features, traditionally regarded as a hallmark of high-luminosity 91T-like supernovae. This challenges the interpretation of Fe III strength as a direct tracer of luminosity or temperature, and instead points to a more complex interplay between ionization and abundance in the outer ejecta.

  In this context, iPTF16abc highlights the intrinsic diversity within supernovae commonly grouped within the same subclass. The comparison is particularly compelling, as 2003fg-like events also exhibit weak Fe III lines despite their high luminosities (Ashall et al., 2021), reinforcing that luminosity alone cannot account for the observed spectroscopic diversity. Furthermore, although iPTF16abc exhibits a lower iron abundance in its outer layers compared to other 91T-like events, it still shows supersolar values. Supersolar iron abundances have been inferred across SNe Ia spanning a range of spectroscopic classes and luminosities, including SN 1999aa (Aouad et al., 2022), SN 2002bo (Stehle et al., 2005), and SN 2010jn (Hachinger et al., 2013). In these outermost layers, iron is unlikely to originate from ^{56}Ni decay and instead likely reflects the progenitor composition. This suggests that progenitors with above-solar metallicity do not necessarily produce dimmer explosions (Timmes et al., 2003).

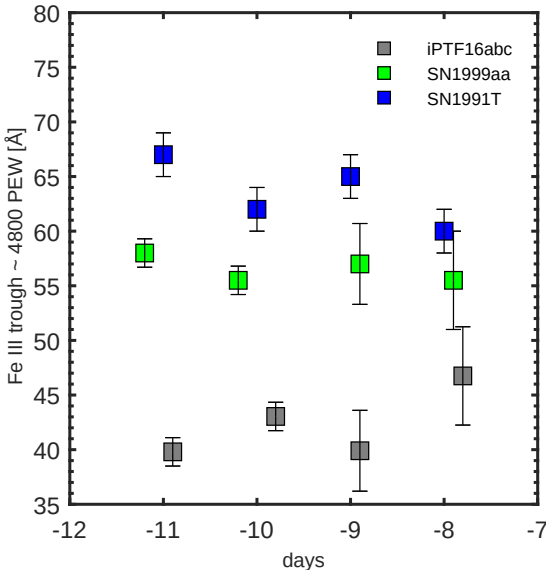


FIGURE 5.20: Comparison of the pseudo equivalent width of the Fe III trough, around 4800 Å, in the early spectra of iPTF16abc with those measured for SNe 1999aa and 1991T. The measurements were carried out following the approach described in Hachinger et al. (2006). Days are with reference to B maximum.

- **Silicon Depletion in the Outermost Layers** In the transition from spectroscopically normal to peculiar 91T-like events, the weakening of the Si II λ 6355 line is attributed more to abundance-related factors than ionization (Aouad et al., 2022, Sasdelli et al., 2014). Comparing abundance profiles (see Fig. 5.23), silicon displays a noticeable decline in the outermost shells across the three modeled 91T-like objects, namely SNe 1999aa, 1991T and iPTF16abc. This behaviour is consistent with the findings of O'Brien et al. (2023), who, through systematic radiative-transfer modeling of a large sample of SNe Ia, demonstrate that 91T-like events exhibit a global deficiency of intermediate-mass elements (IMEs), particularly silicon and sulphur, in their outer layers relative to normal events (see also Mazzali et al., 2007).

  This implies that the weakness of the Si II feature, one of the defining characteristics of 91T-like events, primarily reflects a reduced abundance of IMEs in the outer layers rather than ionization effects. This, in turn, points to a structure in which burning becomes inefficient beyond ∼12,000–13,000 km s^{-1}, leading to a clear separation between an inner region of efficient burning and outer layers dominated by incomplete burning.

- **Evidence for Carbon Pockets in the Ejecta** Persistent carbon features until two weeks post-maximum distinguish iPTF16abc from other 91T-like SNe (1999aa

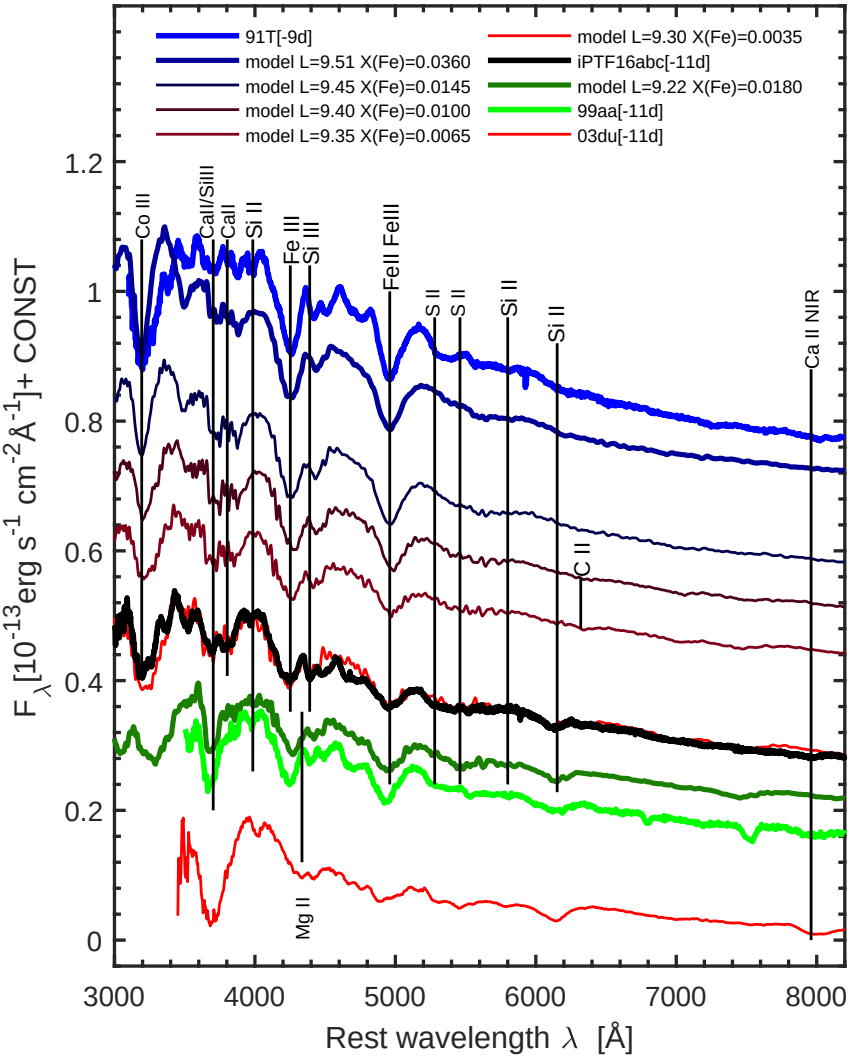


FIGURE 5.21: The observed spectra of SN 2003du, SN 1999aa, iPTF16abc, and SN 1991T are shown at the bottom, ordered from lower to higher luminosity (red, green, black, and blue, respectively). Overlaid is a sequence of synthetic spectra constructed from the best-fit model of iPTF16abc, in which the luminosity is progressively increased in steps of 0.5 dex (in solar units). At the same time, the iron abundance in the outer ejecta is systematically enhanced. As the sequence evolves, the models approach SN 1991T at higher luminosities and SN 1999aa at lower luminosities, demonstrating that iPTF16abc occupies an intermediate position between these objects. However, the comparison also reveals that luminosity alone cannot reproduce the full spectral diversity. Matching the observed sequence requires simultaneous changes in the iron abundance of the outer layers, indicating that the differences are not driven purely by temperature effects. This result highlights that the spectroscopic sequence among these events is governed by both ionization and composition, and underscores the intrinsic complexity within supernovae that are commonly classified within the same subclass.

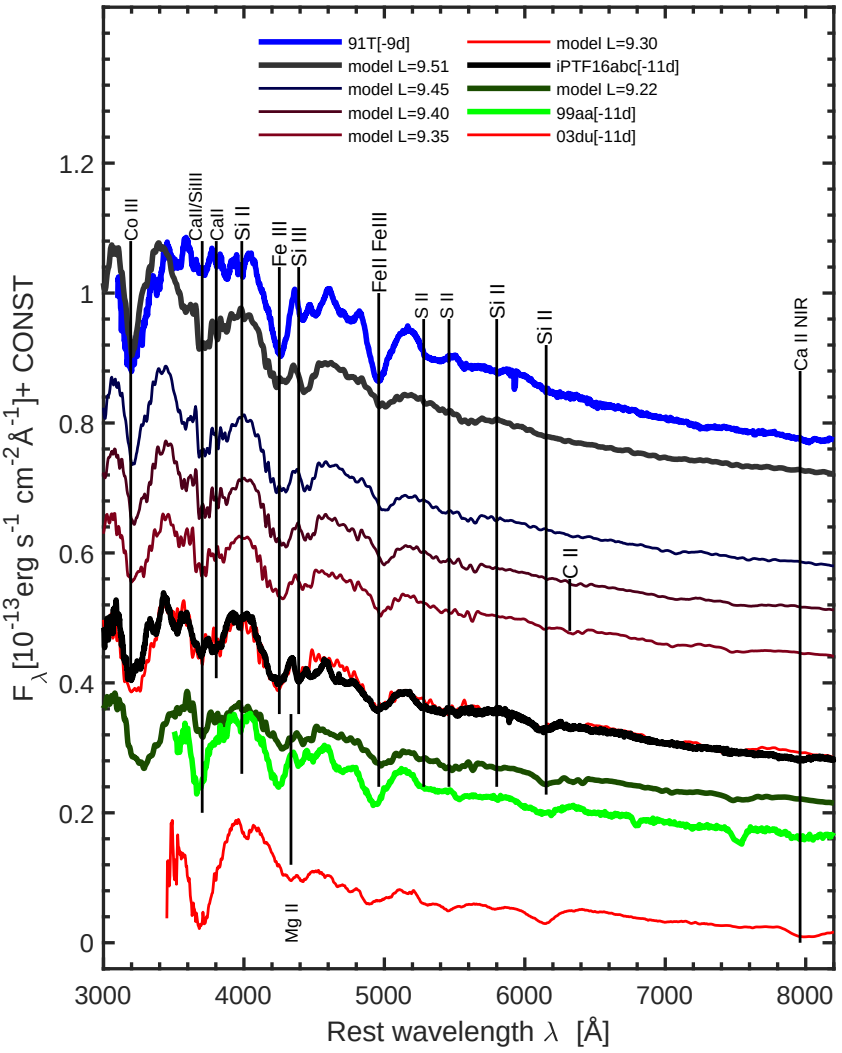


FIGURE 5.22: Same as Fig. 5.21, but with the iron abundance in the outer layers kept fixed while only the luminosity is varied. In this case, increasing the luminosity alone fails to reproduce the observed spectral sequence between SN 1999aa, iPTF16abc, and SN 1991T.

and 1991T). While carbon features may occasionally appear in the earliest spectra of normal SNe Ia, they typically fade before maximum light and are absent thereafter (e.g., SNe 2013du; Zheng et al., 2013) (SNe 2011fe Folatelli et al., 2012, Nugent et al., 2011, Parrent et al., 2011). In contrast, persistent carbon signatures are commonly observed in 03fg-like events (Ashall et al., 2021), including SNe 2009dc, SNe 2006gz, SNe 2012dn, and SNe 2022pul (Chakradhari et al., 2014, Hachinger et al., 2012, Hicken et al., 2007, Siebert et al., 2023a, Taubenberger et al., 2011).

In iPTF16abc, however, the evolution of the C II λ6580 feature follows a distinct

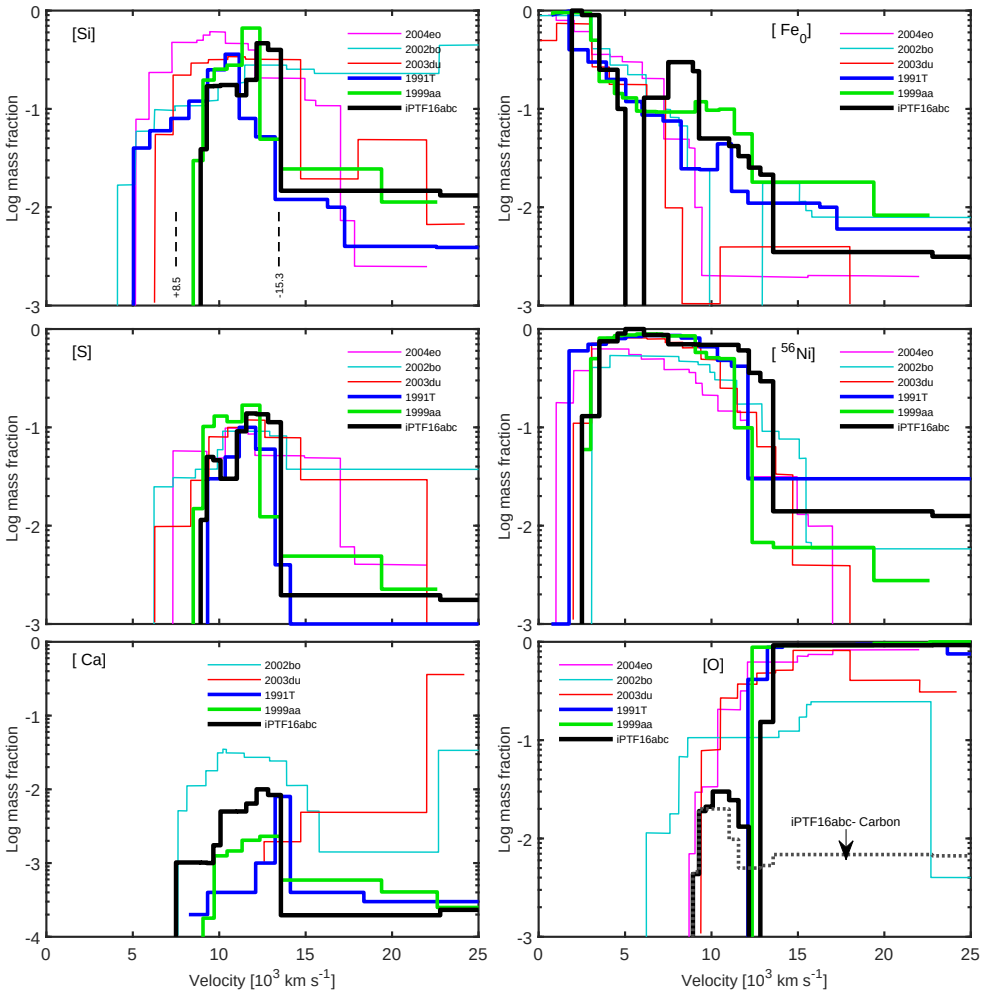


FIGURE 5.23: The distribution of the most important elements in SNe iptf16abc, 1991T, 1999aa and some spectroscopically normal SNe Ia. Left-hand side, top to bottom: Si, S and Ca. Right-hand side, top to bottom: stable Fe, ^{56}Ni, O and C. iptf16abc exhibits very similar stratification properties to SNe 1999aa and 1991T which are different than the spectroscopically normal events: the IMEs shell is narrow and is suddenly depleted above $\sim$ 12,000 km s^{-1}, oxygen dominates the outer shells and is sharply depleted below $\sim$ 12,000 km s^{-1}. Carbon extends deep and increases creating a noticeable peak around 10,000 km s^{-1}. The dashed lines in the first panel represent the velocities probed by our photospheric phase models, spanning from approximately days -15.3 to $+8.5$ relative to B maximum, while the regions below are probed by the nebular phase model.

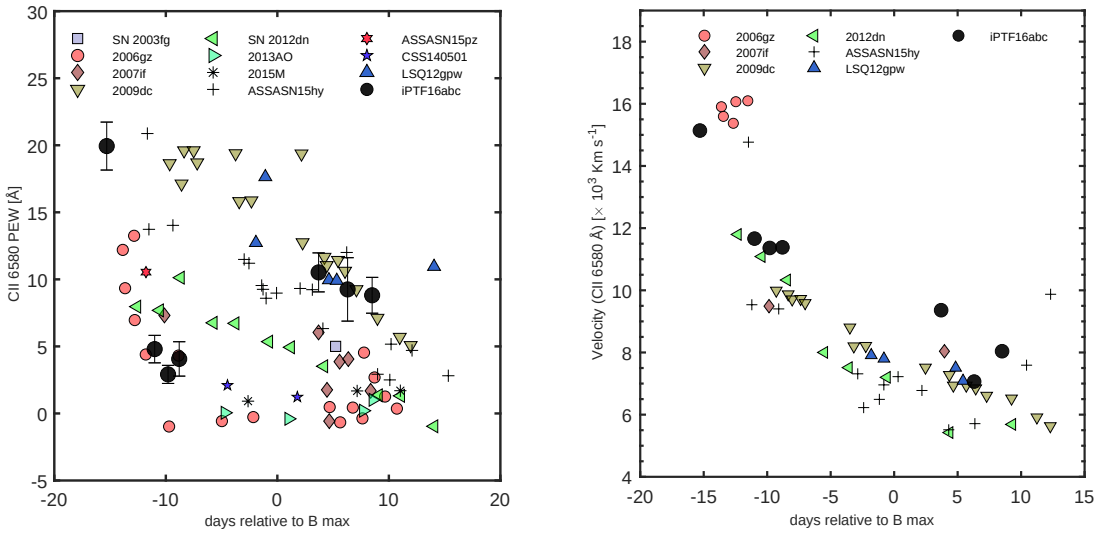


FIGURE 5.24: Left panel: Pseudo equivalent width (PEW) of the C II 6580 Å observed in iPTF16abc, compared to a set of SNe 2003fg-like taken from Ashall et al. (2021). The line initially shows notable strength at an early stage but experiences a subsequent weakening before ultimately strengthening again, approximately one week after maximum light.
Right panel: Velocity of the same line

pattern. While its velocity evolution is broadly consistent with that of 03fg-like events, the pseudo-equivalent width displays a non-monotonic behaviour: it is initially strong, weakens toward maximum light, and then increases again approximately one week after maximum as shown in the left panel of Fig. 5.24. This behaviour is consistent with the inferred abundance stratification, which shows an enhancement of carbon at intermediate velocities, forming a "bump" around ∼10,000 km s^{-1} (See Figs. 5.23, 5.17).

Such a feature is not expected in one-dimensional explosion models and instead indicates a structured distribution of unburned material within the ejecta. A natural interpretation is that carbon is distributed in localized pockets or clumps, likely arising from multidimensional mixing driven by flame propagation asymmetries (Folatelli et al., 2012, Parrent et al., 2011).

- **Progenitor and Explosion Mechanisms**

  Any explosion progenitor channel must account for the main observables of iPTF16abc, which can be summarized by (i) a sharp transition between an inner region dominated by complete burning and outer layers characterized by incomplete burning, and (ii) the presence and unusual distribution of carbon throughout the ejecta, indicating strong mixing and three-dimensional effects.

In this context, pulsation-driven detonation (PDD) models offer an attractive framework (Dessart et al., 2014, Ivanova et al., 1974, Khokhlov, 1991a). In these models, a weak deflagration phase fails to unbind the white dwarf, leading to expansion followed by contraction. Rayleigh–Taylor instabilities during this phase can mix burned and unburned material, and a subsequent detonation propagates through a pre-expanded structure. This creates a sharp density decline and naturally produces a narrow IME region and leaves unburned carbon in the outer layers, broadly consistent with the abundance structure inferred for iPTF16abc.

Multidimensional extensions, such as pulsating reverse detonations (PRD), further introduce buoyant plumes that penetrate the outer ejecta, producing compositional inversions and partial mixing (Bravo & García-Senz, 2009). These effects may account for the presence of carbon at intermediate velocities and deviations from spherical symmetry. Interestingly, the PDDEL1 model of Dessart et al. (2014) produces $0.758\,M_\odot$ of ^{56}Ni and $0.19\,M_\odot$ of silicon, in good agreement with the values inferred in our models. More notably, the silicon and sulphur abundance profiles exhibit a rapid decline over a similar velocity range to that found in our models. However, their model predicts a substantially lower abundance of stable iron and a markedly reduced oxygen content compared to our results.

Although current PDD/PRD models provide an attractive explanation for iPTF16abc, they do not fully reproduce the observations. In particular, they tend to predict a narrow early Si II λ6355 feature, in contrast to what is observed in iPTF16abc. Consequently, they fail to reproduce the defining properties of the 91T-like subclass, whose early Si II λ6355 feature is the hallmark. Instead, these models have been proposed to explain normal SNe Ia, such as SN 2011fe (Dessart et al., 2014).

In addition, some PDD/PRD models attribute part of the early-time luminosity to shock-deposited energy rather than radioactive decay, making them analogous in this respect to ejecta–CSM interaction scenarios proposed for 03fg-like events (Ashall et al., 2021). This has been claimed by Liu et al. (2024) in the context of SN 2023wrk to explain the strong early carbon lines. However, such a contribution is not required for iPTF16abc, as both the light-curve and the abundance stratification inferred from spectral modeling are consistent with radioactive heating alone, with no indication of an additional energy source.

Overall, while PDD-like scenarios provide a compelling qualitative explanation for several key features of iPTF16abc—namely the confinement of IMEs, the presence of carbon, and the role of multidimensional effects—they do not yet offer a complete description. The explosion of iPTF16abc likely reflects a more complex interplay between high-density burning and asymmetric ejecta structure than captured by current models.

Chapter 6

SN 2012dn

6.1 Motivation

SN 2012dn is a particularly important Type Ia supernova within the 03fg-like subclass (Section 2.3.1.4). This sub-class is first identified with SN 2003fg (Howell et al., 2006) and characterised by narrow IME lines, weak or absent Fe III features, persistent C II absorption, low expansion velocities, broad light curves, and peculiar near-infrared evolution (Ashall et al., 2021). While some members such as SN 2003fg, SN 2009dc (Hachinger et al., 2012, Taubenberger et al., 2011), and SN 2007if (Akerlof et al., 2007, Scalzo et al., 2010, Taubenberger et al., 2013a) reach extremely high luminosities requiring ^{56}Ni masses beyond what a Chandrasekhar-mass progenitor can synthesise, earning them the label super-Chandrasekhar, others including SN 2006gz (Hicken et al., 2007), ASASSN-15hy (Lu et al., 2021), and SN 2012dn exhibit near-normal peak luminosities, demonstrating that extreme luminosity is not a defining characteristic of this subclass.

SN 2012dn is therefore particularly valuable as it decouples the 03fg-like spectroscopic appearance from extreme luminosity. It also exhibits an unusual post-maximum evolution characterised by rapid optical fading and a significantly dimmed nebular phase. Most importantly, nebular [O I] emission is detected, a feature exceptionally rare among thermonuclear supernovae. Such emission has been reported in only a handful of SNe Ia: SN 2010lp (Taubenberger et al., 2013b), ASASSN-20jq (Bose et al., 2025), and more recently within the 03fg-like subclass, SNe 2021zny and 2022pul (Dimitriadis et al., 2023, Siebert et al., 2023a), making SN 2012dn a particularly important object for probing the innermost ejecta of this subclass.

The nebular-phase spectrum and light-curve modelling were performed by Paolo Mazzali, while the photospheric spectral models and the observed bolometric luminosity curve

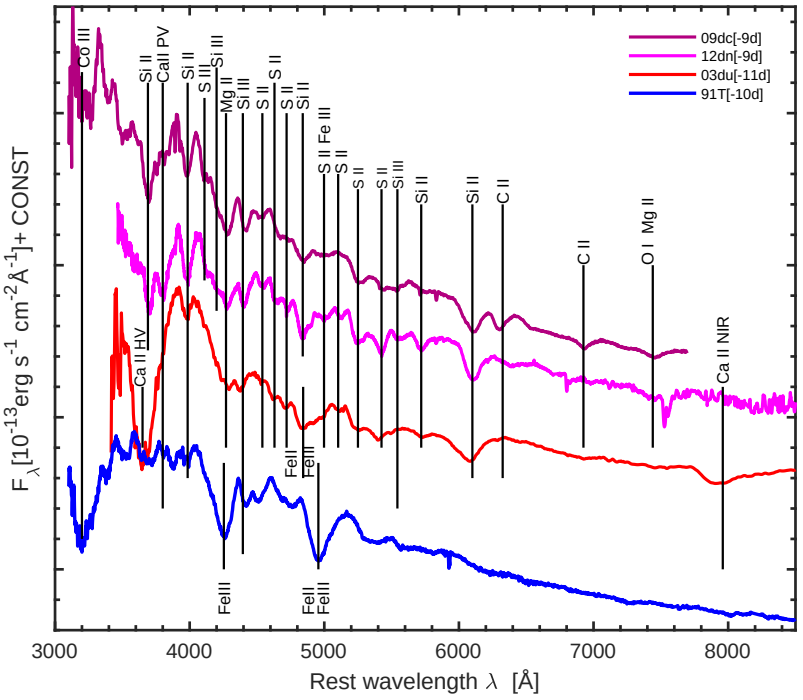


FIGURE 6.1: The early spectra of the 03fg-like, SNe 2012dn, 2009dc compared to SN 1991T, and the normal SN 2003du, highlighting their distinct IME-dominated features and weak Fe III signatures as discussed in the text.

were constructed by Charles J. Aouad. Scientific discussions and manuscript review were provided by C. Ashall, S. Hachinger, and M. Tanaka.

6.2 Data

6.2.1 Host Galaxy, Distance, and Reddening

SN 2012dn was discovered on 2012 July 8.52 UT in the SA(s)cd spiral galaxy ESO462-016 (Bock et al., 2012), which has a redshift of $z = 0.010177$ (Springob et al., 2005).

Estimates of the distance to the host galaxy vary depending on the adopted method. Using the recessional velocity and assuming $H_0 = 72$ km s^{-1} Mpc^{-1}, distance moduli of $\mu = 33.15 \pm 0.15$ mag and $\mu = 33.32 \pm 0.20$ mag have been derived by Chakradhari et al. (2014) and Brown et al. (2014), respectively. Independent determinations based on the Tully–Fisher relation yield $\mu = 33.15 \pm 0.52$ mag (Springob et al., 2007) and $\mu = 33.19 \pm 0.69$ mag (Lagattuta et al., 2013). Additional studies adopt values within this range: $\mu = 33.15 \pm 0.15$ mag (Parrent et al., 2016), $\mu = 33.26 \pm 0.20$ mag (Taubenberger et al., 2019), and $\mu = 33.15$ mag (Yamanaka et al., 2016).

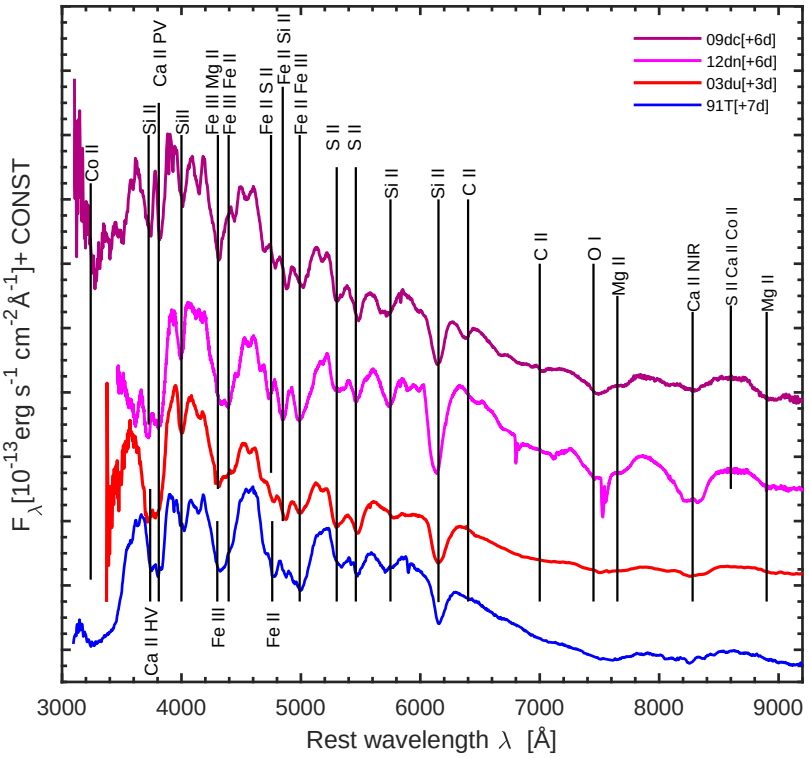


FIGURE 6.2: Spectra one week after B maximum of the 03fg-like, SNe 2012dn, 2009dc compared to SN 1991T, and the normal SN 2003du.

In this work, a distance modulus of $\mu = 33.26 \pm 0.20$ mag is adopted, consistent with Taubenberger et al. (2019). A total reddening of $E(B-V) = 0.09$ is assumed, comprising 0.05 mag from the Milky Way and 0.04 mag from the host galaxy. This value is consistent with Parrent et al. (2016) and Yamanaka et al. (2016) (who adopt $E(B-V) = 0.10$), but is lower than the $E(B-V) = 0.18$ adopted by Chakradhari et al. (2014).

Published values of the light-curve decline rate, $\Delta m_{15}(B)$, also show some dispersion, ranging from 0.92 (Chakradhari et al., 2014, Yamanaka et al., 2016), to 0.97 (Taubenberger et al., 2019), and up to 1.08 (Parrent et al., 2016).

6.2.2 Spectra

The spectra analyzed in this study were obtained from the Weizmann Interactive Supernova Data Repository (WISeREP) (Yaron & Gal-Yam, 2012) and are listed in Table 6.1.

Following Aouad et al. (2022, 2024), the spectra were flux-calibrated in the U, B, V, R, I bands by applying a low-order smoothed spline, as described in section 4.3.1 constructed using the photometric data of Taubenberger et al. (2019).

TABLE 6.1: Spectra of SN 2012dn and modeling parameters.

UT Date 2012	JD[a]	Epoch[b] (days)	Telescope/Instr.	$\log L$ [$L_\odot$]	v (km s^{-1})	$T_{\rm ph}$ (K)
10/07[c]	118.5	−14.1	Gemini-S / GMOS-S	9.10	14000	15100
11/07[d]	119.8	−12.8	Lick-3m / KAST	9.190	13250	13980
14/07[c]	122.5	−10.1	FLWO-1.5M / FAST	9.470	12850	13250
15/07[c]	123.5	−9.8	Gemini-S / GMOS-S	9.500	12550	12990
16/07[d]	125.0	−7.6	Keck1 / LRIS /	9.570	12350	12395
19/07[c]	127.5	−5.1	Gemini-S / GMOS-S	9.600	12000	11398
20/07[e]	129.0	−3.6	ANU-2.3m / WiFes	9.630	11600	11285
23/07[c]	131.5	−1.1	Gemini-N / GMOS	9.670	11200	10800
27/07[c]	135.5	+2.9	Gemini-N / GMOS	9.600	10200	9875
29/07[c]	137.5	+4.9	FTS / FLOYD-S	9.560	9500	9486
30/07[c]	138.5	+5.9	Gemini-N / GMOS	9.550	9100	9438
04/08[c]	146.5	+13.9	FTS / FLOYD-S	9.440	7100	8449
Nebular Phase[f]						
-	423.3	+290.9	ESO 8.2m/FORS2-ISAAC	–	–	–

[a] JD−2,456,000 – [b] Rest-frame time, since B maximum
[c] (Parrent et al., 2016), [d] (Stahl et al., 2020), [e] (Childress et al., 2016), [f] (Taubenberger et al., 2019)

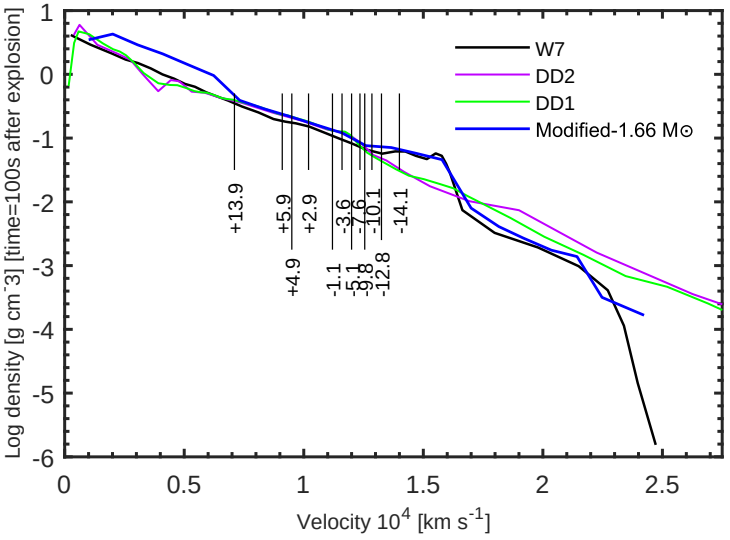


FIGURE 6.3: Density profiles of the W7, DD1, DD2, and DD3 models, each scaled to an epoch of 100 s. The blue line shows the density structure adopted in this work, modified to a total ejecta mass of 1.66 $M_\odot$. Vertical lines mark the photospheric velocities of the synthetic spectra at their respective epochs with respect to B-band maximum light.

6.2.3 Photometric Evolution and Late-Time Dimming

The photometric evolution of SN 2012dn (Taubenberger et al., 2019) exhibits several unusual features. Although its peak luminosity is comparable to that of normal SNe Ia, its post-maximum decline deviates significantly from standard behaviour. Beginning at approximately 60 days after maximum light, the light curves show an accelerated fading relative to normal events.

A comparison with the normal SN 2003du (Fig. 6.4) reveals a nearly wavelength-independent (grey) deficit in luminosity across all *UBVRI* bands, persisting out to ∼300 days (see Secrions 6.5 and 6.4). Similar late-time behaviour has been reported in other 03fg-like candidates, including SN 2006gz (Maeda et al., 2009), LSQ14fmg (Hsiao et al., 2020), and SN 2009dc (Taubenberger et al., 2011). However, in SN 2012dn, the onset of this enhanced fading occurs at significantly earlier epochs.

Several mechanisms have been proposed to explain the rapid late-time decline of SN 2012dn (Taubenberger et al., 2019). Enhanced γ-ray or positron escape appears unlikely. Using the positron-trapping formalism of Jerkstrand (2017), Taubenberger et al. (2019) showed that reproducing the observed late-time luminosity through positron escape alone would require an ejecta mass of only $\sim 0.23, M_{\odot}$, assuming a 40 per cent positron trapping fraction. Such a low ejecta mass is incompatible with the abundance tomography presented in Section 6.6. This estimate already represents the most extreme case of a homogeneous ejecta without magnetic fields. In reality, tangled magnetic fields are expected to trap positrons efficiently, and observational studies of several normal SNe Ia have found no evidence for significant positron escape even at epochs exceeding $\sim$ 800–1000 days (Graur et al., 2016, Kerzendorf et al., 2014, 2017, Leloudas et al., 2009, Shappee et al., 2017). As further noted by Taubenberger et al. (2019), although strong clumping could reduce the positron optical depth, it would simultaneously decrease the γ-ray optical depth, resulting in an early light-curve evolution inconsistent with the observations.

An infrared catastrophe (IRC) is likewise disfavoured. The nebular spectrum remains dominated by thermally excited [Fe II] emission, while the probable detection of [O I] and the observed [Ca II] emission indicate that the ejecta remain in the thermal regime at $\sim$ 300 days, contrary to the expectations of an IRC. More generally, no convincing evidence for an IRC has been reported in any SN Ia (Graur et al., 2016, Kerzendorf et al., 2014, Leloudas et al., 2009).

Taken together, these arguments favour newly formed dust as the most plausible explanation for the observed late-time luminosity deficit (Chakradhari et al., 2014, Nagao et al., 2017, Parrent et al., 2016, Taubenberger et al., 2019, Yamanaka et al., 2016). This interpretation is supported by theoretical models predicting dust condensation in

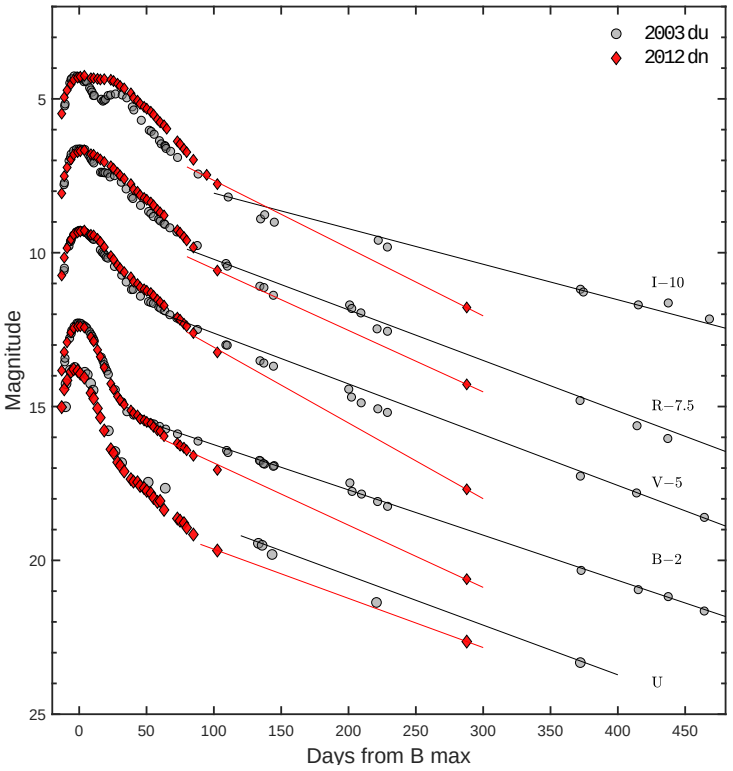


FIGURE 6.4: *UBVRI* light curves or SN 2012dn compared to the ones of SN 2003du (Stanishev et al., 2007) normalized at peak. The evolution of SN 2012dn exhibits a notable wavelength-independent (grey) extinction that persists across all bands through the late phases.

Type Ia ejecta on timescales of $\sim$ 100–300 days (Nozawa et al., 2011), as well as by the delayed onset of the luminosity deficit, which is more naturally explained by dust forming within the expanding ejecta than by pre-existing circumstellar or interstellar dust. The nearly wavelength-independent fading, accompanied by little or no colour evolution, disfavours conventional interstellar-like dust and instead favours either unusually large grains (Aguirre, 1999) or optically thick dust clumps (Taubenberger et al., 2019). In the latter case, the clumps shield newly formed grains from the intense radiation field, allowing smaller grains to survive while naturally producing the observed grey attenuation. Nevertheless, without contemporaneous near- and far-infrared observations, the origin and physical properties of the dust remain poorly constrained.

6.3 Photospheric phase models

A set of 12 spectra, spanning from day -14 to $+14$ relative to B-band maximum, was modelled. Three distinct density profiles were employed (Fig. 6.3), corresponding to different explosion scenarios: W7 (Nomoto et al., 1984)) DD2 and DD1; (Iwamoto et al., 1999)). The input parameters used in the modeling are summarized in Table 6.1. The

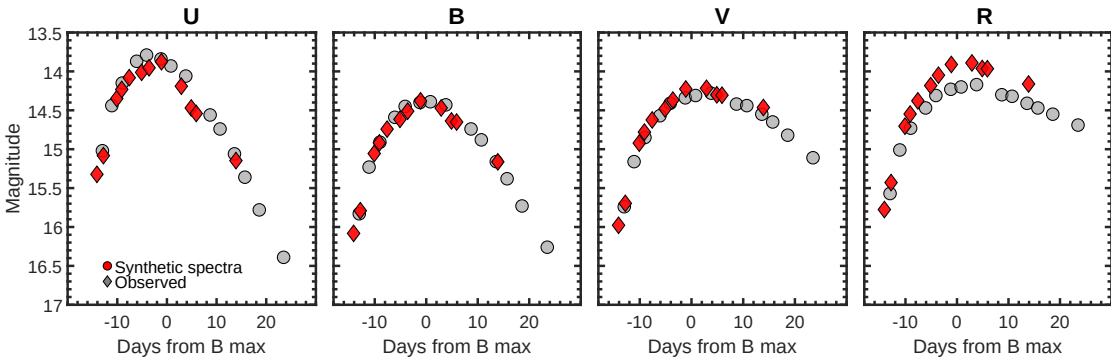


FIGURE 6.5: Light curves from the synthetic spectra compared to the light curves from observation.

resulting synthetic spectra reproduce the observed spectral features and flux distribution across the full wavelength range with a high level of accuracy (see Fig. 6.5).

6.3.1 The pre-maximum spectra

Figures 6.6, 6.7 and 6.8 show synthetic spectra from day −14.1 to day −5.1. At these early phases, the models require higher photospheric velocities than those seen in SNe 2009dc, 1999aa, iPTF16abc, and 2003du at similar epochs. Higher velocities result in lower temperatures for a given luminosity (see Eq 3.15), leading to the low ionization necessary to reproduce the observed spectral features.

Fe-group elements:

Unlike normal SNe Ia, the early spectra of SN 2012dn show no Fe III lines usually prominent near 4250 and 5000 Å. The 4250 Å feature is dominated by Mg II and the 5000 Å feature by Si II $\lambda\lambda$5041, 5056, whereas in 91T-like objects both regions are shaped by strong Fe III absorption. This behaviour is also observed in other 03fg-like events (Ashall et al., 2021, Hicken et al., 2007).

At $v > 15000\,\mathrm{km\ s^{-1}}$, no iron is needed in the models, with an upper limit on the iron mass fraction below 0.0001, well under the solar value ($X(\mathrm{Fe}_\odot) = 0.001$, Asplund et al., 2009). Models with solar or super-solar metallicity overestimate the early flux, worsen the Si II $\lambda\lambda$5041, 5056 fit, introduce unwanted Fe III absorption near 4900 Å, and strengthen the Si III multiplet near 4300 Å, as seen in Fig. 6.9.

The low iron abundance is consistent with the sub-solar metallicities reported for the host galaxy ranging from ~ 0.4 to $0.8\,Z_\odot$ (Childress et al., 2016, Parrent et al., 2016, Taubenberger et al., 2019), and reduces UV line blanketing (Mazzali et al., 2014), explaining the blue pre-maximum $(U-B)$ colours seen in 03fg-like events (Brown et al., 2014, Lu et al., 2021, Taubenberger et al., 2019). The synthetic $(U-B)$ evolution reproduces the

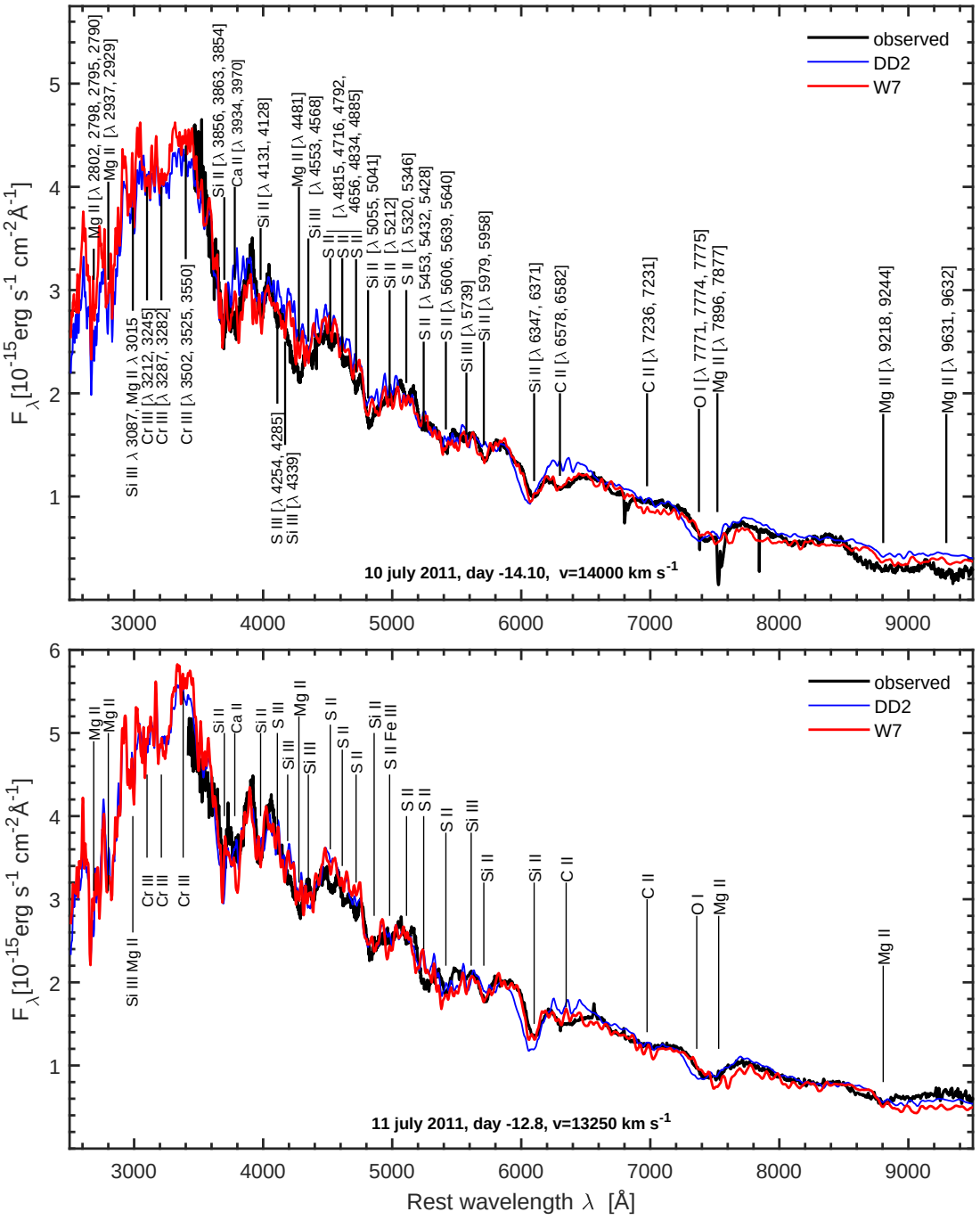


FIGURE 6.6: Early-time spectra of SN 2012dn (at −14.1 and −12.8 days relative to *B*-band maximum) overlaid with the synthetic spectra using the W7 and the DD2 density profiles depicted in red and blue respectively.

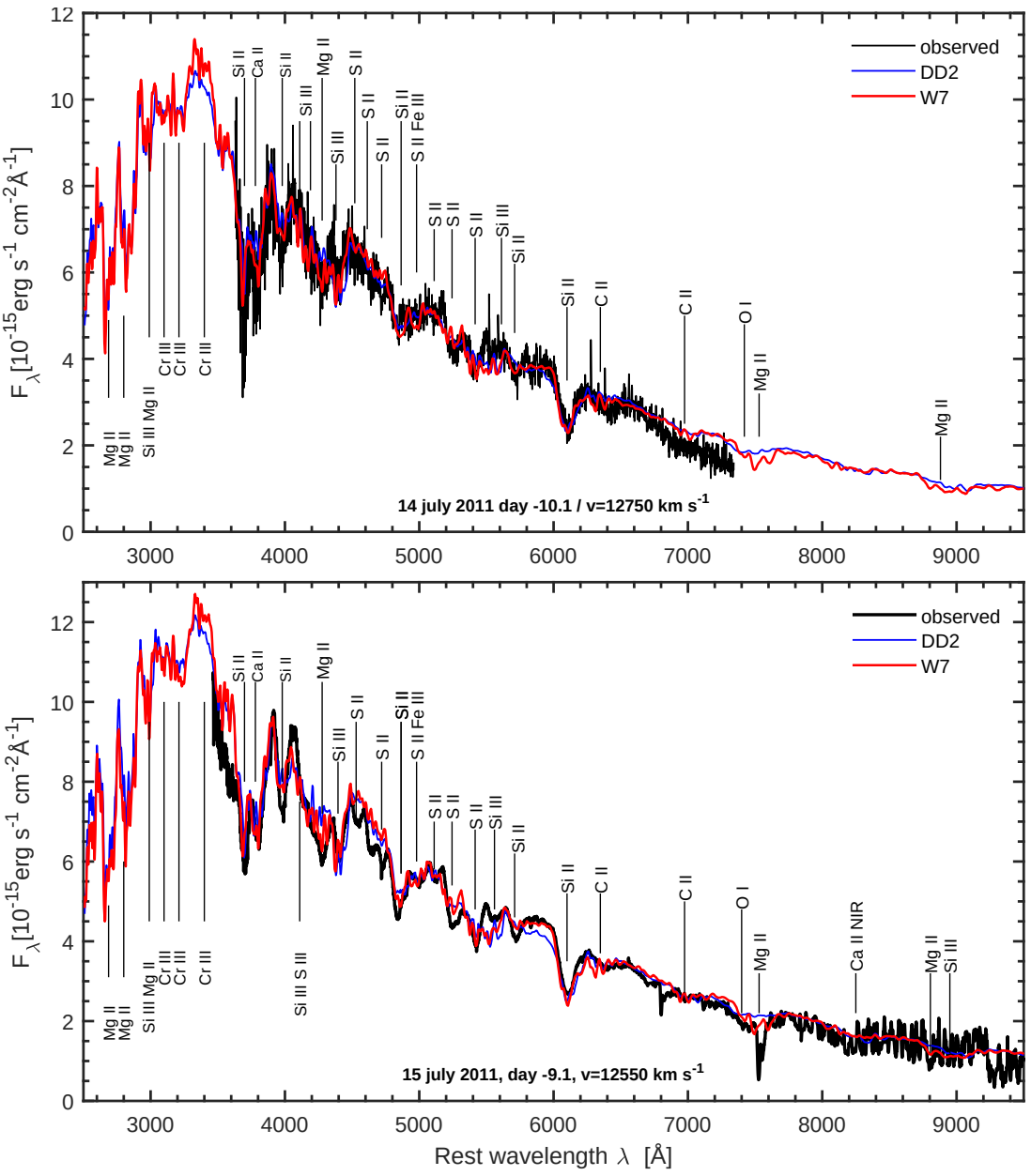


FIGURE 6.7: Early-time spectra of SN 2012dn (at −10.1 and −9.1 days relative to B-band maximum) overlaid with the synthetic spectra using the W7 and the DD2 density profiles depicted in red and blue respectively.

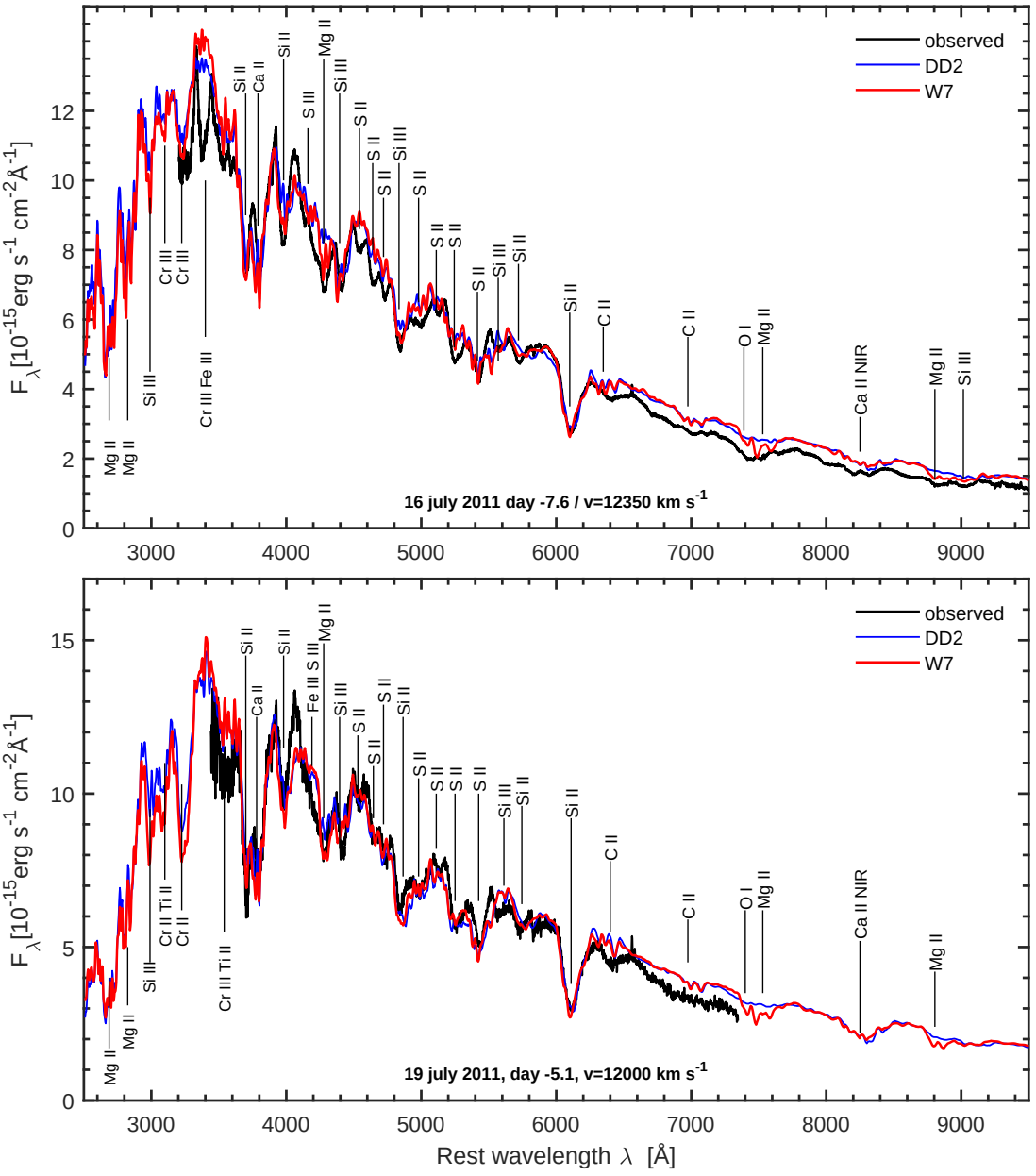


FIGURE 6.8: Early-time spectra of SN 2012dn (at −7.6 and −5.1 days relative to B-band maximum) overlaid with the synthetic spectra using the W7 and the DD2 density profiles depicted in red and blue respectively.

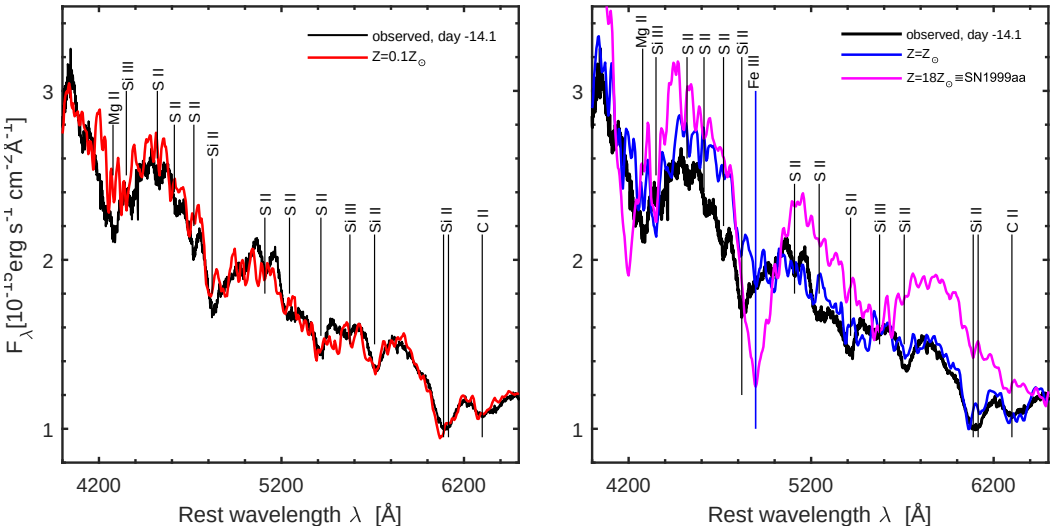


FIGURE 6.9: Comparison of synthetic spectra illustrating the effect of the outer-layer iron abundance. Left panel shows the day −14 spectrum with a sub-solar model ($Z = 0.1\,Z_\odot$) at $v > 15,000$ km s^{-1}. Right panel compares solar (blue) and super-solar (purple; matching SN 1999aa) abundances. Solar and super-solar abundances fail to replicate the observed spectral features. Furthermore, they enhance backscattering, heating the photosphere and shifting the ionization balance from Si II toward Si III. This results in the unobserved strengthening of the Si III $\lambda\lambda$4552, 4567, 4574 multiplet near 4300 Å, which is absent in the observed spectra of SN 2012dn.

observations well (Fig. 6.10), supporting a low-metallicity progenitor for the 03fg-like subclass (Ashall et al., 2021, Childress et al., 2011). By contrast, the outer layers of SN 2003du contain 30–50 times more stable iron than SN 2012dn (Tanaka et al., 2011), and 91T-like events such as SNe 1999aa and 1991T show even higher iron abundances in these regions (Aouad et al., 2022, 2024, Tanaka et al., 2008, 2011).

Moving inward, the iron mass fraction increases to 0.1 at 12000–12300 km s^{-1}. This quantity is required in the models to absorb UV flux and redistribute it to longer wavelengths. At such early phases this must be stable iron (i.e., ^{54}Fe), as ^{56}Ni could not yet have decayed. This iron is therefore the product of explosive nucleosynthesis (Aouad et al., 2022, Tanaka et al., 2011).

The ^{56}Ni mass fraction is set to 0.001 at 14000–15000 km s^{-1}, increasing to 0.1 at 12000–12300 km s^{-1}, though it remains poorly constrained as the available spectra do not cover the Co III $\lambda\lambda$3287, 3305 typical diagnostic line near 3200 Å.

Calcium: Unlike normal SNe Ia, SN 2012dn shows a faint HV Ca II H&K line (Ashall et al., 2021, Taubenberger et al., 2019), with no clear HV component; the blue-side absorption is instead attributed to Si II $\lambda\lambda$3854, 3856, 3863, and only the PV component is very weakly present. In normal and transitional events these two components merge

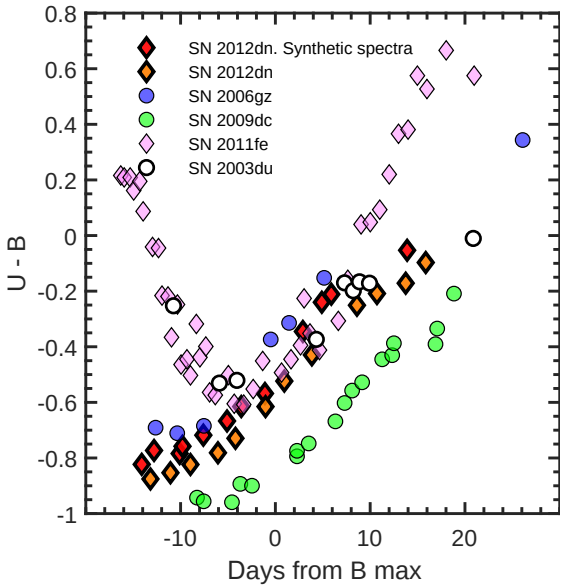


FIGURE 6.10: U–B colour evolution of SN 2012dn compared with synthetic spectra and other SNe (Taubenberger et al., 2019). The 03fg-like events exhibit notably blue pre-maximum colourss, likely due to a lack of iron-group elements (IGEs) reducing UV line blanketing (Mazzali et al., 2014). This contributes to the distinct early colour evolution observed in this subclass.

into a single deep feature (Aouad et al., 2022, 2024), whereas in iPTF16abc this region is dominated by Si III and Co III rather than Si II (Aouad et al., 2024, Liu et al., 2024), further reflecting the lower ionization state of SN 2012dn compared to 91T-like events.

No calcium is required at $v > 16000\,\mathrm{km\ s^{-1}}$, with a mass fraction of 5×10^{-4} at 15000–16000 km s^{-1}, rising to 0.05 at 12500–13500 km s^{-1}. The Ca II NIR triplet in SN 2012dn shows an intermediate behaviour. It is weak at early epochs and becomes clearly visible only at day −7.6. This is later than in normal SNe Ia, where the feature is strong from the earliest epochs, but earlier than in 91T-like events, where it only emerges after maximum light. Separating abundance and ionization effects on the Ca II line is difficult, but given the generally low ionization state of SN 2012dn, the absence of HV Ca II is more likely an abundance effect (Aouad et al., 2022, 2024, Mazzali et al., 2005b).

Silicon, sulphur, magnesium: The early spectra of SN 2012dn are characterised by multiple narrow Si II and S II lines, a defining trait of this subclass (Ashall et al., 2021). The Si II λ6355 and Si II λ5972 lines are visible from the earliest epochs, and the depth ratio $\mathcal{R}$(Si II), a key ionization diagnostic (Hachinger et al., 2008, Nugent et al., 1995b), is well reproduced by the models, indicating a well-constrained temperature and ionization structure.

The Si II λ4130 line is notably stronger than in normal and 91T-like SNe. Si II $\lambda\lambda$3854, 3856, 3863 produces a deep absorption blueward of the Ca II H&K photospheric component near 3700 Å, a feature absent in both normal and 91T-like events. The absorption near 4850 Å, typically dominated by Fe III in normal and 91T-like SNe, is here reproduced by Si II $\lambda\lambda$5041, 5056. The Si III $\lambda\lambda$4553, 4568 feature near 4400 Å is well reproduced, and a feature near 5600 Å, suggested by Taubenberger et al. (2011) to be a blend of Na I D and Si II, is instead identified as Si III λ5739.

The *W*-shaped S II feature near 5400 Å is visible from early epochs and well reproduced, as is the S II $\lambda\lambda$5320, 5346 feature near 5050 Å, uncommon in normal and 91T-like SNe. The Mg II λ4481 line near 4200 Å is well replicated, and Mg II λ7896 blends with O I λ7771 near 7400 Å. A feature near 8800 Å from Mg II $\lambda\lambda$9218, 9244 is present from early epochs, splitting into two components at day −7.6, with the redder component influenced by Si III λ9323 (Fig. 6.8). A magnesium mass fraction of $X(\mathrm{Mg}) = 0.1$ is adopted between 14000 and 16500 km s^{-1}.

Carbon, Oxygen: Carbon lines are consistently visible from the earliest spectra in 03fg-like events (Ashall et al., 2021, Hicken et al., 2007, Taubenberger et al., 2011). In SN 2012dn, both C II λ6580 and C II λ7234 are visible from day −14.1 and persist as the spectra evolve. Carbon lines appear sporadically in normal SNe Ia and are less common in 91T-like events, though they have been observed in iPTF16abc and SN 2023wrk. In these events, however, the behaviour is peculiar: the lines fade and then reappear after maximum light, possibly reflecting a pulsation-driven detonation, mixing, or clumps of unburned material along the line of sight (Aouad et al., 2024, Dessart et al., 2014, Ivanova et al., 1974, Khokhlov, 1991a, Liu et al., 2024). In SN 2012dn, however, carbon remains present continuously down to deeper layers, pointing to a large reservoir of unburned material in the ejecta. The carbon mass fraction is set to 0.3 at 16000–20000 km s^{-1}, decreasing to 0.01 at 13000–15000 km s^{-1}. The right panel of Fig. 6.11 shows how carbon was constrained in these layers.

The O I λ7771 line near 7400 Å, blended with Mg II on its red side, is visible from day −14.1 and well reproduced by the models. Oxygen mass fraction decreases from 0.7 above 16000 km s^{-1}, to 0.024 at $v \leq 12000$ km s^{-1}.

6.3.2 The spectra near maximum light

Figures 6.12 and 6.13 show synthetic and observed spectra from day −3.6 to +4.9. As the supernova approaches maximum, the spectra develop broader features and emerging Fe lines, resembling normal SNe Ia. Photospheric velocities remain elevated maintaining

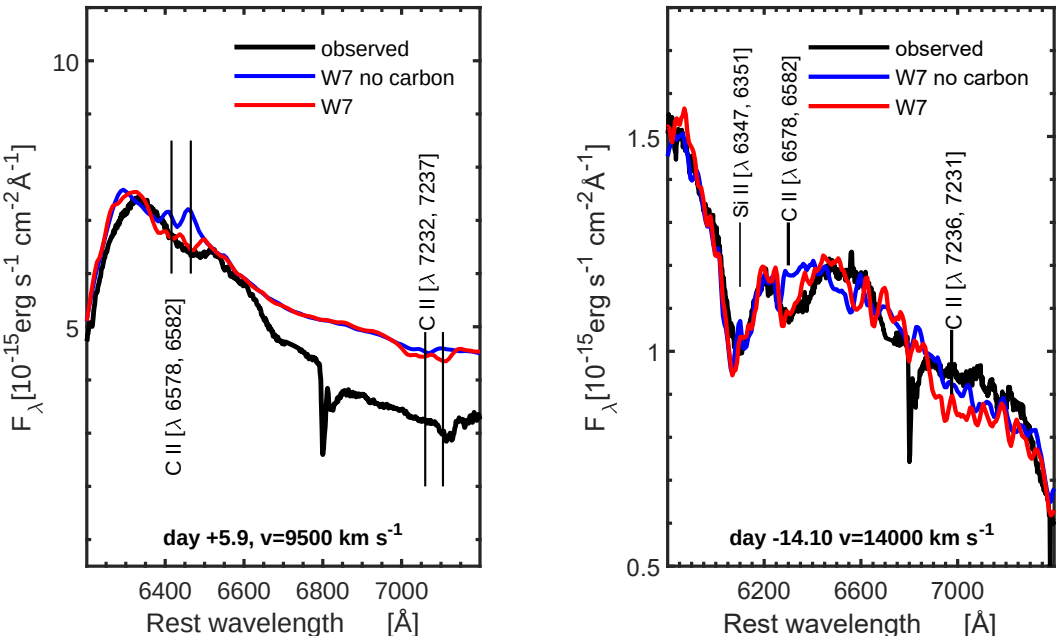


FIGURE 6.11: Comparison between a synthetic model excluding carbon (blue) and a model incorporating 0.01 $M_\odot$ of carbon ($X(C) = 0.05$) within the velocity range 9,100 $< v <$ 10,200 km s^{-1} (red) is shown in the left panel. The right panel displays the results for the outer layers, where the observed C II feature near 6200 Å is accurately reproduced by including 0.003 $M_\odot$ of carbon at $v >$ 14,000 km s^{-1} (red).

the low-ionization conditions needed to match the observed spectra. This slow velocity evolution implies slower transition to the nebular phase than standard events.

Fe-group elements:

From day −1.1, the feature near 4300 Å deepens due to emerging Fe III $\lambda\lambda$4419, 4431, 4395 and Mg II λ4481, while the redder component near 4400 Å remains dominated by Si III $\lambda\lambda$4553, 4568. The feature near 5000 Å remains split into two components: the red wing transitions from S II to Fe III $\lambda\lambda$5156, 5127, while the blue wing remains attributed to Si II $\lambda\lambda$5041, 5056. This differs from normal and 91T-like SNe where this region appears as a broad blend of Fe II and Fe III lines. A comparison is presented in Fig. 6.14.

The stable iron abundance increases from 0.07 to 0.21 at $v >$ 9600 km s^{-1}, an increase required to reproduce the absorption near 5000 Å (Fig. 6.15), with the remaining iron originating from ^{56}Ni decay. The ^{56}Ni mass fraction reaches 0.45 in the shell between 9500 and 10200 km s^{-1}.

Calcium: The feature near 3800 Å remains a blend of Si II $\lambda\lambda$3856, 3863 on the blue side and photospheric Ca II H&K on the red side, with no HV component, contrasting with normal and 91T-like events where deep HV Ca II H&K is present at this epoch. The

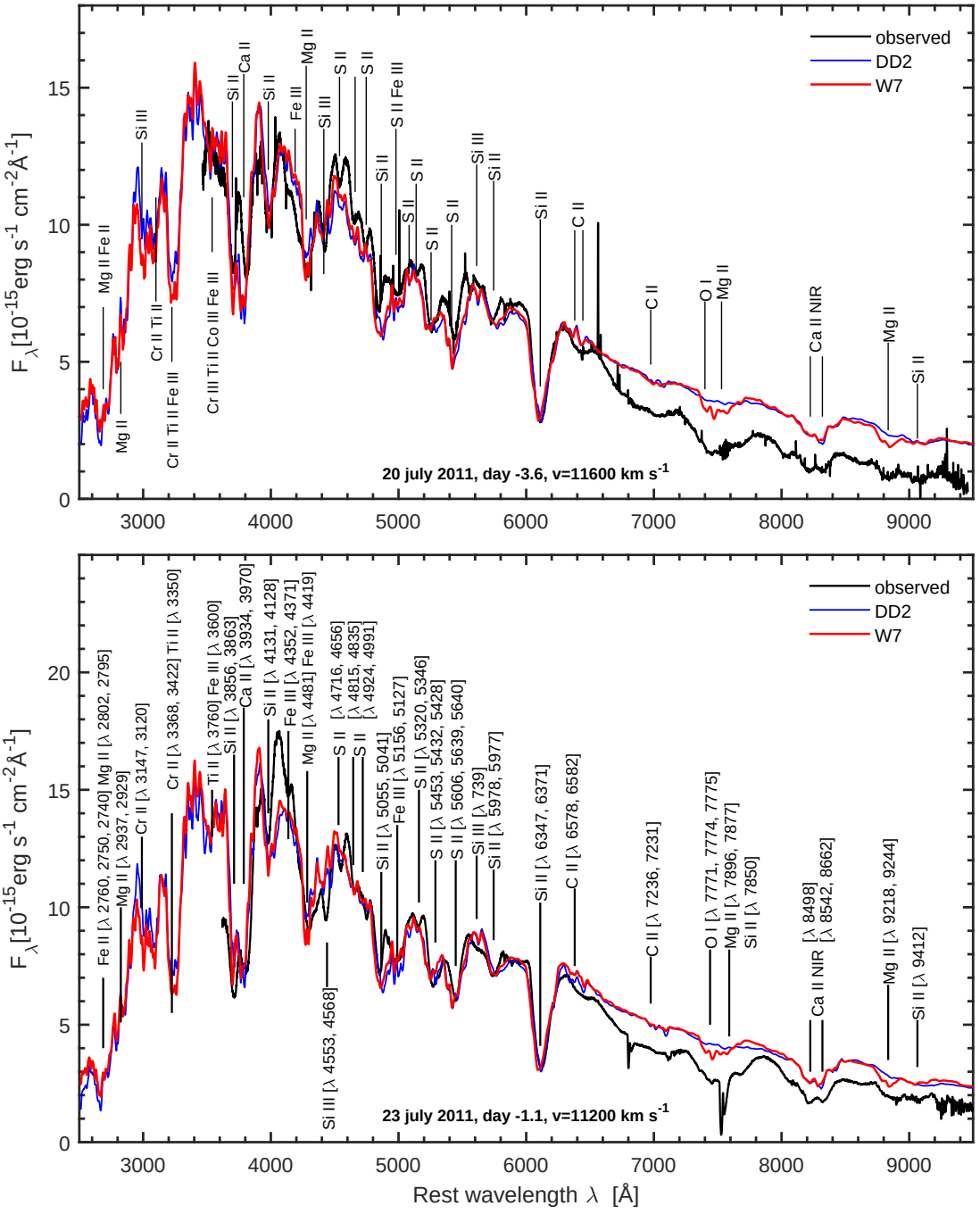


FIGURE 6.12: Spectra of SN 2012dn near maximum light (at −3.6 and −1.1 days relative to B-band maximum) overlaid with the synthetic spectra using the W7 and the DD2 density profiles depicted in red and blue respectively.

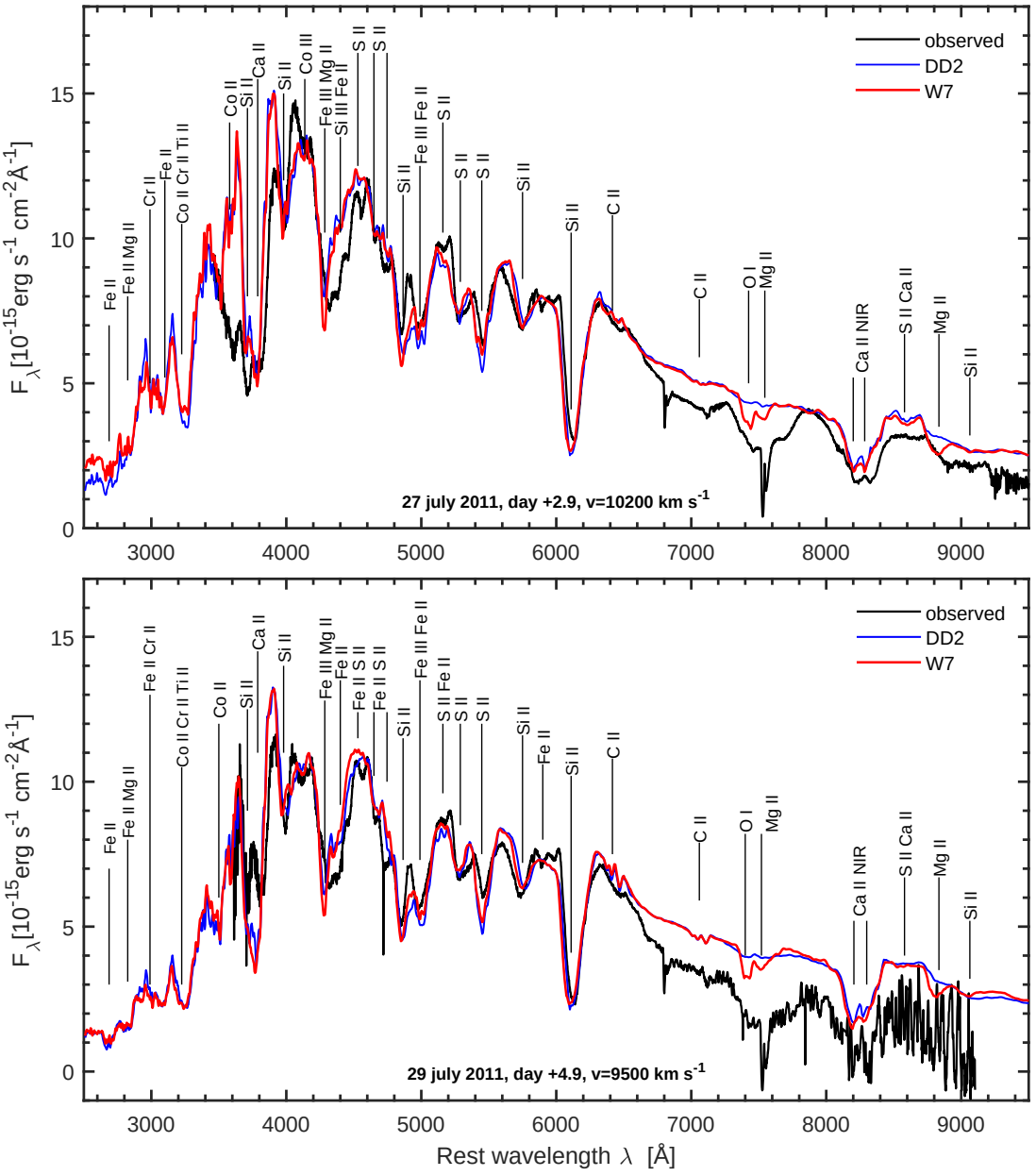


FIGURE 6.13: Spectra of SN 2012dn near maximum light (at +2.9 and +4.9 days relative to B-band maximum) overlaid with the synthetic spectra using the W7 and the DD2 density profiles depicted in red and blue respectively.

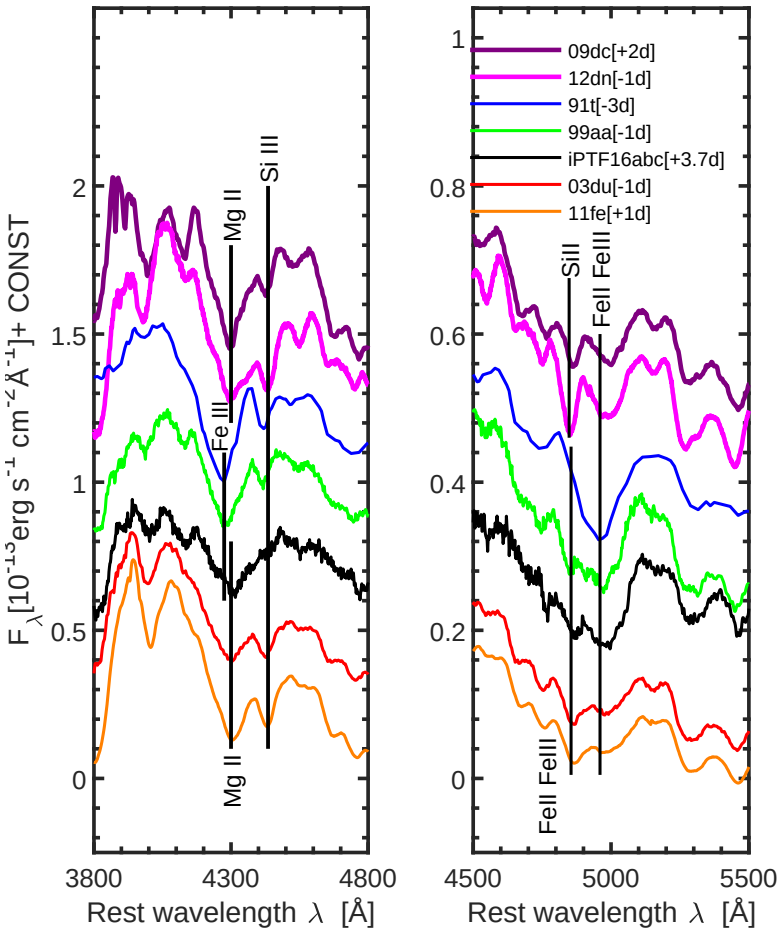


FIGURE 6.14: Left: The 4300 Å region shows Fe III absorption characteristic of 91T-like SNe, whereas Mg II dominates this feature in normal and 03fg-like SNe. The Si III contribution remains consistent across all types. Right: The 5000 Å region distinguishes 03fg-like events, where the blue component is driven by Si II $\lambda\lambda$5041, 5056, unlike the Fe II/Fe III blend seen in normal and 91T-like objects. The degree of blending of the two components reflects the temperature: they are well separated in 03fg-like events but gradually merge into a single absorption feature in the hottest SN 1991T.

Ca II NIR triplet strengthens and splits into two components, well reproduced by the models without requiring additional calcium in these layers.

Silicon, Sulphur, Magnesium: Both Si II λ6355 and λ5972 deepen, with $\mathcal{R}$(Si II) well reproduced, while Si III λ5739 weakens and disappears by day +2.9. The feature near 4400 Å transitions from two distinct components to a single broad absorption, now dominated on the red side by Fe II and Fe III replacing the earlier Si III $\lambda\lambda$4553, 4568 while the blue side remains shaped by Mg II/Fe III. The blue component of the 5000 Å feature remains dominated by Si II $\lambda\lambda$5041, 5056, forming a narrow absorption absent in normal and 91T-like SNe where a broad Fe II/Fe III blend is seen instead. A comparison can be

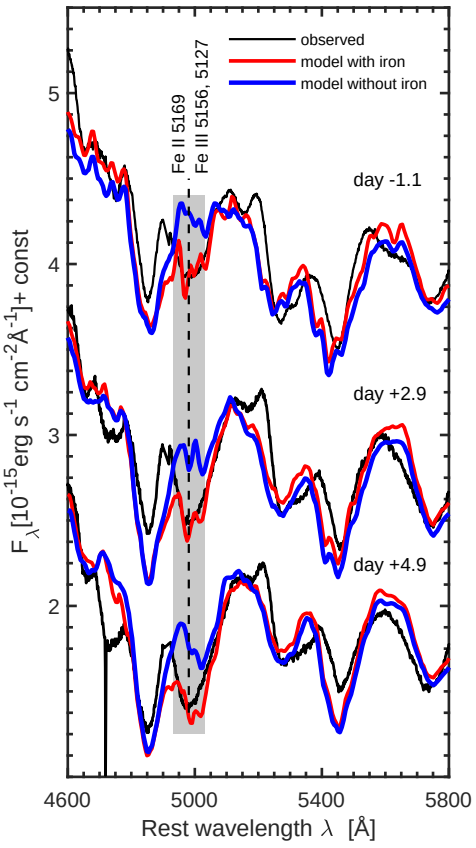


FIGURE 6.15: Comparison of synthetic spectra illustrating the effect of the stable iron abundance in the intermediate shells. A stable iron abundance at the 10% level (increasing from 7% to 21% across the shells) is required to reproduce the absorption feature near 5000Å, which is dominated by a complex of Fe II and Fe III lines.

seen in Fig. 6.14. This double narrow profile is a distinctive characteristic of SN 2012dn and other 03fg-like events. The Si II λ4130 line remains deep and well reproduced.

The *W*-shaped S II feature near 5400 Å remains well reproduced. A blend of S II lines still dominates the 4500–4700 Å region. A blend of S II λ8859 and Ca II $\lambda\lambda$8912, 8927 flattens the emission redward of the Ca II NIR triplet (Fig. 6.13, day +2.9). The silicon mass fraction is adopted as 0.5 at 11600–12000,km s^{-1}, decreasing to 0.2 at $v > 9500$,km s^{-1}, while the sulphur mass fraction decreases from 0.2 to 0.07 over the same range.

Mg II still contributes near 4400 Å, though Fe III increasingly dominates at this epoch. The features near 7500 and 8800 Å are well reproduced with no magnesium required in these layers, consistent with the W7 model (Iwamoto et al., 1999, Nomoto et al., 1984).

Carbon, Oxygen: C II λ6580 remains visible near maximum while λ7234 weakens, both well reproduced by the models. The carbon mass fraction is sustained at 0.05 down to $v > 9500$ km s^{-1}, an order of magnitude higher than in normal SNe Ia (Tanaka et al.,

2011) and consistent with values derived for SN 2009dc (Hachinger et al., 2012). The left panel of Fig. 6.11 illustrates how the carbon abundance is constrained at these velocities.

6.3.3 The spectra post-maximum light

Synthetic spectra for days +5.9 and +13.9 are presented in Fig. 6.16. At these epochs the photosphere has receded into the ^{56}Ni-dominated region, as a consequence, the assumption of a sharp blackbody-emitting surface becomes inadequate. In reality, a significant fraction of radioactive energy is deposited above the photosphere, a physical effect that is not captured by the code's assumption of a blackbody-emitting surface located at the photosphere. This results in a synthetic flux excess beyond 6000 Å, though line formation and ionization conditions in the ejecta are not affected.

Fe-group elements: The feature near 4400 Å becomes dominated by blended Fe II and Fe III absorptions as Mg II and Si III weaken. The 5000 Å feature remains split, with Si II on the blue wing and Fe II/Fe III on the red. This behaviour is similar to that of normal SNe Ia (Tanaka et al., 2011) but contrasts with 91T-like events where higher ionization suppresses the Si II contribution (Aouad et al., 2022, Sasdelli et al., 2014). By day +14, the feature near 4000 Å is increasingly blended with Fe II and Co II, and the emission redward of the Ca II NIR triplet is entirely dominated by Co II; at these epochs a significant fraction of ^{56}Ni has already decayed. The ^{56}Ni mass fraction does not exceed 0.45, with a total iron abundance of ∼0.27, approximately half from ^{56}Ni decay and half from explosive nucleosynthesis.

Calcium: The feature near 3800 Å remains dominated by photospheric Ca II with a minor Si II contribution on the blue side, and the Ca II NIR triplet maintains a double-component profile. No calcium is required in these layers to fit the absorption, though a small fraction is needed to account for later nebular-phase emission.

Silicon, Sulphur, Magnesium: The Si II λ6355 and λ5972 lines continue to deepen, with $\mathcal{R}$(Si II) still well reproduced. However, the velocity of Si II λ6355 could not be fully matched to the observed one, likely due to emerging Fe II blending on its blue wing, as also seen in SN 2009dc (Hachinger et al., 2012). The blue component near 4800 Å continues to be shaped by Si II $\lambda\lambda$5041, 5056 and Fe II.

The absorption near 4000 Å, previously dominated by Si II λ4130, transitions to Fe II and Co II by day +14, and the W-shaped S II feature near 5400 Å fades progressively, becoming barely visible by day +14. The 4500–4700 Å region, formerly shaped by S II, is now dominated by Fe II lines. The silicon mass fraction decreases to 0.12 and sulphur to 0.05 in the range 7500–9100 km s^{-1}.

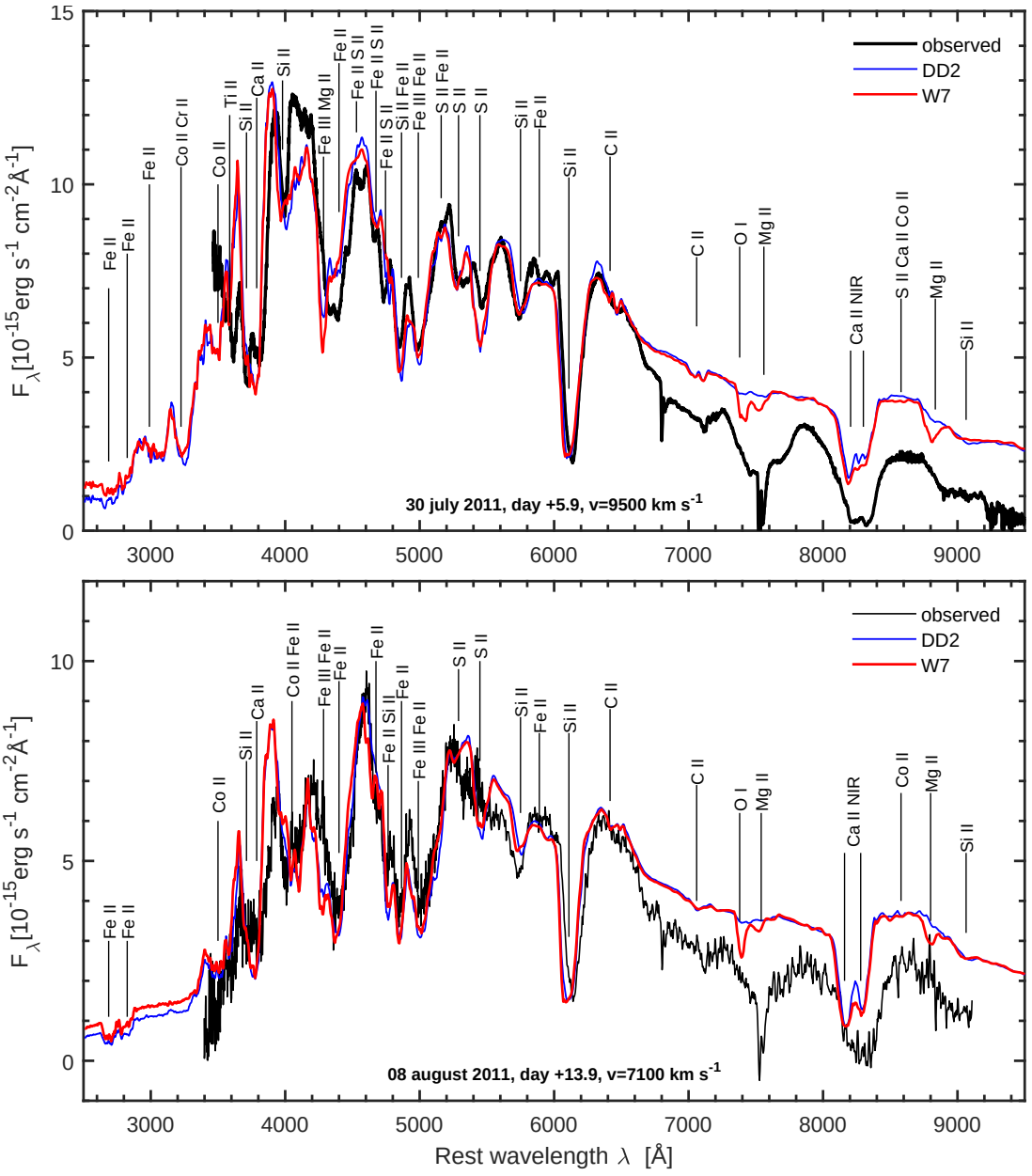


FIGURE 6.16: Spectra one week after maximum light (at +5.9 and +413.9 days relative to B-band maximum) of SN 2012dn overlaid with the synthetic spectra using the W7 and the DD2 density profiles depicted in red and blue respectively.

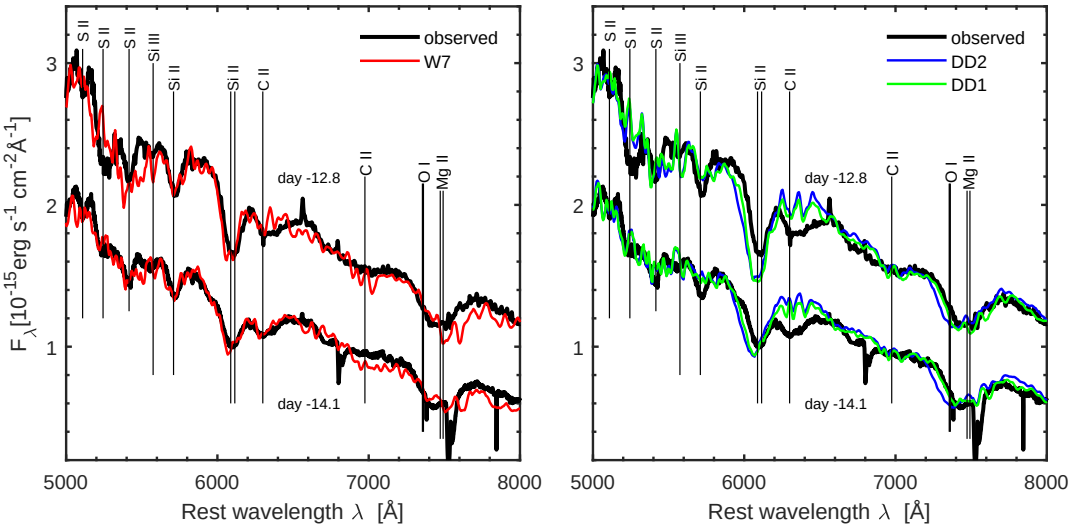


FIGURE 6.17: Comparison of observed and synthetic spectra at days −14 and −13 is presented. The W7 model successfully reproduces the narrow Si II feature near 6000 Å, the Mg II O I blend near 7400 Å, and the Si II feature near 5800 Å, which the DD models fail to capture.

Mg II near 4400 Å weakens progressively, fully replaced by Fe II and Fe III by day +14, though it remains detectable near 7500 Å and in the 8800–9000 Å region, where the feature redward of the flat-topped 8500 Å profile is formed by Mg II λλ9218, 9244.

Carbon, Oxygen: Carbon is required at $X_C = 0.05$ between 7100–9100 km s^{-1} to reproduce the C II λ6580 and λ7234 features. This is supported by the observed velocity evolution of C II λ6580, which decreases from ∼12500 to ∼5900 km s^{-1}, confirming the presence of unburned material at these depths. Oxygen is required in comparable abundances to fit the O I λ7774 feature.

6.3.4 Comparison Between W7 and DD profiles: Density structure and its effect on line formation

Compared to delayed-detonation models (DD1, DD2), W7 better reproduces the IME features as shown in Fig. 6.17. The extended outer density structures of DD models lower the ionization at high velocities, producing overly broad and blueshifted absorptions. In contrast, the density enhancement in W7 at 12000–16000 km s^{-1} (Fig. 6.3) promotes recombination, effectively confining these species to a narrower velocity shell. Ionization analysis (Fig. 6.18) confirms that the ion fractions of Si II, Mg II, S II, and O I peak sharply within this density bump, resulting in the narrower absorption troughs seen in the synthetic spectra and mirroring the observed profiles with good accuracy.

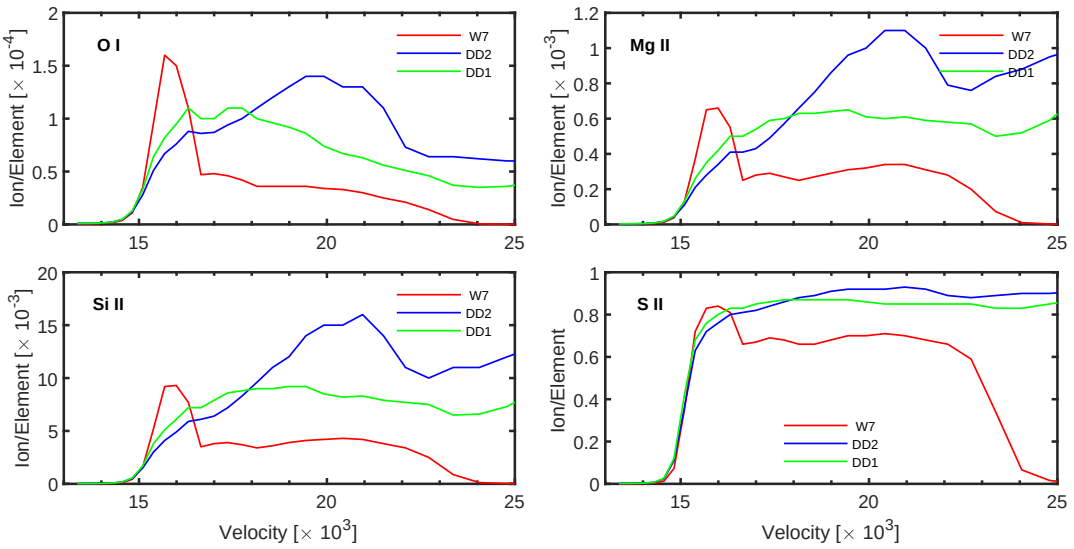


FIGURE 6.18: Ionization conditions in the ejecta at day −13. In the W7 model, the density bump enhances recombination and lowers the overall ionization level, confining singly ionized Mg, Si, and S, as well as neutral O, within a narrow velocity region around ∼16,000 km s^{-1}. In contrast, the DD1 and DD2 profiles distribute these ions over a broader velocity range, causing line formation to occur across a more extended region of the ejecta and producing correspondingly bluer line wings (see Fig. 6.17).

6.4 The Nebular Phase

The nebular spectrum of SN 2012dn is unusual among SNe Ia: it lacks strong [Fe III] emission near 4850 Å and, more strikingly, shows [O I] $\lambda\lambda$6300, 6363, rarely seen in SNe Ia. This comes together with an unexpectedly low late-time luminosity, a property shared with the prototypical "super-chandra" SN 2009dc (Taubenberger et al., 2011). Despite these peculiarities, the nebular spectrum was modelled to complete the tomographic description of the ejecta using the code described in Mazzali et al. (2020) and described in Sec. 4.5, constrained by two key features: the [O I] emission at low velocity, requiring a small mass of oxygen at $v \lesssim 4000$ km s^{-1} additional to the SN ejecta, and the sharp light curve decline after day ∼100, which appears roughly constant across all photometric bands (see Fig. 6.4). This grey dimming consistent with wavelength-independent (grey) extinction. To quantify this dimming, two approaches were used, one by comparing the weighted flux attenuation for each individual band relative to the normal SN 2003du at day 290, and the second, by independently evaluating the late-time bolometric light-curve trends (see also Fig. 4 of Taubenberger et al. 2019). Both approaches yield a consistent dimming factor of 4–5 (as computed in section 6.5).

Dust formed within the ejecta can produce asymmetric nebular emission-line profiles. As first discussed by Lucy et al. (1991), this effect arises because photons emitted from the receding side of the ejecta traverse a larger dust optical depth than those emitted

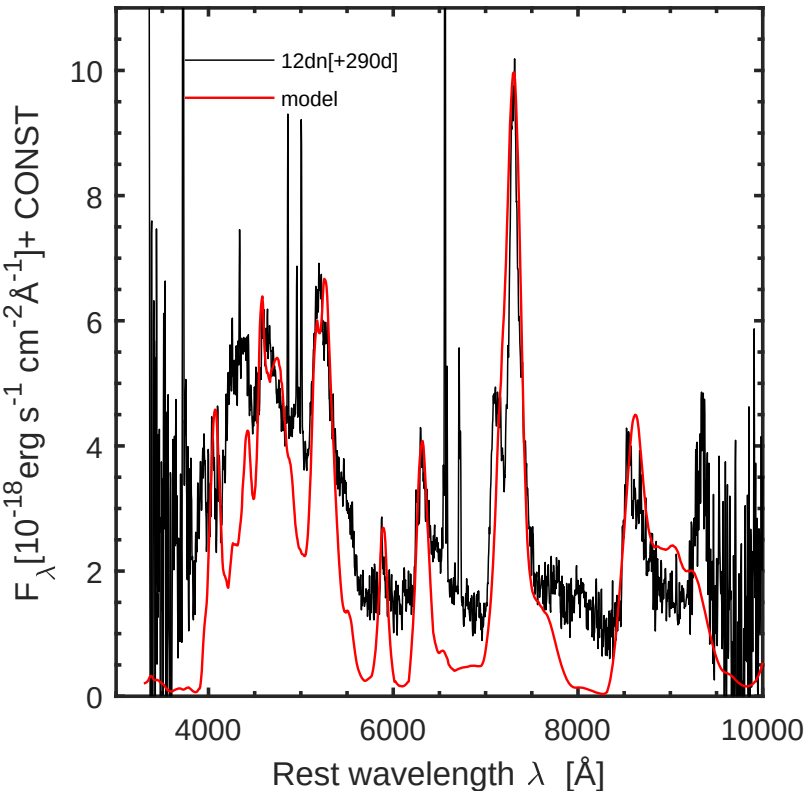


FIGURE 6.19: Nebular spectrum at 290 days after B maximum light. The red line is the model.

from the approaching side, preferentially attenuating the red side of the line profile and producing a blueshifted asymmetry. The magnitude of this effect depends critically on the spatial distribution of the dust relative to the line-forming region. If the dust is uniformly mixed throughout the ejecta, photons from the receding side encounter a substantially larger dust column, resulting in a pronounced asymmetry. In contrast, if the dust is concentrated in a shell surrounding the central line-forming region, the difference in optical depth between the approaching and receding sides is much smaller, leading to significantly weaker line-profile asymmetries. Detailed radiative transfer calculations by Bevan & Barlow (2016) further demonstrate that the degree of asymmetry also depends on the shell geometry, including its inner and outer radii, thickness, expansion velocity, dust optical depth, and albedo.

To account for this dimming, two models were constructed with a ^{56}Ni mass four and five times that required to fit the observed nebular spectrum, with the resulting spectra scaled down accordingly. Additionally, some mass (0.3 $M_\odot$) was added at low velocities below 7000 km s^{-1}, composed of ∼20 per cent oxygen, ∼30 per cent ^{56}Ni, and the remainder IME, giving a total ^{56}Ni mass of 0.45–0.49 $M_\odot$ and bringing the total mass to 1.66 $M_\odot$. The result for the spectrum dimmed by a factor of four is shown in Fig. 6.19. The factor-of-five model is indistinguishable.

TABLE 6.2: Band-dependent extinction values, corresponding flux transmission factors, SED fractions, and weighted transmitted flux contributions used to estimate the bolometric attenuation.

	U	B	V	R	I	Sum
Extinction (mag)	0.78	1.68	2.10	1.07	1.60	
Transmitted flux fraction $_a$	0.49	0.21	0.14	0.37	0.23	
Bolometric flux weight $_b$	0.02	0.45	0.24	0.15	0.14	**1.00**
Weighted transmitted flux $_{(a\times b)}$	0.01	0.10	0.03	0.06	0.03	**0.23**

Another SN Ia which is known to have shown [O I] emission at late times is SN 2010lp (Taubenberger et al., 2013a). This is a low-luminosity 91bg-like event whose nebular spectra were reproduced with ≈0.18 $M_\odot$ of ^{56}Ni and, to replicate the oxygen nebular line emission, 0.04 $M_\odot$ of oxygen at low velocities (Mazzali et al., 2022), a model consistent with a sub-Chandrasekhar progenitor. Interestingly, SN 2010lp showed multiple emission peaks, an observation interpreted as two blobs of material moving in opposite directions pointing to a double-degenerate merger origin. Although such a double profile is not observed in SN 2012dn, the derived oxygen mass is nonetheless consistent with the high-mass DD merger model of Kromer et al. (2013b); other instances include ASASSN-20jq, attributed to an off-centre delayed detonation in a M_{ch} WD (Bose et al., 2025, Hoeflich et al., 2021), and iPTF14atg, where low signal-to-noise precluded detailed analysis (Kromer et al., 2016).

6.5 Estimating of the Bolometric Dimming Factor

To estimate the bolometric extinction, the *UBVRI* light curves of SN 2012dn were normalised to those of the normal SN Ia 2003du at peak brightness (Fig. 6.4), and the residual offset between the two was taken as a measure of the additional extinction; for each band, the corresponding transmitted flux fraction was derived from the measured extinction and weighted according to the contribution of that band to the total bolometric flux, with the adopted weights listed in Table 6.2. The sum of the weighted fractions indicates that only ∼23 per cent of the intrinsic bolometric flux is transmitted, implying a dimming factor of 4.5 ± 0.5, a result independently supported by the nebular bolometric luminosity of SN 2012dn relative to SN 2003du at the same epoch, where the light curve of Taubenberger et al. (2019) points to an attenuation of ∼0.6 dex and the pseudo-bolometric light curve derived in this work (Fig. 6.22) gives ∼0.7 dex, both consistent with a dimming factor in the range 4–5.

TABLE 6.3: Nucleosynthetic yields and kinetic energies from the modelling compared to the original hydrodynamic models. Results from other SNe are also shown.

	^{56}Ni $M_\odot$	Fe [a] $M_\odot$	Ni_{stable} $M_\odot$	IME [b] $M_\odot$	O $M_\odot$	IME/Fe [c]	E_k 10^{51} ergs
2012dn	0.45	0.11	0.000	0.68	0.33	1.21	1.4
original W7	0.59	0.16	0.1220	0.24	0.143	0.27	1.30
original DD2	0.69	0.10	0.0540	0.33	0.066	0.39	1.40
original DD3	0.77	0.10	0.0664	0.25	0.056	0.27	1.43
iPTF16abc [d] (DD2)	0.76	0.20	0.0060	0.19	0.21	0.20	1.32
1991T [e] (DD3)	0.78	0.15	0.0006	0.18	0.29	0.19	1.24
1999aa [f] (DD2)	0.65	0.29	0.0060	0.20	0.22	0.21	1.32
2003du [g] (W7)	0.62	0.18	0.0240	0.26	0.23	0.32	1.25
2002bo [h] (W7)	0.49	0.27	0.0001	0.28	0.11	0.37	1.24
2004eo [i] (W7)	0.32	0.29	0.0005	0.43	0.30	0.70	1.10

[a] Stable isotopes excluding ^{56}Fe; [b] ^{28}Si + ^{32}S; [c] ^{56}Ni + ^{54}Fe + ^{58}Ni; [d] Aouad et al. (2024), [e] Sasdelli et al. (2014), [f] Aouad et al. (2022), [g] Tanaka et al. (2011), [h] Stehle et al. (2005), [i] Mazzali et al. (2008).

6.6 Abundance Tomography

The derived abundance distribution is summarised in Table 6.3 and Fig. 6.20. While broadly similar to a normal SN Ia, it exhibits large-scale mixing. Oxygen extends deep into the core, reaching a total mass of $\sim$0.33 $M_\odot$, with $\sim$0.1 $M_\odot$ located below 3000 km s^{-1}, essential for reproducing the [O I] $\lambda\lambda$6300, 6364 nebular emission. Carbon similarly persists down to $v \approx 6000$ km s^{-1}, with a mass of 0.03 $M_\odot$. Neutron-rich stable iron-group elements (^{54}Fe, ^{58}Ni) are absent from the core, and stable iron (0.11 $M_\odot$) is confined to a shell at 6000–13000 km s^{-1}. ^{56}Ni extends into deeper layers but remains relatively low in the core ($\approx$30%), peaking within the same shell as the stable iron. Silicon (0.54 $M_\odot$) and sulphur (0.14 $M_\odot$) span the entire ejecta. The total burned mass is $\sim$1.25 $M_\odot$, only $\sim$10 per cent higher than in normal SNe Ia (Mazzali et al., 2007), with a total kinetic energy of $\approx 1.4 \times 10^{51}$ erg. A comparison of the abundance distribution with SN 2003du (Tanaka et al., 2011) is shown in Fig. 6.20.

6.7 Bolometric Light Curve

A pseudo-bolometric light curve in the 3000–10000 Å range is constructed from $UBVRI$ photometry of Taubenberger et al. (2019), applying the same method described in Sections 5.7.1 and 4.7.1 assuming $E(B-V) = 0.09$ (Sect. 6.2), and a distance modulus of $\mu = 33.26 \pm 0.20$ mag (Taubenberger et al., 2019); as 03fg-like SNe exhibit enhanced

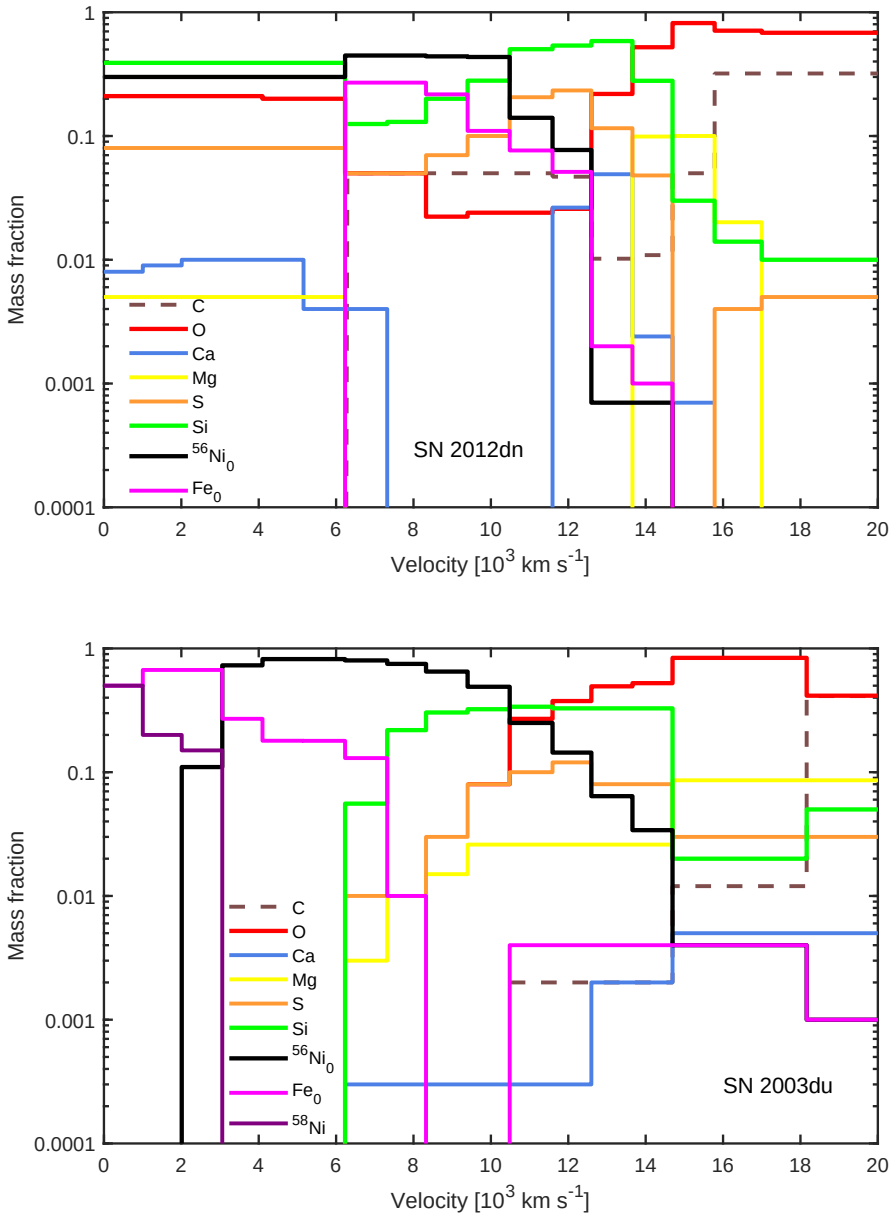


FIGURE 6.20: Abundance distributions of SN 2012dn (upper panel) compared to the normal SN 2003du (lower panel). The two events show markedly different core compositions: while the innermost layers of SN 2003du are dominated by neutron-rich iron-group elements and are entirely depleted of oxygen, SN 2012dn exhibits a central oxygen reservoir. In this model, oxygen extends to the core, intermixed with silicon and sulphur, alongside a notably low ^{56}Ni abundance.

TABLE 6.4: Bolometric luminosity of SN 2012dn in the U, B, V, R, I.

Author	$\log L_{\rm peak}$ erg s^{-1}	Distance modulus	$E(B-V)$
Taubenberger et al. (2019)	43.075	33.26	0.10
Chakradhari et al. (2014)	43.17	33.15	0.18
This paper	43.12	33.26	0.09

NIR emission, this pseudo-bolometric light curve should be regarded as a lower limit to the true bolometric luminosity (Ashall et al., 2021). A rest-frame peak luminosity of $L_{\rm peak} = 1.35^{+0.27}_{-0.22} \times 10^{43}\,{\rm erg\,s^{-1}}$ is obtained with a rest-frame rise time of 18.44 days, comparable to SN 1999aa (Aouad et al., 2022) and SN 2003du. Even when adopting the maximum literature reddening of $E(B-V) = 0.18$ (Chakradhari et al., 2014) the resulting peak of $1.78^{+0.27}_{-0.22} \times 10^{43}\,{\rm erg\,s^{-1}}$ remains significantly fainter than extreme 03fg-like events such as SN 2007if and SN 2009dc, which reach nearly twice this luminosity (Ashall et al., 2021, Taubenberger et al., 2013a). From day +60, the bolometric decline begins to deviate from that of normal SNe Ia, which typically follow a slope slightly steeper than the ^{56}Co decay rate. Interestingly, SN 2009dc follows a strikingly similar decline behaviour, however this deviation only sets in much later, around day +200. Comparisons with other SNe Ia are shown in Fig. 6.21, and different peak bolometric luminosity values reported in the literature are summarised in Table 6.4.

A synthetic bolometric light curve is constructed from the derived abundance distribution using the Monte Carlo radiative transfer code described in Sects. 5.7.2 and 4.7.2 (Cappellaro et al., 1997, Mazzali et al., 2001a). As expected, given the low ^{56}Ni mass derived, the model falls short of the observed peak luminosity (Fig. 6.22), suggesting that an additional energy source beyond radioactive decay may be at play. For comparison, the light curve of SN 2003du (Stanishev et al., 2007) is normalised to SN 2012dn model peak; the two show nearly identical behaviour, with the broader width of SN 2012dn being a direct consequence of its larger ejecta mass (1.66 $M_\odot$), providing a better match to the observed evolution than a standard Chandrasekhar-mass profile.

6.8 Viable Progenitor-Explosion Channels

Powering the peak of SN 2012dn by radioactive decay alone would require $\sim$0.65 $M_\odot$ of ^{56}Ni, based on its luminosity similarity to SN 1999aa and SN 2003du (Aouad et al., 2022, Tanaka et al., 2011). The nebular modelling yields 0.45–0.49 $M_\odot$, and allowing for an additional $\sim$0.05 $M_\odot$ to account for residual continuum discrepancies between the observed and synthetic spectra (Fig. 6.19), the total inferred ^{56}Ni mass rises to $\approx$0.54 $M_\odot$, still below what is needed to explain the peak. This persistent deficit, even at the upper

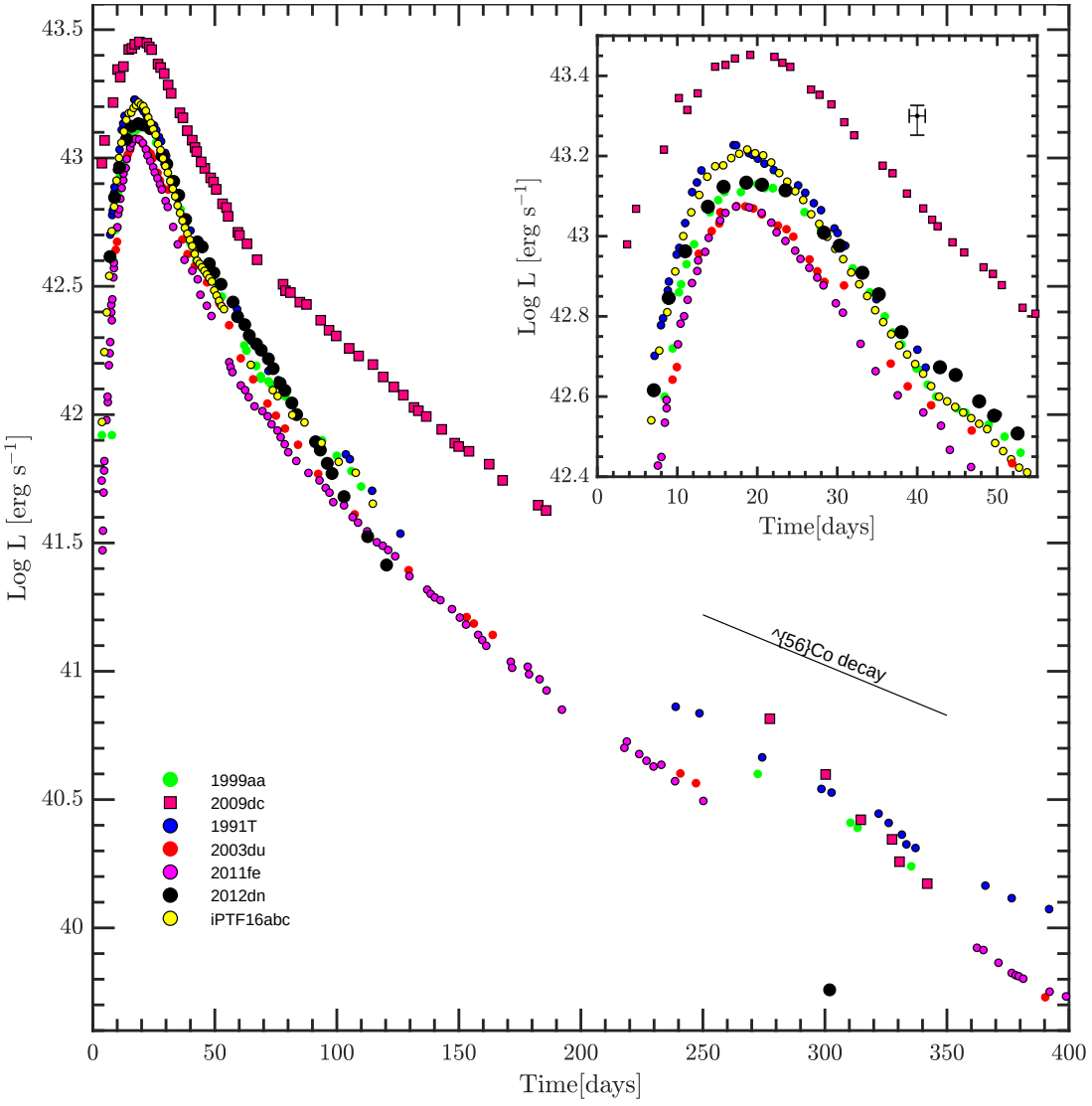


FIGURE 6.21: *UBVRI* pseudo-bolometric light curve of SN 2012dn compared with SNe 1991T, 2003du, 2011fe, 2009dc, 1999aa and iPTF16abc (Aouad et al., 2022, 2024, Sasdelli et al., 2014, Stanishev et al., 2007, Taubenberger et al., 2011, Zhang et al., 2016). By ∼60 days post-maximum, SN 2012dn undergoes a sharp decline, becoming significantly less luminous than the rest of the sample by day 300. SN 2009dc exhibits a similar drop ∼100 days later; notably, both events follow a nearly identical, steep decline slope. The vertical error bar reflects the peak luminosity range of SN 2012dn based on the minimum and maximum distance moduli in the literature.

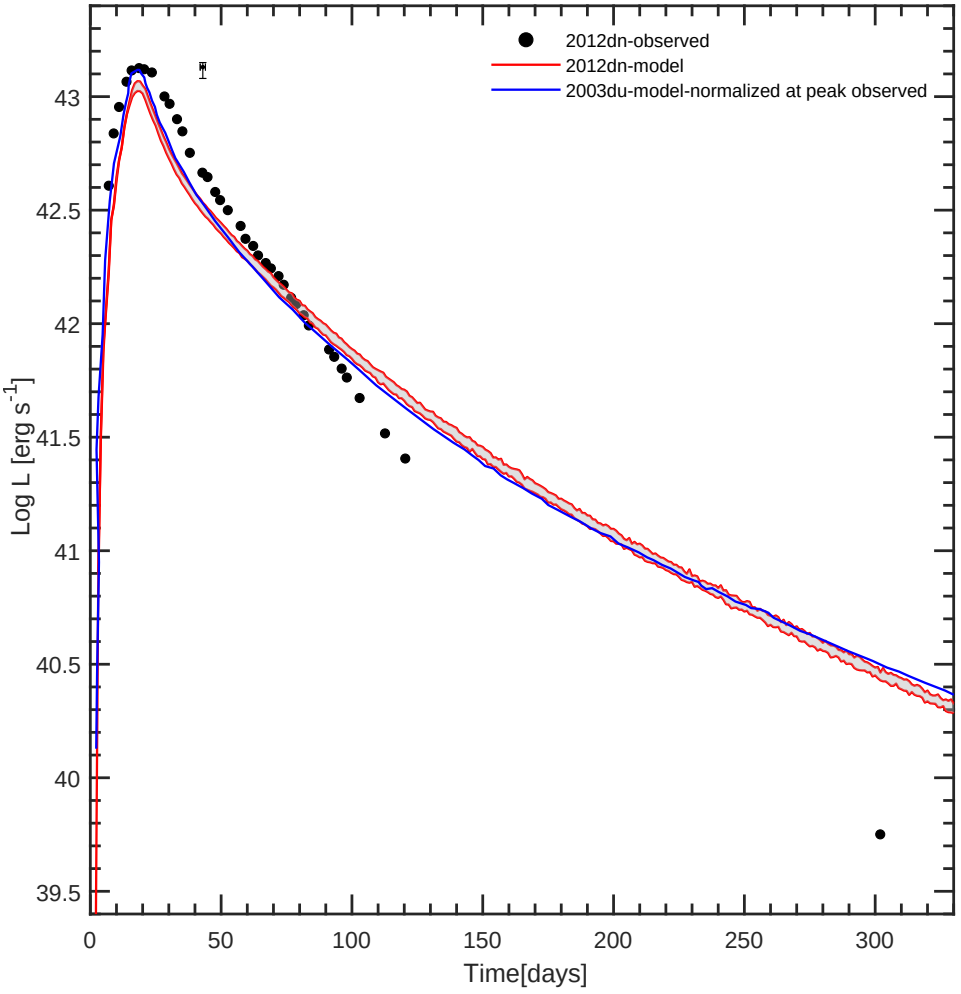


FIGURE 6.22: *UBVRI* pseudo-bolometric light curve of SN 2012dn (black dots) compared to synthetic models (red lines) for $M(^{56}\mathrm{Ni}) = 0.45$–$0.49\,\mathrm{M}_{\odot}$. The light curve of SN 2003du (Tanaka et al., 2011), normalised to the observed peak (dashed blue), reveals a late-time attenuation of $\sim$0.7 dex by day +300 highlighting SN 2012dn's significant late-time luminosity dimming. Despite similar morphology, the SN 2012dn model is broader than that of SN 2003du, reflecting its higher total ejecta mass.

end of the derived ^{56}Ni range, implies that an additional energy source is required. A natural candidate to allow for this shortfall is interaction of the ejecta with a carbon- and oxygen-rich CSM, a scenario frequently invoked for 03fg-like events to explain their enhanced luminosity, persistent carbon features, and low ionization states (Ashall et al., 2021, Hachinger et al., 2012, Noebauer et al., 2016).

Following the methodology of Hachinger et al. (2012), this effect is simulated by reducing the radioactive luminosity and compensating the flux deficit with a blackbody component. At two distinct phases, interaction is found to account for up to 25 per cent of the total flux at early epochs, decreasing to 20 per cent near maximum light, while maintaining the quality of the spectral fits as can be seen in Fig. 6.23. This contribution

is notably less extreme than the 50 per cent required for SN 2009dc (Hachinger et al., 2012), yet is sufficient to bridge the gap between the derived ^{56}Ni mass and the observed peak luminosity. This result suggests that CSM interaction may be a common yet variable power source among 03fg-like events, contributing at different levels across the class regardless of peak magnitude.

Such interaction is a plausible consequence of a double-degenerate merger, a scenario that simultaneously accounts for the central oxygen core, the circumstellar environment responsible for the late-time dimming, and the material necessary for ejecta–CSM interaction inferred for SN 2012dn. Similar characteristics have recently been reported for SNe 2021zny (Dimitriadis et al., 2023) and 2022pul (Siebert et al., 2023b), including an early flux excess consistent with ejecta–CSM interaction, persistent carbon features, low late-time ionization, reduced stable Fe-group abundances, and nebular [O I] emission, all interpreted in the framework of double white dwarf mergers, lending further support to a similar origin for SN 2012dn (Dutta et al., 2022).
Interestingly, recent JWST observations of SN 2022pul provide direct evidence for dust emission, demonstrating that dust formation can occur in 03fg-like Type Ia SNe (Siebert et al., 2023b). However, although SN 2022pul was only ~ 0.3 mag fainter than SN 2012dn at peak B-band luminosity, it remained significantly brighter at late epochs. This comparison indicates that the magnitude of the late-time luminosity deficit varies considerably among members of the 03fg-like subclass.

Remarkably, the derived abundance distribution bears a close resemblance to the 3D hydrodynamic simulations of a $1.1 + 0.9\,M_\odot$ CO–CO white dwarf merger by Pakmor et al. (2012)(see their Fig. 2). Despite the 1D nature of the reconstruction, the general abundance trends are remarkably consistent: oxygen dominates the core, surrounded by a shell of stable iron, silicon extends from the outermost layers to the centre, ^{56}Ni remains low (≈30 per cent) in the innermost layers, and carbon persists to intermediate shells. In their simulations, the primary white dwarf's ashes expand and sweep around the secondary during the burning phase, allowing the secondary's unburned material to eventually dominate the inner ejecta. Another merger model simulated by Kromer et al. (2013b), consisting of a lower-mass $0.9+0.76\,M_\odot$ configuration, does predict nebular oxygen emission; however, despite reproducing the [O I] line, the $0.18\,M_\odot$ ^{56}Ni mass inferred from their model is far too low to account for the peak luminosity of SN 2012dn.

However, despite their success in reproducing the central oxygen, the merger models discussed above predict neutron-rich elements in the core, such as ^{58}Ni, as also seen in the equal-mass $0.9 + 0.9\,M_\odot$ model of Pakmor et al. (2010). These species are notably absent in SN 2012dn. The lack of neutron-rich elements is primarily a consequence of low central density, which reduces electron captures during explosive burning, but it is

also known to be sensitive to the progenitor metallicity, as higher metallicity leads to greater neutronization (Arnett, 1982). Crucially, the spectral modelling for SN 2012dn independently points to a sub-solar metallicity progenitor, a result further supported by reported host galaxy metallicity, lending support to both effects acting simultaneously to suppress neutron-rich species in the core of SN 2012dn.

Constraining the white dwarf mass ratio ultimately requires dedicated hydrodynamical simulations and is further complicated by its degeneracy with progenitor metallicity; nevertheless, the CO–CO merger framework remains the most self-consistent explanation for the full set of observed properties of SN 2012dn.

6.9 Conclusions

An abundance tomography analysis of the 03fg-like SN 2012dn has been presented. This event is highly peculiar: its peak luminosity is comparable to that of normal SNe Ia, yet 03fg-like spectroscopic hallmarks are retained, including narrow IME features, weak Fe III lines, and persistent carbon. In the nebular phase, strong [Fe III] emission near 4850 Å is notably absent, while [O I] emission is detected, rare among SNe Ia. An unusual wavelength-independent dimming is also observed from ∼60 days past maximum, attributed to grey or clumpy dust formation. The main results are summarised as follows:

- The photospheric spectra are well reproduced by a standard W7 Chandrasekhar-mass density profile, which outperforms delayed-detonation models by accurately replicating the narrow absorption troughs. The density enhancement in W7 at 12000–16000 km s^{-1} confines singly ionized species to a narrow velocity shell, preventing the overly broad and blueshifted features produced by DD models.
- Nebular phase modelling is inconsistent with a Chandrasekhar-mass configuration. Reproducing the [O I] emission requires a low-velocity mass component, bringing the total inferred ejecta mass to 1.66 $M_\odot$, including 0.33 $M_\odot$ of oxygen of which 0.1 $M_\odot$ is concentrated in the core. This oxygen-rich core is largely devoid of stable iron, which instead resides in a surrounding shell. The total ^{56}Ni mass is estimated at 0.45–0.54 $M_\odot$, an uncertainty range modulated by the bolometric correction required to account for the grey dust extinction responsible for the anomalously low nebular-phase flux. Carbon persists down to $v \approx 6000$ km s^{-1}, while silicon and sulphur extend from the interior to the outermost layers.
- The derived ^{56}Ni yield is insufficient to power the peak luminosity, and an additional energy source is required regardless of the specific mass within the derived

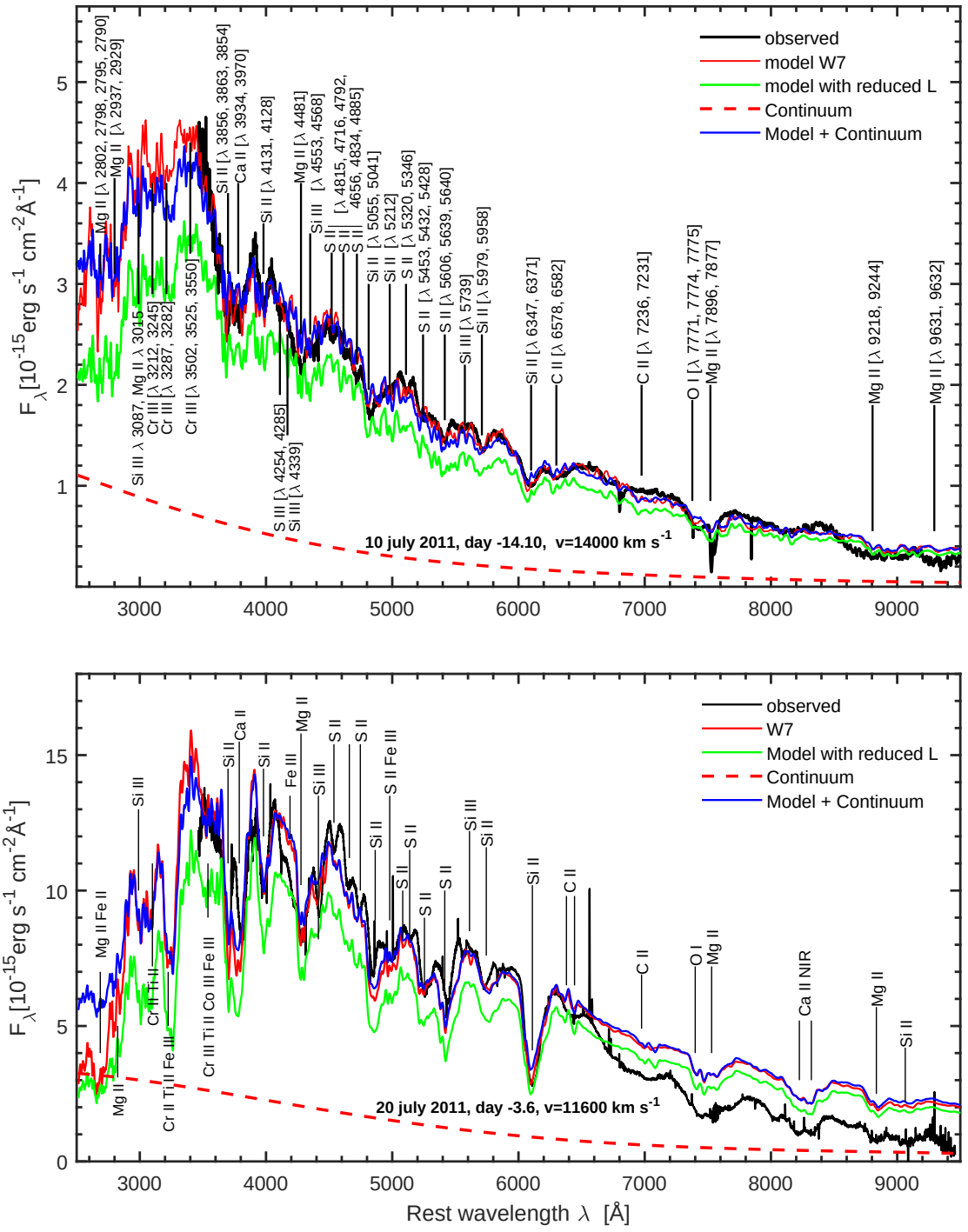


FIGURE 6.23: Comparison of observed and modeled spectra incorporating a blackbody (BB) component at two epochs (early and near-maximum light). The observed spectra are shown in black. The initial models are represented by red solid lines, while the models with reduced radioactive luminosity are shown in green. In these final models, the input luminosity was reduced by 25% for the early spectrum and 20% for the near-maximum spectrum. The red dashed lines represent the additional BB component required to account for the total luminosity, with temperatures of 14,000 K and 11,000 K for the early and near-maximum epochs, respectively. The blue solid lines represent the total synthetic flux (the sum of the green model and the BB component).

range. This deficit is reconciled by ejecta–CSM interaction, modelled as a blackbody component contributing up to 20 per cent of the maximum-light luminosity, with which a high-quality spectral fit is achieved.

- The derived abundance distribution closely resembles the outcomes of double-degenerate merger simulations, in which unburned material from the secondary white dwarf is dragged into the centre, resulting in an innermost region dominated by unburned fuel rather than complete nucleosynthesis products.

- The progenitor is constrained to sub-solar metallicity, as inferred from the low iron abundance in the outer ejecta derived from the spectral modelling and supported by the reported metallicity of the host galaxy. This naturally accounts for the unusually blue pre-maximum colours of SN 2012dn and reinforces the view that 03fg-like events preferentially arise in metal-poor environments, which may imply a higher occurrence rate at elevated redshifts; given the significant Hubble residuals associated with this subclass, they represent a potential source of contamination in future high-redshift cosmological supernova surveys.

- Late-time infrared observations are shown to be essential for recovering the full bolometric budget of 03fg-like transients, a requirement underscored by the significant NIR contribution inferred for SN 2012dn.

- The double-degenerate merger scenario remains the most self-consistent framework for explaining the full range of observed properties of SN 2012dn and possibly the 03fg-like subclass as a whole. It naturally produces the oxygen-rich, iron-poor core inferred from the modelling, establishes the conditions for dust formation responsible for the late-time dimming observed in several members of the subclass, and provides a natural site for ejecta–CSM interaction, which sustains the persistent carbon features and contributes an additional luminosity source. The diversity in peak luminosity across 03fg-like events may ultimately reflect variations in both ^{56}Ni production and the strength of this CSM interaction.

- While available hydrodynamical simulations of double-degenerate mergers can reproduce the central oxygen inferred for SN 2012dn, they either synthesise too little ^{56}Ni to account for the peak luminosity or predict neutron-rich species in the core that are absent in SN 2012dn. Dedicated simulations spanning a broader range of white dwarf mass ratios are therefore required.

Chapter 7

Conclusions and future work

7.1 Conclusions

The goal of this thesis was to investigate the origin of the subtle spectroscopic diversity observed wihtin the luminous peculiar Type Ia supernovae through abundance tomography. To this end, three objects occupying key positions within the diversity landscape shown in Fig. 7.1 were studied.

SN 1999aa exhibits spectroscopic properties intermediate between normal and 91T-like SNe Ia, with Si II and Ca II features of intermediate strength and an earlier transition to a normal appearance than SN 1991T. Despite this, its abundance structure closely resembles that of SN 1991T, both objects sharing a sharp depletion of silicon and sulphur above $\sim$12,000 km s^{-1}. This points to an explosion mechanism whose burning efficiency drops abruptly in the outer layers, naturally explaining the weak Si II and S II features that define the 91T-like subclass at early times.

These results indicate that the spectroscopic sequence from normal SNe Ia to the brightest 91T-like events cannot be explained by luminosity or temperature alone, but requires differences in the composition and layering of the outer ejecta, reflecting variations either in the progenitor's density structure or in the explosion itself. In addition, the comparison of bolometric light curves reveals a failure of the width–luminosity relation for SN 1999aa. Despite its lower luminosity, SN 1999aa declines more slowly than SN 1991T.

The conclusions drawn from SN 1999aa are reinforced by iPTF16abc. Although comparably luminous to SN 1991T, abundance tomography reveals significantly lower iron abundances in its outer ejecta, explaining its weaker Fe III features, together with carbon extending to unusually low velocities. These variations in the ejecta structure contribute to diversity even within the 91T-like subclass. Nonetheless, like SN 1999aa and

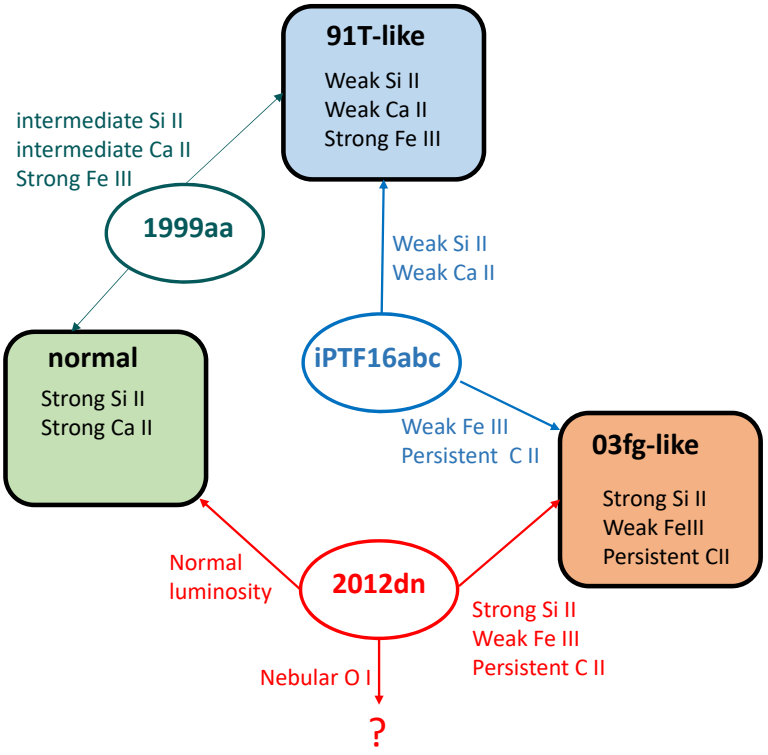


FIGURE 7.1: Schematic representation of the spectroscopic diversity of luminous peculiar SNe Ia. Characteristic spectroscopic properties of the normal, 91T-like, and 03fg-like subclasses are shown together with the features linking SN 1999aa, iPTF16abc, and SN 2012dn to each class. The figure illustrates the overlapping nature of the traditional classifications and the absence of a simple one-parameter sequence among luminous peculiar SNe Ia.

SN 1991T, iPTF16abc shows IMEs confined to a narrow shell, pointing to a common explosion mechanism underlying the subclass

For both SN 1999aa and iPTF16abc, Chandrasekhar-mass progenitors are supported by the inferred kinetic energies, and the presence of neutron-rich stable iron-group elements in the innermost ejecta. While no current explosion model reproduces all the observed properties of SN 1999aa and iPTF16abc, pulsation-driven detonation scenarios (Sec:2.6.1.5) remain an attractive conceptual framework. The pre-expansion of the white dwarf naturally produces steep outer density gradients that may help explain the confinement of IMEs to a narrow velocity range and, the survival of unburned carbon. However, existing PDD/PRD models fail to reproduce the defining spectroscopic characteristics of the 91T-like subclass. The abundance tomography of SN 1999aa and iPTF16abc requires stable nickel (^{58}Ni) to be confined to the innermost $\sim$1,000 km s^{-1}, consistent with previous abundance tomography studies but at odds with current hydrodynamical explosion models, which predict a much more extended distribution.

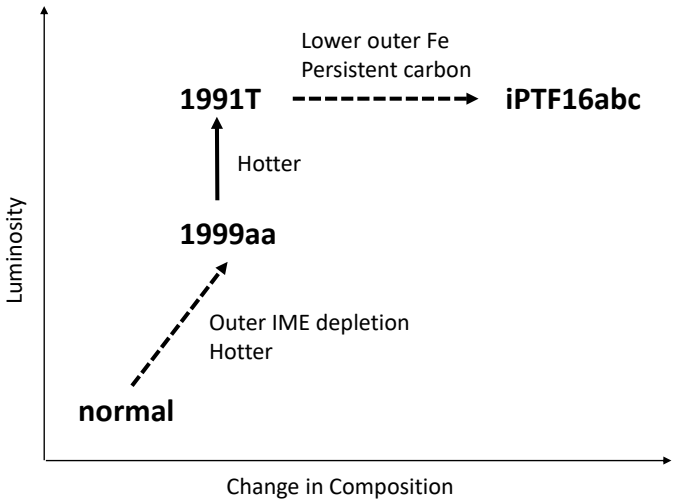


FIGURE 7.2: Schematic summary of the spectroscopic relationships inferred from abundance tomography. The transition from normal SNe Ia to the 91T-like subclass requires the confinement of IMEs to a narrow velocity range. Within the 91T-like subclass, the spectroscopic differences between SN 1999aa and SN 1991T are largely explained by a luminosity (temperature) sequence. The transition from SN 1991T to iPTF16abc requires additional abundance differences, including lower outer iron abundances and the presence of carbon both in the outer ejecta and at intermediate velocities

.

The relationships inferred between normal SNe Ia, SN 1999aa, SN 1991T, and iPTF16abc are summarised schematically in Fig.7.2.

SN 2012dn reveals an even more extreme departure from the notion that the spectroscopic diversity of luminous peculiar SNe Ia is primarily driven by luminosity. Despite displaying the defining 03fg-like hallmarks of persistent carbon, weak Fe III lines, and narrow IME features, its peak luminosity is comparable to that of normal SNe Ia, while its nebular spectrum is unexpectedly dim and shows prominent [O I] emission, rarely seen in Type Ia supernovae.

Nebular modeling requires a total ejecta mass of $\sim$1.66 $M_\odot$ and reveals a central oxygen-rich region largely devoid of stable iron-group elements, a structure difficult to reconcile with Chandrasekhar-mass explosions but natural in double-degenerate mergers, where unburned material from the disrupted secondary white dwarf settles in the innermost ejecta. The inferred ^{56}Ni mass cannot power the observed luminosity alone, implying an additional contribution from ejecta–CSM interaction near maximum light; such interaction in a carbon- and oxygen-rich environment would also favour dust formation, potentially explaining the unusual late-time bolometric dimming seen in SN 2012dn and other 03fg-like SNe.

These results suggest the merger scenario may extend to the 03fg-like subclass as a whole, with luminosity diversity reflecting variations in both ^{56}Ni production and the strength of the ejecta–CSM interaction. Spectral modeling further reveals an exceptionally low iron abundance in the outermost ejecta, pointing to a sub-solar metallicity progenitor that naturally explains SN 2012dn's blue pre-maximum colours and supports a metal-poor origin for 03fg-like events. This would imply a higher occurrence rate of such events at earlier cosmic epochs. Given their large Hubble residuals, 03fg-like supernovae may therefore represent a potential source of contamination in future high-redshift cosmological supernova surveys.

Taken together, the results of this thesis suggest that luminous peculiar SNe Ia do not form a simple continuous sequence. While transitional objects such as SN 1999aa and iPTF16abc blur the boundaries between the traditional subclasses, abundance tomography reveals a more complex physical picture involving variations in the progenitor/-explosion mechanisms channels. The similarities observed among different subclasses therefore reflect overlapping observational properties rather than a single underlying sequence governed by a smoothly varying parameter.

7.2 Future work

The results presented in this thesis open several avenues for future investigation. A natural extension of this work is the study of additional transitional objects occupying the boundaries between the established subclasses. Such events provide a unique opportunity to identify which abundance properties are common to each class and which vary continuously across the population.

Particular attention should be devoted to the 03fg-like subclass. Additional abundance tomography studies of these events, whenever sufficiently complete datasets become available, are needed to determine whether the properties inferred for SN 2012dn are representative of the population as a whole. In particular, exploring ejecta–CSM interaction across a larger sample may help determine whether variations in its strength contribute to the wide range of peak luminosities observed within the subclass, alongside differences in ^{56}Ni production.

One of the clearest illustrations of the conclusions reached in this thesis is provided by the synthetic spectral sequences shown in Figs. 7.3 and 7.4. Starting from a normal SN Ia syntheic spectrum (SN 2011fe) and progressively increasing its luminosity fails to reproduce the defining spectroscopic characteristics of the 91T-like subclass. Conversely,

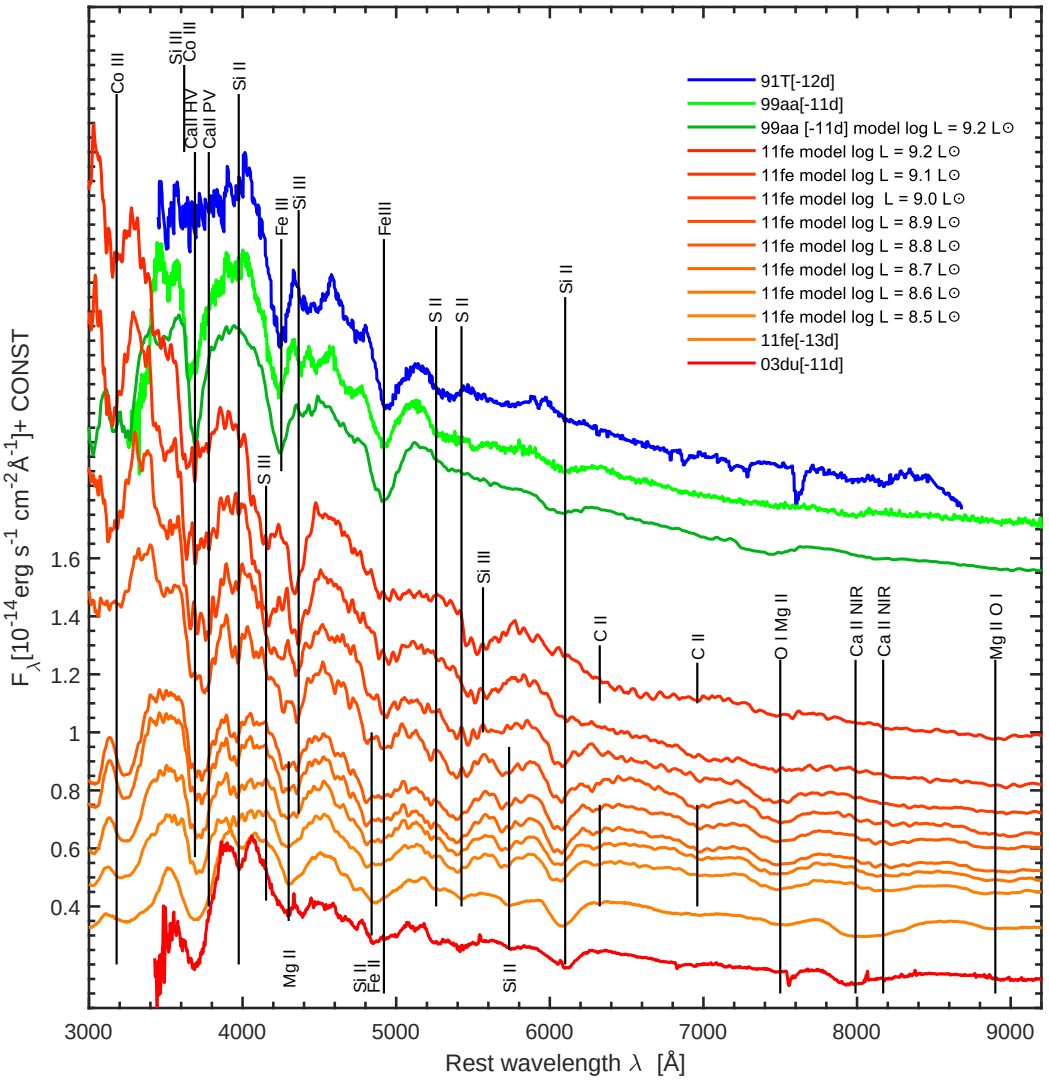


FIGURE 7.3: Starting with a model of 2011 fe (Mazzali et al., 2014), luminosity is increased in steps of 0.1 dex. The evolution of the spectra does not converge to a 91T-like event. In particular, even though the Si II 6355 feature starts fading for *log* L > 9.1 $L_\odot$, a Si III feature near 5500 Å becomes prominent, a feature absent in all members of the 91T-like class. Most importantly, the Fe III features, typical of the 91T-like class, do not appear in the spectra. The Fe III feature near 5000 Å remains weak, and the Fe III feature near 4200 Å does not strengthen with increasing temperature. Instead, it becomes split into two components, both dominated by Si III, replacing the Mg II line observed in all normal events. Finally, the most luminous model of SN 2011fe, with *log* L=9.2 $L_\odot$,similar to the model input in 99aa, shows no sign of convergence toward 91T-like behaviour. This suggests that luminosity evolution alone cannot account for the spectral transition from normal to 91T-like events.

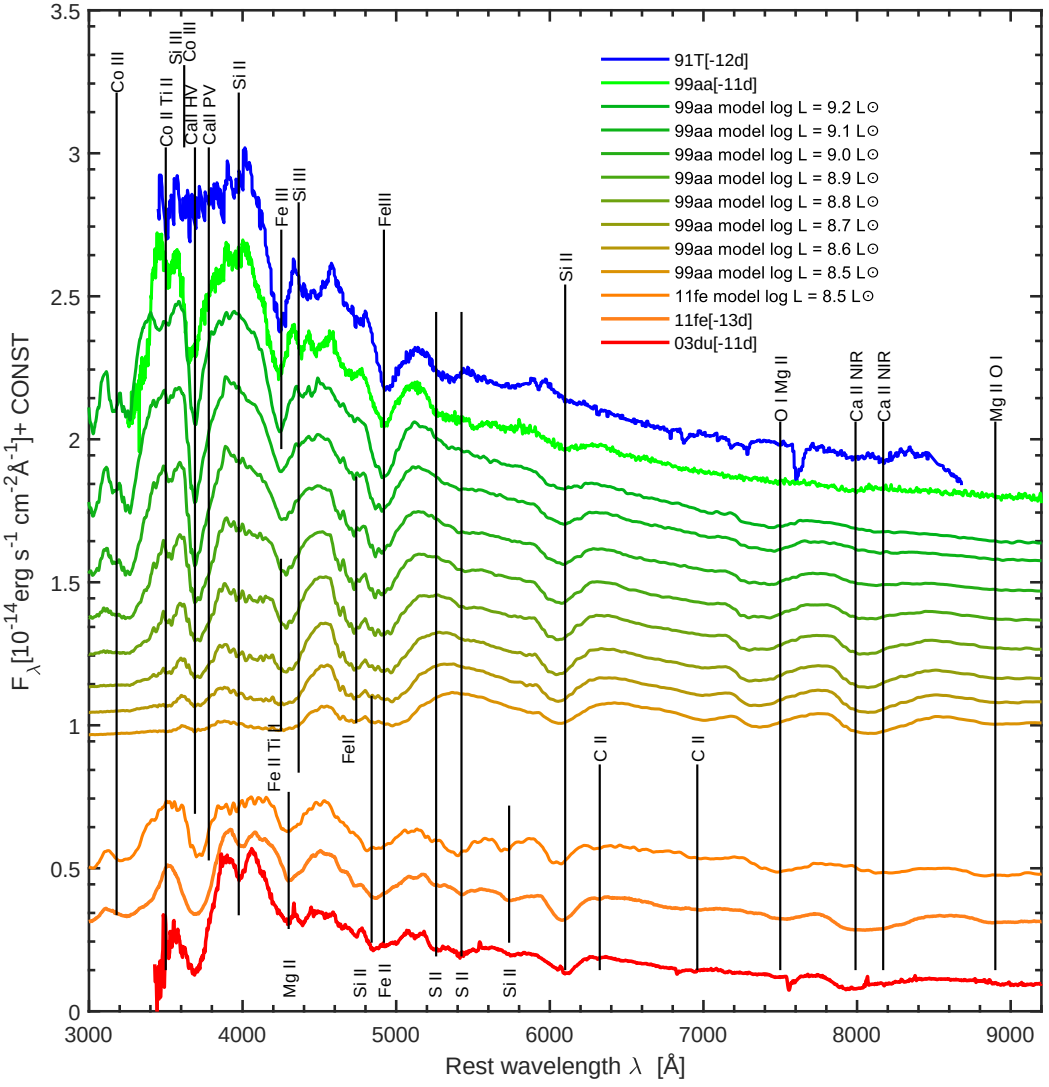


FIGURE 7.4: Starting with a model of SN 1999aa, the luminosity is decreased in steps of 0.1 dex while keeping the composition unchanged. The evolution of the spectra does not converge toward a normal-like event. In particular, although the Si II 6355 feature begins to emerge as luminosity decreases, the S II complex near 5400 Å does not develop. The feature near 4300 Å, typically dominated by Mg II and Si III in normal events, fails to form, and the Ca II H&K feature near 3700 Å completely fades. An Fe II feature near 4700 Å appears in the models, a feature not typically observed in events classified as normal. Additionally, the flux in the U band decreases substantially.

decreasing the luminosity of a SN 1999aa synthetic spectrum does not yield spectra resembling those of normal SNe Ia. These experiments therefore provide independent support for the conclusion that the transition between normal and 91T-like events cannot be explained by a simple temperature or luminosity sequence. Instead, fundamental differences in the abundance structure of the ejecta are required. Equally intriguing are the intermediate synthetic spectra produced along these parameter sequences (See Figs. 7.3 and 7.4). A systematic search for observational counterparts to these synthetic objects represents an important avenue for future investigation. To date, no SNe Ia exhibiting these predicted intermediate spectroscopic characteristics have been identified. If this absence is confirmed with larger observational samples, it would provide further evidence against the existence of a smooth luminosity sequence connecting normal and 91T-like events, and would instead reinforce the interpretation advanced in this thesis that the diversity between normal and 91T-like SNe Ia arises from more fundamental differences in their explosion physics and ejecta structures. Although these calculations are presented here only as a preliminary investigation, they reinforce the principal findings of this thesis and establish the foundation for a more systematic theoretical exploration of spectroscopic diversity

Another promising avenue for future investigation is the systematic determination of the outer boundary of the silicon-rich shell through modelling of the Si and S lines in the earliest spectra, thereby probing the outermost ejecta layers for intermediate-mass elements. Whether silicon undergoes a sharp depletion at a well-defined velocity or instead extends smoothly into the outer ejecta provides a direct probe of the outer extent of efficient burning, and therefore offers a powerful diagnostic of the explosion physics. The abrupt silicon cutoff identified in SN 1999aa and iPTF16abc should be investigated across a broader sample of transitional 99aa-like and 91T-like events to determine whether it represents a defining characteristic of this subclass and to establish its relationship to the observed spectroscopic diversity.

Appendix A

Derivation of the Arnett's law

This appendix presents the complete algebraic steps underlying the Arnett's law model equations quoted in the main text (Section 2.1.1.3), following Arnett (1996). Each substitution that was compressed in the main text is shown explicitly here.

The evolution of matter and radiation is governed by the first law of thermodynamics, i.e., the change in internal energy, ΔU, plus work done, W, equals the total net heat supplied to the system, Q.

$$\Delta U + W = Q \tag{A.1}$$

this can be written as

$$\frac{dE}{dt} + P\frac{dV}{dt} = \epsilon_{\rm rad} - \frac{E}{\tau_d(t)}. \tag{A.2}$$

Here, $\frac{dE}{dt}$ represents the rate of change of the internal (thermal) energy stored in the ejecta; how quickly the gas is heating up or cooling down internally. The term $P\frac{dV}{dt}$ is the rate at which the gas does work on its surroundings as it expands; since the ejecta is expanding rapidly following the explosion, this term describes the energy lost to adiabatic expansion (the gas cools as it pushes outward, converting internal energy into kinetic energy of expansion).

The right-hand side describes the two competing physical processes that set the energy budget: $\epsilon_{\rm rad}$ is the rate of energy input per unit mass from radioactive decay (mainly ^{56}Ni $\rightarrow$ ^{56}Co $\rightarrow$ ^{56}Fe), which continuously injects energy into the ejecta as the unstable isotopes decay. The term $E/\tau_d(t)$ represents the rate at which energy escapes the ejecta as radiation, on a characteristic photon diffusion timescale $\tau_d(t)$, since photons cannot escape instantaneously through the optically thick ejecta, this term captures how efficiently the trapped energy leaks out as observable luminosity.

In short, equation A.2 states that the internal energy of the ejecta changes according to the balance between radioactive heating, adiabatic cooling from expansion, and radiative losses as photons diffuse out.

For a radiation-dominated gas, the internal energy and pressure are given by:

$$E = aT^4V, \qquad P = \frac{1}{3}aT^4. \tag{A.3}$$

Since both T and V depend on time, the product rule gives:

$$\frac{dE}{dt} = \frac{d}{dt}\left(aT^4V\right) = a\left(4T^3\dot{T}\right)V + aT^4\dot{V} = 4aT^3\dot{T}\,V + aT^4\dot{V}. \tag{A.4}$$

Using $P = \frac{1}{3}aT^4$ directly:

$$P\frac{dV}{dt} = \frac{1}{3}aT^4\dot{V}. \tag{A.5}$$

Substituting equations A.4 and A.5 into the left-hand side of equation A.2:

$$\frac{dE}{dt} + P\frac{dV}{dt} = 4aT^3\dot{T}\,V + aT^4\dot{V} + \frac{1}{3}aT^4\dot{V} = 4aT^3\dot{T}\,V + \frac{4}{3}aT^4\dot{V}. \tag{A.6}$$

leads to

$$\frac{dE}{dt} + P\frac{dV}{dt} = 4aT^3V\left(\dot{T} + \frac{T\dot{V}}{3V}\right). \tag{A.7}$$

The radioactive heating rate per unit mass, ϵ_{rad}, can be written in terms of a heating timescale τ_H defined by:

$$\epsilon_{\mathrm{rad}} = \frac{E}{\tau_H}. \tag{A.8}$$

Substituting equation A.8 into the right-hand side of the original energy balance, equation A.2, and equating it to the factored left-hand side of equation A.7:

$$4aT^3V\left(\dot{T} + \frac{T\dot{V}}{3V}\right) = \frac{E}{\tau_H} - \frac{E}{\tau_d}. \tag{A.9}$$

Since $E = aT^4V$, the prefactor on the left-hand side can be rewritten in terms of E:

$$4aT^3V = \frac{4aT^4V}{T} = \frac{4E}{T}. \tag{A.10}$$

Substituting equation A.10 into equation A.9:

$$\frac{4E}{T}\left(\dot{T} + \frac{T\dot{V}}{3V}\right) = \frac{E}{\tau_H} - \frac{E}{\tau_d}. \tag{A.11}$$

Dividing both sides by E and simplifying:

$$4\left(\frac{\dot{T}}{T}+\frac{1}{3}\frac{\dot{V}}{V}\right)=\frac{1}{\tau_H}-\frac{1}{\tau_d}. \tag{A.12}$$

For a uniformly and homologously expanding sphere, the volume is $V=\frac{4}{3}\pi R^3$. Differentiating with respect to time:

$$\dot{V}=4\pi R^2\dot{R} \quad\Longrightarrow\quad \frac{\dot{V}}{V}=\frac{4\pi R^2\dot{R}}{\frac{4}{3}\pi R^3}=3\frac{\dot{R}}{R}. \tag{A.13}$$

Substituting equation A.13 into equation A.12 leads to:

$$4\left(\frac{\dot{T}}{T}+\frac{\dot{R}}{R}\right)=\frac{1}{\tau_H}-\frac{1}{\tau_d}. \tag{A.14}$$

Derivation of the Bolometric Luminosity Expression

The luminosity is given by the diffusion approximation, $L=E/\tau_d$, where the diffusion timescale is given by equation 2.16:

$$\tau_d=\frac{3R^2}{\pi^2\lambda c}, \tag{A.15}$$

with the photon mean free path $\lambda=1/(\rho\kappa)$, where the opacity κ is taken to be constant in time (e.g. electron-scattering opacity), and the density given by

$$\rho=\frac{M}{V}=\frac{M}{\frac{4}{3}\pi R^3}=\frac{3M}{4\pi R^3}. \tag{A.16}$$

The mean free path can be expressed in terms of R and M.

$$\lambda=\frac{1}{\rho\kappa}=\frac{4\pi R^3}{3M\kappa}. \tag{A.17}$$

Substitute into the diffusion timescale.

$$\tau_d=\frac{3R^2}{\pi^2 c}\cdot\frac{1}{\lambda}=\frac{3R^2}{\pi^2 c}\cdot\frac{3M\kappa}{4\pi R^3}=\frac{9M\kappa}{4\pi^3 cR}. \tag{A.18}$$

Substitute E and τ_d into $L=E/\tau_d$.

Using $E = aT^4V = \frac{4}{3}\pi aT^4R^3$ from equation A.3 together with equation A.18:

$$L = \frac{E}{\tau_d} = \left(\frac{4}{3}\pi aT^4R^3\right) \Big/ \left(\frac{9M\kappa}{4\pi^3 cR}\right) = \frac{4}{3}\pi aT^4R^3 \cdot \frac{4\pi^3 cR}{9M\kappa}. \tag{A.19}$$

which can be simplified to:

$$L = \frac{16\pi^4\, a\, c\, T^4 R^4}{27\,\kappa\, M}. \tag{A.20}$$

Time Derivative of the Luminosity

To locate the peak of the light curve we require dL/dt. The maximum occurs when $\frac{dL}{dt} = 0$. Since R, T, κ, and M can all in principle vary with time, the total time derivative of $L = L(R, T, \kappa, M)$ is

$$\frac{dL}{dt} = \frac{\partial L}{\partial R}\frac{dR}{dt} + \frac{\partial L}{\partial T}\frac{dT}{dt} + \frac{\partial L}{\partial \kappa}\frac{d\kappa}{dt} + \frac{\partial L}{\partial M}\frac{dM}{dt}. \tag{A.21}$$

From equation A.20, each variable enters as a pure power, so:

$$\frac{\partial L}{\partial R} = \frac{4L}{R}, \qquad \frac{\partial L}{\partial T} = \frac{4L}{T}, \qquad \frac{\partial L}{\partial \kappa} = -\frac{L}{\kappa}, \qquad \frac{\partial L}{\partial M} = -\frac{L}{M}. \tag{A.22}$$

Substituting the partial derivatives into equation A.21, leas to:

$$\frac{dL}{dt} = \frac{4L}{R}\dot{R} + \frac{4L}{T}\dot{T} - \frac{L}{\kappa}\dot{\kappa} - \frac{L}{M}\dot{M} = 4L\left(\frac{\dot{T}}{T} + \frac{\dot{R}}{R}\right) - L\frac{\dot{\kappa}}{\kappa} - L\frac{\dot{M}}{M}. \tag{A.23}$$

The Arnett model assumes a fixed ejecta mass, so $\dot{M} = 0$, and a constant opacity, so $\dot{\kappa} = 0$. Both terms in equation A.23 therefore vanish, leaving:

$$\frac{dL}{dt} = 4L\left(\frac{\dot{T}}{T} + \frac{\dot{R}}{R}\right). \tag{A.24}$$

To locate the peak, $\frac{dL}{dt} = 0$ which requires $\left(\frac{\dot{T}}{T} + \frac{\dot{R}}{R}\right) = 0$, and from equation A.14 this in turn requires

$$\frac{1}{\tau_H} - \frac{1}{\tau_d} = 0 \quad \Longrightarrow \quad \tau_H = \tau_d, \tag{A.25}$$

i.e. the light curve peaks when the instantaneous heating timescale equals the diffusion timescale.

Bibliography

Abbott T. M. C., et al., 2019, ApJL, 872, L30

Aguirre A., 1999, ApJ, 525, 583

Akerlof C., et al., 2007, Central Bureau Electronic Telegrams, 1059, 2

Aldering G., et al., 2006, ApJ, 650, 510

Alexander R. D., Wynn G. A., King A. R., Pringle J. E., 2011, MNRAS, 418, 2576

Altavilla G., et al., 2004, MNRAS, 349, 1344

Amanullah R., et al., 2010, ApJ, 716, 712

Aouad C. J., et al., 2022, MNRAS, 515, 4445

Aouad C. J., Mazzali P. A., Ashall C., Tanaka M., Hachinger S., 2024, MNRAS, 529, 3838

Armstrong M., Schwartz M., 1999, IAU Circ., 7108, 1

Arnett W. D., 1969, Ap&SS, 5, 180

Arnett W. D., 1982, ApJ, 253, 785

Arnett D., 1996, Supernovae and Nucleosynthesis: An Investigation of the History of Matter from the Big Bang to the Present

Ashall C., Mazzali P. A., 2020, MNRAS, 492, 5956

Ashall C., Mazzali P. A., Pian E., James P. A., 2016, MNRAS, 463, 1891

Ashall C., et al., 2018, MNRAS, 477, 153

Ashall C., et al., 2020, ApJL, 895, L3

Ashall C., et al., 2021, ApJ, 922, 205

Asplund M., Grevesse N., Sauval A. J., Scott P., 2009, ARA&A, 47, 481

Axelrod T. S., 1980, in Wheeler J. C., ed., Texas Workshop on Type I Supernovae. pp 80–95

Ayani K., Yamaoka H., 1998, IAU Circ., 7059, 1

Aznar-Siguán G., García-Berro E., Lorén-Aguilar P., Soker N., Kashi A., 2015, MNRAS, 450, 2948

Baade W., 1943, ApJ, 97, 119

Barbon R., Ciatti F., Rosino L., 1979, A&A, 72, 287

Barkat Z., 1975, ARA&A, 13, 45

Baron E., Jeffery D. J., Branch D., Bravo E., García-Senz D., Hauschildt P. H., 2008a, ApJ, 672, 1038

Baron E., Jeffery D. J., Branch D., Bravo E., García-Senz D., Hauschildt P. H., 2008b, ApJ, 672, 1038

Benetti S., et al., 2005, ApJ, 623, 1011

Bersten M. C., Mazzali P. A., 2017a, in Alsabti A. W., Murdin P., eds, , Handbook of Supernovae. p. 723, doi:10.1007/978-3-319-21846-5_25

Bersten M. C., Mazzali P. A., 2017b, in Alsabti A. W., Murdin P., eds, , Handbook of Supernovae. p. 723, doi:10.1007/978-3-319-21846-5_25

Bevan A., Barlow M. J., 2016, MNRAS, 456, 1269

Bildsten L., Shen K. J., Weinberg N. N., Nelemans G., 2007, ApJL, 662, L95

Blondin S., Dessart L., Hillier D. J., Khokhlov A. M., 2017, MNRAS, 470, 157

Bloom J. S., et al., 2012, ApJL, 744, L17

Bock G., Parrent J. T., Howell D. A., 2012, Central Bureau Electronic Telegrams, 3174, 1

Boehner P., Plewa T., Langer N., 2017, MNRAS, 465, 2060

Borkowski K. J., Reynolds S. P., Roberts M. S. E., 2016, ApJ, 819, 160

Bose S., et al., 2025, A&A, 699, A169

Bottinelli L., Gouguenheim L., Paturel G., de Vaucouleurs G., 1985, A&AS, 59, 43

Botyánszki J., Kasen D., 2017, ApJ, 845, 176

Bours M. C. P., Toonen S., Nelemans G., 2013, A&A, 552, A24

Branch D., Wheeler J. C., 2017, Supernova Explosions, doi:10.1007/978-3-662-55054-0.

Branch D., van den Bergh S., 1993, AJ, 105, 2231

Branch D., Romanishin W., Baron E., 1996, ApJ, 465, 73

Branch D., et al., 2006, PASP, 118, 560

Bravo E., García-Senz D., 2009, ApJ, 695, 1244

Bravo E., García-Senz D., Cabezón R. M., Domínguez I., 2009, ApJ, 695, 1257

Brecher K., 1978, Nature, 273, 728

Brown P. J., et al., 2014, ApJ, 787, 29

Burns C. R., et al., 2014, ApJ, 789, 32

Burns C. R., et al., 2018, ApJ, 869, 56

Camilo F., et al., 2002, ApJL, 571, L41

Cappellaro E., 2014, SNOoPy: a package for SN photometry, `http://sngroup.oapd.inaf.it/snoopy.html`

Cappellaro E., Mazzali P. A., Benetti S., Danziger I. J., Turatto M., della Valle M., Patat F., 1997, A&A, 328, 203

Cardelli J. A., Clayton G. C., Mathis J. S., 1989, ApJ, 345, 245

Chakraborti S., Childs F., Soderberg A., 2016, ApJ, 819, 37

Chakraborty S., et al., 2024, ApJ, 969, 80

Chakradhari N. K., Sahu D. K., Srivastav S., Anupama G. C., 2014, MNRAS, 443, 1663

Chamulak D. A., Brown E. F., Timmes F. X., Dupczak K., 2008, ApJ, 677, 160

Chen Y., Kumar S., Ratra B., 2017, ApJ, 835, 86

Chevalier R. A., 1998, ApJ, 499, 810

Childress M., et al., 2011, ApJ, 733, 3

Childress M. J., Filippenko A. V., Ganeshalingam M., Schmidt B. P., 2014, MNRAS, 437, 338

Childress M. J., et al., 2016, , 33, e055

Chomiuk L., et al., 2016, ApJ, 821, 119

Chonis T. S., Gaskell C. M., 2008, AJ, 135, 264

Cikota A., Patat F., Cikota S., Spyromilio J., Rau G., 2017, MNRAS, 471, 2111

Claeys J. S. W., Pols O. R., Izzard R. G., Vink J., Verbunt F. W. M., 2014, A&A, 563, A83

Clifford F. E., Tayler R. J., 1965, , 69, 21

Colgate S. A., McKee C., 1969, ApJ, 157, 623

Colgate S. A., Petschek A. G., Kriese J. T., 1980, ApJL, 237, L81

Contardo G., Leibundgut B., Vacca W. D., 2000, A&A, 359, 876

Courtois H. M., Tully R. B., 2015, MNRAS, 447, 1531

Dan M., Rosswog S., Brüggen M., Podsiadlowski P., 2014, MNRAS, 438, 14

Desai D. D., et al., 2024, MNRAS, 530, 5016

Dessart L., Blondin S., Hillier D. J., Khokhlov A., 2014, MNRAS, 441, 532

Dhawan S., et al., 2018, MNRAS, 480, 1445

Di Stefano R., Kilic M., 2012, ApJ, 759, 56

Di Stefano R., Voss R., Claeys J. S. W., 2011, ApJL, 738, L1

Dilday B., et al., 2012, Science, 337, 942

Dimitriadis G., et al., 2023, MNRAS, 521, 1162

Dong S., Katz B., Kushnir D., Prieto J. L., 2015, MNRAS, 454, L61

Dutta A., Anupama G. C., Chakradhari N. K., Sahu D. K., 2022, ApJL, 938, L22

Elias J. H., Frogel J. A., Hackwell J. A., Persson S. E., 1981, ApJL, 251, L13

Elias J. H., Matthews K., Neugebauer G., Persson S. E., 1985, ApJ, 296, 379

Epinat B., et al., 2008, MNRAS, 388, 500

Ferretti R., et al., 2017, A&A, 606, A111

Filippenko A. V., 1997, ARA&A, 35, 309

Filippenko A. V., et al., 1992a, AJ, 104, 1543

Filippenko A. V., et al., 1992b, ApJL, 384, L15

Fink M., Hillebrandt W., Röpke F. K., 2007, A&A, 476, 1133

Fink M., Röpke F. K., Hillebrandt W., Seitenzahl I. R., Sim S. A., Kromer M., 2010, A&A, 514, A53

Flörs A., et al., 2020, MNRAS, 491, 2902

Folatelli G., et al., 2012, ApJ, 745, 74

Foley R. J., et al., 2009, AJ, 138, 376

Foley R. J., et al., 2013a, ApJ, 767, 57

Foley R. J., et al., 2013b, ApJ, 767, 57

Fox O. D., et al., 2015, MNRAS, 447, 772

Fujimoto M. Y., Sugimoto D., 1982, ApJ, 257, 291

Fukugita M., Shimasaku K., Ichikawa T., 1995, PASP, 107, 945

Gal-Yam A., 2016, Transient Name Server Discovery Report, 2016-261, 1

Galbany L., et al., 2016, A&A, 591, A48

Ganeshalingam M., Li W., Filippenko A. V., 2011, MNRAS, 416, 2607

Garavini G., et al., 2004, AJ, 128, 387

Gardner F. F., Milne D. K., 1965, AJ, 70, 754

Gilfanov M., Bogdán Á., 2010, Nature, 463, 924

Godon P., Sion E. M., Starrfield S., Livio M., Williams R. E., Woodward C. E., Kuin P., Page K. L., 2014, ApJL, 784, L33

González Hernández J. I., Ruiz-Lapuente P., Tabernero H. M., Montes D., Canal R., Méndez J., Bedin L. R., 2012, Nature, 489, 533

Graham M. L., Nugent P. E., Sullivan M., Filippenko A. V., Cenko S. B., Silverman J. M., Clubb K. I., Zheng W., 2015, MNRAS, 454, 1948

Graham M. L., et al., 2019, ApJ, 871, 62

Graur O., Zurek D., Shara M. M., Riess A. G., Seitenzahl I. R., Rest A., 2016, ApJ, 819, 31

Green D. A., Reynolds S. P., Borkowski K. J., Hwang U., Harrus I., Petre R., 2008, MNRAS, 387, L54

Greggio L., 2005, A&A, 441, 1055

Greggio L., Renzini A., 1983, , 54, 311

Guillochon J., Dan M., Ramirez-Ruiz E., Rosswog S., 2010, ApJL, 709, L64

Guy J., Astier P., Nobili S., Regnault N., Pain R., 2005, A&A, 443, 781

Hachinger S., 2011, PhD thesis, Munich University of Technology, Germany

Hachinger S., Mazzali P. A., Benetti S., 2006, MNRAS, 370, 299

Hachinger S., Mazzali P. A., Tanaka M., Hillebrandt W., Benetti S., 2008, MNRAS, 389, 1087

Hachinger S., Mazzali P. A., Taubenberger S., Fink M., Pakmor R., Hillebrandt W., Seitenzahl I. R., 2012, MNRAS, 427, 2057

Hachinger S., et al., 2013, MNRAS, 429, 2228

Hachisu I., Kato M., Nomoto K., 1996, ApJL, 470, L97

Hachisu I., Kato M., Nomoto K., 2008, ApJ, 679, 1390

Hachisu I., Kato M., Nomoto K., 2010, ApJL, 724, L212

Hachisu I., Kato M., Saio H., Nomoto K., 2012a, ApJ, 744, 69

Hachisu I., Kato M., Nomoto K., 2012b, ApJL, 756, L4

Hakobyan A. A., Barkhudaryan L. V., Karapetyan A. G., Gevorgyan M. H., Mamon G. A., Kunth D., Adibekyan V., Turatto M., 2020, MNRAS, 499, 1424

Hamers A. S., Pols O. R., Claeys J. S. W., Nelemans G., 2013, MNRAS, 430, 2262

Hamuy M., Phillips M. M., Suntzeff N. B., Schommer R. A., Maza J., Aviles R., 1996, AJ, 112, 2391

Hamuy M., Trager S. C., Pinto P. A., Phillips M. M., Schommer R. A., Ivanov V., Suntzeff N. B., 2000, AJ, 120, 1479

Hamuy M., Phillips M., Suntzeff N., Maza J., 2003, IAU Circ., 8151, 2

Han Z., Podsiadlowski P., 2004, MNRAS, 350, 1301

Han Z., Podsiadlowski P., 2006, MNRAS, 368, 1095

Hanbury Brown R., Hazard C., 1952, Nature, 170, 364

Helmholtz 1868, The London, Edinburgh, and Dublin Philosophical Magazine and Journal of Science, 36, 337

Hicken M., Garnavich P. M., Prieto J. L., Blondin S., DePoy D. L., Kirshner R. P., Parrent J., 2007, ApJL, 669, L17

Hillebrandt W., Niemeyer J. C., 2000, ARA&A, 38, 191

Hillebrandt W., Kromer M., Röpke F. K., Ruiter A. J., 2013, Frontiers of Physics, 8, 116

Hoeflich P., Khokhlov A. M., Wheeler J. C., 1995, ApJ, 444, 831

Hoeflich P., Khokhlov A., Wheeler J. C., Phillips M. M., Suntzeff N. B., Hamuy M., 1996, ApJL, 472, L81

Hoeflich P., et al., 2021, ApJ, 922, 186

Hoflich P., Khokhlov A., Wheeler C., 1995, in Haas M. R., Davidson J. A., Erickson E. F., eds, Astronomical Society of the Pacific Conference Series Vol. 73, From Gas to Stars to Dust. pp 441–444

Howell D. A., 2001, ApJL, 554, L193

Howell D. A., et al., 2006, Nature, 443, 308

Hsiao E. Y., et al., 2020, ApJ, 900, 140

Hubble E. P., 1928, Leaflet of the Astronomical Society of the Pacific, 1, 55

Iben I. J., Tutukov A. V., 1984, ApJS, 54, 335

Ilkov M., Soker N., 2012, MNRAS, 419, 1695

Inserra C., et al., 2014, MNRAS, 437, L51

Ivanova L. N., Imshennik V. S., Chechetkin V. M., 1974, Ap&SS, 31, 497

Iwamoto K., Brachwitz F., Nomoto K., Kishimoto N., Umeda H., Hix W. R., Thielemann F.-K., 1999, ApJS, 125, 439

Jeffery D. J., Leibundgut B., Kirshner R. P., Benetti S., Branch D., Sonneborn G., 1992, ApJ, 397, 304

Jerkstrand A., 2017, in Alsabti A. W., Murdin P., eds, , Handbook of Supernovae. p. 795, doi:10.1007/978-3-319-21846-5_29

Jha S. W., 2017, in Alsabti A. W., Murdin P., eds, , Handbook of Supernovae. p. 375, doi:10.1007/978-3-319-21846-5_42

Jha S., et al., 2006, AJ, 131, 527

Jha S., Riess A. G., Kirshner R. P., 2007, ApJ, 659, 122

Jha S. W., Maguire K., Sullivan M., 2019, Nature Astronomy, 3, 706

Johansson J., et al., 2013, MNRAS, 435, 1680

Justham S., 2011, ApJL, 730, L34

Karachentsev I. D., Kudrya Y. N., Karachentseva V. E., Mitronova S. N., 2006, Astrophysics, 49, 450

Kasen D., 2010, ApJ, 708, 1025

Kasen D., Plewa T., 2005, ApJL, 622, L41

Kasen D., Woosley S. E., 2007, ApJ, 656, 661

Kashi A., Soker N., 2011, MNRAS, 417, 1466

Katz B., Dong S., 2012, arXiv e-prints, p. arXiv:1211.4584

Keegans J. D., et al., 2023, ApJS, 268, 8

Kelly P. L., Hicken M., Burke D. L., Mandel K. S., Kirshner R. P., 2010, ApJ, 715, 743

Kerzendorf W. E., et al., 2013, ApJ, 774, 99

Kerzendorf W. E., Taubenberger S., Seitenzahl I. R., Ruiter A. J., 2014, ApJL, 796, L26

Kerzendorf W. E., et al., 2017, MNRAS, 472, 2534

Khan R., Stanek K. Z., Stoll R., Prieto J. L., 2011, ApJL, 737, L24

Khokhlov A. M., 1991a, A&A, 245, L25

Khokhlov A. M., 1991b, A&A, 245, 114

Klein Y. Y., Katz B., 2017, MNRAS, 465, L44

Kobayashi C., Nomoto K., 2009, ApJ, 707, 1466

Kozai Y., 1962, AJ, 67, 591

Krause O., Birkmann S. M., Usuda T., Hattori T., Goto M., Rieke G. H., Misselt K. A., 2008a, Science, 320, 1195

Krause O., Tanaka M., Usuda T., Hattori T., Goto M., Birkmann S., Nomoto K., 2008b, Nature, 456, 617

Krisciunas K., Hastings N. C., Loomis K., McMillan R., Rest A., Riess A. G., Stubbs C., 2000, ApJ, 539, 658

Kromer M., et al., 2013a, MNRAS, 429, 2287

Kromer M., et al., 2013b, ApJL, 778, L18

Kromer M., et al., 2016, MNRAS, 459, 4428

Kushnir D., Katz B., Dong S., Livne E., Fernández R., 2013, ApJL, 778, L37

Lagattuta D. J., Mould J. R., Staveley-Smith L., Hong T., Springob C. M., Masters K. L., Koribalski B. S., Jones D. H., 2013, ApJ, 771, 88

Leibundgut B., et al., 1993, AJ, 105, 301

Leigh N. W. C., Geller A. M., 2013, MNRAS, 432, 2474

Leloudas G., et al., 2009, A&A, 505, 265

Lentz E. J., Baron E., Hauschildt P. H., Branch D., 2002, ApJ, 580, 374

Leonard D. C., 2007, ApJ, 670, 1275

Leonard D. C., Li W., Filippenko A. V., Foley R. J., Chornock R., 2005, ApJ, 632, 450

Lepo K., van Kerkwijk M., 2013, ApJ, 771, 13

Li W., et al., 2003, PASP, 115, 453

Li W., et al., 2011a, MNRAS, 412, 1441

Li W., et al., 2011b, Nature, 480, 348

Lidov M. L., 1962, , 9, 719

Liu W., Jeffery D. J., Schultz D. R., 1997, ApJL, 483, L107

Liu Z. W., Pakmor R., Röpke F. K., Edelmann P., Wang B., Kromer M., Hillebrandt W., Han Z. W., 2012, A&A, 548, A2

Liu J., et al., 2024, The Astrophysical Journal, 973, 117

Livio M., 1989, Space Sci. Rev., 50, 299

Livio M., Mazzali P., 2018, Phys. Rep., 736, 1

Livio M., Pringle J. E., 1998, ApJ, 505, 339

Livio M., Riess A. G., 2003, ApJL, 594, L93

Livio M., Truran J. W., 1992, ApJ, 389, 695

Lorén-Aguilar P., Isern J., García-Berro E., 2010, MNRAS, 406, 2749

Lü G., Zhu C., Wang Z., Wang N., 2009, MNRAS, 396, 1086

Lu J., et al., 2021, ApJ, 920, 107

Lucy L. B., 1999, A&A, 345, 211

Lucy L. B., Danziger I. J., Gouiffes C., Bouchet P., 1991, in Woosley S. E., ed., Supernovae. p. 82

Lundmark K., 1921, PASP, 33, 225

Lundqvist P., et al., 2013, MNRAS, 435, 329

Maeda K., Iwamoto K., 2009, MNRAS, 394, 239

Maeda K., Kawabata K., Li W., Tanaka M., Mazzali P. A., Hattori T., Nomoto K., Filippenko A. V., 2009, ApJ, 690, 1745

Maeda K., et al., 2010a, Nature, 466, 82

Maeda K., Taubenberger S., Sollerman J., Mazzali P. A., Leloudas G., Nomoto K., Motohara K., 2010b, ApJ, 708, 1703

Maguire K., et al., 2013, MNRAS, 436, 222

Makarov D., Prugniel P., Terekhova N., Courtois H., Vauglin I., 2014, A&A, 570, A13

Mannucci F., Della Valle M., Panagia N., Cappellaro E., Cresci G., Maiolino R., Petrosian A., Turatto M., 2005, A&A, 433, 807

Margutti R., Parrent J., Kamble A., Soderberg A. M., Foley R. J., Milisavljevic D., Drout M. R., Kirshner R., 2014, ApJ, 790, 52

Marietta E., Burrows A., Fryxell B., 2000, ApJS, 128, 615

Marion G. H., Höflich P., Wheeler J. C., Robinson E. L., Gerardy C. L., Vacca W. D., 2006, ApJ, 645, 1392

Marion G. H., et al., 2016, ApJ, 820, 92

Matheson T., et al., 2008, AJ, 135, 1598

Matteucci F., Greggio L., 1986, A&A, 154, 279

Mazzali P. A., 2000, A&A, 363, 705

Mazzali P. A., 2001, MNRAS, 321, 341

Mazzali P. A., Hachinger S., 2012, MNRAS, 424, 2926

Mazzali P. A., Lucy L. B., 1993, A&A, 279, 447

Mazzali P. A., Podsiadlowski P., 2006, MNRAS, 369, L19

Mazzali P. A., Lucy L. B., Danziger I. J., Gouiffes C., Cappellaro E., Turatto M., 1993, A&A, 269, 423

Mazzali P. A., Danziger I. J., Turatto M., 1995, A&A, 297, 509

Mazzali P. A., Chugai N., Turatto M., Lucy L. B., Danziger I. J., Cappellaro E., della Valle M., Benetti S., 1997a, MNRAS, 284, 151

Mazzali P. A., Chugai N., Turatto M., Lucy L. B., Danziger I. J., Cappellaro E., della Valle M., Benetti S., 1997b, MNRAS, 284, 151

Mazzali P. A., Cappellaro E., Danziger I. J., Turatto M., Benetti S., 1998, ApJL, 499, L49

Mazzali P. A., Nomoto K., Cappellaro E., Nakamura T., Umeda H., Iwamoto K., 2001a, ApJ, 547, 988

Mazzali P. A., Nomoto K., Patat F., Maeda K., 2001b, ApJ, 559, 1047

Mazzali P. A., Benetti S., Stehle M., Branch D., Deng J., Maeda K., Nomoto K., Hamuy M., 2005a, MNRAS, 357, 200

Mazzali P. A., et al., 2005b, ApJL, 623, L37

Mazzali P. A., Röpke F. K., Benetti S., Hillebrandt W., 2007, Science, 315, 825

Mazzali P. A., Sauer D. N., Pastorello A., Benetti S., Hillebrandt W., 2008, MNRAS, 386, 1897

Mazzali P. A., Maurer I., Stritzinger M., Taubenberger S., Benetti S., Hachinger S., 2011, MNRAS, 416, 881

Mazzali P. A., et al., 2014, MNRAS, 439, 1959

Mazzali P. A., et al., 2015, MNRAS, 450, 2631

Mazzali P. A., et al., 2020, MNRAS, 494, 2809

Mazzali P. A., Benetti S., Stritzinger M., Ashall C., 2022, MNRAS, 511, 5560

McCully C., et al., 2014, Nature, 512, 54

Meng X., Podsiadlowski P., 2013, ApJL, 778, L35

Meng X., Chen X., Han Z., 2007, PASJ, 59, 835

Messier C., 1781, Catalogue des Nébuleuses et des Amas d'Étoiles (Catalog of Nebulae and Star Clusters), Connoissance des Temps ou des Mouvements Célestes, for 1784, p. 227-267

Miller W. C., 1955, Leaflet of the Astronomical Society of the Pacific, 7, 105

Miller A. A., et al., 2018, ApJ, 852, 100

Minkowski R., 1941, PASP, 53, 224

Moriya T. J., Mueller B., Blinnikov S. I., Ushakova M., Sorokina E. I., Tauris T. M., Heger A., 2025, arXiv e-prints, p. arXiv:2507.05506

Munari U., Dallaporta S., Cherini G., 2016, , 47, 7

Nadyozhin D. K., 1994, ApJS, 92, 527

Nagao T., Maeda K., Yamanaka M., 2017, ApJ, 835, 143

Nakano S., Kushida R., Kushida Y., 1999, IAU Circ., 7109, 4

Neill J. D., et al., 2009, ApJ, 707, 1449

Noebauer U. M., Taubenberger S., Blinnikov S., Sorokina E., Hillebrandt W., 2016, Monthly Notices of the Royal Astronomical Society, 463, 2972

Nomoto K., 1982, ApJ, 253, 798

Nomoto K., Iben Jr. I., 1985, ApJ, 297, 531

Nomoto K., Kondo Y., 1991, ApJL, 367, L19

Nomoto K., Nariai K., Sugimoto D., 1979, PASJ, 31, 287

Nomoto K., Thielemann F. K., Yokoi K., 1984, ApJ, 286, 644

Nomoto K., Kobayashi C., Tominaga N., 2013, ARA&A, 51, 457

Nozawa T., Maeda K., Kozasa T., Tanaka M., Nomoto K., Umeda H., 2011, ApJ, 736, 45

Nugent P., Phillips M., Baron E., Branch D., Hauschildt P., 1995a, ApJL, 455, L147

Nugent P., Phillips M., Baron E., Branch D., Hauschildt P., 1995b, ApJL, 455, L147

Nugent P. E., et al., 2011, Nature, 480, 344

O'Brien J. T., et al., 2023, arXiv e-prints, p. arXiv:2306.08137

Oke J. B., et al., 1995, PASP, 107, 375

Olling R. P., et al., 2015, Nature, 521, 332

Paczynski B., Zytkow A. N., 1978, ApJ, 222, 604

Pakmor R., Kromer M., Röpke F. K., Sim S. A., Ruiter A. J., Hillebrandt W., 2010, Nature, 463, 61

Pakmor R., Hachinger S., Röpke F. K., Hillebrandt W., 2011, A&A, 528, A117

Pakmor R., Kromer M., Taubenberger S., Sim S. A., Röpke F. K., Hillebrandt W., 2012, ApJL, 747, L10

Pan Y.-C., Sullivan M., Maguire K., Gal-Yam A., Hook I. M., Howell D. A., Nugent P. E., Mazzali P. A., 2015, MNRAS, 446, 354

Panagia N., Van Dyk S. D., Weiler K. W., Sramek R. A., Stockdale C. J., Murata K. P., 2006, ApJ, 646, 369

Pankey Titus J., 1962, PhD thesis, Howard University, Washington DC

Papish O., Soker N., García-Berro E., Aznar-Siguán G., 2015, MNRAS, 449, 942

Parrent J. T., et al., 2011, ApJ, 732, 30

Parrent J., Friesen B., Parthasarathy M., 2014, Ap&SS, 351, 1

Parrent J. T., et al., 2016, MNRAS, 457, 3702

Parthasarathy M., Branch D., Jeffery D. J., Baron E., 2007, , 51, 524

Pauldrach A. W. A., Duschinger M., Mazzali P. A., Puls J., Lennon M., Miller D. L., 1996, A&A, 312, 525

Perlmutter S., et al., 1998, Nature, 391, 51

Perlmutter S., et al., 1999, ApJ, 517, 565

Phillips M. M., 1993, ApJL, 413, L105

Phillips M. M., 2012, , 29, 434

Phillips M. M., Lira P., Suntzeff N. B., Schommer R. A., Hamuy M., Maza J., 1999, AJ, 118, 1766

Phillips M. M., et al., 2007, PASP, 119, 360

Phillips M. M., et al., 2022, ApJ, 938, 47

Phillips M. M., et al., 2024, ApJS, 273, 16

Pinto P. A., Eastman R. G., 2000, ApJ, 530, 744

Piro A. L., Chang P., Weinberg N. N., 2010, ApJ, 708, 598

Planck Collaboration et al., 2020, A&A, 641, A6

Plewa T., Calder A. C., Lamb D. Q., 2004, ApJL, 612, L37

Podsiadlowski P., 2010, Astronomische Nachrichten, 331, 218

Qiao Q. Y., Wei J. Y., Qiu Y. L., Hu J. Y., 1999, IAU Circ., 7109, 3

Rasio F. A., Shapiro S. L., 1994, ApJ, 432, 242

Raskin C., Scannapieco E., Rockefeller G., Fryer C., Diehl S., Timmes F. X., 2010, ApJ, 724, 111

Reifenstein E. C., Brundage W. D., Staelin D. H., 1969, , 22, 311

Reynolds S. P., Borkowski K. J., Green D. A., Hwang U., Harrus I., Petre R., 2008, ApJL, 680, L41

Reynoso E. M., Hughes J. P., Moffett D. A., 2013, AJ, 145, 104

Riess A. G., Press W. H., Kirshner R. P., 1996, ApJ, 473, 88

Riess A. G., et al., 1998, AJ, 116, 1009

Riess A. G., et al., 2004, ApJ, 607, 665

Riess A. G., et al., 2022, ApJL, 934, L7

Rosswog S., Kasen D., Guillochon J., Ramirez-Ruiz E., 2009, ApJL, 705, L128

Ruiz-Lapuente P., et al., 2004, Nature, 431, 1069

Russell B. R., Immler S., 2012, ApJL, 748, L29

Sahu D. K., et al., 2008, ApJ, 680, 580

Saio H., Nomoto K., 1998, ApJ, 500, 388

Sasdelli M., Mazzali P. A., Pian E., Nomoto K., Hachinger S., Cappellaro E., Benetti S., 2014, MNRAS, 445, 711

Sato Y., Nakasato N., Tanikawa A., Nomoto K., Maeda K., Hachisu I., 2015, ApJ, 807, 105

Scalzo R. A., et al., 2010, ApJ, 713, 1073

Scalzo R., et al., 2012, ApJ, 757, 12

Schaefer B. E., Pagnotta A., 2012, arXiv e-prints, p. arXiv:1201.2195

Schlafly E. F., Finkbeiner D. P., 2011, ApJ, 737, 103

Schlegel D. J., Finkbeiner D. P., Davis M., 1998, ApJ, 500, 525

Seitenzahl I. R., Cescutti G., Röpke F. K., Ruiter A. J., Pakmor R., 2013, A&A, 559, L5

Shappee B. J., Stanek K. Z., Kochanek C. S., Garnavich P. M., 2017, ApJ, 841, 48

Shen K. J., Moore K., 2014, ApJ, 797, 46

Siebert M. R., et al., 2019, MNRAS, 486, 5785

Siebert M. R., et al., 2023a, arXiv e-prints, p. arXiv:2308.12449

Siebert M. R., et al., 2023b, The Astrophysical Journal, 960, 88

Silverman J. M., Filippenko A. V., 2012, MNRAS, 425, 1917

Silverman J. M., et al., 2012a, MNRAS, 425, 1789

Silverman J. M., Kong J. J., Filippenko A. V., 2012b, MNRAS, 425, 1819

Silverman J. M., Kong J. J., Filippenko A. V., 2012c, MNRAS, 425, 1819

Silverman J. M., et al., 2012d, ApJL, 756, L7

Silverman J., Nugent P. E., Gal-Yam A., Howell D. A., Sullivan M., Filippenko A. V., Transient Factory P., 2013, in American Astronomical Society Meeting Abstracts #221. p. 253.06

Silverman J. M., Vinkó J., Marion G. H., Wheeler J. C., Barna B., Szalai T., Mulligan B. W., Filippenko A. V., 2015, MNRAS, 451, 1973

Sim S. A., Röpke F. K., Hillebrandt W., Kromer M., Pakmor R., Fink M., Ruiter A. J., Seitenzahl I. R., 2010, ApJL, 714, L52

Sobolev V. V., 1960, Moving Envelopes of Stars, doi:10.4159/harvard.9780674864658.

Soker N., 2013, in Di Stefano R., Orio M., Moe M., eds, IAU Symposium Vol. 281, Binary Paths to Type Ia Supernovae Explosions. pp 72–75, doi:10.1017/S174392131201472X

Sollerman J., Ghavamian P., Lundqvist P., Smith R. C., 2003, A&A, 407, 249

Southwell K. A., Livio M., Charles P. A., O'Donoghue D., Sutherland W. J., 1996, ApJ, 470, 1065

Sparks W. M., Stecher T. P., 1974, ApJ, 188, 149

Springob C. M., Haynes M. P., Giovanelli R., Kent B. R., 2005, ApJS, 160, 149

Springob C. M., Masters K. L., Haynes M. P., Giovanelli R., Marinoni C., 2007, ApJS, 172, 599

Stahl B. E., et al., 2020, MNRAS, 492, 4325

Stanishev V., et al., 2007, A&A, 469, 645

Stehle M., Mazzali P. A., Benetti S., Hillebrand t W., 2005, MNRAS, 360, 1231

Steinhardt C. L., Sneppen A., Sen B., 2020, ApJ, 902, 14

Stephenson F. R., 1971, , 12, 10

Stephenson F. R., Green D. A., 2002, International Series in Astronomy and Astrophysics, 5

Stritzinger M., Leibundgut B., 2005, A&A, 431, 423

Sullivan M., et al., 2006, ApJ, 648, 868

Sullivan M., et al., 2010, MNRAS, 406, 782

Taddia F., et al., 2012, A&A, 545, L7

Tanaka M., et al., 2008, ApJ, 677, 448

Tanaka M., Mazzali P. A., Stanishev V., Maurer I., Kerzendorf W. E., Nomoto K., 2011, MNRAS, 410, 1725

Taubenberger S., et al., 2011, MNRAS, 412, 2735

Taubenberger S., et al., 2013a, MNRAS, 432, 3117

Taubenberger S., Kromer M., Pakmor R., Pignata G., Maeda K., Hachinger S., Leibundgut B., Hillebrandt W., 2013b, ApJL, 775, L43

Taubenberger S., et al., 2019, MNRAS, 488, 5473

Taylor G., 1950, Proceedings of the Royal Society of London Series A, 201, 192

Theureau G., Hanski M. O., Coudreau N., Hallet N., Martin J. M., 2007, A&A, 465, 71

Thompson T. A., 2011, ApJ, 741, 82

Thoroughgood T. D., Dhillon V. S., Littlefair S. P., Marsh T. R., Smith D. A., 2001, MNRAS, 327, 1323

Timmes F. X., Brown E. F., Truran J. W., 2003, ApJL, 590, L83

Torii K., Tsunemi H., Dotani T., Mitsuda K., Kawai N., Kinugasa K., Saito Y., Shibata S., 1999, ApJL, 523, L69

Trundle C., Kotak R., Vink J. S., Meikle W. P. S., 2008, A&A, 483, L47

Tsebrenko D., Soker N., 2015, MNRAS, 447, 2568

Turatto M., Benetti S., Pastorello A., 2007, in Immler S., Weiler K., McCray R., eds, American Institute of Physics Conference Series Vol. 937, Supernova 1987A: 20 Years After: Supernovae and Gamma-Ray Bursters. pp 187–197 (arXiv:0706.1086), doi:10.1063/1.3682902

Vanvan van Driel W., et al., 2016, A&A, 595, A118

Vink J., Bleeker J., van der Heyden K., Bykov A., Bamba A., Yamazaki R., 2006, ApJL, 648, L33

Wang B., Han Z., 2010, A&A, 515, A88

Wang L., Wheeler J. C., 2008, ARA&A, 46, 433

Wang X., et al., 2009, ApJL, 699, L139

Wang L., et al., 2016, Imaging Polarimetry of Light Echoes around SN 2014J, HST Proposal. Cycle 24, ID. #14663

Waxman E., Katz B., 2017, in Alsabti A. W., Murdin P., eds, , Handbook of Supernovae. p. 967, doi:10.1007/978-3-319-21846-5_33

Webbink R. F., 1984, ApJ, 277, 355

Wei J.-J., Wu X.-F., 2017, ApJ, 838, 160

Wheeler J. C., Harkness R. P., 1986, in Madore B. F., Tully R. B., eds, NATO Advanced Study Institute (ASI) Series C Vol. 180, Galaxy Distances and Deviations from Universal Expansion. pp 45–54

Whelan J., Iben Icko J., 1973, ApJ, 186, 1007

Willick J. A., Courteau S., Faber S. M., Burstein D., Dekel A., Strauss M. A., 1997, ApJS, 109, 333

Wolf W. M., Bildsten L., Brooks J., Paxton B., 2013, ApJ, 777, 136

Wood-Vasey W. M., Sokoloski J. L., 2006, ApJL, 645, L53

Woods T. E., Gilfanov M., 2013, MNRAS, 432, 1640

Woosley S. E., Weaver T. A., 1986, The Physics of Supernovae. p. 91, doi:10.1007/3-540-16764-1_7

Woosley S. E., Weaver T. A., 1994, ApJ, 423, 371

Woosley S. E., Arnett W. D., Clayton D. D., 1973, ApJS, 26, 231

Woosley S. E., Kasen D., Blinnikov S., Sorokina E., 2007a, ApJ, 662, 487

Woosley S. E., Kasen D., Blinnikov S., Sorokina E., 2007b, ApJ, 662, 487

Yamanaka M., et al., 2016, PASJ, 68, 68

Yang J., et al., 2022, ApJ, 938, 83

Yaron O., Gal-Yam A., 2012, PASP, 124, 668

Yaron O., Prialnik D., Shara M. M., Kovetz A., 2005, ApJ, 623, 398

Yoon S. C., Langer N., 2005, A&A, 435, 967

Yoon S. C., Podsiadlowski P., Rosswog S., 2007, MNRAS, 380, 933

Yoshida S., Kadota K., Kiss L., Csak B., Moretti S., Tomaselli S., 1999, IAU Circ., 7139, 3

Yungelson L., Livio M., 1998, ApJ, 497, 168

Yungelson L. R., Livio M., 2000a, ApJ, 528, 108

Yungelson L. R., Livio M., 2000b, ApJ, 528, 108

Zhang K., et al., 2016, ApJ, 820, 67

Zheng W., et al., 2013, ApJL, 778, L15